


# NUMERICAL MODELLING OF THE TILT CASTING PROCESSES

by

Hong Wang



Centre for Numerical Modelling and Process Analysis, School of Computing and  
Mathematical Sciences, the University of Greenwich,  
London, U.K.



A thesis submitted in partial fulfilment of the requirements of the University of  
Greenwich for the Degree of Doctor of Philosophy

November 2008

# Abstract

This research has investigated the modelling and optimisation of the tilt casting process of Titanium Aluminides (TiAl). This study is carried out in parallel with the experimental research undertaken in IRC at the University of Birmingham. They propose to use tilt casting inside a vacuum chamber and attempt to combine this tilt casting process with Induction Skull Melting (ISM). A totally novel process is developing for investment casting, which is suitable for casting gamma TiAl.

As it is known, gamma TiAl alloys has great properties including low density, high specific yield strength, high specific stiffness, good oxidation resistance and good creep resistance at high temperature [Clemens -2000][Appel *et al.* -2000]. A worldwide research effort has been made to develop gamma TiAl because it can offer a great potential for reducing the weight of high performance components and also engine of power generation gas turbine. Titanium alloys are very reactive at molten condition, and so, they are melted in an ISM crucible in order to avoid crucible contamination. There is still a big challenge to produce a long blade, up to 40 cm, due to the low superheat provided by the Induction Skull Melting (ISM) furnace which is widely used to melt the alloys. Here computational simulation has been seen important to predict the casting defects and to help optimise the experimental process.

Computational modelling for the casting process involves a range of interactions of physical phenomena such as heat transfer, free surface fluid flow, solidification and so on. A number of free surface modelling techniques are applied to simulate the interface between the molten metal entering the mould in the filling phase, and the gas escaping.



The CFD code PHYSICA developed in the University of Greenwich is used to simulate the above physical phenomena and to simulate the fluid flow both within the rotating mould cavity/crucible assembly and in the porous mould wall (including vents).

Modelling the mould in a finite volume method is cumbersome, so an alternative 3D/1D coupled transient heat transfer model has been developed in this study. It is based on the fact that the mould filling for titanium aluminide (TiAl) is carried out during a few seconds and the thermal conductivity of the mould material is very low. Heat can be assumed to transfer mainly in a direction perpendicular to the mould wall—1D. 1D transient heat transfer model is governed by 1D heat conduction equation in the mould part where the coordinates of each defined cell centre were calculated rather than meshing them. The coupling method between 1D and 3D model is presented. The model is then validated using two simple geometries which describe two similar states in the mould filling as test cases. It has been applied to model short thin and long blades, especially to obtain accurate thermal boundaries. Comparisons with experiments have also been done. Across the presentation of the results, the factors affect the quality of the casting in the mould filling have been discussed.

This thesis also presents a novel Counter Diffusion Method which was developed with suggestions from my supervisors as a corrective mechanism to counter numerical diffusion. This is a novel method to discretise the free surface equation fully implicitly in a fast, efficient way without numerical diffusion. Validation of the novel method was undertaken against the classical collapsing column experiment. The results showed that they are in good agreement. Then the method has been used to model a long thin blade for TiAl. A huge reduction in computational time is seen when the geometry is complex and massive amount of mesh cells are generated. That greatly speeds up the simulations.

Solidification is modeled during the cooling which is following the filling stage. Gap formation between metal and mould is covered and the effects of the gap and gap size are presented by the application of model on a long twisted turbine blade.

# Acknowledgements

Firstly, I would like to express my gratitude to my supervisors Professor Koulis Pericleous and Dr. Georgi Djambazov for their advice, encouragement and guidance throughout my PhD studies. I would like to thank colleagues at the University of Greenwich who have provided support. I would also like to make a mention to Dr. Mayur Patel and Dr. Stoyan Stoyanov who have given me help for using Rhino and Harpoon.

I would like to thank my parents for their understanding during these years. In particular, I am grateful for their support for taking care of my daughter who is born in my last year's PhD study. And my husband, Mr. Pengfei Liu, his encouragement and support have helped me pass the difficult times during these years' overseas studies.

Finally, I would like to acknowledge European Union Project IMPRESS (Inter-metallic Materials Processing in Relation to Earth and Space Solidification) which is co-funded by the European Space Agency and the European Commission in the 6<sup>th</sup> Framework Programme for funding this research.

# Table of Contents

<b>ABSTRACT</b> .....	<b>I</b>
<b>ACKNOWLEDGEMENTS</b> .....	<b>III</b>
<b>TABLE OF CONTENTS</b> .....	<b>IV</b>
<b>LIST OF FIGURES</b> .....	<b>X</b>
<b>LIST OF TABLES</b> .....	<b>X</b>
<b>NOMENCLATURE</b> .....	<b>XVII</b>
<b>PREFACE</b> .....	<b>1</b>
<b>CHAPTER 1: INTRODUCTION</b> .....	<b>2</b>
1.1 Objectives of this Research .....	2
1.2 Challenges in Casting TiAl Alloys.....	3
1.3 Contributions of this Study.....	4
1.4 Layout of this Thesis.....	6
<b>CHAPTER 2: LITERATURE REVIEW</b> .....	<b>9</b>
2.1 Casting Methods .....	9
2.1.1 Tilt Casting .....	9
2.1.2 Counter Gravity Casting .....	11
2.1.3 Centrifugal Casting.....	12
2.2 Titanium Aluminides and Challenges in Melting TiAl Alloys .....	13

2.3	Numerical Methods .....	17
2.3.1	Review of codes for mould filling in castings.....	18
2.3.2	Review of Computational Methods for Free Surface Flows.....	19
2.4	Discretisation Techniques.....	21
2.4.1	Finite Difference Method.....	21
2.4.2	Finite Volume Method .....	22
2.5	Multi-physics modelling software package- PHYSICA .....	24
<b>CHAPTER 3: THE NUMERICAL MODELS .....</b>		<b>26</b>
3.1	General Transport Equations.....	26
3.2.1	Fluid Flow Equations .....	27
3.2.2	Heat Transfer and Solidification.....	27
3.2.3	Free Surface Model .....	29
3.2.3.1	Van Leer Method .....	30
3.2.3.2	Donor Acceptor Method .....	32
3.2.3.3	Surface Tension Coupled with Van Leer and Donor Acceptor Method .....	35
3.2.3.4	Level Set Method .....	36
3.2.3.4.1	Review of Level Set Method.....	36
3.2.3.4.2	Governing Equations .....	38
3.2.3.4.3	Surface Tension Coupled with Level Set Method .....	43
3.2.4	Turbulence Flow Model.....	45
3.2.4.1	Standard $k-\varepsilon$ Model .....	45
3.2.4.2	$k-\omega$ Model .....	46
3.2.4.3	LVEL Turbulence Model.....	47
3.3	Summary .....	48
<b>CHAPTER 4: TILT CASTING METHOD .....</b>		<b>49</b>
4.1	Introduction.....	50
4.2	Mathematical Description.....	50
4.3	Modelling Tilt Casting with PHYSICA.....	52

4.4	Validation: ‘I’-shaped Test Piece .....	52
4.4.1	Experimental Descriptions .....	52
4.4.2	Dimensions of Test Piece and Design of Mould .....	53
4.4.3	Geometry and Computational Mesh .....	56
4.4.4	Initial Conditions and Boundary Conditions .....	57
4.4.5	Filling Modes .....	57
4.4.6	Presentation of Results .....	58
4.4.6.1	Effects of Surface Tension .....	58
4.4.6.2	Comparisons of the Experimental and Numerical Results .....	61
4.4.6.3	Other Parameters Affecting on the Tilt Casting Process .....	67
4.4.6.3.1	Filling Modes .....	67
4.4.6.2.2	Orientation of the Mould .....	69
4.6	Summary .....	70
<b>CHAPTER 5: 3D/1D COUPLED TRANSIENT HEAT TRANSFER MODEL .....</b>		<b>72</b>
5.1	Introduction .....	73
5.2	Model Descriptions .....	74
5.3	Mathematical Descriptions .....	75
5.3.1	Assumptions and Boundary Conditions: .....	75
5.3.2	Numerical Methods: Finite Difference Method .....	76
5.4	Coupling .....	77
5.4.1	Stability .....	79
5.4.2	Approximation .....	79
5.5	Algorithm .....	80
5.6	Validation of 3D/1D Coupled Transient Heat Transfer .....	80
5.6.1	Test case1 .....	81
5.6.1.1	Computational Mesh .....	81
5.6.1.2	Initial and Boundary Conditions .....	81
5.6.1.3	Presentation of Results .....	83
5.6.1.4	Computational Comparisons .....	87
5.6.2	Test Case 2 .....	88

5.6.2.1	Computational Mesh .....	88
5.6.2.2	Initial and Boundary Conditions.....	89
5.6.2.3	Presentation of Results .....	90
5.6.2.4	Run-time Comparisons .....	92
5.7	Summary .....	92
5.8	Model Application: Validation of a Short Turbine Blade and Discussion of the Tilt Casting Parameters.....	93
5.8.1	Experimental Description.....	93
5.8.2	Dimensions of a Short Turbine Blades and Mould Design .....	94
5.8.3	Computational Mesh .....	95
5.8.4	Initial Conditions .....	96
5.8.5	Venting .....	97
5.8.6	Filling Mode .....	98
5.8.7	Presentation of Results .....	100
5.8.7.1	Impact of the number and the position of vent on mould filling.....	101
5.8.7.2	Validation and comparisons of the experimental and numerical results .....	103
5.8.7.3	Comparisons of the simulations with 1D transient heat transfer boundary and using the fixed heat transfer coefficient as a thermal boundary condition .....	107
5.8.8	Melt Weight.....	110
5.8.8.1	Geometry and Computational Mesh.....	111
5.8.8.2	Initial and Boundary Conditions.....	111
5.8.8.3	Presentation of Results.....	112
5.9	Summary .....	113
<b>CHAPTER 6: THE COUNTER DIFFUSION METHOD.....</b>		<b>115</b>
6.1	Introduction.....	116
6.2	Mathematical Description.....	117
6.3	Algorithm .....	119
6.4	Validation of the Counter Diffusion Method (CDM).....	120

6.4.1	Test case specification.....	120
6.4.2	Initial and Boundary Conditions.....	120
6.4.3	Results and discussion.....	121
6.4.3.1	Comparisons of CDM with experimental results.....	121
6.4.3.2	Comparisons of CDM with others usual numerical methods.....	124
6.5	Application of the Counter Diffusion Method (CDM).....	128
6.5.1	Geometry and Computational Mesh.....	128
6.5.2	Boundary and Initial Conditions.....	136
6.5.3	Presentations of Results .....	136
6.5.3.1	Effect of the locations of the blade .....	136
6.5.3.2	Predictions of Defects at the End of Filling .....	143
6.5.3.3	Comparison of Two Methods: Van Leer and CDM .....	144
6.5.3.4	Comparison of the mould filling between straight and twisted blades .....	146
6.6	Summary .....	148
<b>CHAPTER 7: SOLIDIFICATION.....</b>		<b>150</b>
7.1	Introduction.....	151
7.2	Mathematical Description.....	152
7.2.1	Assumptions and Boundary Conditions .....	152
7.2.2	Coupling .....	153
7.4	Numerical Examples.....	155
7.4.1	Geometry and Computational mesh .....	155
7.4.2	Initial and Boundary Conditions.....	157
7.5	Results and Discussion .....	158
7.5.1	Effects of Gap.....	158
7.5.2	Temperature.....	164
7.5.3	Effects of Gap Size.....	169
7.6	Summary .....	172

<b>CHAPTER 8: CONCLUSIONS AND FUTURE WORK.....</b>	<b>173</b>
8.1 Conclusions.....	173
8.2 Future Work .....	176
8.2.1 Further Investigation on Surface Tension.....	176
8.2.2 Solidification .....	176
8.2.2 Casting Defects during Solidification.....	177
<b>REFERENCES.....</b>	<b>178</b>
<b>APPENDIX A: INFORM FILE FOR THE VALIDATION OF THE 3D/1D MODEL</b> .....	<b>195</b>
<b>APPENDIX B: MATHEMATIC DESCRIPTIONS FOR POROUS MEDIUM AND</b> <b>PIPE FLOW .....</b>	<b>202</b>
<b>APPENDIX C: MOULD FILLING FOR A TWISTED BLADE .....</b>	<b>206</b>
<b>APPENDIX D: INFORM FILE FOR MODELLING THE SOLIDIFICATION ...</b>	<b>229</b>



# List of Figures

Figure 2.1: Schematic view of tilt casting..... 10

Figure 2.2: Schematic view of counter gravity casting (a) and centrifugal casting (b). ..... 11

Figure 2.4: Vacuum or under a partial pressure of argon melting chamber containing an  
ISM furnace [taken by M. Wickins, Birmingham University]..... 15

Figure 2.5: Schematic view of the ‘semi-levitation’ melting furnace (courtesy of Zhu and  
Harding [Zhu and Harding -96]) ..... 16

Figure 2.6: One example of experimental result and numerical prediction of casting  
defects for one vent, i.e. mis-run [Harding *et al.* -07]. ..... 17

Figure 2.7: Improved experimental result under help of numerical results: one more vent is  
made at the end of the trailing edge [Harding –Sep 06] ..... 18

Figure 3.1: Configuration of Van Leer Method..... 30

Figure 3.2: Configuration of Donor-Acceptor Method ..... 32

Figure 3.3: Solution Procedure for Van Leer and Donor Acceptor Methods. .... 34

Figure 3.4: Configuration of the Level Set Method..... 38

Figure 3.5: Solution Procedure for Level Set Method..... 42

Figure 3.6: Illustration of contact angle. .... 44

Figure 4.1: Process of tilt casting ..... 50

Figure 4.2: Schematic view of the gravity in tilt casting model..... 51

Figure 4.3: Tilt casting wheel used (Note: this does not show the mould used in the  
trials)[Harding -05]. ..... 53

Figure 4.4: The design and dimensions of ‘I’-shaped test piece. .... 54

Figure 4.5: Set-up for validating trials. .... 55

Figure 4.6: The design of the mould in the trials. .... 55

Figure 4.7: Computational meshes of the model for two orientations of the test ‘I’ piece. .56

Figure 4.8: Comparisons of numerical results with different surface tension values at 8.5s.	59
Figure 4.9: Comparisons of numerical results with different surface tension values at 9.5s.	60
Figure 4.10: Comparisons of numerical results with different surface tension values at 10.5s.	61
Figure 4.11: Comparison of experimental and numerical results at 8.0s and 9.0s.	62
Figure 4.12: Comparison of experimental and numerical results at 8.0, 8.5 and 9.0s.	64
Figure 4.13: Comparison of experimental and numerical results at 9.5, 10 and 10.5s.	65
Figure 4.14: Comparison of experimental and numerical results at 11, 11.5 and 12.0s.	66
Figure 4.16: Surface turbulence during quick mould filling: programmed rotation (upper) and 20 degree/s (lower).	68
Figure 4.17: Comparison of two orientations in free surface contour at 120 degrees.	69
Figure 4.18: Comparison of two orientations in free surface contour at 180 degrees.	70
Figure 5.1: The velocity profiles in the boundary layer during the mould filling when solidification first starts at the wall.	73
Figure 5.2: Coupling of 3D PHYSICA model and 1D transient heat transfer.	75
Figure 5.4: Solution Procedure for the 3D/1D model.	80
Figure 5.5: Computational mesh for PHYSICA (above) and 3/1D model (below)	81
Figure 5.6: Comparisons of temperature ‘TN’ (a) and liquid fraction ‘LFN’ (b) with the two different methods: PHYSICA and 3D/1D model at 0.1s.	84
Figure 5.7: Comparisons of temperature ‘TN’ (a) and liquid fraction ‘LFN’ (b) with the two different methods: PHYSICA and 3D/1D model at 0.2s.	84
Figure 5.8: Comparisons of temperature ‘TN’ (a) and liquid fraction ‘LFN’ (b) with the two different methods: PHYSICA and 3D/1D model at 0.3s.	85
Figure 5.9: Comparisons of temperature ‘TN’ (a) and liquid fraction ‘LFN’ (b) with the two different methods: PHYSICA and 3D/1D model at 0.4s.	85
Figure 5.10: Comparisons of temperature ‘TN’ (a) and liquid fraction ‘LFN’ (b) with the two different methods: PHYSICA and 3D/1D model at 0.5s.	86
Figure 5.11: Comparisons of the mould temperature using PHYSICA and 3D/1D model at 0.5s at x=1.25 mm (a) and x=46.25 mm (b) along x direction.	87
Figure 5.12: Schematic figure of test piece and computational mesh.	89

Figure 5.13: Comparisons of the contours of temperature with PHYSICA and 3D/1D model at 30.s .....90

Figure 5.14: Comparisons of the mould temperature for methods, PHYSICA and 3D/1D model at cell 1, cell 48, cell 5 and cell 6 at 30.s.....91

Figure 5.15: Tilt casting equipment (ISM) is heating the mould and mould heater is moved away in an open position. ....94

Figure 5.16: (a) The design and dimensions of the blades and (b) mould. ....95

Figure 5.17: Computational mesh. ....96

Figure 5.18: (a) Example of the porous medium and (b) Approximated vent in a mould. ..97

Figure 5.19: Tilt casting process: (a) Schematic; (b) Different stages of filling.....99

Figure 5.20: Parabolic programmed cycle: the theoretical Greenwich code and experimental cycle adopted in the actual trial by IRC Birmingham. .... 100

Figure 5.21: Difference of one vent and two vents in free surface contours at the 3.1s.... 101

Figure 5.22: Difference of one vent and two vents in stream traces at the 2.6s. .... 102

Figure 5.23: Difference of one vent and two vents in stream traces at the 3.1s. .... 102

Figure 5.24: Comparisons of the experimental and numerical results with one vent..... 103

Figure 5.25: Comparisons of the experimental and numerical results with two vents. .... 104

Figure 5.26: Numerical results of the blade cross-section in heat transfer and in free surface contour with two vents at the 4.5s (6.0s)..... 105

Figure 5.27: Numerical results of the blade cross-section in heat transfer and in free surface contour with two vents at the 5.0s (6.0s)..... 106

Figure 5.28: Poor top surfaces of experimental short turbine blades [Harding –Sep 06]... 107

Figure 5.29: Comparison of the numerical results for one vent with 1D transient heat transfer boundary (method A: on the left) and the fixed heat transfer coefficient as the thermal boundary conditions (method B: on the right). .... 108

Figure 5.30: Comparison of the numerical results for two vents with 1D transient heat transfer boundary (method A: on the left) and the fixed heat transfer coefficient as the thermal boundary conditions (method B: on the right). .... 109

Figure 5.31: Comparison of simulated temperatures in various melt weights of TiAl during a typical stepwise melting schedule using a 7kHz AC field [Bjarevics -04]..... 110

Figure 5.32: Comparisons of the simulations with large (left) and small bush (right) at the end of filling in liquid temperature.....	112
Figure 5.33: Comparisons of the simulations with large and small bush at 1.2s.....	113
Figure 6.1: Solution Procedure for Counter Diffusion Methods.....	119
Figure 6.2: Configuration of water column collapsing.....	120
Figure 6.3: Comparisons of the numerical results with experimental results for the front position of the collapsing water column (Martin & Moyce in 1952).....	122
Figure 6.4: Comparisons of the numerical results with experimental results for the residual height of the collapsing water column (Martin & Moyce in 1952) .....	122
Figure 6.5: Free surface profiles for the collapse of water column with the CDM method	123
Figure 6.6: Free surface profiles of the collapsing water column in experiment (Martin & Moyce in 1952) .....	124
Figure 6.7: Comparisons of the numerical results in Van Leer, Donor Acceptor, LSM and CDM for the residual height of the collapsing water column. ....	125
Figure 6.8: Comparisons of the numerical results in Van Leer, Donor Acceptor, LSM and CDM for the residual height of the collapsing water column. ....	125
Figure 6.9: Comparisons of the numerical results in Van Leer, Donor Acceptor, LSM and CDM in $\Phi$ at 2s. ....	126
Figure 6.10: Real shape of 400mm long turbine blade.....	129
Figure 6.11: Computational mesh of real shape turbine blade in Harpoon. ....	130
Figure 6.12: Approximated straight turbine blade. ....	131
Figure 6.13: Sectioned view of the computational mesh of the approximated straight turbine blade length of 400mm in Harpoon. ....	132
Figure 6.14: Locations: 1) Blade root perpendicular to tilt plane and located to maintain full contact with basin and; 2) Blade root perpendicular to tilt plane and as far to right as possible.....	133
Figure 6.15: Computational mesh: blade located in the middle of pouring basin .....	134
Figure 6.16: Computational mesh: blade located at the edge of the pouring basin .....	135
Figure 6.17: Comparisons of the volume fraction of metal ( $\Phi$ ) at 2.7 s for the two alternative blade ingate locations. ....	137

Figure 6.18: Comparisons of the volume fraction of metal ( $\Phi$ ) at 3.2s for the two alternative blade ingate locations. ....	138
Figure 6.19: Comparisons of cross-section of the blade at the height 35, 45 and 55cm in volume fraction of metal ( $\Phi$ ) and in temperature at 2.7s for ingate location 1. ....	139
Figure 6.20: Comparisons of cross-section of the blade at the height 35, 45 and 55cm in volume fraction of metal ( $\Phi$ ) and in temperature at 2.7s for ingate location 2. ....	140
Figure 6.21: Comparisons of cross-section of the blade at the height 35, 45 and 55cm in volume fraction of metal ( $\Phi$ ) and in temperature at 3.2s for ingate location 1. ....	141
Figure 6.22: Comparisons of cross-section of the blade at the height 35, 45 and 55cm in volume fraction of metal ( $\Phi$ ) and in temperature at 3.2s for ingate location 2. ....	142
Figure 6.23: Comparisons of the liquid fraction (LFN) at 5.5 and 6s for ingate location 2.	143
Figure 6.24: The volume fraction of metal ( $\Phi$ ) at 6s for ingate location 2.....	144
Figure 6.25: Comparisons of the volume fraction of metal ( $\Phi$ ) at 3.2s for the two methods: Van Leer and CDM. ....	145
Figure 6.26: Comparisons of computational mesh between straight and twisted blades. ..	146
Figure 6.27: Comparisons of the volume fraction of metal ( $\Phi$ ) between straight and twisted blades at 3.2s. ....	147
Figure 6.28: Comparisons of the volume fraction of metal ( $\Phi$ ) between straight and twisted blades at the end of filling.....	148
Figure 7.1: variable air gap in a casting (courtesy of John Campbell [Campbell -91]).....	151
Figure 7.2: An air gap in a casting.....	153
Figure 7.4: Computational mesh. ....	156
Figure 7.5: Comparisons of the temperature contours 'TN' of the blade between having a gap and no gap at 90s.....	159
Figure 7.6: Comparisons of the liquid fraction contours 'LFN' of the x-y cross sections of the blade between having a gap and no gap at 130s. ....	160
Figure 7.7: Comparisons of the liquid fraction contours 'LFN' of the x-y cross sections of the blade between having a gap and no gap at 150s. ....	161
Figure 7.8: Comparisons of the liquid fraction contours 'LFN' of the y-z cross sections of the blade between having a gap and no gap at 130s. ....	162

Figure 7.9: Comparisons of the liquid fraction iso-surface ‘LFN=0.35’ of the blade between having a gap and no gap at 130s. ....	163
Figure 7.10: Reference location of simulations in the blade. ....	164
Figure 7.11: Temperatures in the last cell centre of metal and in the mould wall with no gap at variable time. ....	165
Figure 7.12: Temperatures in the last cell centre of metal and in the mould wall with a gap (0.0005 mm) at variable time. ....	167
Figure 7.13: Temperatures of the interface between metal and mould with a gap and with no gap during 150s. ....	168
Figure 7.14: Temperatures of the external mould wall with a gap and no gap during 150s.	168
Figure 7.15: Comparisons of the liquid fraction contours ‘LFN’ of the x-y cross sections of the blade between variable gap sizes at 150s. ....	169
Figure 7.16: Comparisons of the liquid fraction contours ‘LFN’ of the y-z cross sections of the blade between variable gap sizes at 150s. ....	170
Figure 7.17: Temperatures of the interface between metal and mould with variable gap sizes during 150s. ....	171
Figure 7.18: Temperatures of the external mould wall with variable gap sizes during 150s.	171
Figure B.1: Moody chart for pipe flow. ....	204

# List of Tables

Table 4.1: The experimental details in the trial.....	57
Table 4.2: The programmed filling mode .....	58
Table 5.1: The initial conditions of the numerical model.....	82
Table 5.2: Description of the parameters in the 1D model.....	83
Table 5.3: Comparisons of the simulations using 3D/1D transient model (A) and using PHYSICA (B) to model the heat transfer through the mould wall. ....	88
Table 5.4: The initial conditions of the numerical model.....	89
Table 5.5: Comparisons of the simulations using 3D/1D transient model (A) and using PHYSICA (B) to model the heat transfer through the mould wall. ....	92
Table 5.6: The initial conditions of the numerical model.....	96
Table 5.7: Standard Programmed Cycle .....	100
Table 5.8: Comparisons of the simulation with 1D transient heat transfer boundary (A) and that using fixed heat transfer coefficient as the heat boundary conditions (B).....	109
Table 5.9: The initial conditions of the numerical model for small bush .....	111
Table 5.10: The initial conditions of the numerical model for large bush.....	111
Table 6.1: The fluid properties .....	121
Table 6.2: Comparisons of the efficiency of CDM with others numerical methods .....	127
Table 6.3: The initial conditions of the numerical model.....	136
Table 6.4: Comparison of computational time in Van Leer, Donor Acceptor and CDM ..	145
Table 7.1: The boundary conditions of the numerical model.....	157
Table 7.2: The initial conditions of the numerical model.....	157
Table 7.3: Description of the parameters in the 1D model.....	158
Table 7.4: The metal temperature in the last cell centre to the mould wall during solidification (the freezing temperature 1534.5 °C).....	167

# Nomenclature

## *Roman letters*

$A$	area.....	33
$A_f$	area of a face.....	24
$c_p$	specific heat.....	27
$C$	model constant.....	29
$C_\mu$	model constant.....	45
$C_{1\varepsilon}$	model constant .....	45
$C_{2\varepsilon}$	model constant .....	45
$C_x$	coefficient of scalar equation.....	116
$D_x$	diffusion coefficient of scalar equation.....	116
$d_{AP}$	distance between cell centres.....	40
$f_L$	liquid fraction.....	28
$F_\sigma$	force caused by surface tension.....	35
$g$	gravity.....	28
$J$	curvature.....	36
$k$	thermal conductivity.....	28
$k$	turbulent kinetic energy.....	45
$K$	permeability.....	28
$L$	latent heat.....	28



$L$	a distance from the nearest wall in LEVEL model.....	47
$L_{max}$	maximum distance between a element centre and one of its neighbourings'..	44
$m$	unit vector tangential to the interface and normal to the volume of fluid.....	35
$n$	normal.....	20
$n_{ijk}$	normal.....	43
$p$	pressure.....	35
$q$	convection flux.....	116
$Q$	artificial counter diffusion flux.....	116
$R$	radius of curvature.....	35
$Re$	Reynolds number.....	48
$R_t$	turbulent Reynolds number.....	46
$S$	sign function.....	39
$S_\phi$	source term in general equation.....	27
$S_u$	source term in momentum equation.....	27
$S_h$	source term in enthalpy conservation equation.....	27
$S_\gamma$	source term including surface tension effect.....	35
$S_x$	source term of scalar equation.....	116
$t$	time.....	23
$T$	Temperature.....	28
$T_L$	liquidus temperature.....	28
$T_l$	metal temperature.....	74
$T_{freezing}$	freezing temperature.....	151
$T_S$	solidus temperature.....	28
$T_w$	temperature between metal and mould.....	74

$T_x$	coefficient of scalar equation.....	116
$\underline{u}$	velocity vector.....	23
$u$	velocity in y-direction.....	45
$u_e$	velocity at the east face of the cell.....	31
$u_w$	velocity at the west face of the cell.....	31
$v$	velocity in y-direction.....	45
$V$	volume.....	43
$V_D$	volume of donor element.....	33
$w$	velocity in z-direction.....	45
$\Gamma$	diffusion coefficient.....	27

*Greek letters*

$\alpha$	coefficient in general equation.....	27
$\alpha$	thermal diffusivity.....	75
$\alpha^*$	model constant.....	46
$\alpha_{metal}$	thermal expansion coefficient of metal.....	151
$\alpha_m$	thermal expansion coefficient of mould.....	151
$\beta$	model constant.....	46
$\phi$	scalar variable.....	27
$\Phi$	fluid maker.....	29
$\Phi_{AD}$	value of $\Phi$ in either donor or acceptor element.....	33
$\Phi_D$	value of $\Phi$ in donor element.....	33
$\Phi_e$	value of $\Phi$ at the eastern cell.....	31
$\Phi_{down}$	downwind value of $\Phi$ .....	117

$\Phi_{up}$	upwind value of $\Phi$ .....	117
$\Phi_f$	value of $\Phi$ in each face.....	39
$\Phi_P$	value of $\Phi$ at cell centre .....	31
$\Phi_w$	value of $\Phi$ at the western cell .....	31
$\rho$	density.....	23
$\rho_f$	face density .....	23
$\theta$	rotation angle at time t.....	51
$\theta_0$	rotation angle at time $t_0$ .....	51
$\theta_t$	rotation angle at time $t_t$ .....	51
$\theta_c$	contact angle.....	44
$\mu$	dynamic viscosity.....	27
$\mu_l$	laminar viscosity.....	45
$\nu_l$	laminar kinematic viscosity.....	47
$\nu_t$	effective turbulent viscosity.....	27
$\gamma$	surface tension.....	35
$\gamma_{LG}$	surface tension between liquid and gas.....	44
$\gamma_{SG}$	surface tension between solid and gas.....	44
$\gamma_{SL}$	surface tension between solid and liquid.....	44
$\delta_{ij}$	Kronecker delta function.....	43
$\sigma$	Stefan-Boltzmann constant.....	154
$\sigma_k$	model constant.....	45
$\sigma_\omega$	model constant.....	45
$\sigma_\epsilon$	model constant.....	45
$\sigma_T$	turbulent Prandtl.....	28

$\tau$	pseudo time.....	40
$\lambda_{liq}$	thermal conductivities of metal.....	77
$\lambda_{gas}$	thermal conductivities of gas.....	153
$\lambda_{mix}$	combination of thermal conductivities of gas and metal.....	153
$\lambda_{mod}$	thermal conductivities of mould.....	77
$\varepsilon$	turbulent dissipation rate.....	45
$\varepsilon_l$	emissivity of metal.....	153
$\varepsilon_m$	emissivity of mould material.....	152
$\Delta t$	time-step size.....	23
$\Delta t_{1D}$	time-step size.....	79
$\Delta t_{3D}$	time-step size.....	79

## Preface

The work presented in this thesis is sponsored by the European Union project—*IMPRESS (Intermetallic Materials Processing in Relation to Earth and Space Solidification)*. *IMPRESS* is an integrated project in the EC's 6<sup>th</sup> Framework Programme (FP6) and is managed by the European Space Agency (ESA) and is co-funded by the European Commission. That is a total of 5-year project in the field of applied material science and stated in November 2004. *IMPRESS* comprises of 42 research groups and companies involving over 150 leading scientists from 15 countries.



*IMPRESS* objective is to understand, develop and test the properties of new intermetallic alloys which have potential for the different applications in the future:

- 40cm light weight cast  $\gamma$ -TiAl gas turbine blades for the next generation of aero-engine and components to power generation systems.
- Advanced catalytic powders for hydrogen fuel cells and hydrogenation reactions.



The research presented in this thesis belongs to the first part: Modelling the castings of  $\gamma$ -TiAl turbine blades. Using the data gained by the experimentation performed in space is to validate the computer models and the numerical results will ultimately provide support to optimise experimental or industrial casting processes.

# Chapter 1

## Introduction

### 1.1 Objectives of this Research

The main objective of this PhD study is to develop numerical methods for modelling the tilt casting process, housed inside a chamber in combination with an Induction Skull Melting crucible which is used to melt alloys. This is a completely novel process, experimentally studied by IRC-Birmingham. The numerical results will provide a support to help validate and optimise the experimental process.

The filling of the mould is the essential part on the tilt casting process, which basically has three phases as it involves liquid metal, gas and possibly solidified metal. The computational model should have the ability to efficiently model free surface fluid flow, heat transfer and solidification, or sometimes turbulent flow. In this study, further improvements are made to traditional methods in order to meet the requirement for simulating TiAl Turbine blades. Initially the target was to model the casting of a 20 cm turbine blade and eventually to simulate a length up to 40 cm.

## 1.2 Challenges in Casting TiAl Alloys

Now it is well known that gamma TiAl has great potential as the material of certain high performance components such as turbine blades, turbocharger rotors due to the attractive high temperature properties. TiAl alloys offer low density, high temperature oxidation resistance and a relatively high modulus of elasticity [Wu -06]. Although extensive efforts have been made to develop the application of the gamma titanium aluminide alloys, there are still some challenges in technology which hold back from further development.

The essential difficulty is that TiAl alloys in molten condition are very reactive. That makes them easily contaminated when the alloys are molten in a melting crucible made using conventional materials (i.e. Calcium oxide, ceramic) and when the filling is carried out in the mould. The alloy reacts with the material of the crucible when being melted. Oxygen pick up from the ceramic moulds often occurs during casting. That leads to a deleterious effect in the mechanical properties, such as a strong increase of fragility and alloy embrittlement [Harding -05].

To avoid crucible contamination, Induction Skull Melting (ISM) furnaces now with a water-cooled copper crucible are typically applied to melt the alloys. The water cooling will result in great heat loss. Although modern ISM furnaces have improved and reduced the heat loss, the superheat reached is just to 40~50°C [Harding *et al.* -05]. When pouring is undertaken, heat is rapidly lost due to the contact of the melt alloys and the copper crucible wall. This could lead to incomplete filling, particularly for producing a long thin turbine blade. Therefore, the low superheat provided by ISM is still thought as a challenge to cast TiAl components [Harding *et al.* -07].

The IMPRESS project aim is to deliver a long (up to 40) cm turbine blade and this study's is to simulate a long turbine blade, up to 40 cm. Because of the challenges of a strong counter flow of gas, concurrent solidification, low superheat mentioned, computing accurate thermal boundary conditions is essential to correctly predict mis-runs, i.e.

premature freezing (the solidification occurs before mould filling is finished), trapped gas bubbles and eventual macro-porosities.

The geometry of the pouring basin and the blade such as turbine blade (including root and shroud section) is complicated. Resolution mesh is generally unstructured, non-orthogonal, even with some very thin triangular cells. This easily causes numerical instability problem. Moreover, thin edges or narrow cavity are present in the geometry. A very fine mesh is required which could accurately capture the flow features. Under these circumstances, computational mesh often contains a massive amount of cells. Typically, an algorithm is under demand to speed up the simulations since the existing methods are time-consuming or numerical diffusion..

### **1.3 Contributions of this Study**

This study has been concerned with the development of the free surface flow and the solidification by rapid heat transfer during mould filling in a multi-physics simulation. The contributions of the work can be categorised as follows:

- 1) Numerical models were developed to simulate a novel process which combines tilt casting with Induction Skull Melting, where tilt casting is located inside a vacuum chamber for casting TiAl alloys.
- 2) The factors which significantly affect the quality of casting components have been investigated and discussed. Numerical results have been used to demonstrate the impact of these factors, such as venting, melt weight, rotating speed and mould wall wetting, on the mould filling process. The model was useful in supporting the experimental process design.



- 3) A new model, named 3D/1D Coupled Transient Heat Transfer Model, was developed and was implemented into the CFD code PHYSICA of the University of Greenwich in this research. This model provides a more accurate thermal boundary condition. That makes it more reliable to predict potential casting defects, i.e. incomplete filling of thin sections. Furthermore, this model also simplifies mesh generation.
- 4) A novel method, Counter Diffusion Method (CDM), was implemented and tested within CFD code PHYSICA. This method is an alternative VOF technique used to track the interface of two media, present during the mould filling. One of the advantages is that greater time step size can be used when computing free surface fluid flow since a fully implicit scheme is applied. That significantly saves computational cost.
- 5) Solidification was studied with consideration of gap formation between mould and metal. This is achieved by a further development based on the 3D/1D coupled transient heat transfer model. The effects of heat transfer and radiation in the gap are included and the radiation boundary condition was employed on the external mould wall. An accurate thermal boundary conditions and solidification pattern during cooling have been made. The effects of gap have also been presented.
- 6) The validations of the model containing the new developments: 3D/1D model and Counter Diffusion Method were all made against the numerical benchmarks and experimental data from actual castings.
- 7) In terms of dissemination, the results of this research were presented atIMPRESS Progress meetings and also in the form of a number of publications:

K.A. Pericleous, G. Djambazov, H. Wang. 'Numerical Modelling of the Low-superheat casting of Thin-section components.' TMS 2005, Nice, France.

R.A. Harding, M. Wickins, H. Wang, G. Djambazov, K.A. Pericleous. ‘The Tilt Casting of Titanium Aluminides.’ LMPC 2007 Symposium, Nancy, France, Sept. 2007.

R.A. Harding, M. Wickins, H. Wang, G. Djambazov, K. Pericleous. ‘The Development of a Tranquil Tilt Pouring Process for Casting Titanium Aluminides.’ TMS Symposium on Structural Aluminides for Elevated Temperature Applications, New Orleans, 2008.

H. Wang, G. Djambazov, K. Pericleous, R.A. Harding, M. Wickins. ‘Modelling the Tilt-Casting Process for the Tranquil Filling of Titanium Alloy Turbine Blades.’ TMS Symposium on Structural Aluminides for Elevated Temperature Applications, to be proved.

### **1.4 Layout of this Thesis**

This thesis consists of 8 chapters. Chapter 1 firstly introduces the challenges faced in tilt casting for TiAl at present. This is followed by an outline of the other chapters in this thesis. Finally there is a description of the contributions made in response to the challenges in this research.

Chapter 2 reviews the relevant literature which has presented the casting methods including tilt casting, counter gravity casting and centrifugal casting, titanium aluminides and challenges in melting, the numerical methods and discretisation techniques used in modelling the process of tilt casting.

Chapter 3 introduces the mathematical equations and the numerical techniques used in modelling the mould filling process. The procedure involves a couple of physical

## Chapter 1. Introduction

---

phenomena which are described by the following models, fluid flow, heat transfer and solidification, free surface and turbulence models.

Chapter 4 gives brief descriptions of the tilt casting procedure and the way to simulate the rotation in mathematics. Validation is made against the X-ray movies of the tilt filling of a simple I-shaped test piece cast in aluminium, which is undertaken at the University of Birmingham, one of the partners of the IMPRESS project. The main factors, surface tension, mould orientation and filling cycle, are discussed.

Chapter 5 describes the development of the 3D/1D Coupled Transient Heat Transfer Model which is used to model a more accurate thermal boundary and simplify the meshing. The model is validated using two test cases: one is similar to the mould filling that molten TiAl alloy is filling in a thin component; the other is similar to the molten metal solidifying in a mould. Numerical results have been discussed in computational time and the number of the iteration based on the comparisons of this method with PHYSICA. Finally one application of the model, simulating the short turbine blades, is presented. This is followed by comparing the numerical results with the experimental ones. Through this chapter, main factors which affect the quality of the casting in the mould filling are discussed, such as, venting, melt weight.

Chapter 6 presents a novel Counter Diffusion Method which is proposed as a corrective mechanism to counter the numerical diffusion. This method discretises the free surface equation fully implicit in a fast efficient way, and minimises numerical smearing of the interface. The validation is made against the classical collapsing column experiment and shows good agreement. Comparisons of the CDM with other numerical methods, Van Leer, Donor Acceptor and Level Set Method have been given. A detailed analysis of this method is then presented including a discussion on the advantages in reducing the computational time. Finally the Counter Diffusion Method (CDM) is applied to modelling a long turbine blade.

## Chapter 1. Introduction

---

Chapter 7 studies the solidification pattern during cooling. Based on the 3D/1D Coupled Transient Heat Transfer model, a further development has been made to get accurate thermal boundary conditions, i.e. the radiation boundary conditions are applied on the external wall of the mould. The gap formation between mould and metal is involved in the model. Heat conduction and radiation in the gap are considered. The effects of the gap and the gap size have been discussed by the model application on a twisted turbine blade.

Chapter 8 provides the conclusions based on this research and discusses the possible extended work in the future.

## Chapter 2

# Literature Review

This chapter firstly reviews three casting methods: tilt casting, counter gravity casting and centrifugal casting. Relevant experimental work and the material used for tilt casting have also been discussed.

The numerical methods used are then reviewed, and methods to track a free surface are mainly discussed. Also the discretisation techniques used to solve fluid flow and heat transfer are briefly presented: the Finite Volume Method (FVM) and the Finite Difference Method (FDM). They are employed to develop the models in this research. Finally, the PHYSICA multi-physics software package is presented.

## 2.1 Casting Methods

### 2.1.1 Tilt Casting

A method for tilt casting ingot moulds was patented in 1919 by Durville [Durville -13], also called Durville casting. The method was developed to reduce the formation of oxide

## Chapter 2. Literature Review

---

film. This has been applied to sand castings [Cox and Townsend -00] and aluminium die castings [Stahl -86]. The basic principle of tilt casting is shown in Figure 2.1.

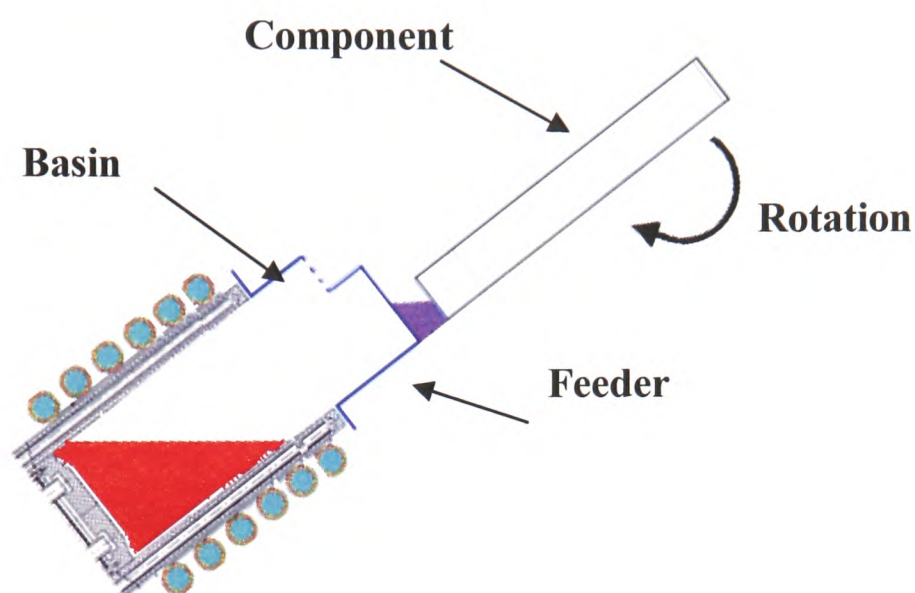


Figure 2.1: Schematic view of tilt casting

The mould is attached to the crucible holding the molten metal, then the two are rotated together to transfer the metal into the mould. The important feature of tilt casting is that much of the metal is transferred horizontally into the mould if an appropriate filling cycle is used.

Tilt casting was initially carried out using a prototype Vacuum Induction Rollover (VIR) furnace [Kuang -00] at the University of Birmingham. There were many limitations such as the difficulties to measure the metal temperature and mould temperature, poor vacuum level and the reaction between the molten metal and the crucible. Lately, a Computer-controlled casting wheel was used for tilt casting [Mi -02]. This equipment can realise either single or multi-stage mould filling cycles. A real-time X-ray cabinet could be fitted inside to capture the metal flow during mould filling at least for aluminium castings. Nowadays, because of the low superheat for TiAl in this study, internal defects are often found in gravity cast TiAl components, which are thought to result from turbulent mould filling. Attempts at combining tilt casting with Induction Skull Melting have been made by IRC of University of Birmingham [Harding -01][Harding -06] [Harding *et al.* -05][Cox



## Chapter 2. Literature Review

---

and Harding -07]. Using tilt casting inside a vacuum chamber with ISM is a totally novel process for casting TiAl.

In this study, the tilt casting method has been focused on. Numerical models have been developed to combine tilt casting with Induction Skull Melting (ISM), where tilt casting is located inside a vacuum chamber for casting TiAl alloys (more details about ISM melting in the following section). However, two other methods exist: Counter Gravity Casting and Centrifugal Casting.

### 2.1.2 Counter Gravity Casting

Counter gravity casting was patented by Hitchiner Manufacturing Company [Hitchiner - 8]. Since the 1960s, Hitchiner started to investigate the development of counter gravity casting. Other early licenses included Daido Steel of Japan [Daido -08]. Until now, Daido Co. Ltd widely uses Counter gravity casting and its combination counter gravity casting with the levitation melting under low pressure for Ti alloys [Noda -98].

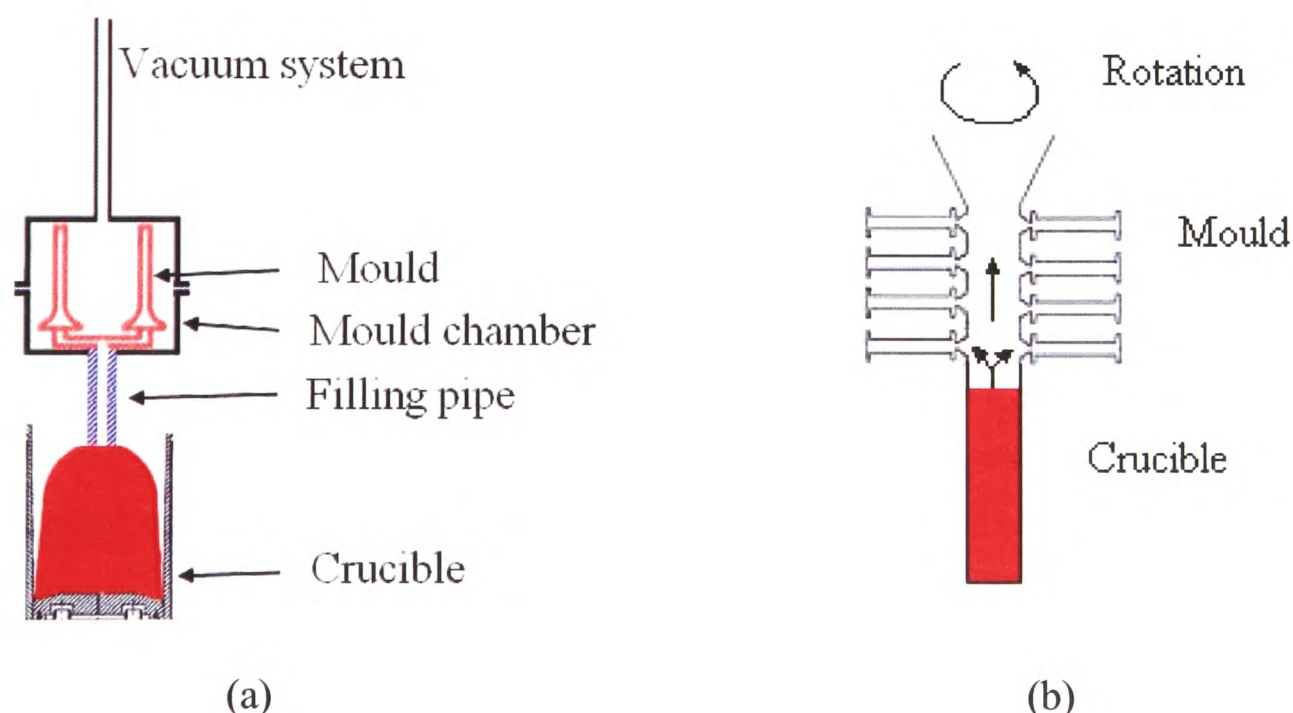


Figure 2.2: Schematic view of counter gravity casting (a) and centrifugal casting (b).

## Chapter 2. Literature Review

---

Through the years of efforts, many advances have been made. However, the fundamental process remains the same. It includes that the mould is placed in a mould chamber which is attached to a vacuum system and then vacuumed. A fill pipe protrudes from the bottom of the mould and is sealed to the mould. The mould chamber moves downwards and make sure the fill pipe is inserted into the molten metal which is induction heated and contained in the crucible. Then pressure is applied to the molten metal, thus forcing the metal upward through the fill pipe and into the mould. Pressure control over the melt surface results in a controlled rate of filling of the mould, as illustrated in Figure 2.2 (a).

One of the advantages of this method is to be able to cast thin sections because the back air pressure which causes fluid flow resistance is not present (it is carried out within a vacuum chamber). And more castings could be achieved per cycle which lowers the production cost. However, it is very difficult to keep the metal velocity under control [Campbell -04].

### 2.1.3 Centrifugal Casting

Centrifugal casting is described as using a permanent mould that is rotated about its axis at speed as the molten metal is poured, then centrifugal forces cause the metal to be pushed out towards the inside of the mould where it solidifies after cooling. The schematic view of centrifugal casting is demonstrated in Figure 2.2 (b). One of the IMPRESS project partners ACCESS [Choudhury *et al.* -97] developed a process to cast titanium blades. ACCESS has shown the successful casting of short turbine blades.

However, centrifugal casting has its disadvantages. In terms of the mould filling, centrifugal casting is subject to the occurrence of turbulent flow. In terms of the alloy structure, centrifugal casting has effects on alloy macro-segregation due to the density difference of different components of the casting alloys [Watanbe -00].

The tilt casting method is chosen for this study based on:



- 1) The tilt casting is able to realize a tranquil mould filling process by carefully designing the tilt cycle. That can avoid internal defects which result from turbulent filling of the mould and gas entrapment when metal has a low superheat;
- 2) Tilt cycle is more easily controlled compared to the pressure control for counter gravity castings.

## 2.2 Titanium Aluminides and Challenges in Melting TiAl Alloys

Gamma-titanium aluminides have excellent mechanical and physical properties at high temperature up to 800 Celsius. They have a high melting point, high strength, minimal creep and low density which make them lightweight by up to 50% compared to equivalent Ni-based super alloys and are resistant to oxidation/corrosion. That gives them the potential to be used to produce high performance components including exhaust valves and turbocharger rotors and turbine blades for aero-engine and modern power stations [Austin and Kelly -95] [Hartfield-Wunsch -95][Noda -98][Blum *at el.* -01]. Great weight reduction of turbine components would lead to higher efficiency, reduced fuel consumption and lower exhaust emissions.

Studies of cast Titanium Aluminides are carried out by many researchers for years. Industrial applications of TiAl alloys have been intensively focused on. However all titanium alloys are very reactive in molten condition. It is hard to apply conventional process to develop productions for titanium alloys. The expensive processing prevents TiAl alloys from quick advance of practical applications [Wu -04]. This urges researchers to develop robust foundry techniques for production of near-net shape components.

The induction skull melting(ISM) process is currently the most effective means of melting the alloys. Melting is carried out in a water-cooled copper crucible with the supply of a high-intensity induction field, illustrated in Figure 2.3 [Harding -05]. In theory, the first metal to melt immediately re-solidifies on the inside of the copper crucible to form a 'skull' and acts as a protective layer for the remainder of the melt, where there is contact

## Chapter 2. Literature Review

---

with a thin solidified 'skull' forms which reduces the risk of further reaction. Furthermore the electromagnetic induction field is able to push the molten metal away from the side wall. This process has been extensively studied at Greenwich with the development of a spectral code specifically for this purpose [Bojarevics *et al.* -03][ Bojarevics *et al.* -04].

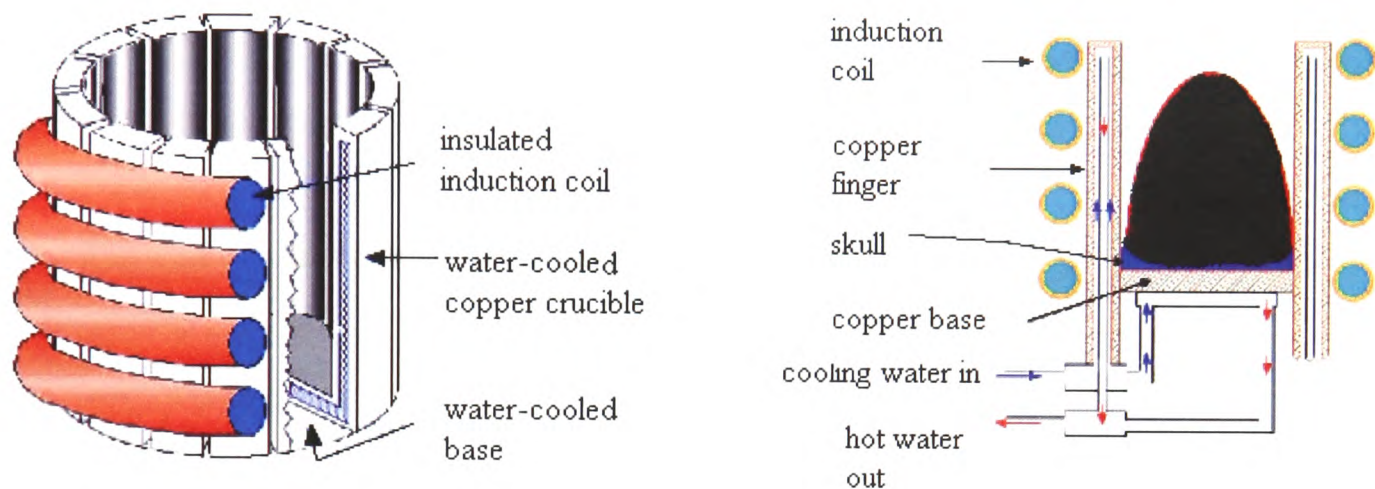


Figure 2.3: Schematic views of an Induction Skull Melting furnace [Harding -05].

ISM is widely used to melt reactive alloys such as gamma titanium aluminides either in a vacuum chamber or under a partial pressure of argon, seen in Figure 2.4 (used at the University of Birmingham).

TiAl alloys are molten under argon to reduce the evaporation of Al [Harding -01]. However the energy efficiency of ISM is not very good due to the heat loss to cold water cooled copper crucible although methods to increase the superheat have been suggested [Harding *et al.* -05]. It only provides limited superheat,  $\sim 40\text{-}50^\circ\text{C}$  [Rishel -99] [Pericleous -02][Harding and Wickins -03][Bojarevics -04]. For TiAlNb alloys, the Liquidus temperature is  $\sim 1569^\circ\text{C}$ . Temperatures over  $1569^\circ\text{C}$  are necessary to melt the metal. And a superheat of at least  $100^\circ\text{C}$  would be desirable for casting thin section components such as long thin turbine blades. Otherwise low superheat may lead to premature solidification during the mould filling. This makes it difficult to fill thin section castings unless rapid pouring is used. But rapid filling results in surface turbulence. Once surface undulations fold onto themselves, two oxide coated surfaces will contact each other and form double



## Chapter 2. Literature Review

---

oxide film defects, called 'bi-film' defects. The bi-film defects have a significant effect on the reliability of castings [Campbell -91][Green and Campbell -93][Cox -00, Cox -03][Mi -03, Mi -04]. Even though it is not certain that oxides form in TiAl alloys, surface turbulence easily generates trapped bubbles [Harding -01, Harding -03] by the rapidly solidifying metal and so forms casting defects. Based on the above fact that low superheat gained in an ISM furnace leads to mis-run and turbulent mould filling results in casting defects, some appropriate casting processes which can provide quiescent filling are required. Tilt casting process is thought to be able to meet the needs if used properly.

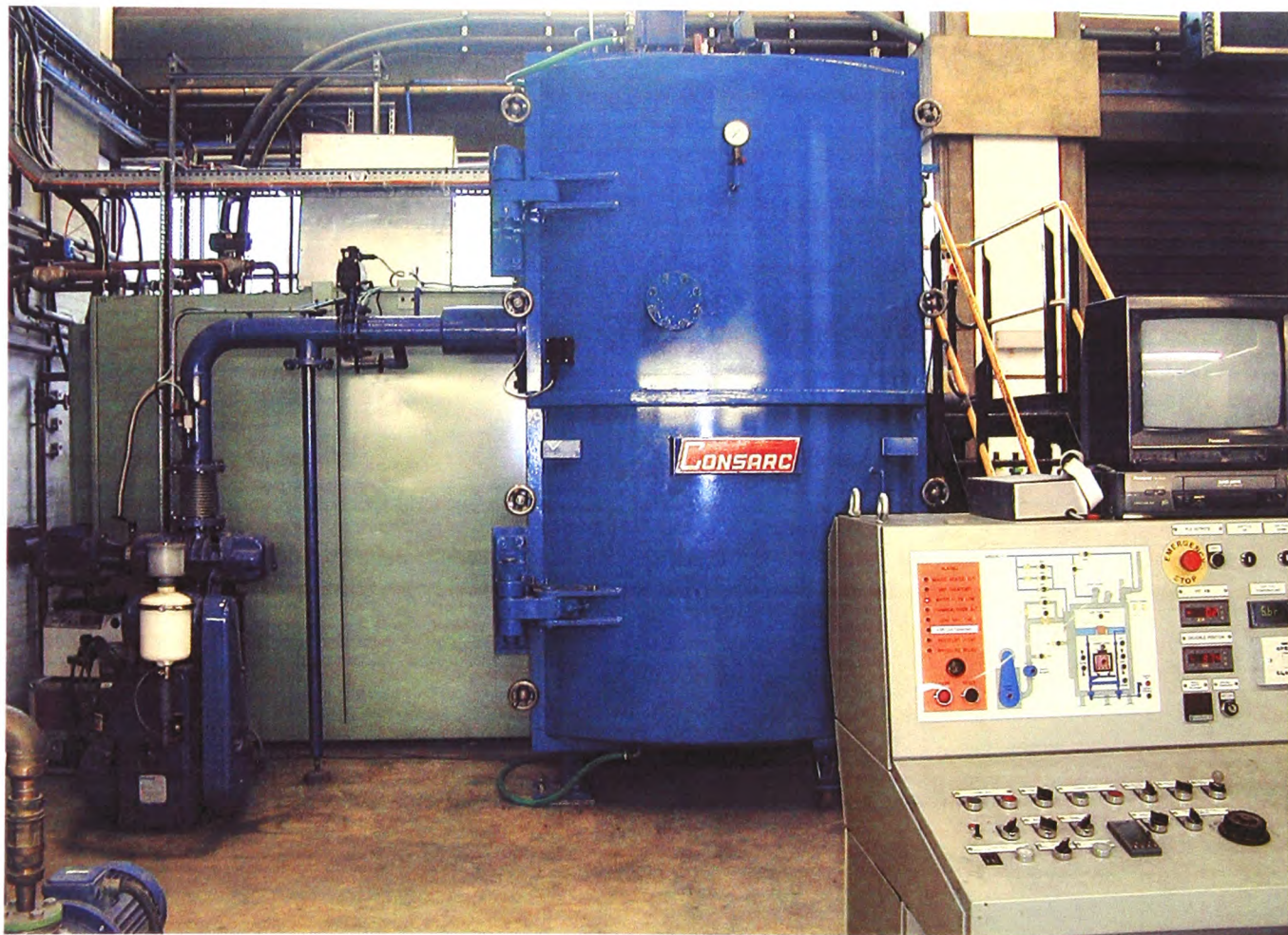


Figure 2.4: Vacuum or under a partial pressure of argon melting chamber containing an ISM furnace [taken by M. Wickins, Birmingham University]

Many researchers tried to develop a melting technique to overcome the low energy efficiency of Induction Skull Melting. A 'semi-levitation' melting has been developed [Bhamidipati -91] which provides a way of melting reactive alloys without using a crucible, illustrated in Figure 2.5. Semi-levitation melting is similar to ISM. It uses a special induction coil to produce an electro-magnetic field which can melt a cylindrical

## Chapter 2. Literature Review

alloy billet placed on a cooled annular base. Once the metal is molten, the liquid alloy easily pours into the mould through a hole in the base under gravity, as described in [Bhamidipati -95]. Then Zhu X.R. and Harding R.A. in the IRC of University of Birmingham [Zhu and Harding -96] sought to develop the technique experimentally and a computer model was used to assist the design of the process. Pericleous and his colleague also developed CFD model to simulate this semi-levitation melting process [Pericleous -97]. However, for this method it should be very careful to design the coil to prevent the molten alloy from spilling out from the billet support. Moreover, only gravity pouring can be used to complete the mould filling. Therefore, this method melting consequentially subjects to severe surface turbulence.

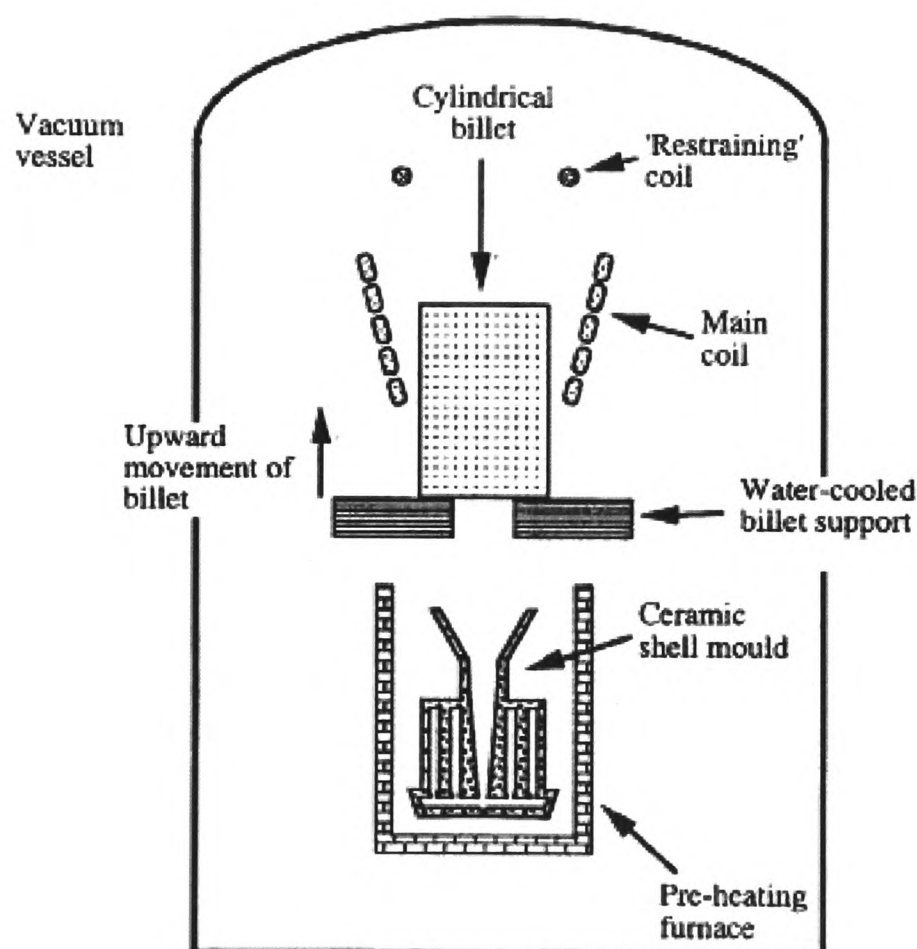


Figure 2.5: Schematic view of the 'semi-levitation' melting furnace (courtesy of Zhu and Harding [Zhu and Harding -96])

The combination of ISM and tilt casting has capacities of not only melting a reactive alloys but also achieving a tranquil mould filling. Even though suffering from the low superheat, high quality casting can be reached if carefully designing tilt cycle.



## 2.3 Numerical Methods

Mould filling is a very complex process which involves a range of interaction of physical phenomena such as heat transfer, solidification, free surface fluid flow and others. Numerical models are developed using the Computational Fluid Dynamics (CFD) approach for understanding the process.

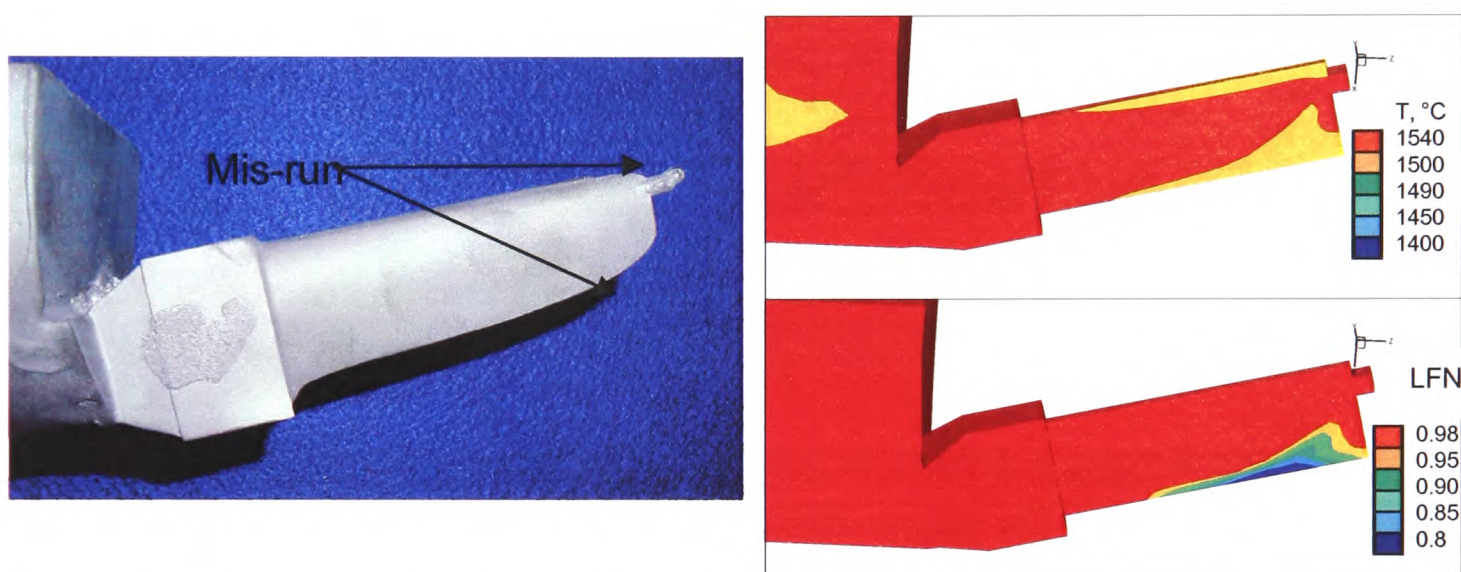


Figure 2.6: One example of experimental result and numerical prediction of casting defects for one vent, i.e. mis-run [Harding *et al.* -07].

Computational Fluid Dynamics (CFD) is currently a very active area of research and development. CFD simulations in industrial domains have been in existence since the early 1970's. However, the application of CFD was initially restricted to the high technology calculations by the limitations in computer power. With the rapid development in the computing power and the affordability of the computer since the 1990's, the improvements of CFD software have been very fast. CFD is applied across all the industry domains. For example, in the castings, numerical modelling is thought as an important tool in product design and process development to improve the practical application and casting quality. Figure 2.6 gives an example for predicting the temperature pattern. Casting defects, such as mis-run due to premature freezing and bubbles, in the final product may be formed from the numerical results. The numerical results showed that venting is not enough, more vent is required to help gas evacuate at the end of the trailing

## Chapter 2. Literature Review

---

edge (the thinner one). Figure 2.7 shows the experimental results when one more vent is made at the end of the trailing edge.

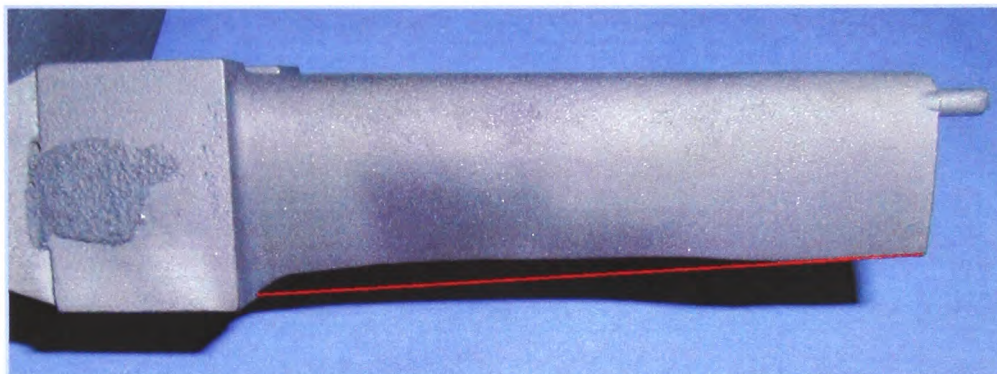


Figure 2.7: Improved experimental result under help of numerical results: one more vent is made at the end of the trailing edge [Harding –Sep 06]

Currently many of popular commercial codes have succeeded in modelling mould filling, such as [MAGMASOFT], [PROCAST], [FLOW3D], [CFX], [FLUENT] and [PHYSICA] the last of which has been developed at the University of Greenwich and has been used in this research.

### 2.3.1 Review of codes for mould filling in castings

MAGMASOFT uses a single block-structured mesh for flow with a staggered variable discretization and SIMPLE-like [Patankar -80][Versteeg and Malalasekera -95] pressure-correction FV methods. It works for 3D domain and very complex geometries.

ProCAST is developed based on FE methods and it is fully unstructured [PROCAST]. It is good when it is applied to simulate the solidification and predict the porosities. It has the facilities for the microstructure and thermo-mechanical simulations. ProCAST could be used for very complex meshes with massive numbers of cells. However, only a single phase method is used to simulate free surface flow. Some physical phenomena can not be simulated, such as casting defects prediction, air entrainment.



## Chapter 2. Literature Review

---

FLOW3D was originally developed based on the development of the Volume of Fluid (VOF) by [Hirt and Nicholas -81]. It is widely used to simulate complex free-surface simulation.

FLUENT is widely used in general purpose. FLUENT is developed based upon unstructured mesh technology. The free surface model employs a VOF technique. It is used to effectively model the mould filling. It couples with heat transfer module, but it does not simulate free surface flow and solidification simultaneously;

CFX is a powerful commercial CFD software. It has many facilities for modelling multi-physics flow problems. It has been widely used for general application of free surface flows as well as in metal castings.

### **2.3.2 Review of Computational Methods for Free Surface Flows**

From the emergence of numerical codes to modelling the mould filling nowadays, the major efforts for researchers have always been made on tracking the free boundary, called free surface which is the key feature of the casting processes. The free surface separates one fluid from the other. As the mould filling progresses, the boundaries move and change with time, described by Crank [Crank -84]. Tracking or capturing free surface flows is the most difficult task in modelling the casting problem since the free surface develops and changes in time.

Since the 1960's, researchers have been working on finding a good numerical method to capture the free surface. A lot of computational techniques for tracking free surface have been employed and are classified into: front tracking and capturing methods, volume tracking methods and moving grid methods. The first two are based on a fixed grid approach and the last is that the grid is changed in a Lagrangian way to match the change of the free surface. In this study, the methods used are for the fluid domain only with a fixed grid. In the later section, volume tracking will be mainly reviewed.

## Chapter 2. Literature Review

---

One of the earliest volume tracking methods is the Marker and Cell method (MAC). The method was initially proposed by Harlow and Welch [Harlow and Welch -68]. Basically, the idea is that the initial free surface is tracked with a series of massless particles which were used as markers in a cell to indicate the cell is full or not. These particles follow the free surface development in time by a velocity calculation. This method was further improved by [Hirt and Shannon -68], [Chan and Street -70] and [Nichols and Hirt -71]. The MAC method was applied to the simulations of different free surface fluid flow problems. Based on the MAC, some new developments have been made, such as the Simplified MAC (SMAC) method by [Amsden and Harlow -70] and later the Solution Algorithm MAC (SOLA-MAC) method by [Lin and Hwang -89]

Another approach of volume tracking methods is the Volume of Fluid Method. The method uses a volume fraction or concentration fraction to identify if a cell is full of liquid (the value of the volume fraction is 1 in the cell) or full of gas, 0. The free surface is contained in cells where the values of fractions are in-between. This method was developed by [Hirt and Nichols -81]. The VOF method and the later extended SOLA-VOF have been widely used to variable fluid problems. For instance, Partom [Partom -87] used the VOF method to simulate the sloshing of fluid in a partially filled cylindrical container in 1987; the SOLA-VOF method was applied to study the mould filling by [Lin and Hwang -88], and so on. Many popular commercial codes for mould filling, such as [MAGMASOFT], [PROCAST], [FLOW3D], [CFX] and [FLUENT], have used the VOF method.

The Scalar Equation Algorithm (SEA) has essentially employed the Volume of Fluid Method (VOF) concept. In both methods a scalar advection equation, which determines the volume fraction of each cell in the domain of interest, is employed to track the position of the interface. The SEA covers both the air and liquid phases when solving the momentum equation in which the VOF method only covers the liquid phase. The SEA method was developed by Liu and Spalding [Liu –March 86] [Liu –October 86] [Liu and Spalding -88]. This method was applied to simulate mould filling problems with



solidification in three-dimensions [Chan -91][Pericleous -93]. The SEA method is one of the methods used in this study.

After many years of efforts, much progress on the development of modelling the casting process which also involves heat transfer and solidification has been made. Some models were developed to simulate the free surface flow and heat transfer without describing the phase change [Foran -95] [Barkhudarov and Hirt -95]. Simulating the free surface flow and solidification can not be carried out at the same time. However that is a huge limit when a thin finger or narrow cavity present in the casting component is investigated, where mis-runs, premature freezing, these kinds of defects occur. The accuracy of the numerical results was not reliable.

In this study, a coupled simulation of mould filling, heat transfer and solidification for the casting processes is studied and free surface flow, heat transfer and solidification are simultaneously calculated. The phase change has been considered based on the research of Voller [Voller and Cross -93][Voller -90].

## **2.4 Discretization Techniques**

In this study, two discretization techniques are related: Finite Difference Method (which is used when developing the 3D/1D Coupled Transient Heat Transfer Model); Finite Volume Method (PHYSICA is based on FV techniques). This research is carried out using the PHYSICA framework and some new developments will be implemented into it.

### **2.4.1 Finite Difference Method**

The Finite Difference Method [Richtmyer and Morton -67][Thomas -99][Ferziger and Peric -02] is the oldest method for numerical solution of Partial Differential Equation (PDE's), introduced by Euler in the 18<sup>th</sup> century. It is also the easiest method to use for simple geometries.

## Chapter 2. Literature Review

---

Finite Difference method utilizes the Taylor series expansion to approximate the derivatives of a variable as the differences between values of the variable at various points in space and time. Taylor series are used to discretize the derivative of a dependent variable. When the approach is used, the entire flow field, defined in terms of a mesh of grid points, must be discretized. The flow field values at each mesh (or grid) point need to be found by discretizing the governing equation at each mesh point which leads to a system of simultaneous algebraic equations. A number of mesh points are usually required to accurately obtain the details of the flow field, such as velocity, temperature, pressure and so on, and this could be written in a very large matrix, a huge system of equations, especially in three dimensions.

The higher order approximations can be obtained by applying the Taylor series expansion for more points. The above difference equations are used to produce the numerical analogue of the partial differential equations which describe the flow. This is the process of replacing derivatives by finite difference approximations. It replaces continuous derivatives with an approximation at a discrete set of points (grid). This discretization is applied to the whole domain where many points are placed. The derivatives of the flow variables are written in differential forms at each point connecting the values of the variable to its neighbouring points. Once this process is done to all the points in the domain, a set of equations are obtained which are solved numerically [Hildebrand - 56][Chapra and Canale -88].

Finite difference methods are restricted to simple geometries and regular meshes in CFD. However other methods are also very successful, such as the Finite Volume Methods (FVM). These methods are used in the most successful codes due to their ability to be locally conservative and also able to cope with arbitrarily complex geometry, necessary in castings.

### 2.4.2 Finite Volume Method

The Finite Volume Method [Versteeg and Malalasekera -95] [Chung -02] is currently the most popular method in CFD. The first use of finite volume method was in 1966

## Chapter 2. Literature Review

---

by Winslow [Winslow -66] in solving the Poisson Equation. Later on, P.W.McDonal [McDonal-71] introduced this method into CFD problems. Further application of the finite volume in CFD has been discussed by [Patankar and Spalding -72] and more details discussed in [Patankar -80].

The finite volume method is a method for representing and evaluating partial differential equations (PDE) as algebraic equations. Similar to the finite difference, instead of discretising the PDE, the volume integrals in a PDE that has a divergence term are converted to surface integrals using the divergence theorem. The integral form is more fundamental while not depending on continuous partial derivatives.

When using the FVM, the problem domain is firstly divided into non-overlapping polyhedral Control Volume (CV). Then each terms of equation is integrated over a control volume and appropriate approximations are used for fluxes across the boundary of each CV. Instead of solving the continuous partial derivatives, a set of discrete linear equations which consist of volume integrals can be solved to obtain the value of the variables at each CV centre. The values of variables at the centres of the CVs are assumed to be the average value over the whole CV, for example see the continuity equation below. Each term in the equation will be treated separately.

$$\frac{\partial \rho}{\partial t} + \nabla(\rho \underline{u}) = 0 \quad (2.1)$$

The transient term,

$$\int_V \frac{\partial(\rho)}{\partial t} dV \approx \frac{(\rho_P V_P - \rho_P^O V_P^O)}{\Delta t} \quad (2.2)$$

Where the subscripts  $P$  represents the current point; the superscripts  $O$  previous time step variable values at the CV respectively;  $V_P$  is the volume of the CV;  $\Delta t$  is the time step size.

The convection term,

$$\int_V \nabla \cdot (\rho \underline{u}) dV = \int_S (\underline{n} \cdot \underline{u}) \rho dS \approx \sum_f \rho_f (\underline{n} \cdot \underline{u})_f A_f \quad (2.3)$$

Where  $\rho_f$  is the face density;  $A_f$  is the area of each face.

As the above introduction, it is known that the results of the finite volume approach can lead to the exact same equations to solve as the finite difference method on a Cartesian mesh. However the way of interpretation is different:

- Finite volume: approximate the governing equation over a volume;
- Finite difference: approximate the governing equation at a point.

Both the finite volume and finite difference methods are very similar. However there are some differences. In some ways, the finite volume method is better than the finite difference method:

- Easier to treat complicated domains (integral discretisation is easier to figure out, implement);
- Good local conservation of mass, momentum and energy using integrals when mesh is finite size.

Whichever method is to be used it has to be capable of tackling the multi-physics problems encountered in castings. The code PHYSICA was designed with this principle.

## 2.5 Multi-physics Modelling Software Package- PHYSICA

PHYSICA is a framework for modelling coupled physical phenomena where material may be a solid or fluid during its processing. The package can be used for the prediction of continuum physical processes which include both Computational Fluid Dynamics (CFD) and Computational Solid Mechanics (CSM), and interactions between the two. Fluid flow, heat transfer, phase-change and thermal stress modules are involved to solve steady-state or transient problems. PHYSICA is based on Finite Volume techniques on 3D structured or unstructured meshes and it has been widely used to model the casting process [Bailey - 96] [Moran *et al.* -98] [Pericleous -98] [Bounds *et al.* -00].

## Chapter 2. Literature Review

---

When PHYSICA is used to run a problem, an **inform** text file should be prepared in which the commands for all parameters which describe the boundary conditions, material properties, etc and modules switched are specified. The **inform** file is the data file which includes problem information represented by commands and keywords.

PHYSICA links to commercial pre/post processors called [FEMGV]. FEMGV is then used to generate a mesh and FEMVIEW to visualize the simulation results. The other possibility is that PHYSICA is able to export data files which can be ported in a post processor such as [TECPLOT] to do the visualisation of the solutions.

For more complex meshes, a combination of CAD and grid generation software was used. For example, the [Rhino] and [Harpoon] were used for the long twisted turbine blade.

## Chapter 3

### The Numerical Models

This chapter will present the mathematical equations and the numerical techniques used in modelling the tilt casting process. The procedure involves several physical phenomena which are described by the following models: fluid flow, heat transfer, solidification, free surface and flow turbulence. Attention is focused on the methods used in the free surface model, where three algorithms, Van Leer, Donor Acceptor and the Level Set Method, are discussed.

#### 3.1 General Transport Equations

Casting is known as a manufacturing process by which a liquid metal (molten metal) is introduced into a mould where it solidifies, finally taken out by breaking the mould to make an integral component. The procedure involves a range of interactions of physical phenomena: free surface fluid flow, heat transfer, solidification when the molten metal cools during the mould filling and others, such as surface radiation, convection, residual stress and deformation of the solidified component. Liquid metal, resident gas and partially solidified metal are involved in this process, resulting in a very complex flow

problem. Here, a general transport equation is employed to express the multi-physics phenomena:

$$\frac{\partial(\alpha\phi)}{\partial t} + \nabla \cdot (\alpha \underline{u}\phi) = \nabla \cdot (\Gamma \nabla \phi) + S_\phi \quad (3.1)$$

Where,  $t$  is the time;  $\underline{u}$  is the fluid velocity vector,  $\phi$  is the solved variable,  $S_\phi$  is the variable's source term that can be associated either with the domain boundaries or with internal regions. It is noted that the equation depends on the values of the coefficients  $\phi, \alpha, \Gamma, S_\phi$ .

### 3.2.1 Fluid Flow Equations

When  $\phi, \alpha, \Gamma, S$  are 1,  $\rho, 0, 0$ , the general equation is the mass continuity equation;

when  $\phi, \alpha, \Gamma, S$  respectively represent  $\underline{u}, \rho, \mu + \rho\nu_t, S_u$ , the general equations described here are the momentum equations which govern three-dimensional transient fluid flow.

They are:

$$\frac{\partial}{\partial t}(\rho \underline{u}) + \nabla \cdot (\rho \underline{u}\underline{u}) = \nabla \cdot ((\mu + \rho\nu_t)\nabla \underline{u}) + S_u \quad (3.2)$$

$$\frac{\partial \rho}{\partial t} + \nabla \cdot (\rho \underline{u}) = 0 \quad (3.3)$$

Where  $\underline{u}$ , the velocity vector;  $\rho$ , the material density;  $\mu$ , the dynamic viscosity and the pressure  $p$ ;  $\nu_t$ , the effective turbulent viscosity;  $S_u$ , the source term represents body forces, such as gravity  $g$ , and the influence of the boundaries in the equation.

### 3.2.2 Heat Transfer and Solidification

When  $\phi, \alpha, \Gamma, S$  respectively represent  $T, \rho c_p, k + \rho c_p \underline{u} / \sigma_T, S_h$ , the general equations are written into Equation (3.4) which is the equation of enthalpy conservation for incompressible flow:

$$\frac{\partial}{\partial t}(\rho c_p T) + \nabla \cdot (\rho c_p T \underline{u}) = \nabla \cdot ((k + \rho c_p \underline{u} / \sigma_T)\nabla T) + S_h \quad (3.4)$$

### Chapter 3. The Numerical Models

---

where  $k$ , the thermal conductivity;  $c_p$ , the specific heat;  $\sigma_T$  the turbulent Prandtl number;  $S_h$  represents the change of heat energy in the fluid. If for the case with the change of phase, such as a solidification problem, this term includes the evolution of the latent heat  $L$  during solidification and it is defined as [Bounds et al. -00]:

$$S_h = -L \left( \frac{\partial f_L}{\partial t} + \nabla \cdot (\rho \underline{u} f_L) \right) \quad (3.5)$$

where  $f_L$ , the liquid fraction of the metal component of the fluid. Typically, the liquid fraction is a function of the metal temperature:

$$f_L = \begin{cases} 1 & T > T_L \\ \frac{T - T_S}{T_L - T_S} & T_S \leq T \leq T_L \\ 0 & T < T_S \end{cases} \quad (3.6)$$

$T_L$ , the liquidus temperature of the metal;  $T_S$ , the solidus temperature of the metal. Other possible liquid fractions representation can be found in [Voller -90].

When solidification occurs, a zone called “the mushy zone” will present where it’s not yet a solid, it’s not a liquid, it’s a state in-between. The source term  $S_u$  in the momentum Equation (3.2) is rewritten as:

$$S_u = g - \frac{\mu u}{K} \quad (3.7)$$

Where  $K$ , the permeability of mushy zone, the transition phase of solidifying materials. In the mushy zone, the liquid fraction of the metal is assumed to be linear, which is based on the assumption that solidification occurs at a constant rate across the freezing range. Solid fraction is  $(1 - f_L)$ . The permeability is typically given by the Carman-Kozeny equation [Hulin -86]:

$$K = \frac{f_L^3}{C(1 - f_L)^2} \quad (3.8)$$



where,  $C$  is a constant that characterises the nature of the porous mushy zone. It is noticed that the liquid fraction  $f_L$  is used in Equation (3.2) and Equation (3.4) to couple solidification into the fluid flow equations and the enthalpy equations.

### 3.2.3 Free Surface Model

The values of  $\phi, \alpha, \Gamma, S$  are respectively  $\Phi, 1, 0, 0$ . Equation (3.1) is written as:

$$\frac{\partial \Phi}{\partial t} + \underbrace{\nabla \cdot (\Phi \underline{u})}_{\text{convection term}} = 0 \quad (3.9)$$

The general equation becomes the advection equation which describes the position of the interface of two fluids, free surface flow. It is the standard VOF equation for interface motion in a fixed grid solution domain. The marker  $\Phi$  has values of 0 and 1 to define the two fluids.

This free surface flow formulation was first proposed by [Harlow and Welch -65] who applied marker particles to track the water. This work was improved by [Raad -95] and [Chen -95] which respectively proposed to improve the pressure boundary condition and the velocity boundary conditions. Then the level set method [Chen -97] was used to only track particles near the interface.

In this study, the Scalar Equation Method (SEM) is applied which was proposed by [K.A.Pericleous *et al.* -95] to solve fluid flow and heat transfer. The method used a scalar  $\Phi$ , a fluid marker, to track the interface of the two fluids which represents the metal volume fraction in a control volume. In a gas cell,  $\Phi = 0$ ; in a metal cell,  $\Phi = 1$ ; for a partially filled cell  $\Phi$  takes on an intermediate value. The advection equation is solved using the Finite Volume Method (FVM). The equation in integral form over the control volume is:

$$\int_V \frac{\partial \Phi}{\partial t} dV + \int_S (\underline{n} \cdot \underline{u}) \Phi dS = 0 \quad (3.10)$$

Equation (3.10) is then discretised to give:

$$\frac{(\Phi_P - \Phi_P^O)V_P}{\Delta t} + \sum_{face} (n \cdot u)_f A_f \Phi_f = 0 \quad (3.11)$$

$A_f$  is the area of the face;  $\Phi_f$  is the value of  $\Phi$  in each face. A value of  $\Phi$  will be calculated for each cell. The value of  $\Phi$  indicates the proportion of each fluid in a cell which contains a mixture of the two fluids. This could lead to some numerical smearing of the fluid interface. The handling of the advection term in Equation (3.9) can greatly affect the sharpness of the interface. Three free surface methods, Van Leer, Donor Acceptor (these two methods were used to treat the convection terms) and Level Set Method, are studied.

### 3.2.3.1 Van Leer Method

The SEA was first used in conjunction with the Van Leer flux limiter method [Van Leer -77] which was used to handle convection terms in the advection Equation (3.9). Van Leer method applied a second order up-winding procedure for differencing the convection terms in order to keep the interface sharp. The configuration of Van Leer Method is demonstrated in Figure 3.1.

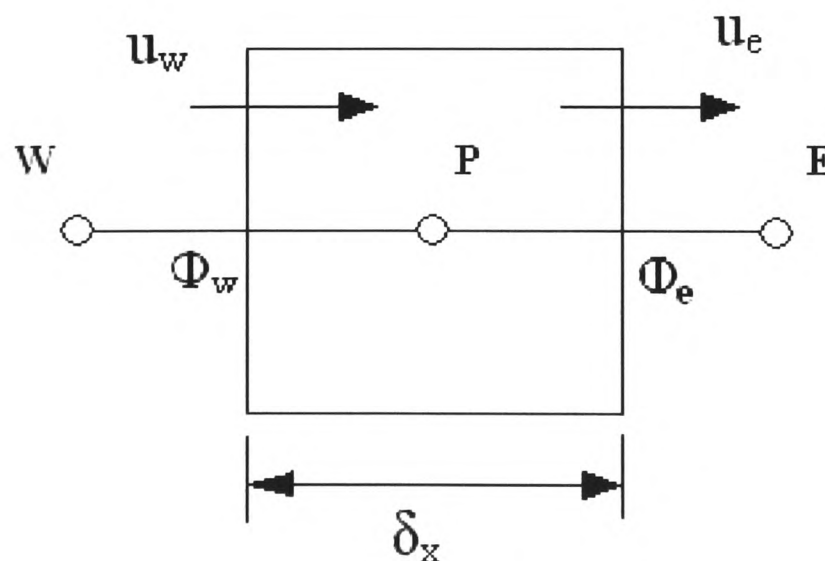


Figure 3.1: Configuration of Van Leer Method

The following Equation (3.12) is used in this method:

$$\Phi_P|^{n+1} = \Phi_P|^{n} - \frac{\delta t}{\delta x} (u_e \Phi_e - u_w \Phi_w) \Big|^{n} \quad (3.12)$$

$u_e, u_w$  the velocity at the east and west face of the cell respectively;  $\Phi_w, \Phi_P, \Phi_e$  are the values of  $\Phi$  at the western cell, the cell centre and the eastern cell. The Van Leer scheme is used to calculate the face value of  $\Phi$  :

$$\begin{aligned} \Phi_e &= \Phi_P + \frac{\delta x}{2} \left[ \frac{\partial \Phi}{\partial x} \right]_P \left[ 1 - \frac{u_e \delta t}{\delta x} \right] & \text{for } u_e > 0 \\ \Phi_e &= \Phi_P - \frac{\delta x}{2} \left[ \frac{\partial \Phi}{\partial x} \right]_E \left[ 1 + \frac{u_e \delta t}{\delta x} \right] & \text{for } u_e < 0 \end{aligned} \quad (3.13)$$

The gradient term  $\frac{\partial \Phi}{\partial x}$  is:

$$\left[ \frac{\partial \Phi}{\partial x} \right]_P = \begin{cases} \frac{2 \operatorname{sgn}(\delta \Phi_e)}{\delta x} \min \left( |\delta \Phi_e|, \frac{1}{2} (|\delta \Phi_e| + |\delta \Phi_w|), |\delta \Phi_w| \right) & \text{if } \operatorname{sgn}(\delta \Phi_e) = \operatorname{sgn}(\delta \Phi_w) \\ 0 & \text{otherwise} \end{cases} \quad (3.14)$$

With

$$\begin{aligned} \delta \Phi_e &= \Phi_E - \Phi_P, & \delta \Phi_w &= \Phi_P - \Phi_W \\ \operatorname{sgn}(\delta \Phi_e) &= +1 & \text{if } \delta \Phi_e &\geq 0 \\ \operatorname{sgn}(\delta \Phi_e) &= -1 & \text{if } \delta \Phi_e &< 0 \end{aligned} \quad (3.15)$$

For any internal face which has no upwind (i.e. the boundary of the domain), the face value of  $\Phi_F$  associated with upwind element is given by:

$$\Phi_F = \Phi_w \quad (3.16)$$

It is noted that the above derivation is explicitly treated, the values of  $\Phi$  should be known at the beginning of each time step. This method is restricted by Courant–Friedrichs–Lewy condition (CFL):

$$\left| u \frac{\Delta t}{\Delta x} \right| < 1 \quad (3.17)$$

For 3-Dimensional case, the condition is expressed as:

$$\Delta t < \min \left\{ \left| \frac{\Delta x}{u} \right|, \left| \frac{\Delta y}{v} \right|, \left| \frac{\Delta z}{w} \right| \right\} \quad (3.18)$$

where the time step size is firmly associated to the cell size and the velocity.

### 3.2.3.2 Donor Acceptor Method

An alternative method used to handle the convection term is the Donor Acceptor method [Ramshaw and Trapp -76]. This method is based on the identification of a cell that donates fluid and the other which accepts fluid. The flux between the donor and acceptor cells is calculated from the velocity of the fluid and the front of the interface between the two cells. The front is evaluated from the amount of fluid in the upstream and downstream cells. The front is evaluated from the amount of fluid in the upstream and downstream cells. The definition of position is shown in Figure 3.2.

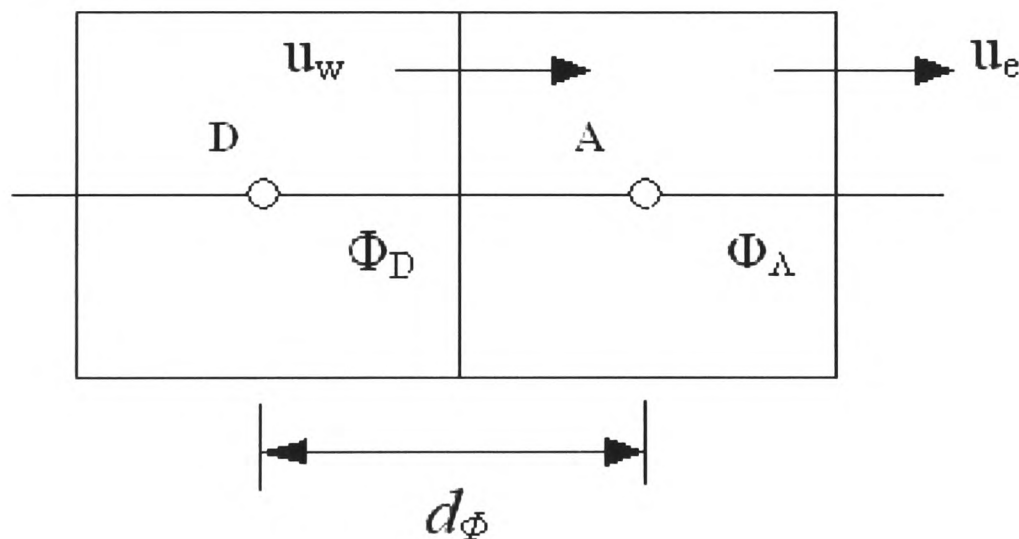


Figure 3.2: Configuration of Donor-Acceptor Method

The upwind cell of a face is called the donor and the downwind cell is called the acceptor. The values of  $\Phi$  in the cell centre are respectively  $\Phi_D$  and  $\Phi_A$ . The value of  $\Phi$  on a face is calculated as:

$$\Phi = \max(0.0, \min(d_\phi / cr, 1.0)) \quad (3.19)$$

Where,

$$cr = |\mathbf{u} \cdot \mathbf{n}| \cdot \delta t \quad \text{and} \quad d_\Phi = \min(\Phi_{AD} \cdot cr + C_\Phi, \Phi_D \cdot A/V_D)$$

The value of  $C_\Phi$  is calculated by:

$$C_\Phi = \max(0.0, (1.0 - \Phi_{AD}) \cdot cr - (1.0 - \Phi_D) \cdot A/V_D) \quad (3.20)$$

A is the face area;  $V_D$  is the volume of donor element; subscript  $\Phi_{AD}$  indicates value of  $\Phi$  in either donor or acceptor element.

The mixture densities in a cell which contains both the gas and the liquid are given for these two numerical methods, Van Leer and Donor Acceptor, as the following:

$$\rho = \rho_1 + \Phi(\rho_2 - \rho_1) \quad (3.21)$$

The mixture viscosity based on the value of  $\Phi$  is:

$$\mu = \mu_1 + \Phi \left( \left( \mu_1 \frac{\rho_2}{\rho_1} \right) - \mu_2 \right) \quad (3.22)$$

Where  $\rho_1$  and  $\rho_2$  are respectively the liquid and the gas density.  $\Phi = 0$ , the momentum equations use the gas density;  $\Phi = 1$ , the metal density is used. It is noticed that the scalar  $\Phi$  is used in Equation (3.21) and Equation (3.22) to couple the advection equation into the momentum equations. The solution procedure for these two methods is depicted in Figure 3.3.

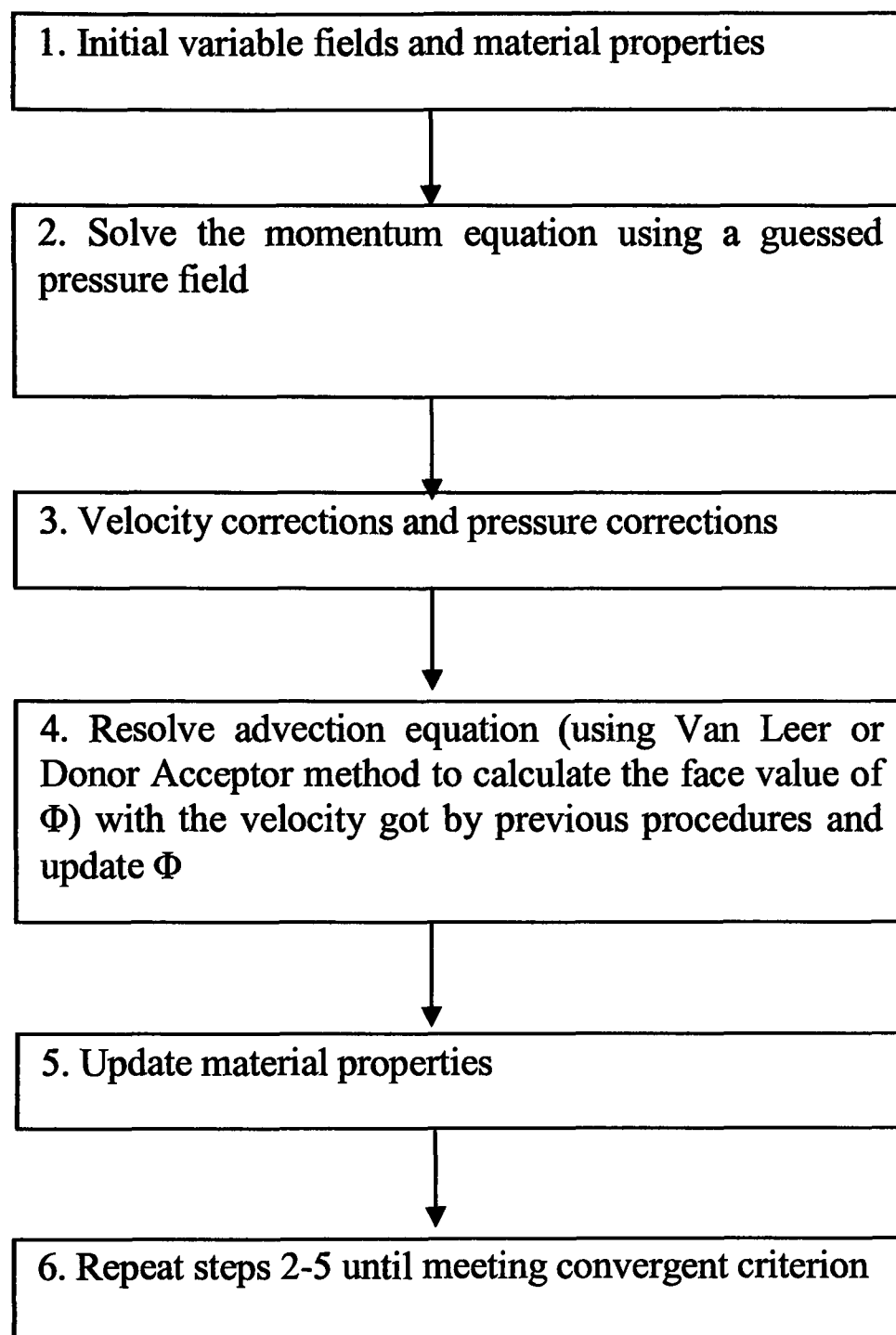


Figure 3.3: Solution Procedure for Van Leer and Donor Acceptor Methods.

### 3.2.3.3 Surface Tension Coupled with Van Leer and Donor Acceptor Method

Surface tension is a force that holds liquid molecules together. When the force acts on a liquid-gas interface, it tends to minimize the area of the surface and results in thin film on the surface [Batchelor -67]. Thus for any volume of fluid including an interface, the force caused by surface tension will be:

$$F_{\sigma} = \oint_l m \cdot \gamma dl \quad (3.23)$$

Where  $l$  is the line where the interface cuts the volume of fluid;  $m$  is the unit vector tangential to the interface and normal to the volume of fluid and  $\gamma$  is surface tension (N/m). Across the interface with the effects of surface tension, there is a pressure jump which is used to balance the surface tension. The Laplace Young equation describes the force balance per unit area in the normal direction to the interface

$$\Delta p = \frac{\gamma}{R} \quad (3.24)$$

Where  $\Delta p$  is pressure difference across the interface;  $R$  is the radius of curvature. Surface tension on the interface of two media can lead to the interface moving once the balance is broken. Surface tension effects are included in the source term as part of forces causing the motion in the momentum equation. If Van Leer and Donor Acceptor methods are employed in simulating a free surface fluid flow and the effects of surface tension is under consideration, the source term contributed by surface tension in the momentum equation is rewritten into:

$$S_{\gamma} = n \cdot \gamma \cdot J \cdot |\nabla \Phi| \quad (3.25)$$

Where,  $\gamma$  is surface tension;  $\nabla \Phi$  is the gradient of  $\Phi$ . Before computing the gradient, an artificial treatment is made to smear the free surface variable by averaging each element's four neighbours and itself, then substituting the average value for the original one. A smooth function across the interface is obtained. The averaging procedure may have to be repeated several times. The gradient of the smeared function can be calculated at the surface with Finite Volume Methods:

$$\int_V \nabla \Phi \cdot dV = \int_S n \cdot \Phi \cdot dS \quad (3.26)$$

The gradient can be obtained from the approximation of the above integral:

$$\nabla\Phi = \sum_f \frac{n_f \Phi_f A_f}{V_p} \quad (3.27)$$

$V_p$ , the cell volume;  $A_f$ , the face area;  $n_f$ , the outward face normal; the values of the element face.

The curvature is given by the widely used definition of the curvature:

$$J = \nabla \cdot n \quad (3.28)$$

Where the normal  $n$  is given:

$$n = \frac{\nabla\Phi}{|\nabla\Phi|} \quad (3.29)$$

The magnitude of gradient is calculated from:

$$|\nabla\Phi| = \sqrt{(\nabla\Phi)^2} \quad (3.30)$$

### 3.2.3.4 Level Set Method

#### 3.2.3.4.1 Review of Level Set Method

The Level Set Method (LSM) was first developed by [Osher and Sethian -88] to track moving interfaces in a wide arrange of problems. The idea behind the Level Set Method is to track the evolution of a function of a scalar  $\Phi$  whose zero level set always corresponds to the position of the propagating interface and apply a function  $\Phi(\underline{x}, t)$  in space and in time to the space where the interface develops. The work demonstrated the advantages of the level set method, such as automatic handling of topological changes as well as geometric information. However there is some weakness of this method, i.e. mass loss. One of the early developers at using LSM to computing solutions to incompressible two-phase flow is by [Sussman *et al.* -94]. Their work introduced a partial differential equation to weaken this problem. A second-order projection method was used and large density, viscosity ratios and surface tension were also included in.

In response to the mass loss, an algorithm for combining the level set method with volume of fluid method (CLSVOF) was proposed [Sussman and Puckett -00]. It is thought that the results were better than those got by using of the two methods.



### Chapter 3. The Numerical Models

---

Another method was suggested in [Enright -02]: Particle Level Set (PLS). This method was developed to improve the mass conservation properties of the level set method when the interface is passively advected in a flow field. The mass conservation of this method was improved by adding passively advected marker particles. These particles are used near the interface. It is required to keep a track of the particles and to redistribute the particles. The velocity field has to be interpolated at the particle positions.

The discretisation of the convection equation can cause a numerical dissipation. In order to ease numerical dissipation, higher order accurate numerical methods were introduced by [Harten *et al.* -87] based on essentially non-oscillatory (ENO) polynomial interpolation of data. [Shu and Osher -88] [Shu and Osher -89] extended the methods to a finite difference. [Osher and Sethian -88] extended the ENO method to Hamilton-Jacobi based on the fact that Hamilton-Jacobi equations in one spatial dimension are integrals of conservation laws. Unfortunately, higher order accurate numerical methods are not enough.

In order to obtain more accuracy in areas of the flow, adaptive methods were applied. Adaptive mesh refinement (AMR) methods for solving interface problems are presented [Berger and Oliger -84][Berger and Colella -89]. A number of uniform grids of different resolution were used in this approach. A more efficient method was quad-tree based and octree based level set methods were developed in [Strain -99 a, b] [Losasso -04, 06]. Fast adaptive numerical methods combine a level set approach with frequent re-distancing and semi-Lagrangian time stepping schemes which are explicit yet unconditionally stable. An octree mesh is used to concentrate computational effort on the interface. This is achieved by refining the mesh near the interface and coarse mesh away from it.

## Chapter 3. The Numerical Models

In this study, the level set method used was based on the work of M. Sussman, P. Smereka and S. Osher in 1994 [Sussman *et al.* -94].

### 3.2.3.4.2 Governing Equations

The two incompressible fluids are separated by an interface  $\Gamma$ :

$$\begin{aligned}\Phi(\bar{r}) &= 0 & \text{if } \bar{r} \in \Gamma \\ \Phi(\bar{r}) &> 0 & \text{if } \bar{r} \in \Gamma_l \\ \Phi(\bar{r}) &< 0 & \text{if } \bar{r} \in \Gamma_g\end{aligned}$$

$\Phi$  is assumed to take positive values inside the region delimited by the curve  $\Gamma$  and negative outside. The zero level set of a variable  $\Phi$  is used to represent the position of the free surface interface. Value of  $\Phi$  represents the distance from the zero level set shown in Figure 3.4.

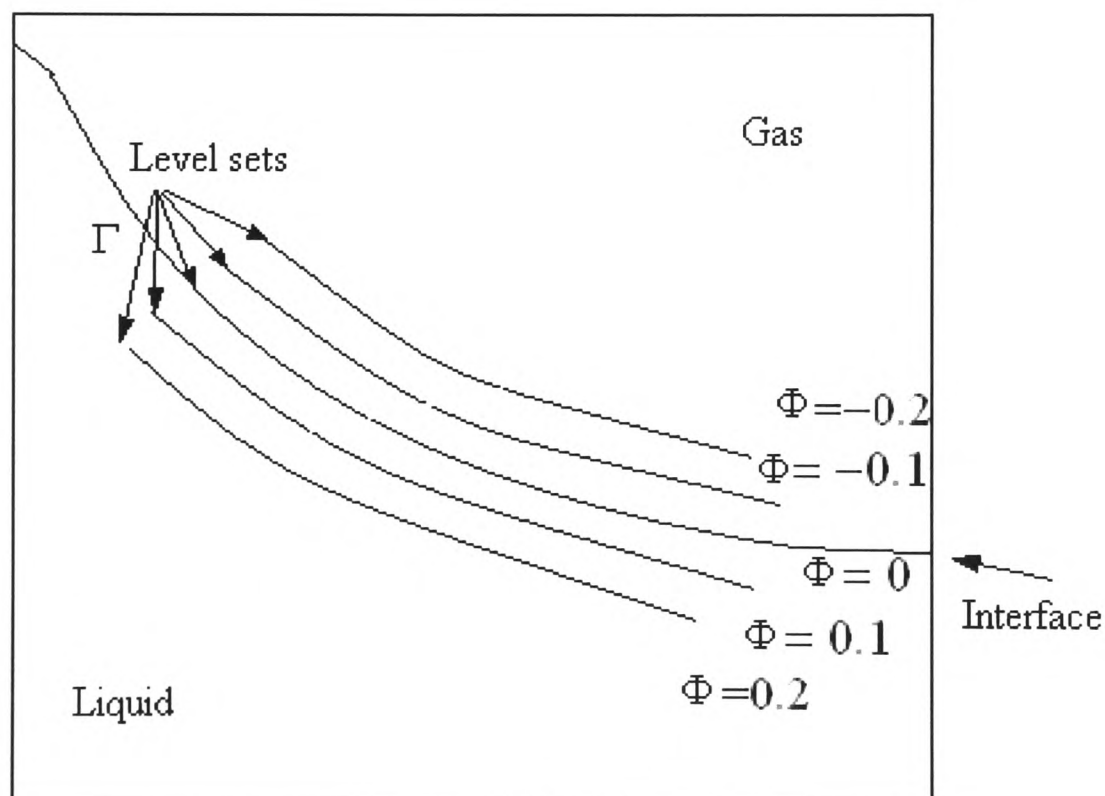


Figure 3.4: Configuration of the Level Set Method

A known velocity field is used to advect the variable  $\Phi$  to predict the evolution of the interface using advection equation (3.9). It is noted that  $\Phi$  is initially a distance function. However it will keep remaining so. To ensure  $\Phi$  to be maintained as a distance function

### Chapter 3. The Numerical Models

---

throughout the calculation, a function is used to reinitialize  $\Phi$  so that it remains a distance function:

$$\Phi_\tau = S(\Phi_0)(1 - |\nabla\Phi|) \quad (3.31)$$

$\Phi_0$  is the value of  $\Phi$  at the beginning of the re-initialisation procedure and  $\tau$  is its own time step;  $S(\Phi)$  is the sign function, normally given by:

$$S(\Phi_0) = \frac{\Phi_0}{\sqrt{(\Phi_0)^2 + (d_{AP}^{\max})^2}} \quad (3.32)$$

$d_{AP}^{\max}$  is the maximum distance between the present cell centre and the adjacent cell centres.

The gradient,  $\nabla\Phi$ , can be calculated as Equations (3.26) and (3.27). The values of  $\Phi_f$  are given in upwinding:

$$\Phi_f = \Phi_P \quad \text{if} \quad w \cdot n \geq 0 \quad (3.33)$$

$$\Phi_f = \Phi_A \quad \text{if} \quad w \cdot n < 0 \quad (3.34)$$

The following modification is used:

$$\nabla\Phi = \frac{\Delta\Phi}{V_P} \quad (3.35)$$

Where

$$\Delta_i\Phi = \max \text{mag}(\delta_i^+, \delta_i^-, \delta_i) \quad (3.36)$$

with:

$$\delta_i^+ = \sum_{f^+} (A_f n_i \Phi_P) + \sum_{f^-} (A_f n_i \Phi_f) \quad (3.37)$$

$$\delta_i^- = \sum_{f^+} (A_f n_i \Phi_f) + \sum_{f^-} (A_f n_i \Phi_P) \quad (3.38)$$

$$\delta_i = \sum_f (A_f n_i \Phi_f) \quad (3.39)$$

Where  $f^+$  is summed over all positive terms and all negative terms for  $f^-$ . This modification allows information to travel from the interface while allowing extremities not to be smoothed.

### Chapter 3. The Numerical Models

---

The magnitude of gradient is given from:

$$|\nabla\Phi| = \sqrt{\sum_i \left(\frac{\Delta_i\Phi}{V_P}\right)^2} \quad (3.40)$$

The Equation (3.31) is written in a discretised form:

$$\Phi_P^{n+1} = \Phi_P^n + \nabla\tau \cdot S(\Phi_0)_P (1 - |\nabla\Phi_P|) \quad (3.41)$$

The time-step  $\tau$  in the re-initialisation is calculated as:

$$\Delta\tau = \min\left(\frac{d_{AP}^{\min}}{10}\right) \quad (3.42)$$

A volume re-initialisation technique is used since the level set method does not need to preserve the volume [Chang et al. -96]. The volume re-initialisation is made every time-step  $\tau$  :

$$\Phi_\tau = V_{pre} - V(\tau) \quad (3.43)$$

The volume is calculated from:

$$\begin{aligned} V &= V_P \left(1 + \sin\left(\frac{\pi\Phi_P}{2\alpha}\right)\right) & \text{if } |\Phi_P| \leq \alpha \\ V &= V_P & \text{if } \Phi > \alpha \\ V &= 0 & \text{if } \Phi < \alpha \end{aligned} \quad (3.44)$$

Where the interface  $\alpha$  is defined by:

$$\alpha = \frac{3d_{AP}^{\max}}{2} \quad (3.45)$$

In order to prevent the instabilities which are caused by a highly variant material property in one cell, a smoothing material property can be calculated in a finite thickness interface by:

### Chapter 3. The Numerical Models

---

$$\begin{aligned}v &= \frac{v_1 + v_2}{2} + \frac{v_1 - v_2}{2} \sin\left(\frac{\pi\Phi}{2\alpha}\right) & \text{if } |\Phi| \leq \alpha \\v &= v_1 & \text{if } \Phi > \alpha \\v &= v_2 & \text{if } \Phi < -\alpha\end{aligned} \tag{3.46}$$

$2\alpha$  is interface thickness. The solution procedure adopted for LSM is given in Figure 3.5.

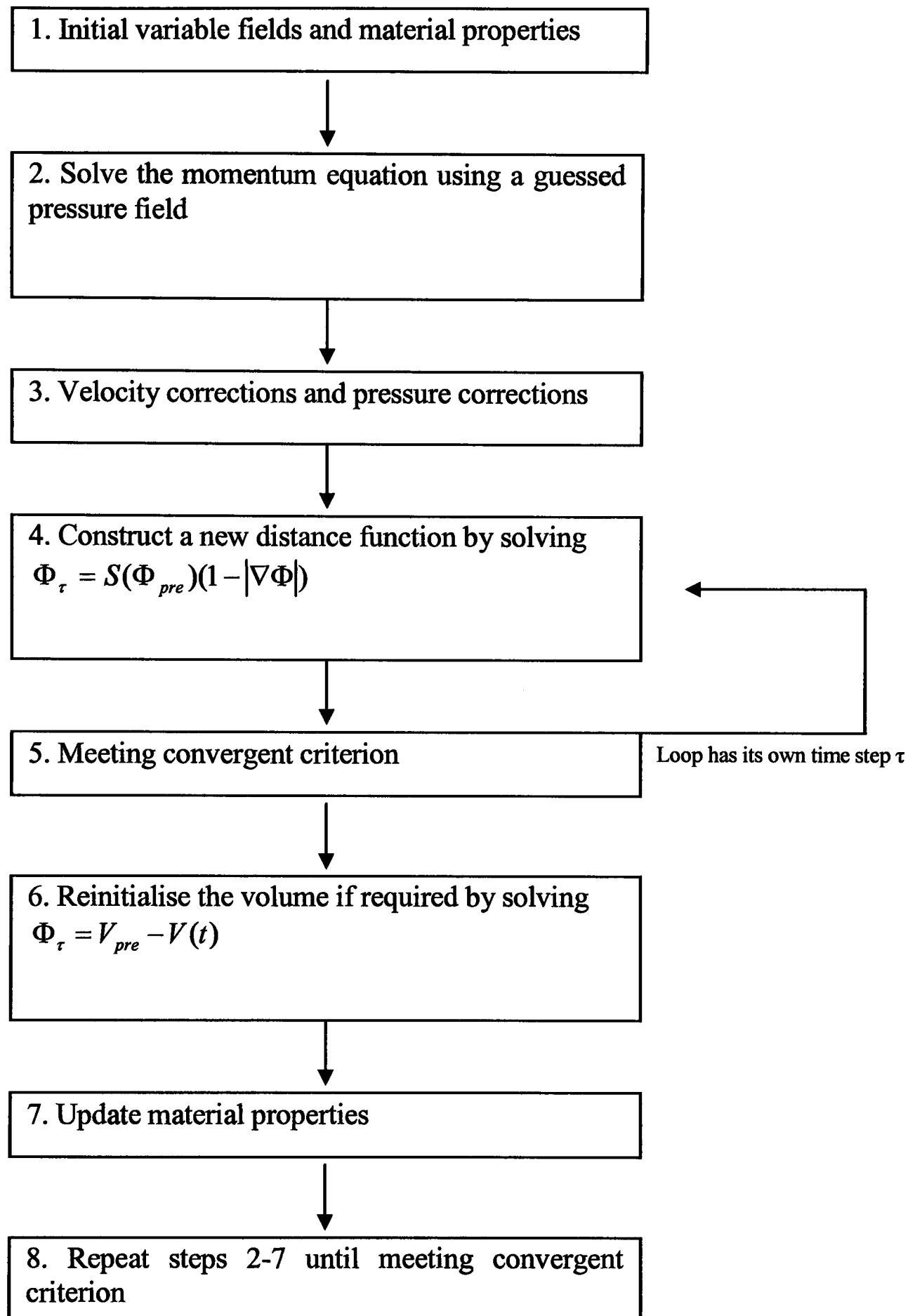


Figure 3.5: Solution Procedure for Level Set Method.

### 3.2.3.4.3 Surface Tension Coupled with Level Set Method

If the Level Set method is employed in simulating a free surface fluid flow, the momentum equation for a fluid with surface tension can be written:

$$\frac{\partial(\rho \underline{u})}{\partial t} + \nabla \cdot (\rho \underline{u} \underline{u}) = -\nabla p + \nabla \cdot (\mu \nabla \underline{u}) + S_\gamma + \rho g \quad (3.47)$$

where  $S_\gamma$  surface tension source term [Wheeler -00] is:

$$S_\gamma = \nabla \Phi J(\Phi) \gamma \delta(\Phi) + \delta(\Phi) |\nabla \Phi| \nabla \gamma - \frac{\delta(\Phi)}{|\nabla \Phi|} (\nabla \Phi \cdot \nabla \gamma) \nabla \Phi \quad (3.48)$$

$J$  curvature,  $\gamma$  surface tension and  $\nabla \gamma$  is calculated in the same way as for  $\nabla \Phi$ ; delta function  $\delta(\Phi)$  [confine the sources to cells which lie near the interface], which is given by:

$$\delta(\Phi) = \frac{1}{2\alpha} \left( 1 + \cos\left(\frac{\pi\Phi}{\alpha}\right) \right) \quad \text{if } |\Phi| \leq \alpha \quad (3.49)$$

$$\delta(\Phi) = 0 \quad \text{if } |\Phi| > \alpha$$

The curvature  $J$  is calculated:

$$J = \frac{1}{V} \left( \delta_{jk} - \frac{\nabla_j \Phi \nabla_k \Phi}{|\nabla \Phi|^2} \right) \sum_f \left( A_f \frac{n_j (\nabla_k \Phi)_f}{|\nabla \Phi|_f} \right) \quad (3.50)$$

For a circle of radius  $R$ , Equation (3.23) gives a curvature of  $J=1/R$ . Where the summation is over all faces bounding the elements;  $A_f$  is the face area and  $\delta_{jk}$  is the Kronecker delta function.

When the fluid is flowing in (i.e. molten metal is filling in the mould during tilt casting), the free surface contacts with the boundary. The surface between different media could form an angle, called 'contact angle' (illustrated in Figure 3.6).

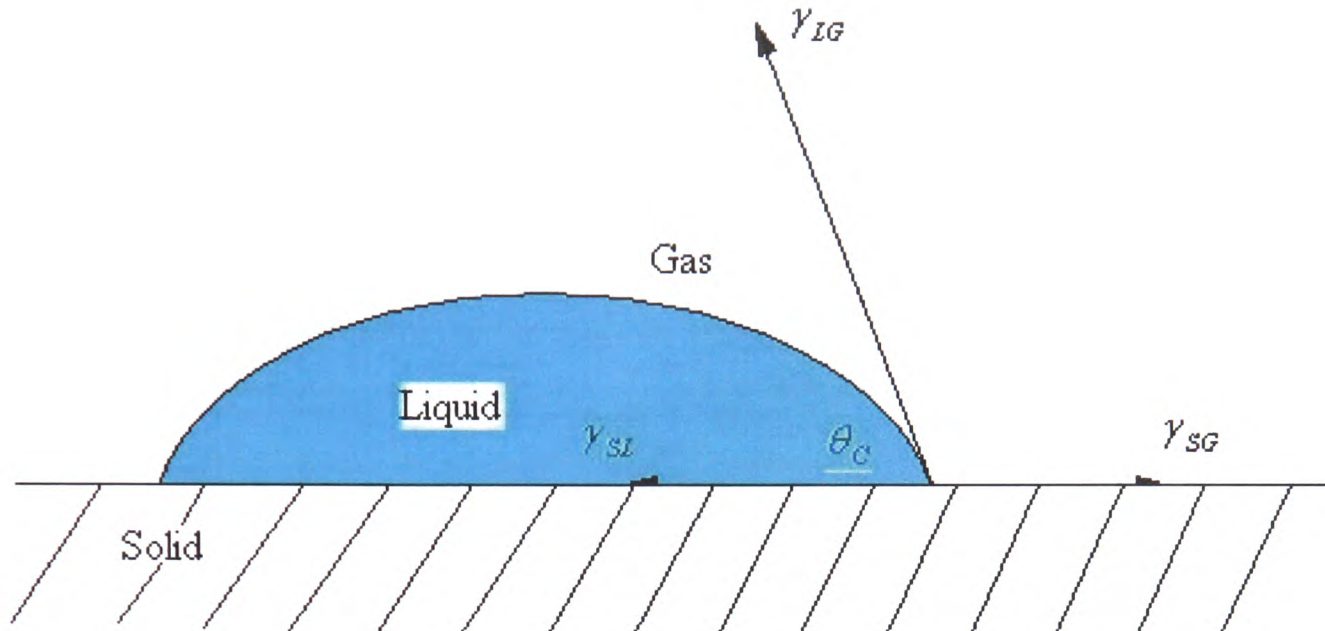


Figure 3.6: Illustration of contact angle.

The contact angle is specific for any given system and is determined by the interactions across the three interfaces. The contact angle is not limited to a liquid/vapour interface; it is equally applicable to the interface of two liquids or two vapours. It is known that Young Equation [Neumann and Spelt -96] governs the equilibrium which is written as:

$$\gamma_{LG} \cos(\theta_C) = \gamma_{SG} - \gamma_{SL} \quad (3.51)$$

Where,  $\gamma_{LG}, \gamma_{SG}, \gamma_{SL}$  are the surface tension between liquid, gas and solid.

If the contact angle is defined, the boundary conditions for Equation (3.50) can be given by the contact angle conditions. The curvature is calculated using:

$$J = \frac{1}{L_{max}} \left( \cos(\theta_C) - n_k \frac{\nabla_k \Phi}{|\nabla \Phi|} \right) \quad (3.52)$$

Where  $\theta_C$  is the contact angle;  $L_{max}$  is the maximum distance between the element centre and one of its neighbouring element centres.



### 3.2.4 Turbulence Flow Model

In this study, three turbulence models have been used, standard  $k$ - $\varepsilon$  model,  $k$ - $\omega$  model and LVEL turbulence model.

#### 3.2.4.1 Standard $k$ - $\varepsilon$ Model

The  $k$ - $\varepsilon$  model is the most commonly used of all the turbulence models. It is known as a two-equation model. That is based on the fact that the  $k$ - $\varepsilon$  model transports two turbulent properties  $k$  (turbulent energy) and  $\varepsilon$  (dissipation). The two properties are defined through  $k$  and  $\varepsilon$  equations:

$$\frac{\partial(\rho k)}{\partial t} + \nabla \cdot (\rho \underline{u} k) = \nabla \cdot \left( \left[ \mu_t + \frac{\rho \nu_t}{\sigma_k} \right] \nabla k \right) + \rho \nu_t G - \rho \varepsilon \quad (3.53)$$

$$\frac{\partial(\rho \varepsilon)}{\partial t} + \nabla \cdot (\rho \underline{u} \varepsilon) = \nabla \cdot \left( \left[ \mu_t + \frac{\rho \nu_t}{\sigma_\varepsilon} \right] \nabla \varepsilon \right) + C_{1\varepsilon} \rho \nu_t G \frac{\varepsilon}{k} - C_{2\varepsilon} \rho \frac{\varepsilon^2}{k} \quad (3.54)$$

Where the turbulent viscosity is identified as:

$$\nu_t = C_\mu \frac{k^2}{\varepsilon} \quad (3.55)$$

$\sigma_k, \sigma_\varepsilon, C_\mu, C_{1\varepsilon}, C_{2\varepsilon}$  are five empirical constants. In standard Launder and Spalding's  $k$ - $\varepsilon$  model [Launder and Spalding -74] they are given respectively:

$$\sigma_k = 1.00$$

$$\sigma_\varepsilon = 1.30$$

$$C_\mu = 0.09$$

$$C_{1\varepsilon} = 1.44$$

$$C_{2\varepsilon} = 1.92$$

Where  $G$  represents turbulent generation rate which is:

$$G = 2 \left( \left[ \frac{\partial u}{\partial x} \right]^2 + \left[ \frac{\partial v}{\partial y} \right]^2 + \left[ \frac{\partial w}{\partial z} \right]^2 \right) + \left( \frac{\partial u}{\partial y} + \frac{\partial u}{\partial z} \right)^2 + \left( \frac{\partial v}{\partial x} + \frac{\partial v}{\partial z} \right)^2 + \left( \frac{\partial w}{\partial y} + \frac{\partial w}{\partial x} \right)^2$$

### 3.2.4.2 $k$ - $\omega$ Model

The  $k$ - $\omega$  model is the second most widely used turbulence model. It is also classified as a two-equation model. The definition of the first variable  $k$  is similar to the  $k$ - $\varepsilon$  model. However the main difference is in the selection of the second variable  $\omega$  which represents the frequency of the vorticity fluctuations described by the  $\omega$  equation. The  $k$  and  $\omega$  equations are:

$$\frac{\partial(\rho k)}{\partial t} + \nabla \cdot (\rho \underline{u} k) = \nabla \cdot \left( \left[ \mu_t + \frac{\rho \nu_t}{\sigma_k} \right] \nabla k \right) + \rho \nu_t G - \beta^* \rho \omega k \quad (3.56)$$

$$\frac{\partial(\rho \omega)}{\partial t} + \nabla \cdot (\rho \underline{u} \omega) = \nabla \cdot \left( \left[ \mu_t + \frac{\rho \nu_t}{\sigma_\omega} \right] \nabla \omega \right) + \rho \alpha G \frac{\omega}{k} - \beta \rho \omega^2 \quad (3.57)$$

Where the turbulent viscosity is identified as:

$$\nu_t = \frac{\alpha^* k}{\omega} \quad (3.58)$$

The values of Prandtl number  $\sigma_k, \sigma_\omega$  are:

$$\sigma_k = 2.0$$

$$\sigma_\omega = 2.0$$

The values of  $\beta, R_t, \alpha^*, \alpha, \beta^*$  are got by:

$$\beta = 0.075$$

$$R_t = \frac{k}{\omega \nu_t}$$

$$\alpha^* = \frac{0.15 + R_t}{6.0 + R_t}$$

$$\alpha = \frac{5}{9} \cdot \frac{0.27 + R_t}{2.7 + R_t} \cdot \frac{1}{\alpha^*}$$

$$\beta^* = 0.09 \cdot \frac{5/18 + (R_t/8.0)^4}{1.0 + (R_t/8.0)^4}$$

Where  $\nu_t$  is the laminar viscosity.

The major difference between  $k-\varepsilon$  model and  $k-\omega$  model is to model the turbulence near the wall. Comparing with  $k-\varepsilon$  model,  $k-\omega$  model requires a quite fine mesh close to wall to transport a relatively accurate turbulent feature. The values of  $k$  in the elements which are close to wall are set to 0. However  $k-\varepsilon$  model only resolves the turbulent quantities when they are becoming important compared to laminar effects. The dimensionless wall distance is placed within an approximate range between 30 and 100.

### 3.2.4.3 LVEL Turbulence Model

One another turbulence model involved is LVEL model [Agonafer, Liao and Spalding - 96]. This model is classified as a Zero-equation turbulence model. As it is known, zero-equation turbulence models are the least computationally consuming. It can be used to describe the turbulent features in homogeneous, incompressible flows when the geometry is not complicated with simple flow characteristics in the boundary layer.

LVEL employed a distance from the nearest wall ( $L$ ), the local velocity ( $VEL$ ). The approximate wall distance  $L$  is computed by solving equations given by equation (3.59) and (3.60):

$$\nabla^2 W = -1 \quad (3.59)$$

$W$  an auxiliary variable in the moving fluid field with  $W=0$  at solid-fluid boundaries.

$$L = \sqrt{(\nabla W)^2 + 2W} - |\nabla W| \quad (3.60)$$

This distance is used with the laminar viscosity  $\nu_l$  and the local velocity to calculate the local Reynolds number.

$$\text{Re} = \frac{VL}{\nu_l} \quad (3.61)$$

The value of the local effective viscosity  $\nu_l$  is obtained by using a universal dimensionless velocity away from the wall and the local Reynolds number  $Re$ . LVEL model has been implemented within PHYSICA, (further details seen in [Dhinsa -06][PHYSICA]).

### **3.3 Summary**

This chapter has presented the fundamental theory concerned dynamic fluid flow and heat transfer during the mould casting. Three methods have been used to track the free surface between two media. Three turbulent models which will be involved in the following study have been introduced. They have been implemented in the current version of PHYSICA. In the following chapters, some novel advances and new development will be carried through based on the existing governing equations.

## Chapter 4

### Tilt Casting Method

This chapter firstly presents the tilt casting process and the numerical model to simulate this process.

The validation of the numerical model is made against experiments undertaken at the University of Birmingham, one of the partners of the IMPRESS project, using an 'I'-shaped test casting. Since the experiment is subjected to the limitation of the equipment, that real-time X-ray radiography technique can not be used with ISM furnace, aluminium is chosen as molten metal for different cases where different mould orientations and filling modes are employed.

The numerical model is used to simulate this process with the free surface method Van Leer. The results are discussed with the comparisons of the experimental and numerical results aiming to show the capability of software in modelling tilt casting process. The factors in Tilt Casting Process which have impact on the mould filling, such as surface tension, mould orientation and filling cycle, are also discussed.

## 4.1 Introduction

Tilt casting is arranged so that a mould is attached to the crucible holding the molten metal, then the two are rotated together to transfer the metal into the mould as seen in Figure 4.1. The procedure involves a range of interactions of physical phenomena:

- Free surface fluid flow as the mould fills;
- Heat transfer from the metal to the mould;
- Solidification of the molten metal as it cools;
- Other effects, such as surface radiation, convection, residual stress and deformation of the solidified component.

Liquid metal, resident gas and solidified metal as the liquid metal is cooling down are involved during mould filling, a very complex flow problem. Investigations have been made to simulate the tilt casting process so that the dynamics of the filling, heat transfer plus solidification can be modelled.

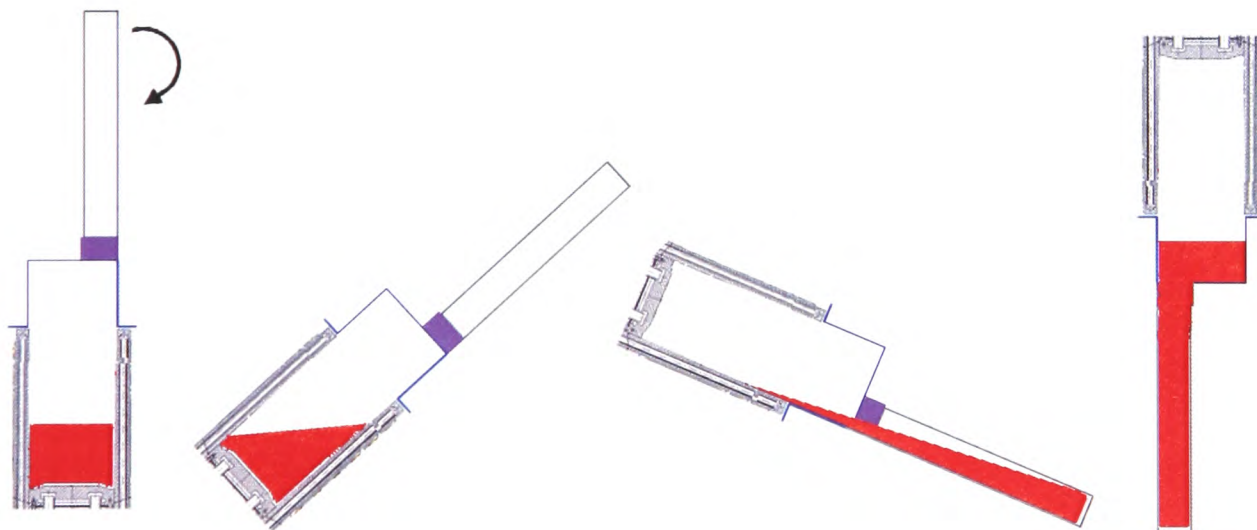


Figure 4.1: Process of tilt casting

## 4.2 Mathematical Description

The prescription of general equations involved and numerical techniques applied for the casting can be found in Chapter 3. In PHYSICA, the tilt casting technique is numerically

## Chapter 4. Tilt Casting Method

modelled by keeping the geometry stationary and rotating the gravitational force vector, as shown in Figure 4.2(a). Figure 4.2(b) shows the position and the liquid level if the relative position is kept the same between the geometry and the gravity.

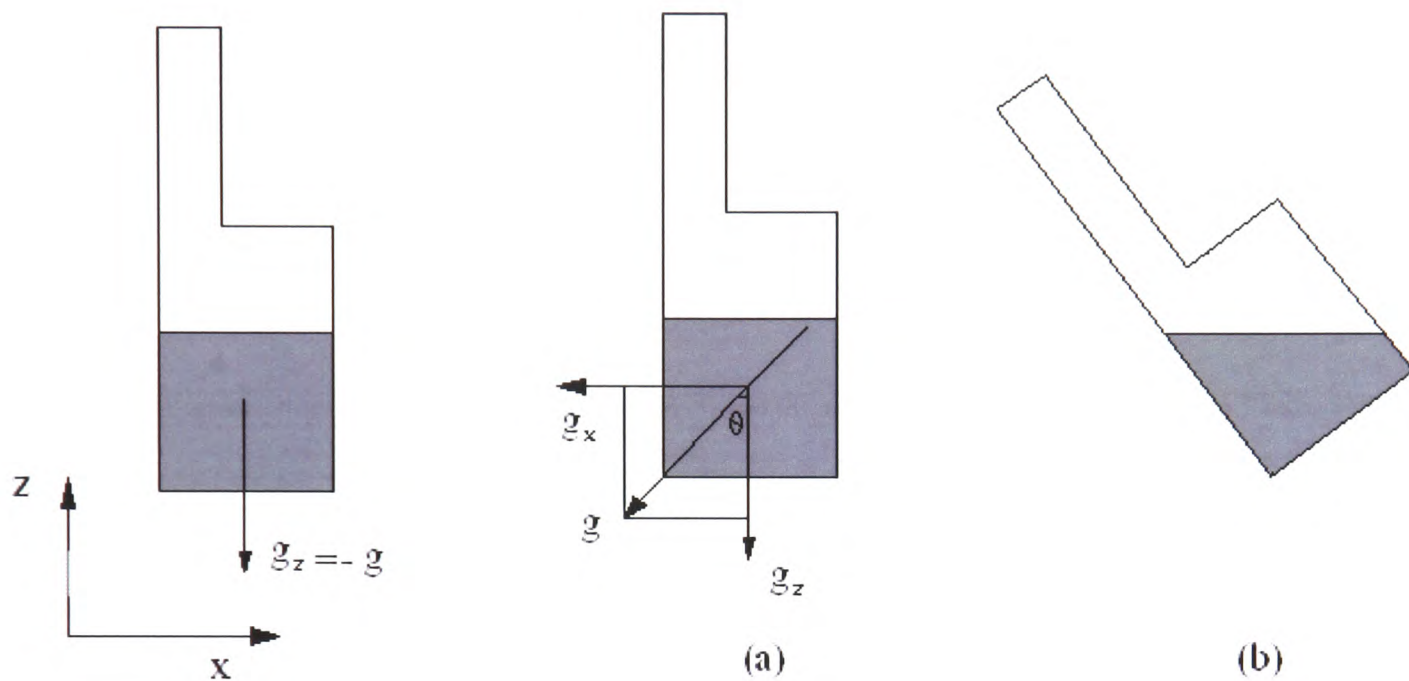


Figure 4.2: Schematic view of the gravity in tilt casting model

A mathematical expression relating tilting angle  $\theta$  to the tilting speed has been proposed so that an optimal value of tilting speed can be predicted by minimising splashing effects. Tilt speed is expressed by rate of change with respect to angle. If the initial time and the angle at this moment are  $t_0$  and  $\theta_0$ , the total time of tilting is  $t_t$  and the position at this moment is  $\theta_t$ , then the angle  $\theta$  at some time  $t$  is expressed:

$$\theta = \theta_0 + \frac{t-t_0}{t_t-t_0}(\theta_t - \theta_0) \quad (4.1)$$

and at this moment the gravitational force vectors become :

$$\begin{aligned} g_x &= -g \sin(\theta) \\ g_y &= 0 \\ g_z &= -g \cos(\theta) \end{aligned} \quad (4.2)$$

$g$ , a function of the time as  $\theta$  is. The new gravitational force vectors are used in Equation (3.2) for the tilt casting process. This technique neglects rotation forces within the fluid (centrifugal, Coriolis).

### **4.3 Modelling Tilt Casting with PHYSICA**

The simulations were attempted to validate the software for casting the thin section component, where fluid flow, heat transfer, solidification and free surface modules were switched on. The results are analysed for two orientations, two filling cycles and surface tension.

### **4.4 Validation: 'I'-shaped Test Piece**

Before starting any further investigation of the tilt casting process, the model needs to be validated. In this study, the validation has been done against a real-time X-ray radiography trial for a simple mould, carried out at the University of Birmingham. Since this technique can not be used in conjunction with the ISM furnace, the filling patterns were established with molten aluminium tilt cast in air using the tilt casting wheel, as shown in Figure 4.3. It was considered that good agreement between the predicted and actual flow patterns would provide the confidence that the simulation package could then be used to predict the filling moulds with molten TiAl.

#### **4.4.1 Experimental Descriptions**

As it was mentioned earlier, real-time X-ray radiography can not be used in conjunction with the ISM furnace because of space limitation. A tilt casting wheel was introduced instead to carry out the trials. Controlled tilt pouring was achieved by fitting the ceramic mould on to a 1 metre diameter wheel. The wheel is driven by a servo motor which is controlled by a computer program. During the trials the wheel was positioned between an X-ray source and a photo-multiplier detector connected to a digital camera to record the mould filling. Certain charge of aluminium was melted in a clay graphite crucible in an induction furnace and then transferred and positioned in the base carrier of the wheel. The ceramic mould was positioned on to the crucible. The whole assembly was held securely by a retaining clamp so that they could be rotated together to achieve the quiescent transfer of the liquid metal from the crucible to the mould.



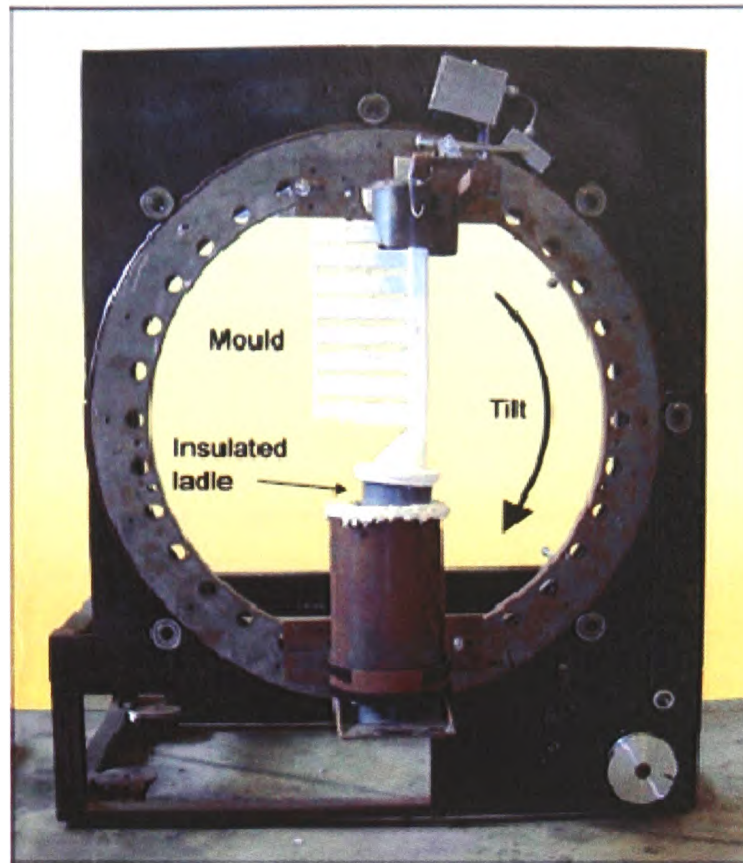


Figure 4.3: Tilt casting wheel used (Note: this does not show the mould used in the trials)[Harding -05].

In this experiment, aluminium alloy 6082 is chosen as the experimental material since its liquidus temperature is only 653 °C. A high superheat could be achieved by a conventional induction melting furnace to melt. There is no worry about premature solidification. Real-time X-ray images can clearly show the liquid metal flow profiles which can be compared directly to the numerical results using the tilt casting modelling code.

### 4.4.2 Dimensions of Test Piece and Design of Mould

In this trial, the 'I'-shaped test piece was used which is a simple representation of a turbine blade. The design and dimensions of the test piece used for the casting trials are shown in Figure 4.4. It is seen that the thickness of the body (like the blade body) of the test is only 4mm, very thin and the length is up to 152mm.

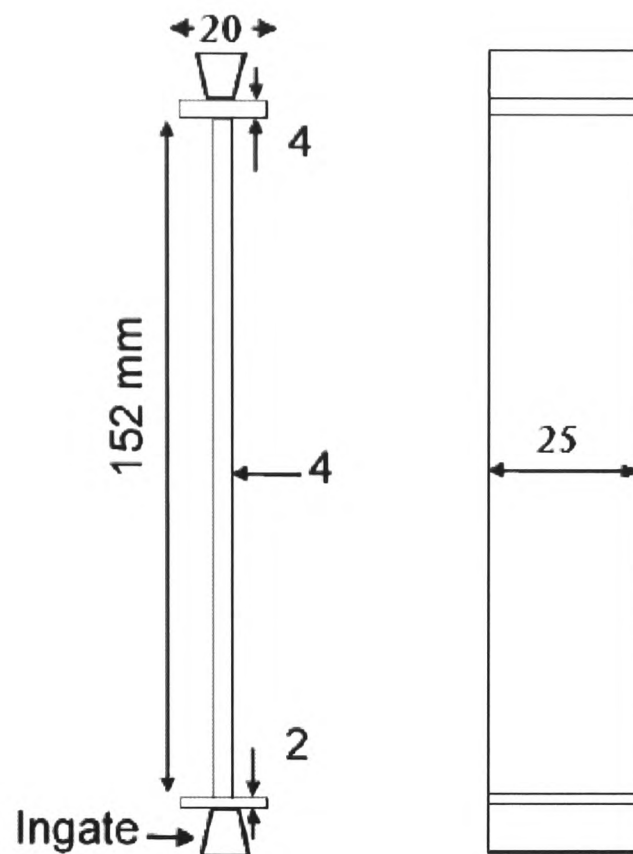


Figure 4.4: The design and dimensions of 'I'-shaped test piece.

The overall layout and dimensions of the mould are illustrated in Figure 4.5. The basic construction consisted of a pouring basin, the test piece and a ring-shaped blank end which allowed the completed mould to be securely held in the rotating device. A ceramic disc was positioned between the test piece and the blank end so that molten alloy filled only the test piece. The test piece was oriented in two ways: one with it perpendicular to the direction of the tilt as shown in Figure 4.5 ((a) on the left) and one with it rotated through 90° seen in Figure 4.5 ((b) on the right). A solid alumina rod was attached between the pouring basin and the wax ring to give the assembly extra strength to survive the shelling process and casting trial. Finally, the moulds are designed as seen in Figure 4.6.

## Chapter 4. Tilt Casting Method

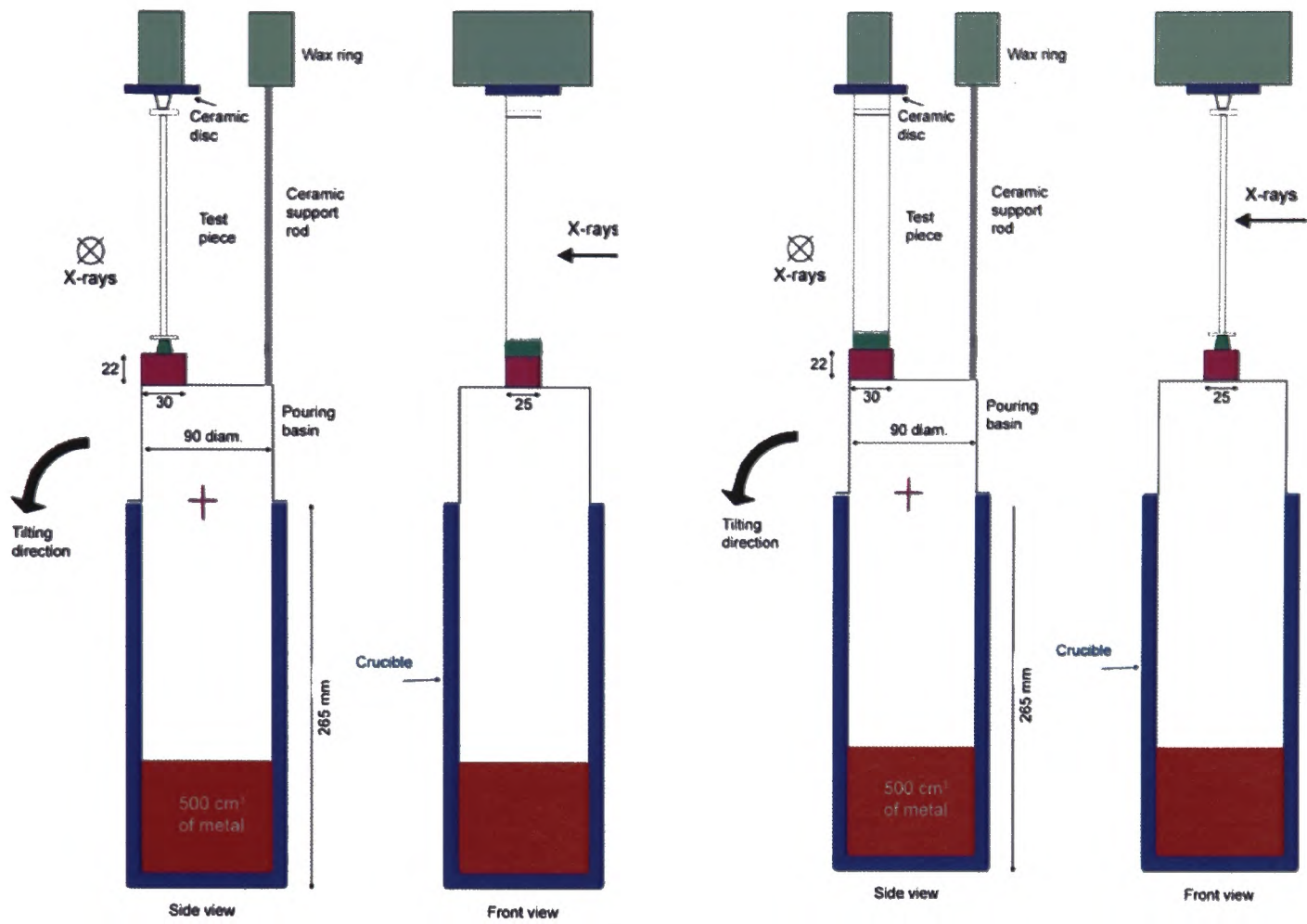


Figure 4.5: Set-up for validating trials.

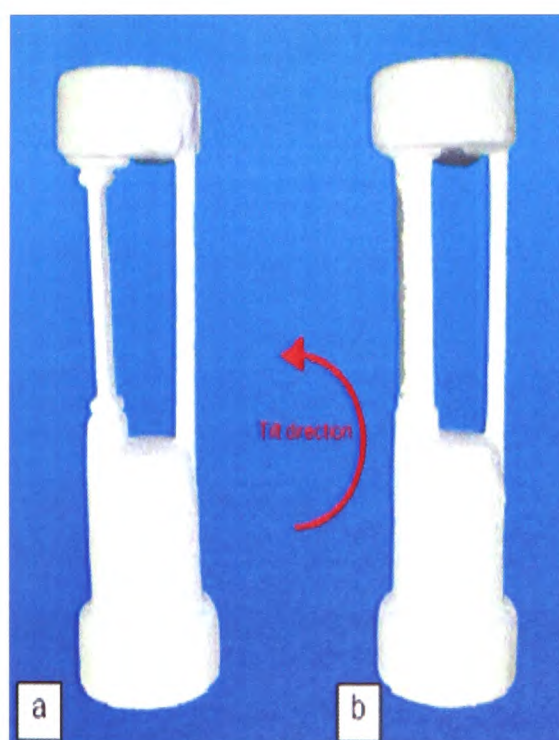


Figure 4.6: The design of the mould in the trials.



### 4.4.3 Geometry and Computational Mesh

As the above pictures show, in the experiment the whole test piece mould was attached to the pouring basin. It is supposed to be symmetrical with respect to the central vertical plane of the test piece (the assembly). So only half of the assembly was meshed and simulated in order to economize the computational cost. The geometry comprises a cylindrical crucible with an attached feeding system and the 'I'-shaped test piece. The mesh is unstructured due to the complexity of the geometry. In this model a 24912-element (left) and a 22464-element (right) mesh are generated. And two orientations are demonstrated in Figure 4.7.

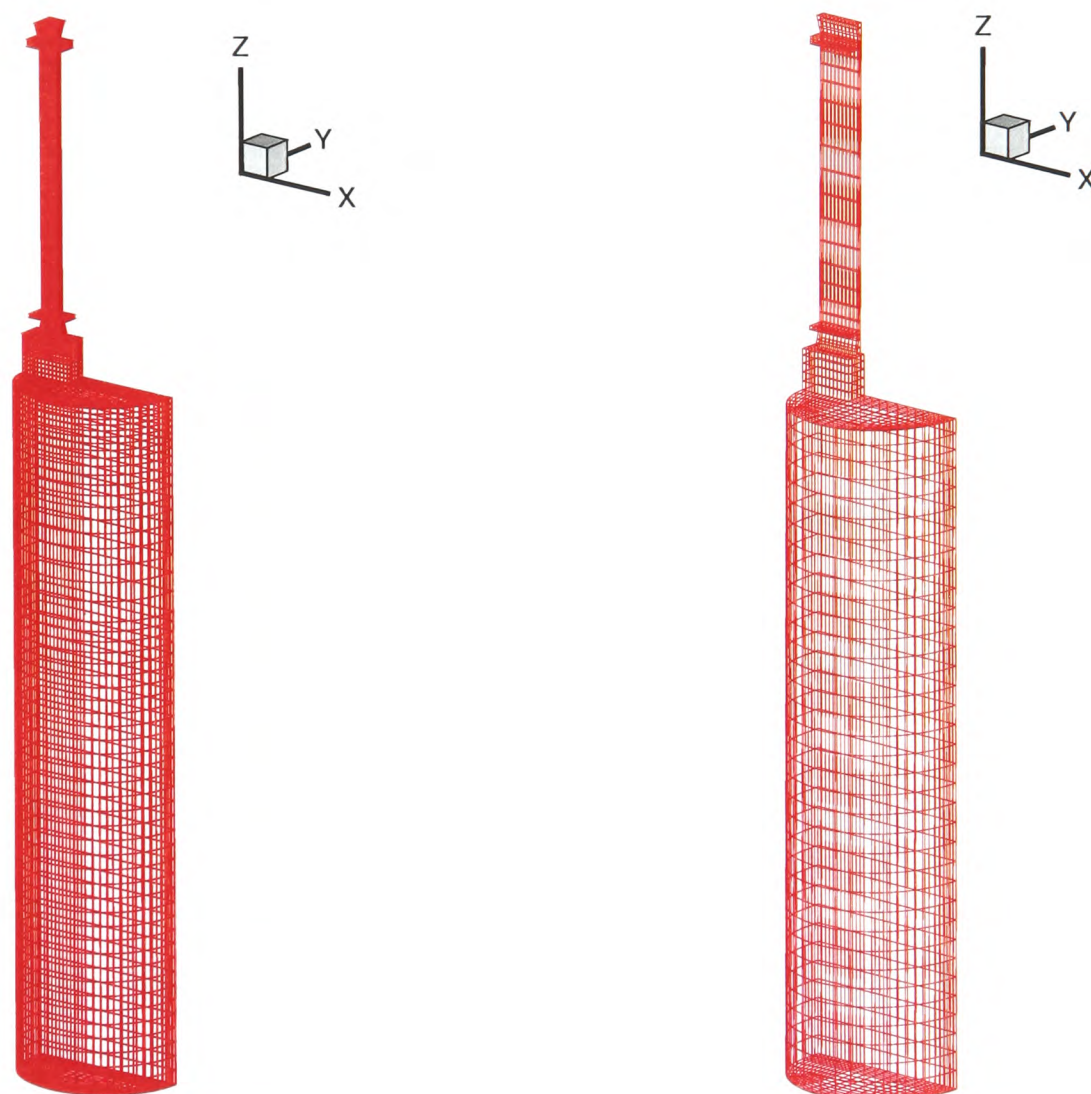


Figure 4.7: Computational meshes of the model for two orientations of the test 'I' piece.

As it is shown, the crucible wall and the mould are not included in the mesh. Only one material, aluminium, is involved. Attention is focused on the free surface fluid flow.

### 4.4.4 Initial Conditions and Boundary Conditions

A series of trials have been carried out for the 'I'-shaped test piece. The experimental details for these four castings were listed as follows:

Table 4.1: The experimental details in the trial

Melt	Filling mode (refer to Table 4.2)	Metal temp, °C	Mould temp, °C	Melt weight, kg	Orientation
Case 1	Program*	Not measured	392	1.294	(b)
Case 2	20 deg/sec	761	448	1.303	(b)
Case 3	Program*	760	482	1.294	(a)
Case 4	Program*	678	508	1.309	(a)

No artificial venting was included in any of the moulds.

\* see Table 4.2

In this model, the crucible wall and the mould were not meshed in order to simplify the meshing and save computational time. As it is shown in the above table, the superheat is up to 100 °C which is desirable for casting thin section components. More attention is paid to the mould filling. In these simulations, a constant heat transfer coefficient, 400W/(m<sup>2</sup>K), was adopted on the blade; on all the solid walls, the no slip condition is valid.

### 4.4.5 Filling Modes

Two filling modes were used in the simulations: one is at a constant 20 deg/sec; the other is the programmed mode presented in Table 4.2. At the first stage of the filling, a fast speed is used to let the metal quickly fill into the pouring basin, then holding few seconds to allow the gas to evacuate the blade and to make the metal calm down. Slow speed is used to permit the metal to take time to slowly move into the blades which would avoid surface turbulence, holding few seconds again, finally quickly finishing the mould filling.

**Table 4.2: The programmed filling mode**

Time, s	Event
0	Rotate at 20°/s to 80°
4	Hold 2.5 s
6.5	Rotate at 6°/s to 100°
9.8	Hold 2.5 s
12.3	Rotate at 20°/s to 180°
18.3	Finish

#### **4.4.6 Presentation of Results**

##### **4.4.6.1 Effects of Surface Tension**

In this validation, the geometry used contains a very narrow cavity in the 'I'-shaped test piece whose thickness is as thin as 4mm. The effects of the surface tension are expected to play an important role. The same surface tracking models are switched on in the simulations using different values of the surface tension since the presence of oxides makes this property uncertain.

Figures 4.8-4.10 show the comparisons of the numerical results with variable values of surface tension, 0.0, 0.94 [Molina- 07] (this value is thought as the value of surface tension when assuming aluminium is not oxidized) and 3.0 N/m for Case 1. It can be seen that there is a slight difference between the case without surface tension and that with the value of surface tension 0.94 N/m. The metal smoothly moves in the narrow test piece. However, it can be noted that the metal is filling the mould with 0.94 (N/m) surface tension much faster than that with 3.0 (N/m) surface tension. The value of surface tension has effects on the filling pattern. The greater the value of surface tension is, the more significant its effects are on the filling.

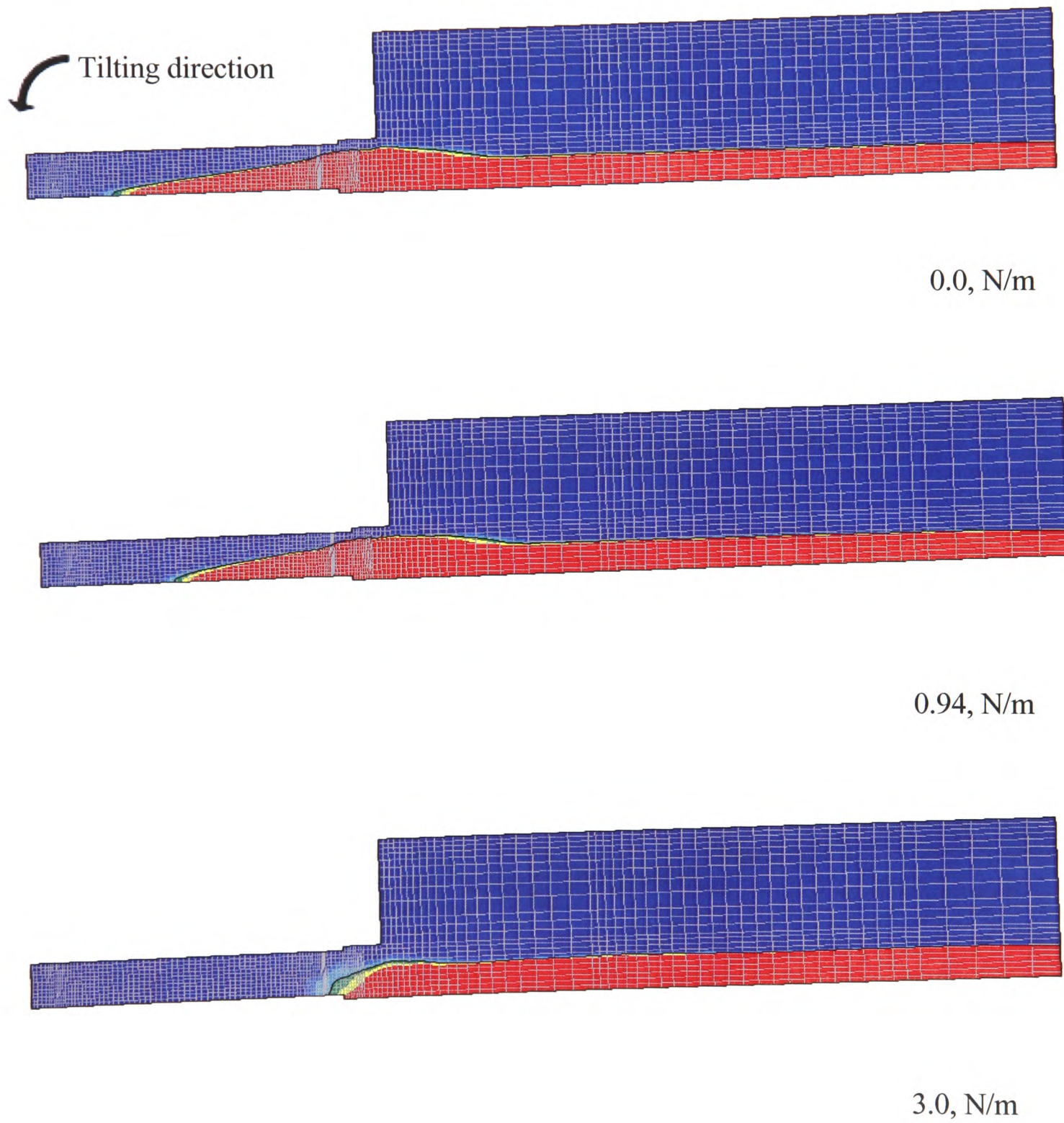


Figure 4.8: Comparisons of numerical results with different surface tension values at 8.5s.



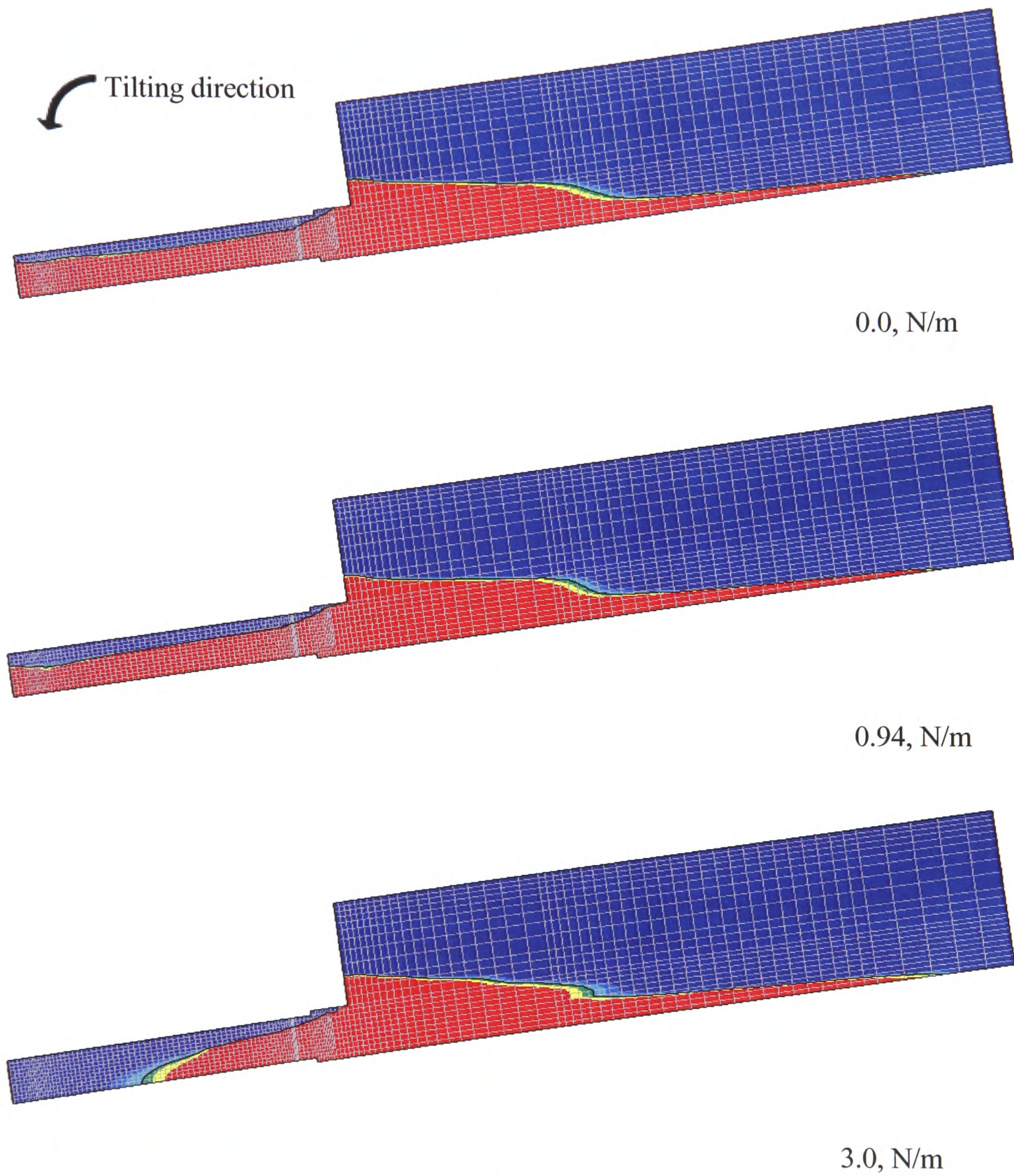


Figure 4.9: Comparisons of numerical results with different surface tension values at 9.5s.



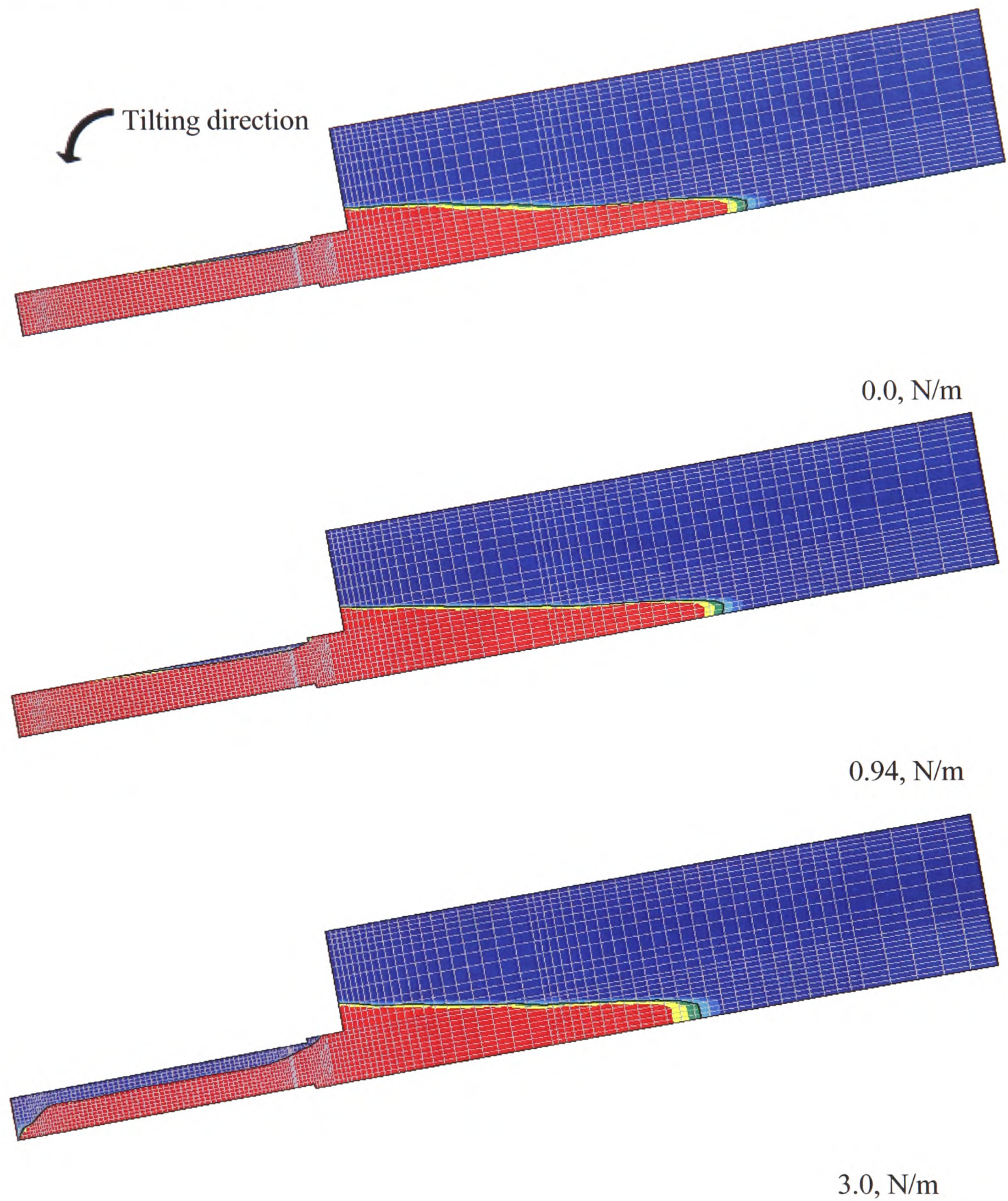


Figure 4.10: Comparisons of numerical results with different surface tension values at 10.5s.

#### 4.4.6.2 Comparisons of the Experimental and Numerical Results

Some of still pictures from X-ray movie of validation Case 1 were captured at different times. The comparisons of the experimental and numerical results are shown in Figure



## Chapter 4. Tilt Casting Method

4.11 with Van Leer when surface tension is 0.94 N/m [Molina- 07]. It is noted that the mould filling is much faster than that taken in experiments. It is known in section 4.4.6.1 that surface tension (0.94 N/m) has tiny impact on the mould filling. However, according the comparison shown in Figure 4.11, the effect of surface tension is not as much as it is expected or the value of surface tension used is not high enough to resist the metal flow. Here one factor may affect the results is that the presence of a thick aluminium oxide on the metal surface. This is expected as the experiment is conducted in air. The oxide film could form and act as an enhanced surface tension force. The other factor is that the effect of surface tension in conjunction with Van Leer and Donor Acceptor in PHYSICA did not include the effect of the contact angle. The default value of contact angle is  $90^\circ$ .

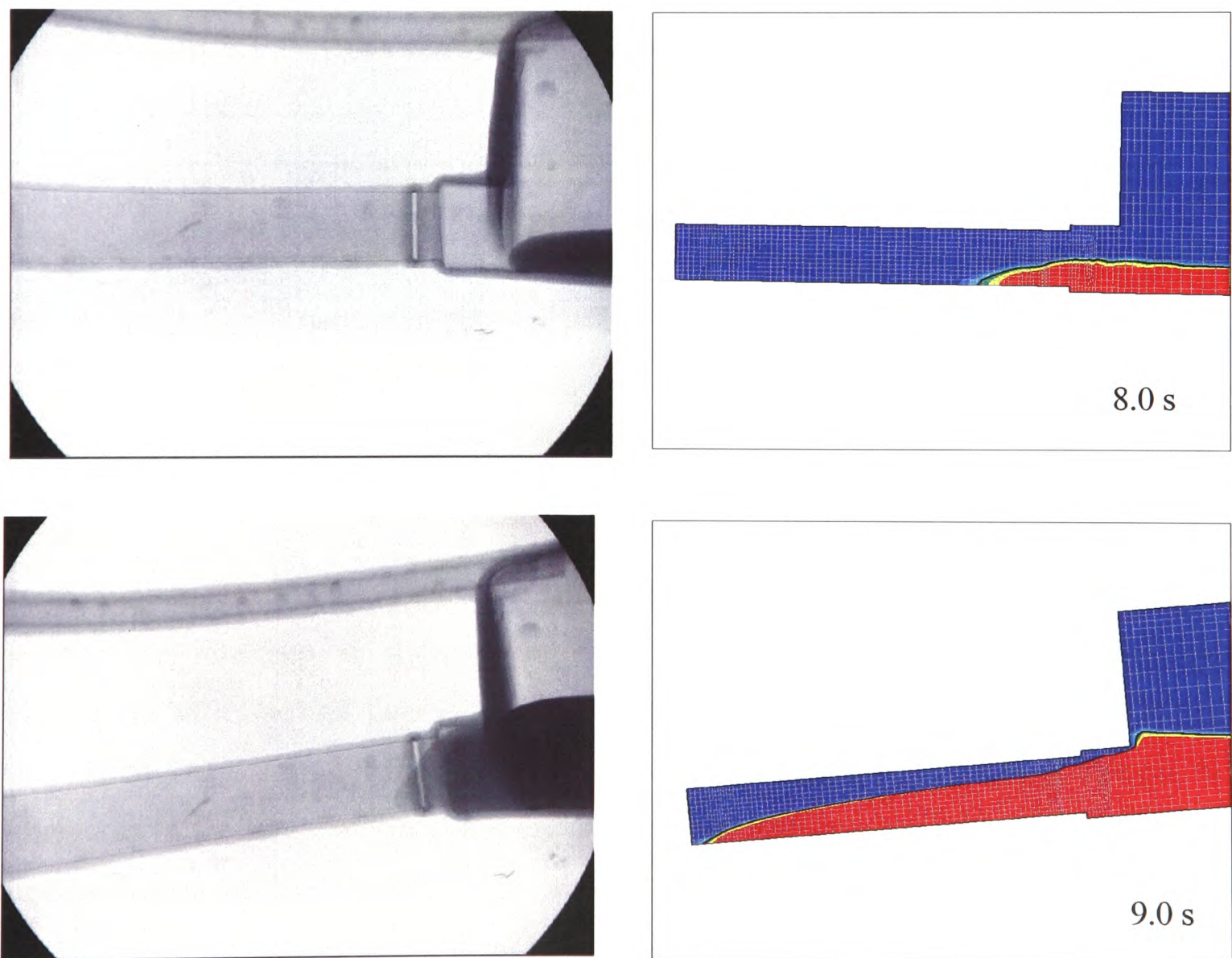


Figure 4.11: Comparison of experimental and numerical results at 8.0s and 9.0s.

## Chapter 4. Tilt Casting Method

---

As it is discussed in the previous section, the greater the value of surface tension the more influence on the filling pattern. A value of 3.0 N/m surface tension could give better correspondence with experiments and it is employed in the following simulations.

Figures 4.12-4.14 show the comparisons of the experimental and numerical results with Van Leer when the value of surface tension is assumed to be 3.0 N/m. The numerical results show that the metal is about to move in the pouring basin at 8.0 s as it is recorded in the experiment. Then the metal slowly moves in the pouring basin and feeder at 8.5 s and 9.0 s as illustrated in Figure 4.12. They show a good match between the experimental and numerical results. The path that the gas is evacuating through between the blade and the pouring basin is clearly present in the simulation results and in X-ray films at 9.0 s, also shown in Figure 4.15. The counter flow occurs at the blade due to the lack of venting at the end of the blade. However, the shape of the metal front in numerical results is not as round and smooth as it is present in experiment.

As the filling continues, the metal slows down into the narrow test piece as shown in the recorded film. The numerical results show that the mould filling is slightly faster than that taken in experiments as in Figure 4.13. It is assumed the delay is due to the resistance presented by a thick oxide film on the aluminium surface.

After the metal reaches the mould far end, a backwave is set up shown in the video and in the numerical results in Figure 4.14. However, the numerical results are not able to present the interface as sharp as in experiment due to numerical diffusion. The simulation with the Van Leer algorithm is suffering from surface smearing. At 11.0 s, it is noted that the mould filling is slower than that shown in X-ray film. That can be attributed to the fact that gas could escape from the ceramic mould wall (porous wall) in experiment. In the numerical simulation, the mould wall is considered as a solid and the gas can only evacuate the mould by the junction between the blade and the pouring basin. When the metal flows in the pouring basin, it is hard for gas to evacuate. The compressed gas in the mould resists the metal.



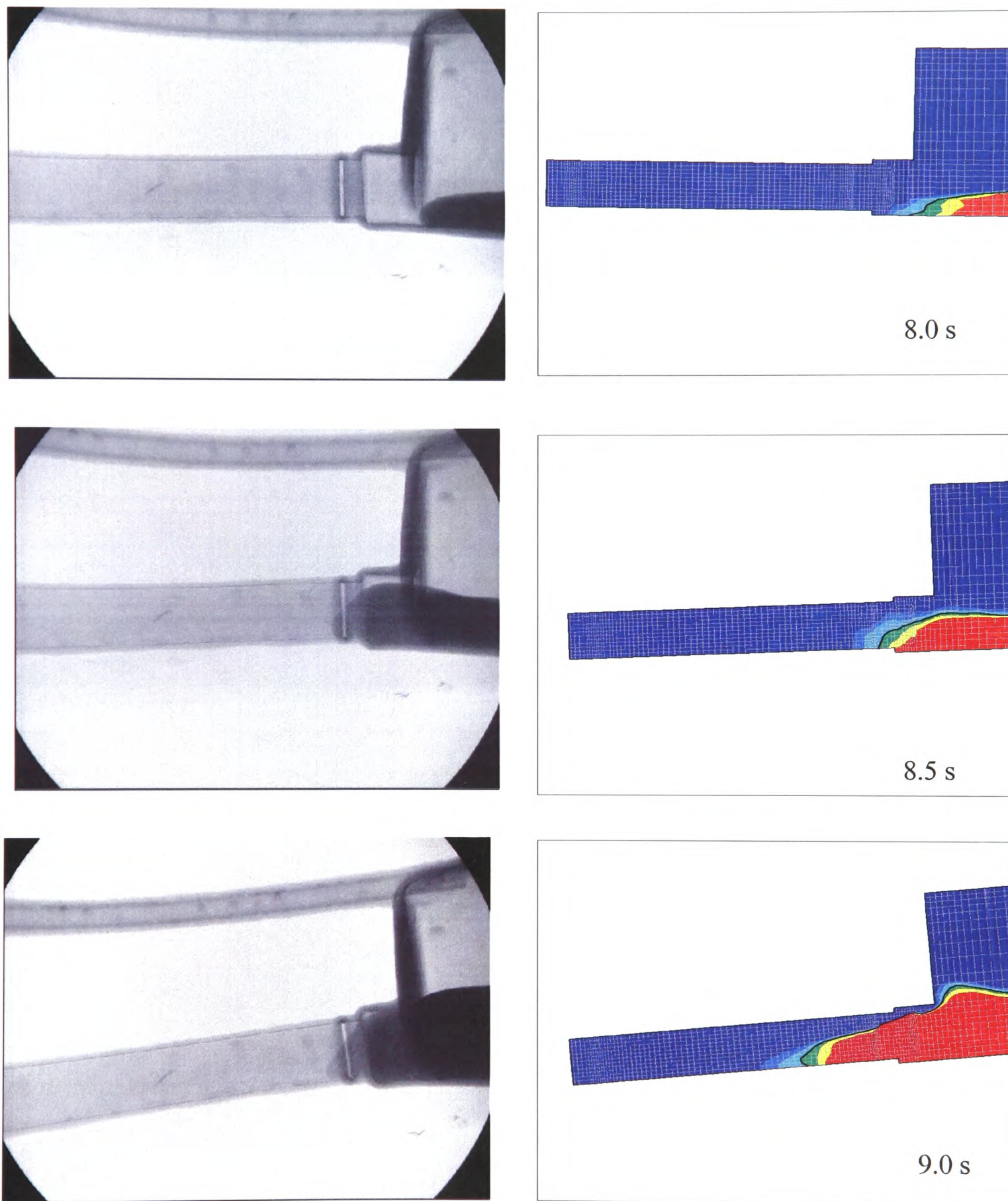


Figure 4.12: Comparison of experimental and numerical results at 8.0, 8.5 and 9.0s.



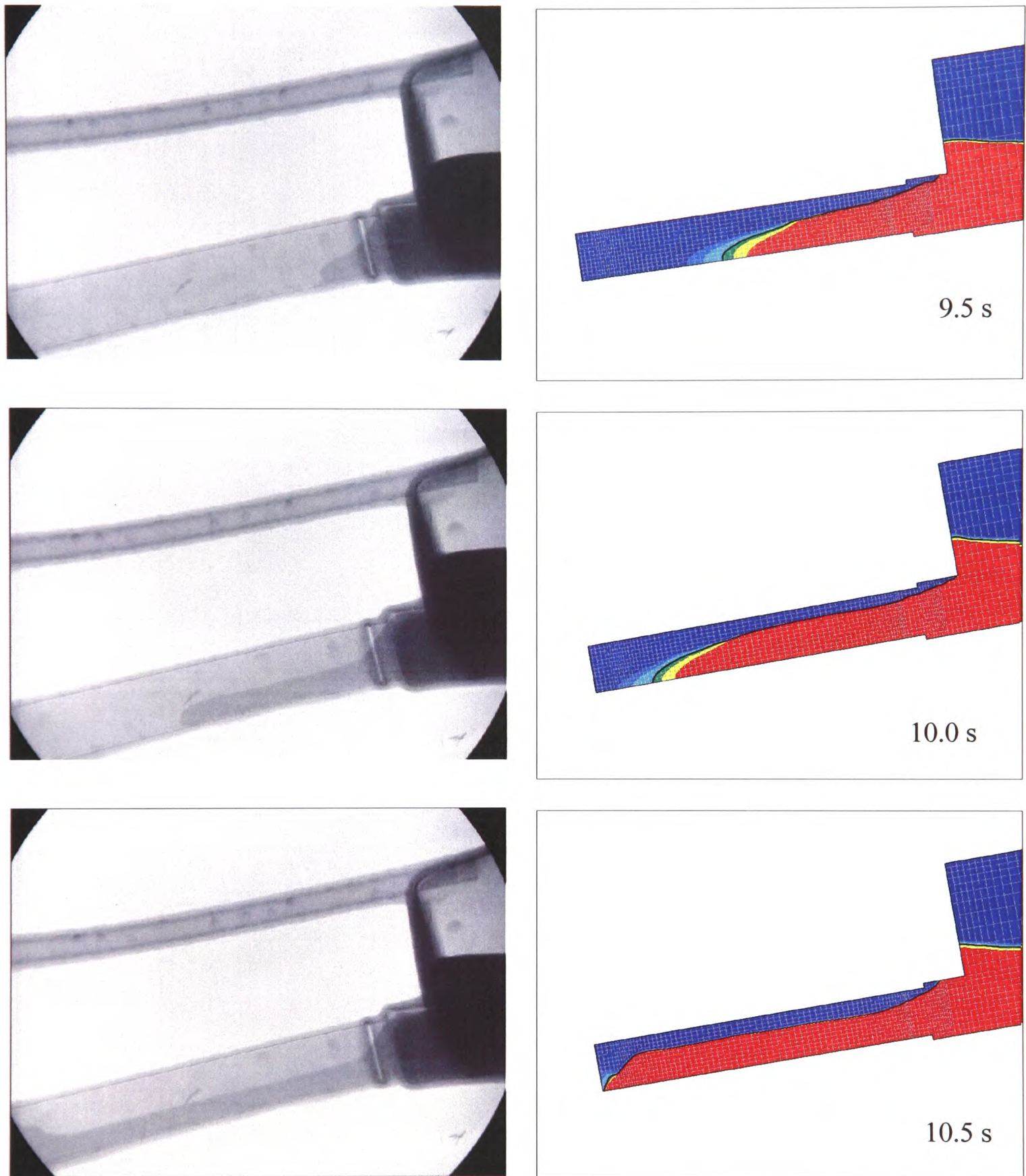


Figure 4.13: Comparison of experimental and numerical results at 9.5, 10 and 10.5s.



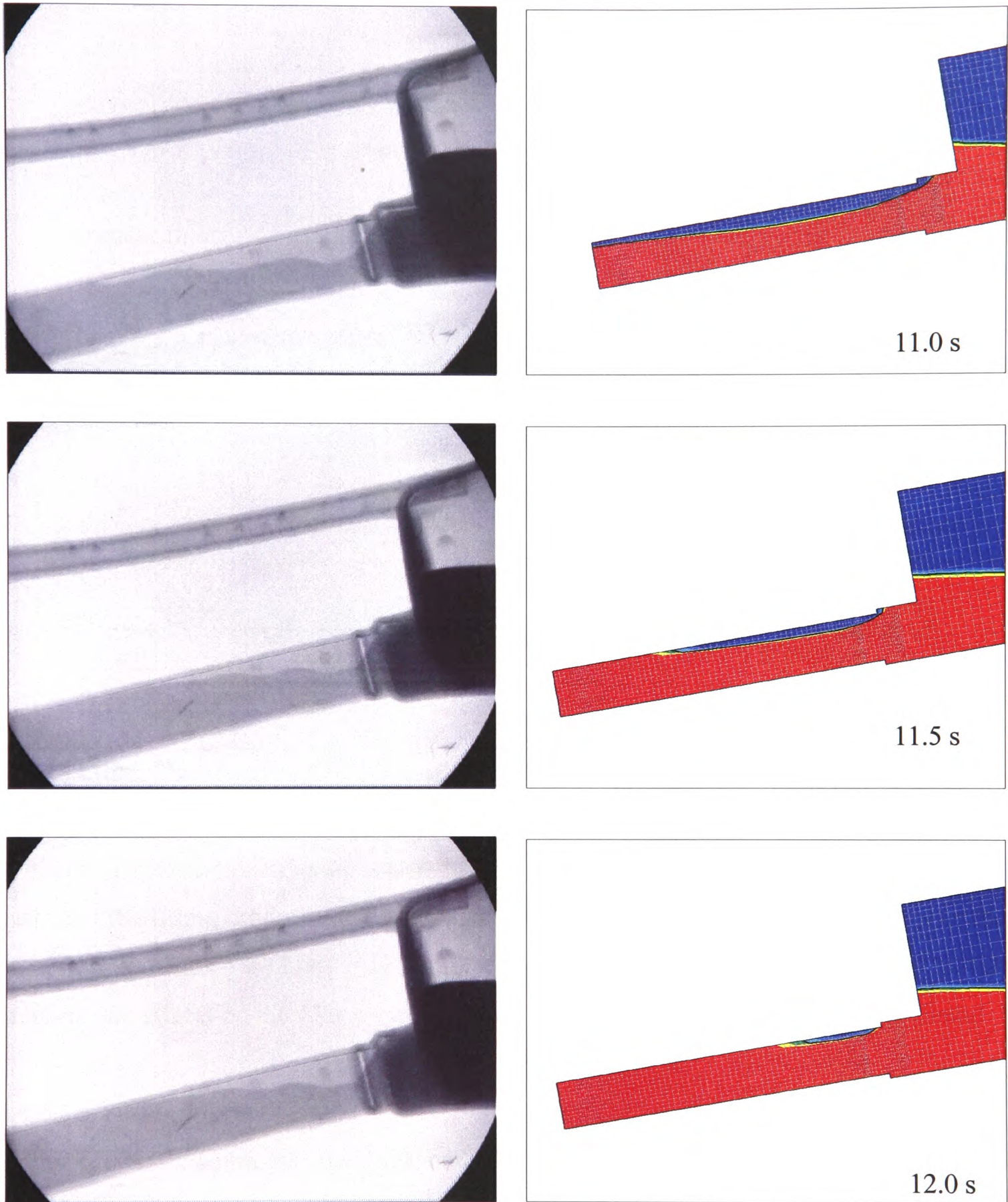


Figure 4.14: Comparison of experimental and numerical results at 11, 11.5 and 12.0s.

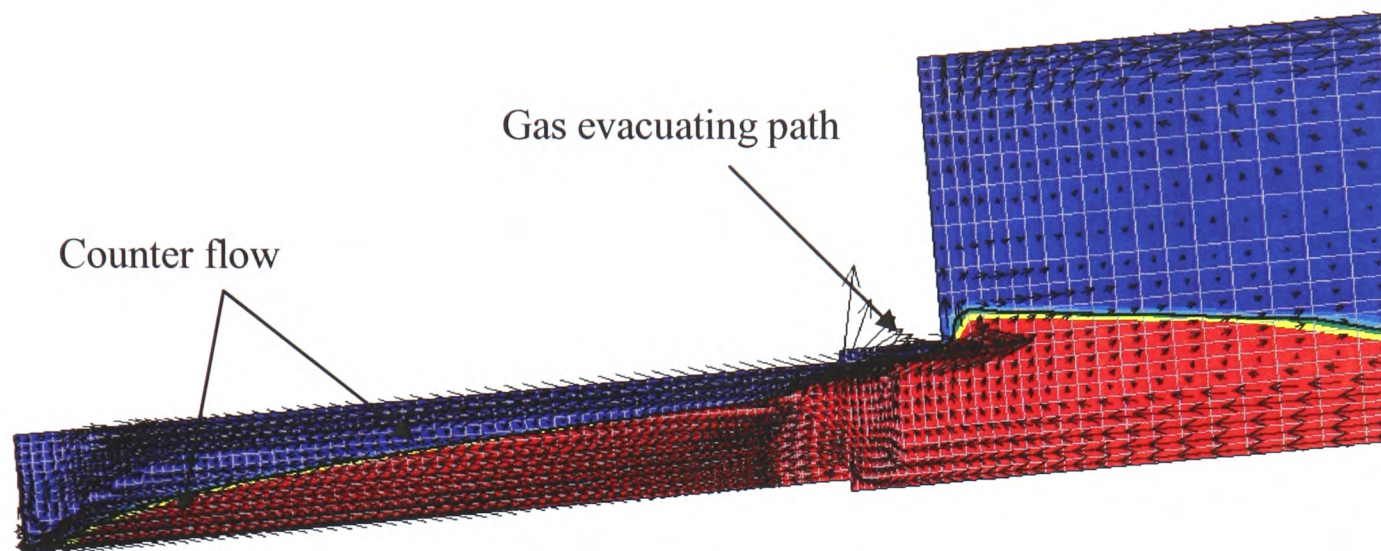


Figure 4.15: Velocity vector with the surface tension value of 0.94 N/s at 9s.

### 4.4.6.3 Other Parameters Affecting on the Tilt Casting Process

As it has been mentioned earlier, the filling speed and the orientation of the test piece are two very important parameters which affect component quality in tilt casting. A good design of the filling mode and the mould is essential to avoid defects. And analysis of the numerical results is very helpful to optimise the number of experiments. In the following sections, the effects on the filling speed and orientation of the test piece will be discussed.

#### 4.4.6.3.1 Filling Modes

In the tilt casting process, the ISM crucible and mould would be rotated together to achieve mould filling. Choosing an appropriate speed of tilting (or rotation) is important in this process: lower speeds should prevent gas entrainment but increase the heat loss due to contact with the cold crucible and radiation loss; higher speeds will reduce premature solidification but increase the risk of bubble formation and oxide entrapment due to surface turbulence. The effect of surface turbulence on the reliability of castings has been studied in [Green and Campbell -93].



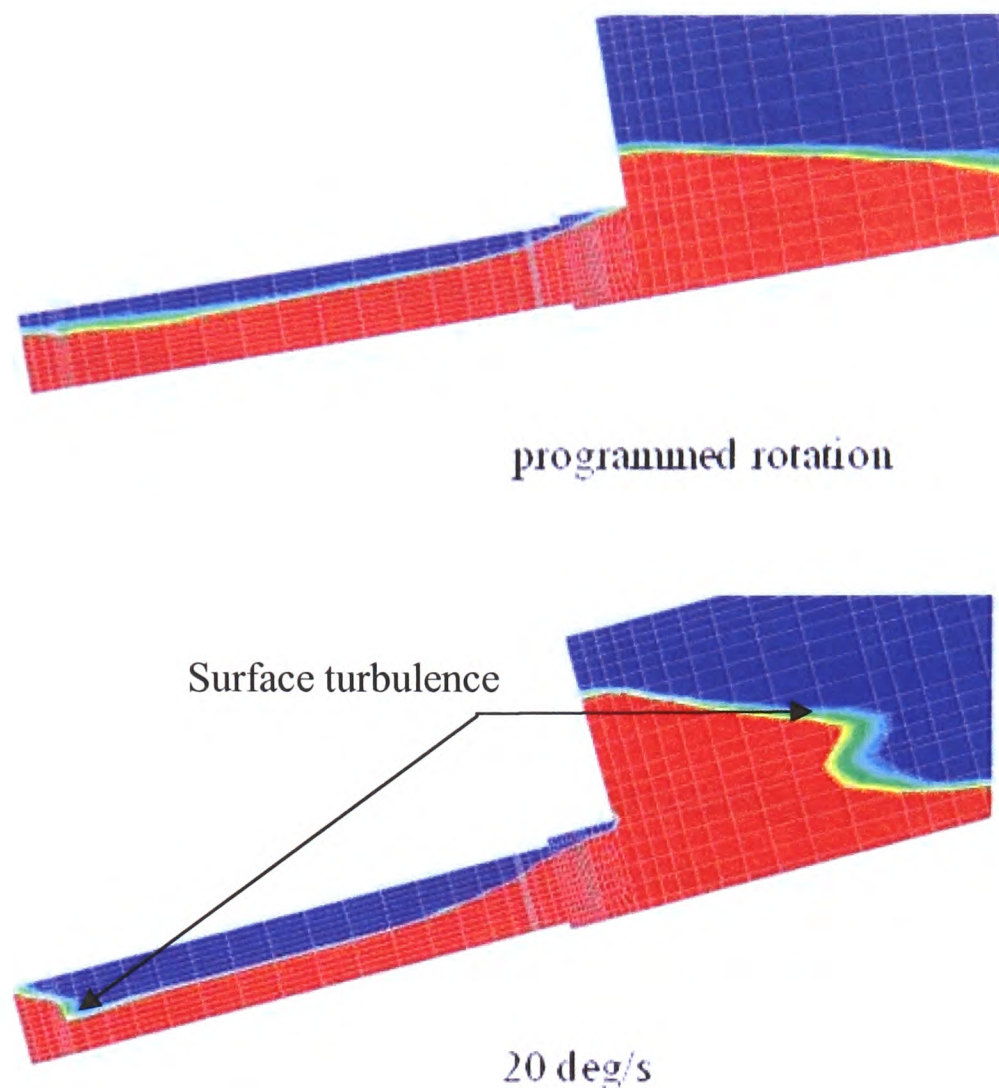


Figure 4.16: Surface turbulence during quick mould filling: programmed rotation (upper) and 20 degree/s (lower).

In this study, two rotation speeds were suggested: one is fairly fast, at a constant 20 deg/sec for Case 2 (details in Table 4.1); the other is slower with programmed cycles for Case 1 (seen in Table 4.1). Both simulations are modelling fluid flow and free surface behaviour using the Van Leer numerical scheme.

Still pictures at the similar position are captured to illustrate the effect of the filling speed, presented in Figure 4.16. A back-wave was set up after the metal reached the mould end at the rotating speed of 20deg/s. This back-wave could cause entrainment defects caused by surface folding during filling cycle. A smooth interface is present when the programmed rotation is employed. Therefore, an appropriate compromise should be adopted between pouring speed and surface turbulence.



### 4.4.6.3.2 Orientation of the Mould

In the Section 4.4.2, it was explained that the test pieces were oriented in two ways: one with it parallel to the direction of tilt (a) and the other with it perpendicular to the direction of tilt (b). Figures 4.17 and 4.18 show the free surface contour ( $\Phi=0.5$ ) at 120 degrees and 180 degrees for these two orientations of the test piece. For orientation (a), a counter-current of metal and gas was observed at 120 degrees in contrast no gas was present at the same position for the other orientation (b); there is enough space for the gas to evacuate the mould as the metal enters. For the orientation (b) the mould filling is faster than that for orientation (a). At the end of the filling, some gas was trapped in the rectangular blades with the metal occasionally blocking the gas exit for the orientation (a).

From the above presentation, it is concluded that the orientation has an important effect on the mould filling. A suitable orientation can decrease the possibility of casting defect due to trapped gas.

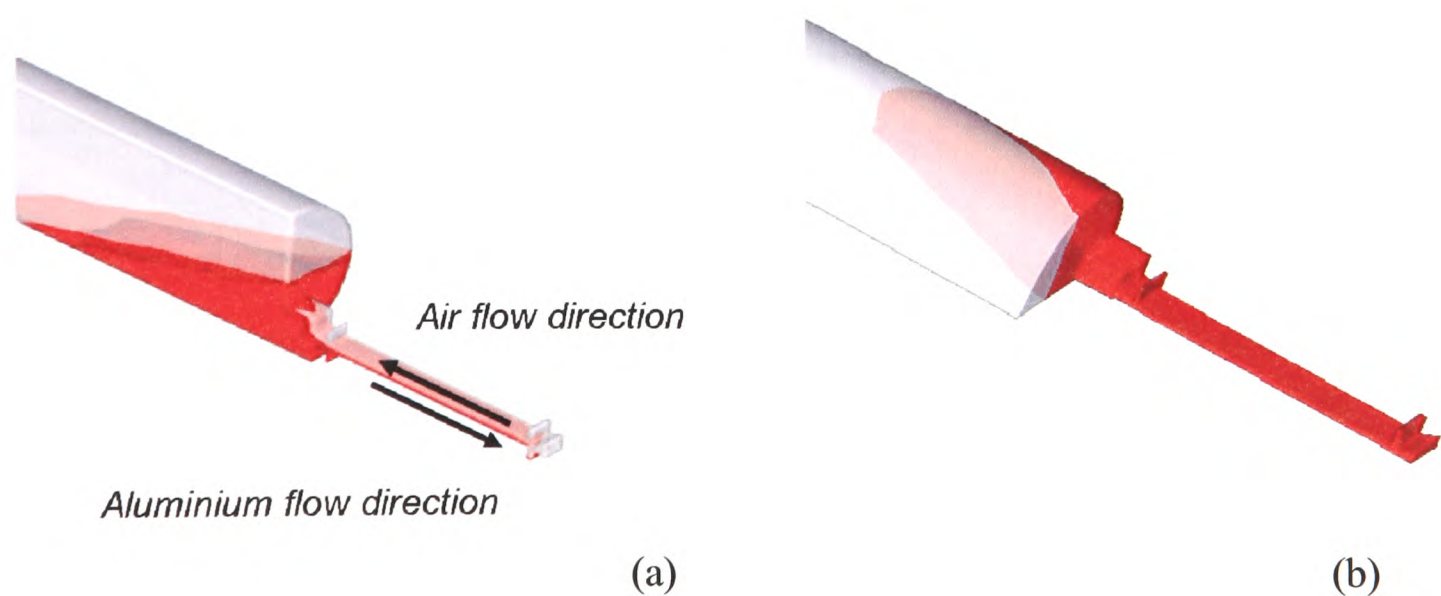


Figure 4.17: Comparison of two orientations in free surface contour at 120 degrees.

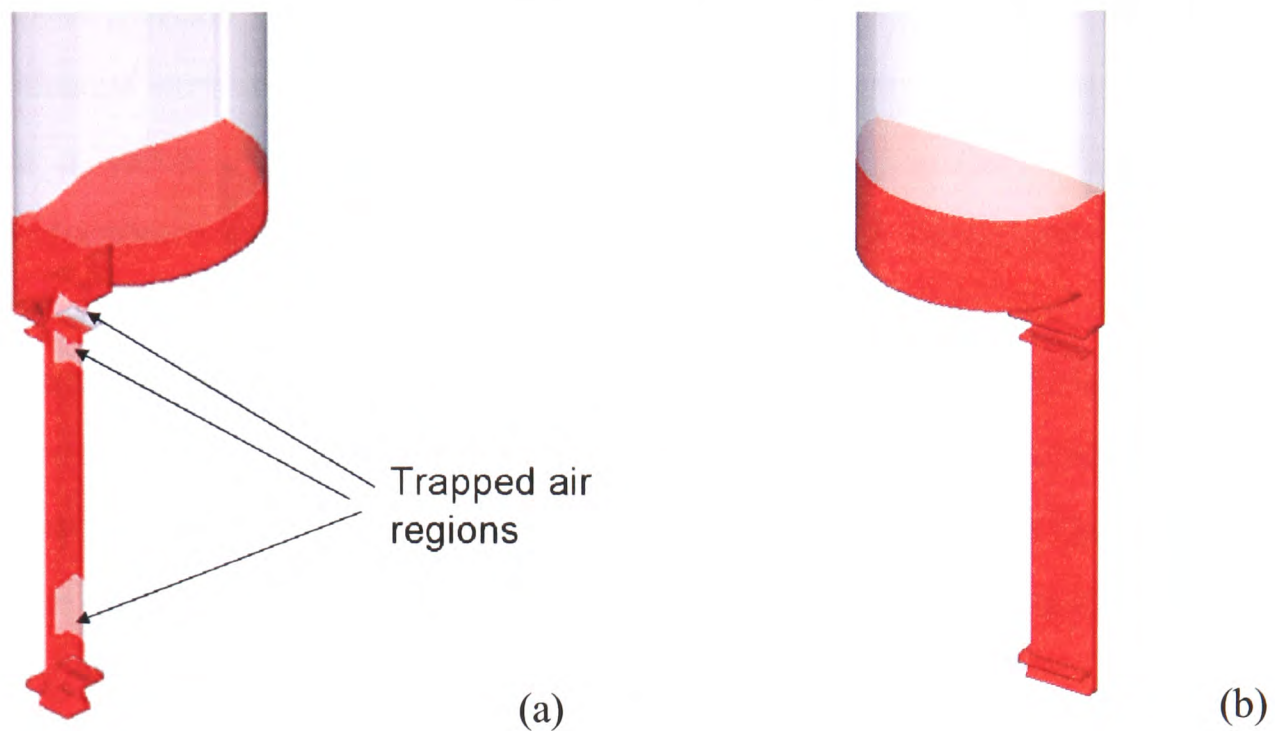


Figure 4.18: Comparison of two orientations in free surface contour at 180 degrees.

### 4.6 Summary

This chapter has described the tilt casting process and the numerical model for simulating the process. The validation of the model has been presented against 'I'-shaped aluminium test piece. The effects of filling cycle, orientation of test piece and surface tension have been discussed.

CFD code PHYSICA models the tilt casting process. The free surface has been well tracked during the mould filling. Gas evacuation path is clearly present in the numerical results as it is observed in trials. Numerical results have shown that the speed of filling and the orientation of the test piece are very important factors which can have significant effects on the quality of the casting. Appropriate orientation can avoid generating some casting defects such as air entrainment and bubbles. Careful control of filling speed is also important to achieve quiescent mould filling. Two filling speeds were tried, one is a programmed rotation and the other is at a constant 20 deg/s. Quick filling resulted in surface turbulence.

## Chapter 4. Tilt Casting Method

---

The results show that the value of surface tension has impact on the mould filling. The greater the value of surface tension is, the more influence the surface tension has on the filling. When a value of surface tension appropriate for aluminium (0.94 N/m) is employed, the comparisons show the predicted filling to be much faster than that observed experimentally. It is suspected that the aluminium is oxidized since the experiment is carried out in air. A thick aluminium oxide on the metal surface could hold the metal from moving forward as a strong surface tension does. When a higher surface tension (3.0 N/m) is used, the comparisons between the numerical and experimental results have improved. One more factor to this difference is that the effect of contact angle in the used free surface method is not included.

It is seen that in general, the numerical model works well for mould filling and in predicting the influence of the orientation and the speed of the filling. However, some improvements need to be made, such as venting needs to be introduced to avoid gas counter-flow in the test piece, and trapped gas; the effect of the surface tension should count the change of contact angle.

## Chapter 5

# 3D/1D Coupled Transient Heat Transfer Model

In this chapter, a new model, called the 3D/1D Coupled Transient Heat Transfer Model, is presented. This model is developed based on the fact that the mould filling for titanium aluminides (TiAl) is carried out within a few seconds and the thermal conductivity of the mould material is very low compared to that of the metal. Heat can be assumed to transfer only in a direction perpendicular to the mould wall. The model is validated for two test cases: one is that the molten TiAl alloy fills an idealised thin component, which is similar to the blade mould filling; the other is when the molten metal is held in a mould, which is like the solidification after filling. The comparisons are given in computational time and the number of the iterations, compared to a full 3D solution.

Finally the model is used to simulate short 20 cm turbine blades. The numerical results are compared with the experimental ones. The parameters affecting the tilt casting process are discussed through the presentations of results.

## 5.1 Introduction

The investment the casting of turbine blades and other thin-section components could be frustrated, especially for if the molten metal has low superheat. At present, the induction skull melting (ISM) or cold crucible technique has been used for the melting stage. In the system, the water-cooled crucible absorbs much of the thermal energy leading to low superheat which is a critical problem during mould filling. That results in a high risk of ‘mis-runs’, i.e. incompletely filled moulds. The metal temperature is falling very fast since there is big temperature drop between the mould and the metal even where the mould is preheated. Within a few seconds, the metal temperature could drop under the liquidus temperature. The velocity pattern in the boundary layer then becomes complex due to the effects of the rapid temperature change. The likely velocity profile at the onset of solidification is like the shown in Figure 5.1.

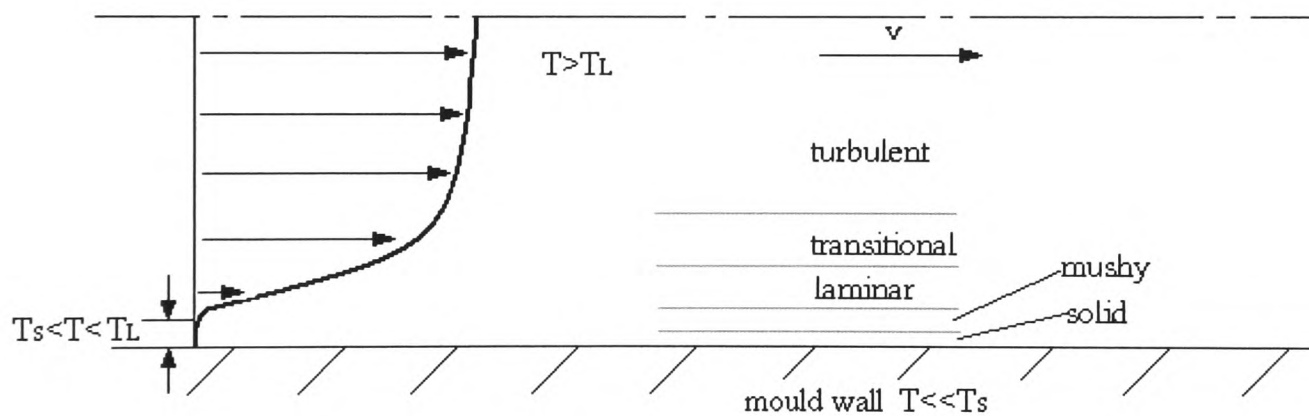


Figure 5.1: The velocity profiles in the boundary layer during the mould filling when solidification first starts at the wall.

The layer closest to the wall could be solidified immediately because the temperature of the ceramic mould is much lower than the molten metal temperature (approximate 400°C temperature difference in trials). Next to the solid layer, there is dendritic in-between layer called ‘mushy’ zone. Laminar, transitional layer and turbulent flow layer are ordered towards the centre. Therefore refining boundary conditions is seen as important for heat



## Chapter 5. 3D/1D Coupled Transient Heat Transfer Model

---

transfer through the mould wall and the crucible when studying the tilt casting for TiAl. However, in 3D this would necessitate a much larger overall grid for the casting simulation which would be impractical for the amount of parameters to be studied and response time required to assess the design of the real process.

In the following section, a coupled 3D/1D model is introduced in order to achieve the more accurate thermal boundary conditions without the necessity of an expensive 3D refinement.

### 5.2 Model Descriptions

The 1D model does not mean one Dimension in geometry. It means that heat only transfers in ‘one’ direction in the mould, that is from the metal to the ambient environmental outside. The objectives of developing the 3D/1D coupled model are:

- Get more accurate thermal boundary conditions;
- Simplify the geometry meshing;

The main idea is that the 1D model supplies the thermal boundary conditions to the main flow field 3D model while the 3D model provides the boundary temperature to the 1D model, as Figure 5.2 shows. The thermal diffusion in the mould wall is neglected in the direction parallel to the mould. The part in grey is the mould, where the coordinates of each cell centre are specified during the computation instead of meshing mould. That simplifies the geometric model generation and accelerates simulations.

The 1D model is coupled with the 3D model by the interface temperature  $T_w$ . When calculating the mould temperature  $T_1...T_n$ ,  $T_l$  is picked up as the boundary temperature from 3D domain. Once  $T_w$  is known, it will be employed as the up-dated boundary temperature of the 3D model.

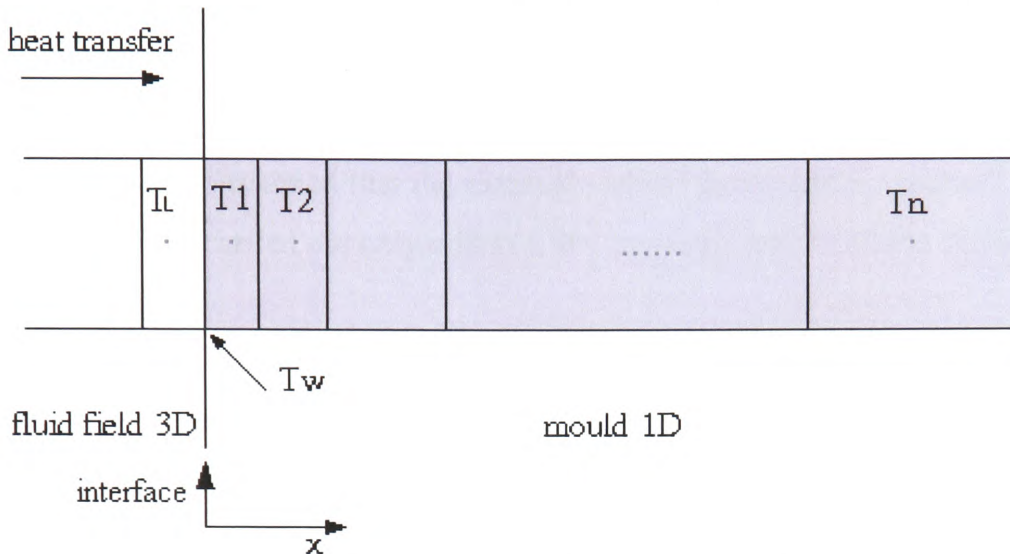


Figure 5.2: Coupling of 3D PHYSICA model and 1D transient heat transfer.

Although in Figure 5.2, the metal and mould are in perfect contact, gaps developing due to metal shrinkage can be easily incorporated as shown later on in Chapter 7.

### 5.3 Mathematical Descriptions

The mathematical descriptions for 3D model have been fully introduced in Chapter 3. For the 1D model, only 1D transient heat conduction equation is employed:

$$\frac{dT}{dt} = \alpha \frac{d^2T}{dx^2} \quad (5.1)$$

$\alpha$ , the thermal diffusivity of the mould;  $x$  represents the direction perpendicular to the mould.

#### 5.3.1 Assumptions and Boundary Conditions:

The change of the thermal conductivity of the metal is not considered when the temperature is varied. The fluid in the boundary layer is laminar. They are:

- The fluid in the boundary layer is a laminar flow if the metal is not frozen;
- The thermal conductivity of the metal in the solid and liquid state is the same, a constant thermal conductivity of the metal is used;

## Chapter 5. 3D/1D Coupled Transient Heat Transfer Model

---

- The thermal diffusion in the mould wall is neglected in the direction parallel to the mould.

In this study, it is assumed that the external wall of the mould is constant for the mould filling (since it is carried out only within a few seconds); and on all the solid walls, no slip condition is valid:

- For the external mould wall,  $T=\text{Constant}$ ;
- On the solid walls,  $\underline{u}=0$ .

### 5.3.2 Numerical Methods: Finite Difference Method

The finite difference method is used to discretise the conduction equation (the details about the finite difference method as seen in Chapter 2). In this case only one variable, the temperature, is involved. The schematic figure of finite difference discretization in space and time for this case is shown in Figure 5.3.

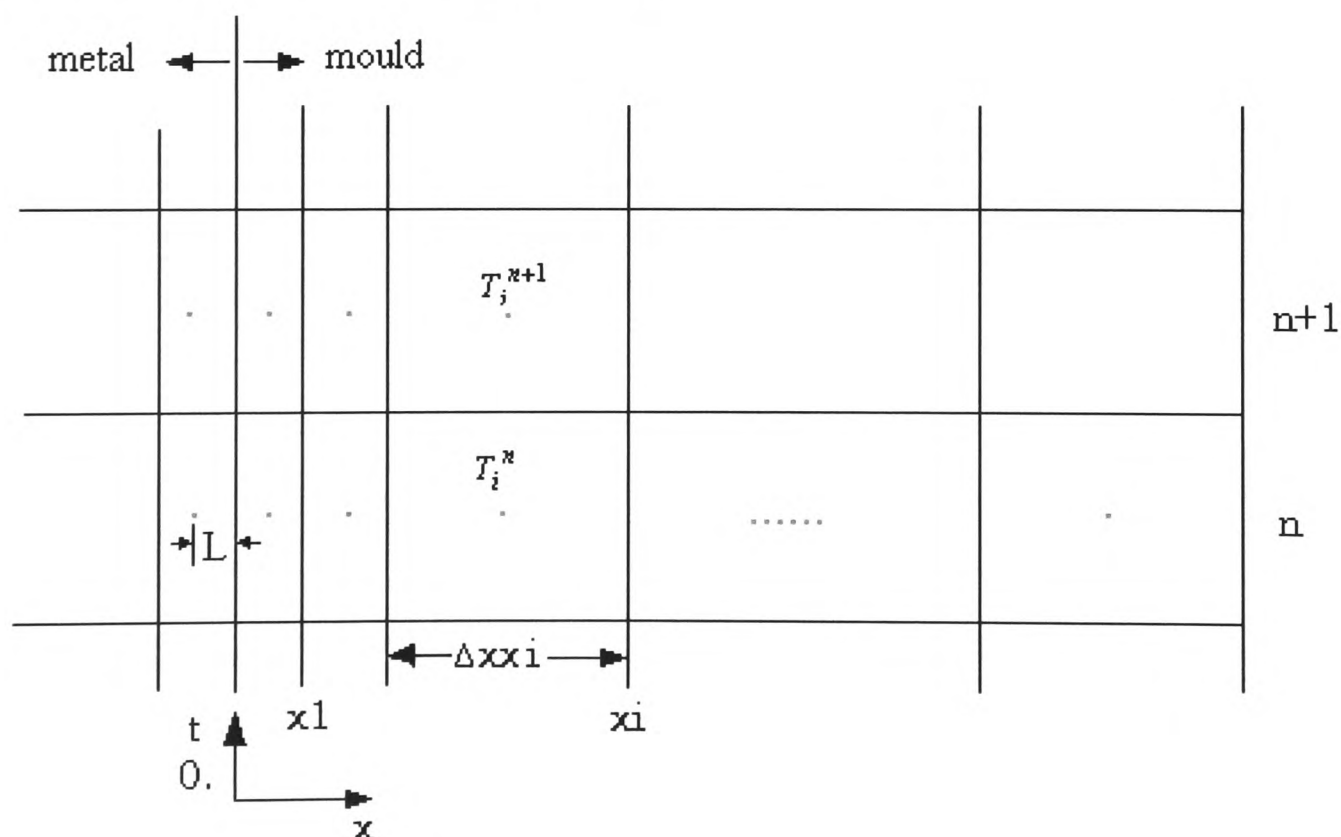


Figure 5.3: Finite Difference Discretization in space and time for this case.



## Chapter 5. 3D/1D Coupled Transient Heat Transfer Model

Based on the discretization, the two differentials can be approximated in time and space using the explicit scheme method:

$$\frac{dT}{dt} = \frac{T_i^{n+1} - T_i^n}{\Delta t} \quad (5.2)$$

$$\frac{d^2T}{dx^2} = \frac{\frac{T_{i+1}^n - T_i^n}{\Delta x_i} - \frac{T_i^n - T_{i-1}^n}{\Delta x_{i-1}}}{\Delta x x_i} \quad (5.3)$$

where  $\Delta x x_i = x_i - x_{i-1}$  and  $x_0 = 0$ ,  $\Delta x_i = (x_{i+1} + x_i)/2$  and  $\Delta x_0 = L + x_1/2$ . Therefore, the discretized heat conduct equation is written:

$$T_i^{n+1} = \frac{A_i}{\Delta x_{i-1}} T_{i-1}^n + \left(1 - A_i \left(\frac{1}{\Delta x_{i-1}} + \frac{1}{\Delta x_i}\right)\right) T_i^n + \frac{A_i}{\Delta x_i} T_{i+1}^n \quad (5.4)$$

where  $A_i = \frac{\alpha \Delta t}{\Delta x x_i}$ .

### 5.4 Coupling

The temperature  $T_l$  refers to the cell-centre temperature in the last mesh cell from the 3D model and is used as the boundary temperature for the mould 1D computation. The heat transfer is then through the mould wall. As the time progresses, the updated temperature  $T_w$  of the interface between the liquid and the mould is obtained and it is thought as the boundary temperature of the fluid field of the 3D model for next time step. This update of boundary temperature of the fluid field is carried out by iteration for each cell next to the mould.

The general heat equilibrium between the fluid field and the mould is governed by:

$$\lambda_{liq} \frac{T_l - T_w}{\Delta x_{liq}} = \lambda_{mod} \frac{T_w - T_1}{\Delta x_{mod}}$$

$$\Rightarrow T_w = \frac{\frac{\lambda_{liq}}{\Delta x_{liq}} T_l + \frac{\lambda_{mod}}{\Delta x_{mod}} T_1}{\frac{\lambda_{liq}}{\Delta x_{liq}} + \frac{\lambda_{mod}}{\Delta x_{mod}}} \quad (5.5)$$

Where  $\lambda_{liq}$  and  $\lambda_{mod}$  are the conductivities of the metal and the mould,  $\Delta x_{liq}$  and  $\Delta x_{mod}$  are the distance of the last cell centre in the liquid to the interface and of the first cell centre in the mould to interface.

The heat flux  $q$  is taken into account and expressed in the source term of Equation (3.4):

$$q = -\lambda_{liq} \frac{T_l - T_w}{\Delta x_{liq}} \quad (5.6)$$

The required source in the equation is given by Equation (5.7) (Heat transfer boundary conditions, i.e. conduction in PHYSICA):

$$S = C(T_{ext} - T_l) \cdot A \quad (5.7)$$

Where  $A$  is cell area;  $S$  the source,  $C$  is the heat transfer coefficient.  $T_{ext}$  is the temperature in the boundary. The boundary temperature of the 1D model is coupled by the two following parameters back into the 3D model:

$$C = \frac{\lambda_{liq}}{\Delta x_{liq}}$$

$$T_{ext} = T_w$$

For this method, Equation (5.5) is used to calculate the temperature of the interface in order to avoid the calculation of the average thermal conductivity and diffusivity for these two materials.

It is noted that the 1D heat conduction equation is only used to balance heat transfer between the fluid field and the mould. During the mould filling, if solidification occurs, the evolution of the latent heat has to be taken into account in the 3D model and defined in the source term. The effect of the latent heat on the 1D heat conduction equation is already

## Chapter 5. 3D/1D Coupled Transient Heat Transfer Model

---

represented by the temperature  $T_i$ . No more consideration about the latent heat is necessary in the 1D model.

The 3D/1D procedure can also account for the presence of air gap between metal and mould as presented in Chapter 7.

### 5.4.1 Stability

In the above coupling, it is noted that the 1D model is under a fully explicit treatment. It will have to obey the CFL condition. During the mould filling, free surface fluid flow is involved and a fine mesh is employed. A fine time step is required, typically the time steps 0.001s when free surface fluid flow modules are switched on. Furthermore, the diffusivity of the mould is very low, about  $7.E10^{-7}$ . The CFL condition (Equation (5.8)) is easy to meet:

$$\alpha \frac{\Delta t}{\Delta x^2} \leq 1 \quad (5.8)$$

### 5.4.2 Approximation

The update of the temperature of the fluid field is carried out by iteration for the each cell next to mould since the source terms, concerning the heat boundary condition, must be updated by iteration. The coupled 1D model should be calculated by iteration within one time step of the 3D model. The time step  $\Delta t_i$  in Equation (5.4) should be smaller than the one of the main 3D model. The relationship between two time steps:  $\Delta t_{3D} = \Delta t_{1D} \cdot n$ , ( $n$  is the number of iteration;  $\Delta t_{3D}$  is the time step of the main 3D model and  $\Delta t_{1D}$  that of the 1D model). Before any simulation, it is unlikely to know the number of iteration for each time step. For the above reason, the following approximation is made. In the INFORM file, the minimum number of iterations, MIN\_SWEEPS, is set and the time step  $\Delta t$  in 1D model is calculated:

$$\Delta t_{1D} = \frac{\Delta t_{3D}}{\text{MIN\_SWEEPS}} \quad (5.9)$$

For each time step, when the number of iterations is bigger than MIN\_SWEEPS, the boundary temperature offered by the 1D model is kept the same as the previous iteration's.

## 5.5 Algorithm

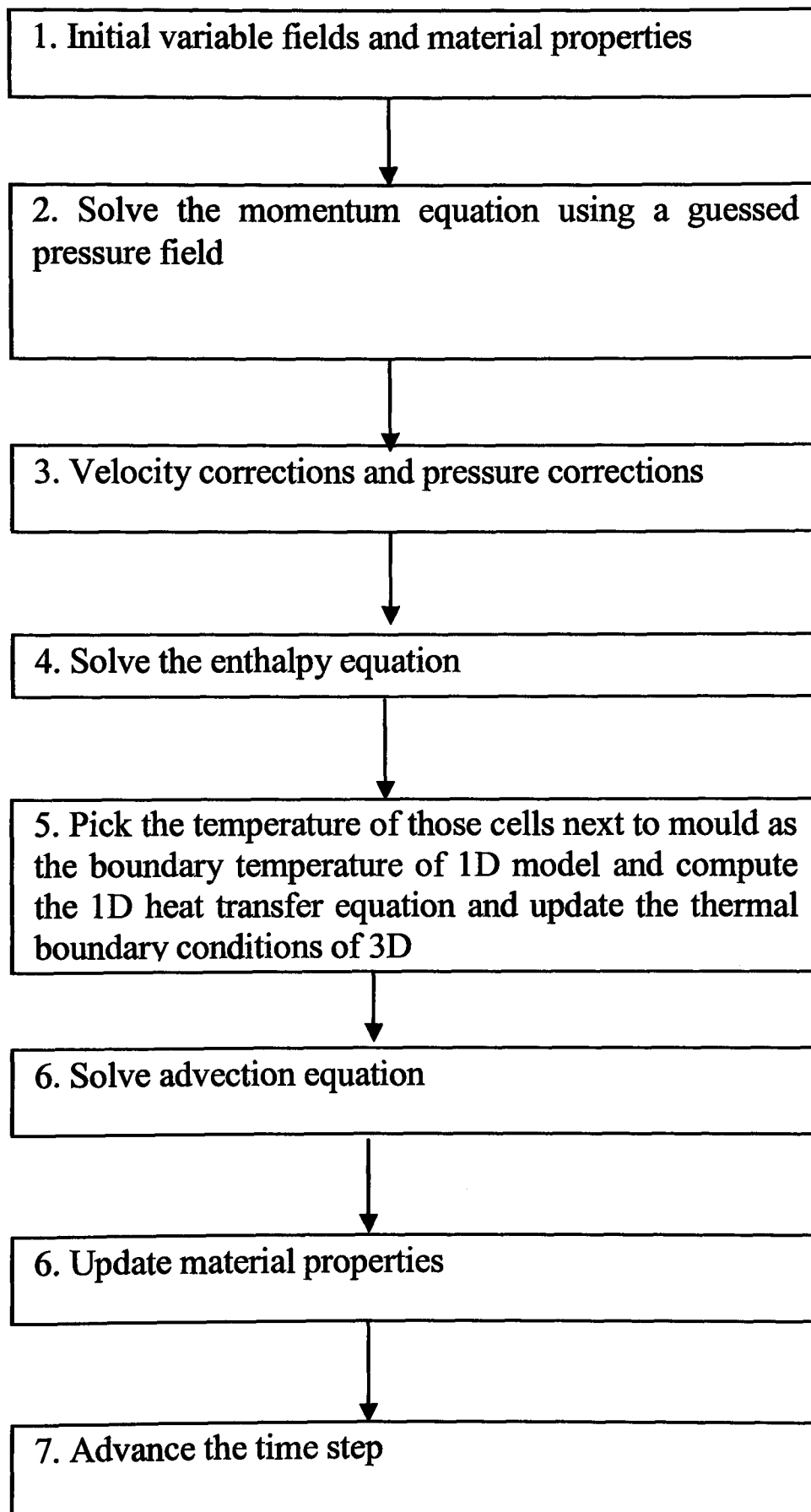


Figure 5.4: Solution Procedure for the 3D/1D model.

## 5.6 Validation of 3D/1D Coupled Transient Heat Transfer

### 5.6.1 Test Case 1

#### 5.6.1.1 Computational Mesh

A 2D test piece is used to validate 3D/1D model shown in Figure 5.5. The grey part represents the mould, 150x5mm, which is meshed for the geometry employed in PHYSICA. The black is the fluid domain, 150x2.5mm. In the direction toward the mould, 7 cells are used to cover the thickness of 2.5 mm. Finally a structured quadrilateral mesh with 420 cells (60x7) is generated. In 3D/1D model, only the fluid domain is present in the geometry.

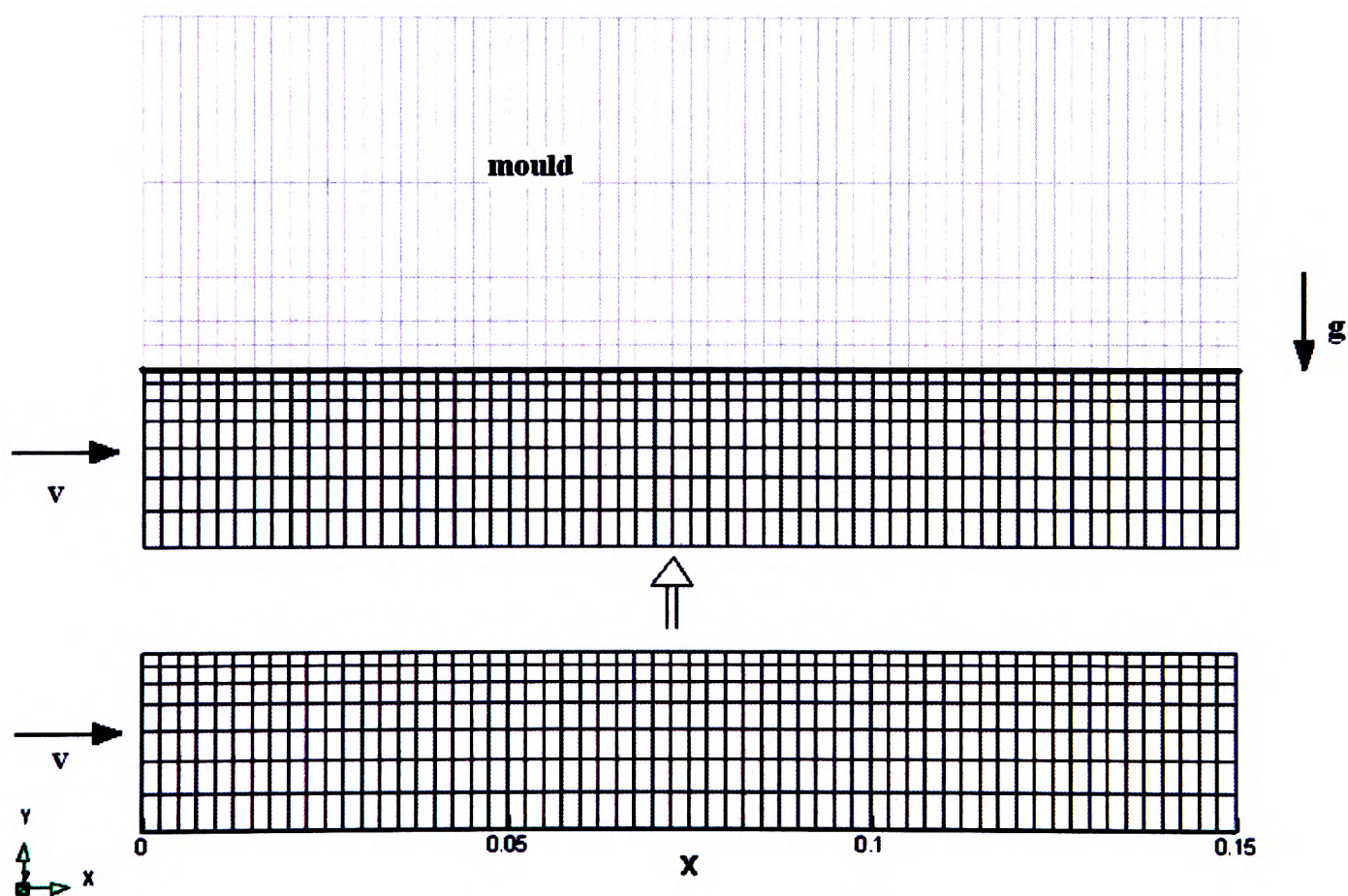


Figure 5.5: Computational mesh for PHYSICA (above) and 3/1D model (below)

#### 5.6.1.2 Initial and Boundary Conditions

In this test, the molten TiAl alloy is filling along the x direction. The mould temperature along the y direction varies at different x positions since the fluid is moving. The

## Chapter 5. 3D/1D Coupled Transient Heat Transfer Model

---

temperature on the external side of the mould is supposed to be constant. The simulations were carried out with the following initial conditions in Table 5.1:

Table 5.1: The initial conditions of the numerical model

Mould preheated temperature, °C	1000
Initial temperature of molten metal , °C	1600
Inlet velocity, m/s	0.2
Superheat, °C	50

At time 0.5s, the mould temperatures at the cell centres are calculated. The same modules are switched on for the two methods. The changes are: 1) one material properties (only metal's) are needed rather than two materials' (material 1: metal and material 2: mould); 2) the boundary conditions in the heat transfer module are:

```
BOUNDARY_CONDITIONS
```

```
PATCH 1 FIXED_VALUE VALUE 1600.
```

```
PATCH 6 FIXED_VALUE VALUE 1000.
```

```
END
```

are replaced by 1D model's:

```
BOUNDARY_CONDITIONS
```

```
PATCH 1 FIXED_VALUE VALUE 1600.
```

```
PATCH 3 USER_ROUTINE mould_heat 9 0.005 5 0.5 3.0 1.6 2200. 1000.  
1000. 1000.
```

```
END
```

Two full INFORM files for these simulations are seen in Appendix A. It should be noted that PATCH 1, 3 and 6 respectively represent the surface number of the inlet, of the

## Chapter 5. 3D/1D Coupled Transient Heat Transfer Model

---

interface between metal and mould, of the external mould wall. The meaning of each parameter in the text 'mould\_heat 9 0.005 5 0.5 3.0 1.6 2200. 1000. 1000. 1000.' is described in Table 5.2:

Table 5.2: Description of the parameters in the 1D model

9	The number of parameters
0.005 m	The thickness of the mould
5	The number of cells on the mould wall
0.5 and 3.0	The factors are used to define the mesh, i.e. the mesh is uniform if 1. and 1.
1.6 W/(m·K)	Thermal conductivity of the mould material
2200 kg/m <sup>3</sup>	The density of the mould material
1000 J/(kg·K)	The specific heat of the mould material
1000 °C	The initial temperature of the mould
1000 °C	The temperature of the outside mould

### 5.6.1.3 Presentation of Results

The same simulations are performed in both methods. The comparisons of the temperature and the liquid fraction with the two methods are shown at the different times in Figures 5.6-5.10. An artificial front which is fully extended cross the mould with certain interface thickness is applied in order to study how fast the heat transfers during the mould filling. The vertical interface is moving forward as the mould is filling.



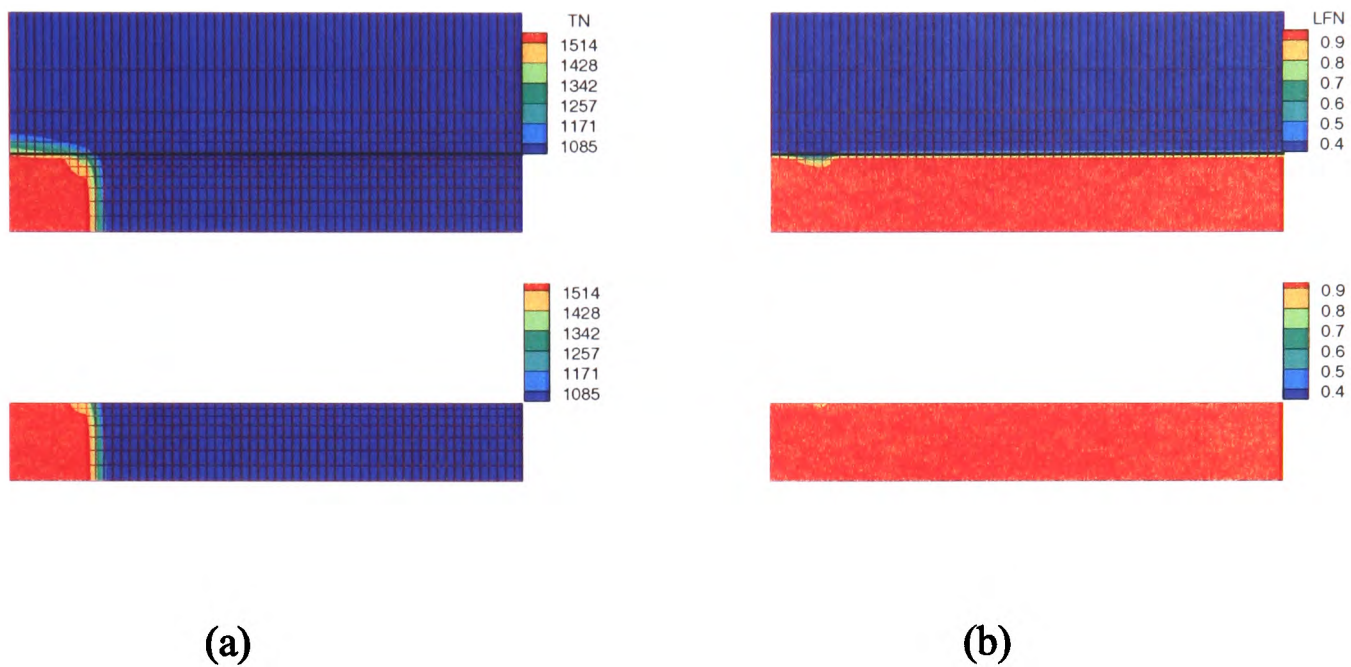


Figure 5.6: Comparisons of temperature 'TN' (a) and liquid fraction 'LFN' (b) with the two different methods: PHYSICA and 3D/1D model at 0.1s.

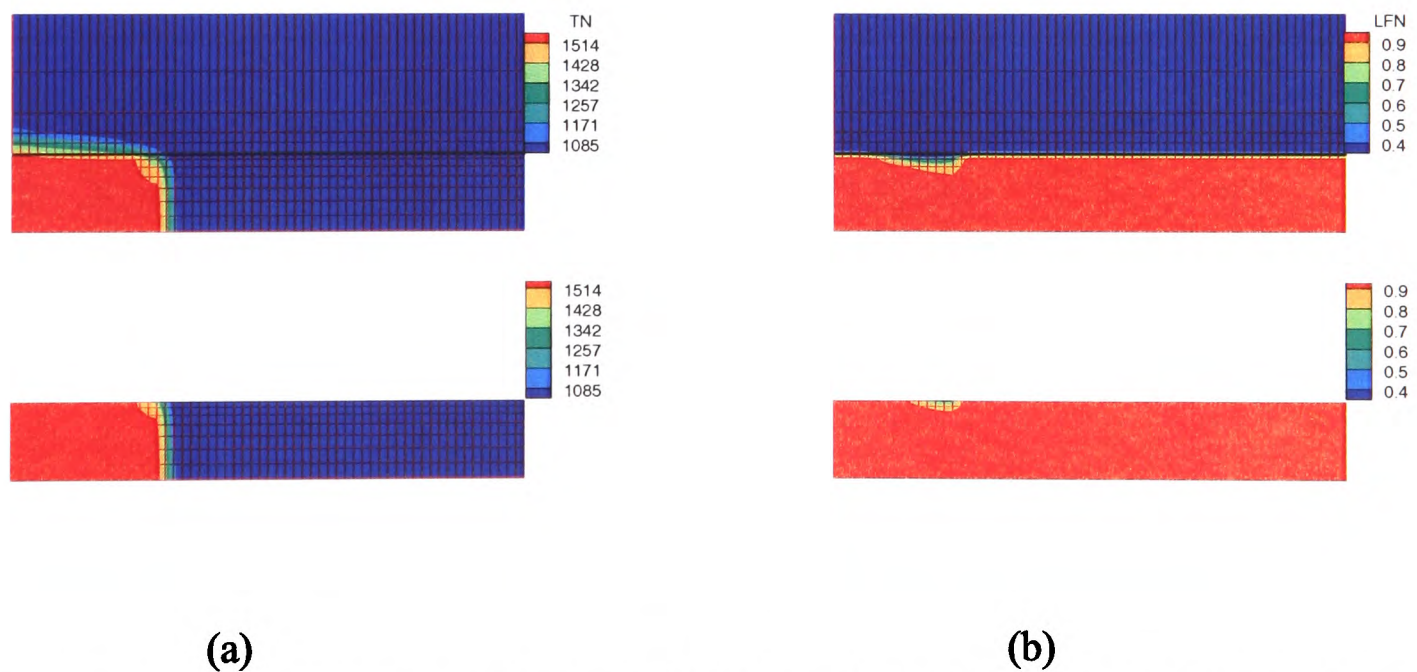


Figure 5.7: Comparisons of temperature 'TN' (a) and liquid fraction 'LFN' (b) with the two different methods: PHYSICA and 3D/1D model at 0.2s.



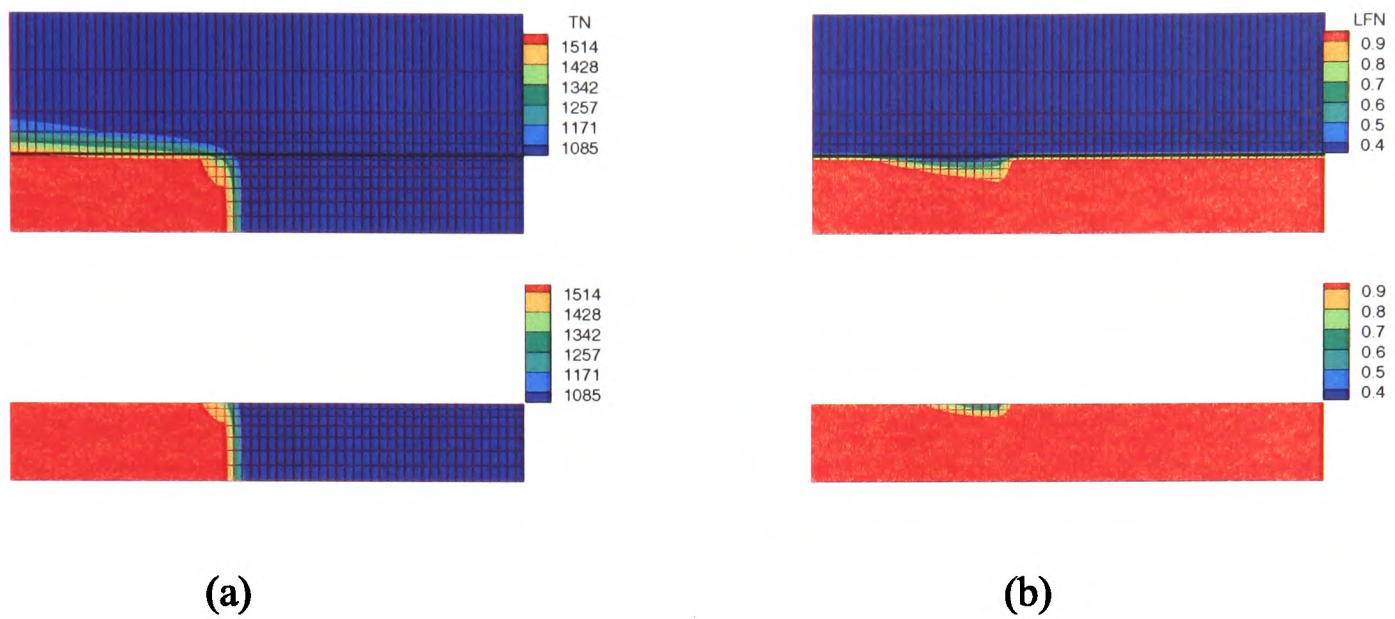


Figure 5.8: Comparisons of temperature 'TN' (a) and liquid fraction 'LFN' (b) with the two different methods: PHYSICA and 3D/1D model at 0.3s.

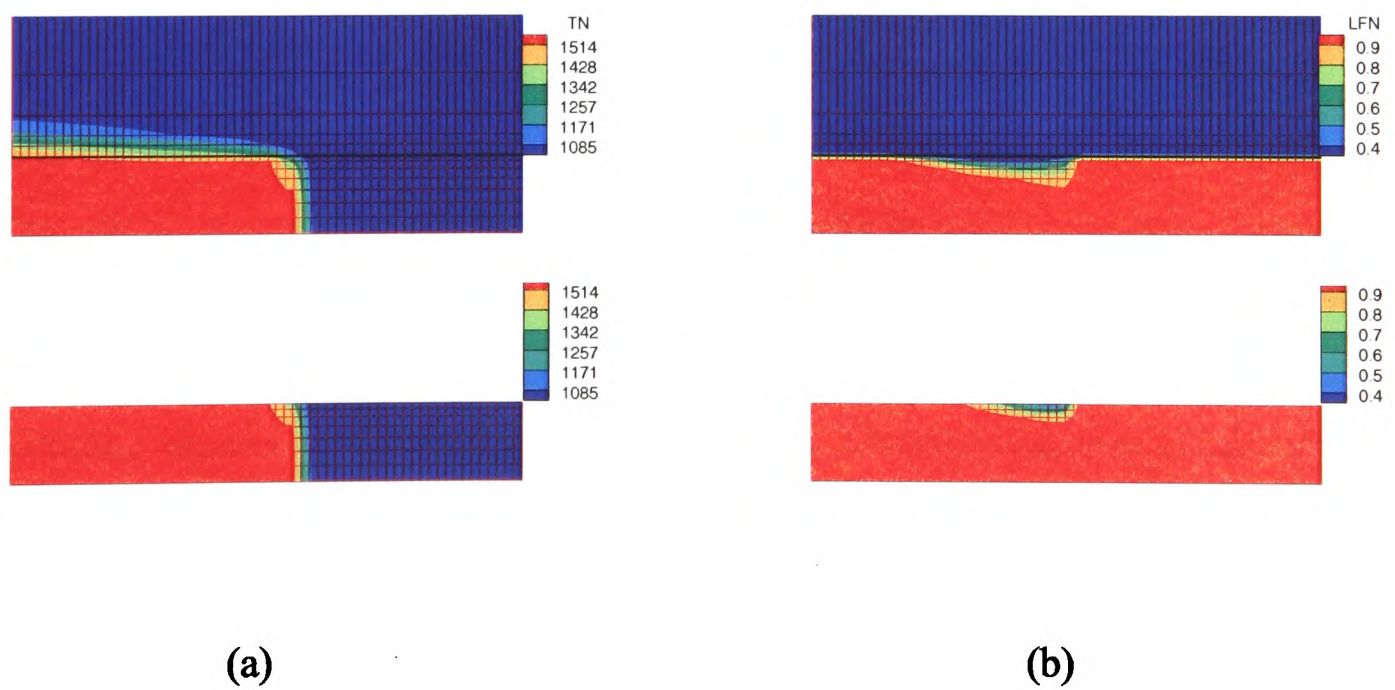


Figure 5.9: Comparisons of temperature 'TN' (a) and liquid fraction 'LFN' (b) with the two different methods: PHYSICA and 3D/1D model at 0.4s.

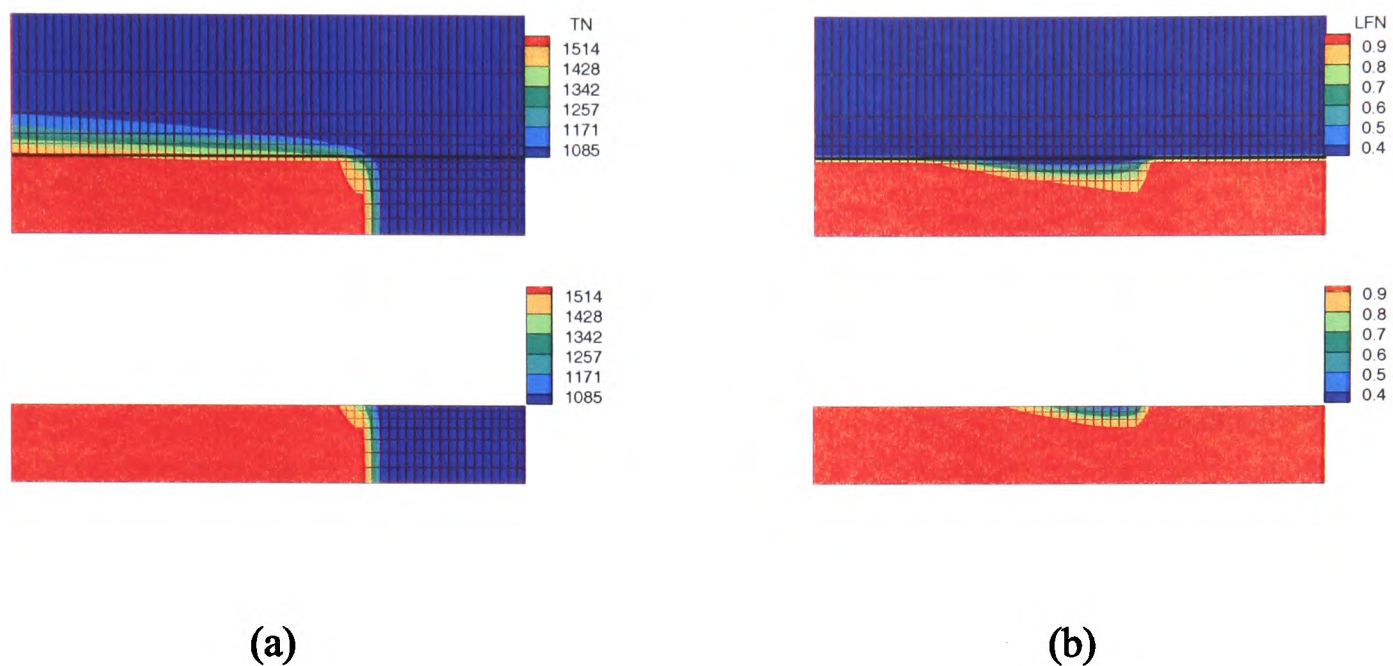


Figure 5.10: Comparisons of temperature ‘TN’ (a) and liquid fraction ‘LFN’ (b) with the two different methods: PHYSICA and 3D/1D model at 0.5s.

From Figures 5.6-5.10, it is noted that heat is quickly transferred to the mould. The temperature of the mould is gradually increased. As the fluid is flowing into the domain, the liquid temperature in the boundary layer along the mould is dropping and some mushy zone is formed. This zone is flowing forward as the fluid fills in. It can be explained that the hot metal is immediately solidified when it touches the cold mould. However, the solidified metal re-melts when it absorbs the heat from the incoming hot metal. The mushy zone is gradually expanding across the domain as the filling progresses. The contours of temperature show a similar shape for two methods although the area of mushy zone in PHYSICA is slightly bigger than that from 1D transient. In order to see the differences between the two methods, two referred positions are chosen to study the heat transfer from liquid to mould in numerical values.



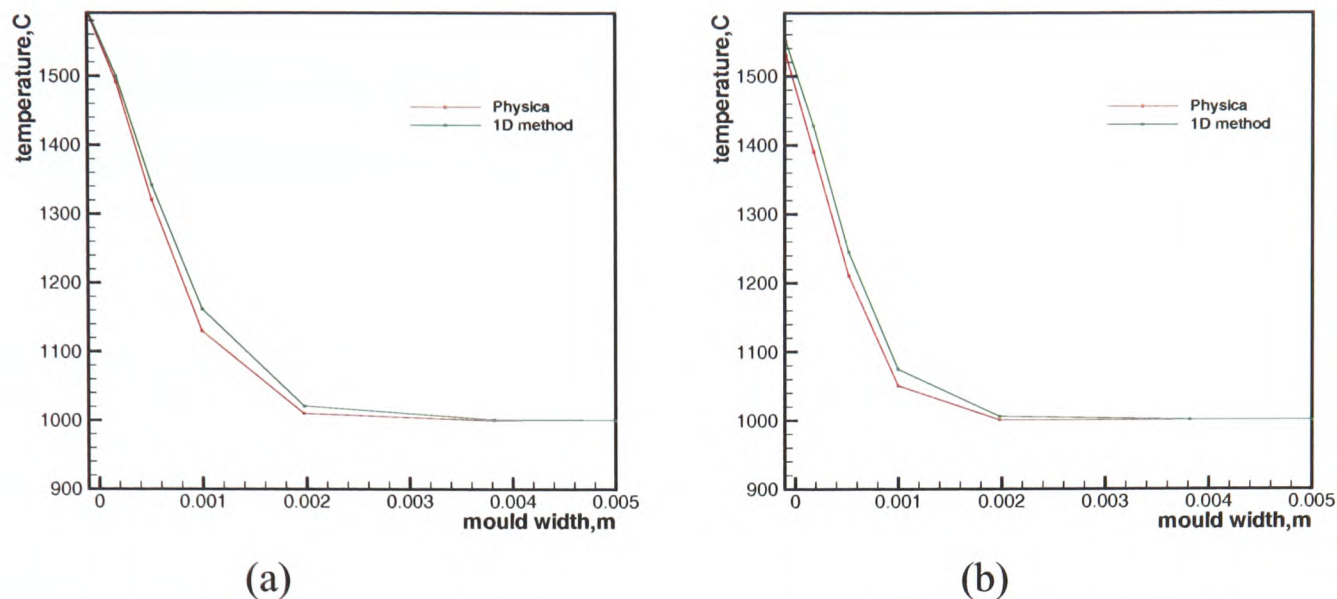


Figure 5.11: Comparisons of the mould temperature using PHYSICA and 3D/1D model at 0.5s at  $x=1.25$  mm (a) and  $x=46.25$  mm (b) along x direction.

Figure 5.11 shows that the temperatures with 1D method are slightly higher than those with PHYSICA at different positions. That explains the differences of the liquid fraction shown in Figures 5.6-5.10. This is because the 1D model neglects heat transfer in the direction parallel to the mould, which would slightly reduce mould temperatures close to the liquid metal front. Generally the curves match very well. The accuracy of the 3D/1D transient model is very good even though some approximation is made.

### 5.6.1.4 Computational Comparisons

Table 5.3 shows the comparisons of the simulations with the two methods in computational time and the average number of iteration for the test case 1. The computational time with Method B is triple that with Method A. The number of iterations per time step with Method B is significantly greater than that with Method A. It is seen that 3D/1D transient model not only saves time in meshing the mould but also this algorithm accelerates the simulations.

Table 5.3: Comparisons of the simulations using 3D/1D transient model (A) and using PHYSICA (B) to model the heat transfer through the mould wall.

	Method A	Method B
Computational time (s)	93	277
Number of iterations per time step	Approx. 19	Approx. 50

### 5.6.2 Test Case 2

Two states of fluid are normally involved during the casting process: moving fluid (mould filling) and static fluid (solidifying after mould filling). Therefore another test case is designed: molten metal is held in the mould. The static fluid is simulated as the molten metal is held in the mould after mould filling.

#### 5.6.2.1 Computational Mesh

The configuration of this test case is illustrated in Figure 5.12. It is axis-symmetric (along the  $z$  axis at  $x=0$ ) 2D geometry. The fluid domain (30x20 mm) is meshed into 48 cells (8x6). Five uniform cells are in the mould (5 mm).

The mesh (left) is numbered so that it is convenient to identify the position. The picture (middle) presents the real domain of simulation with the 3D/1D transient model. The meshes in grey are the domain calculated by 1D model. To the right is the simulation domain in PHYSICA. The geometry includes metal domain and the mould walls. Two materials are involved. The part in blue is called the 'dead corner' where the 3D/1D transient model can not cover. The effects of the dead corner will be shown in the following result presentations.

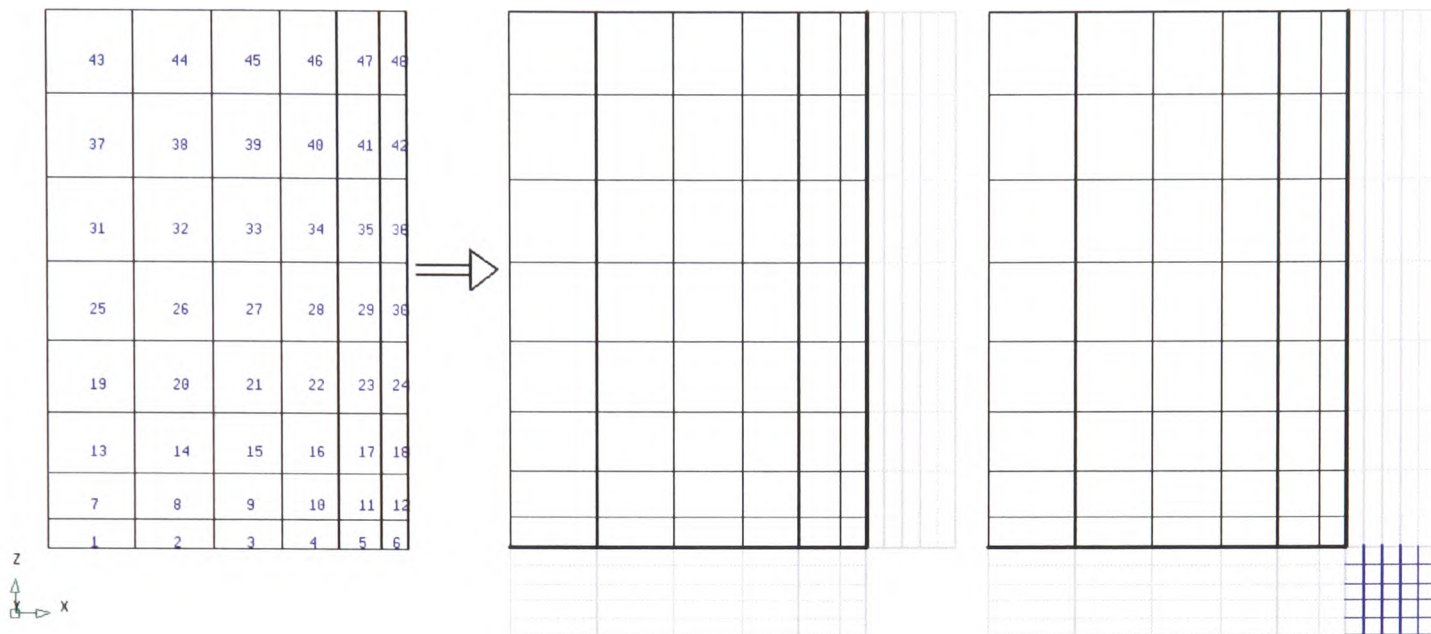


Figure 5.12: Schematic figure of test piece and computational mesh

### 5.6.2.2 Initial and Boundary Conditions

In this test, the molten TiAl alloy is being held in the mould. At the external side of the mould, it is supposed to be insulated. The simulations were carried out with the following initial conditions in Table 5.4:

Table 5.4: The initial conditions of the numerical model

Mould preheated temperature, °C	1000
Initial temperature of molten metal , °C	1600
Superheat, °C	50



### 5.6.2.3 Presentation of Results

The two alternative methods are used to run the same simulations. The comparisons of the temperature contour with the two methods are presented at 30.s in Figure 5.13. The similar contours in temperature are shown. However, different temperature contours in the corner are present. That explains the effects of the ‘dead corner’.

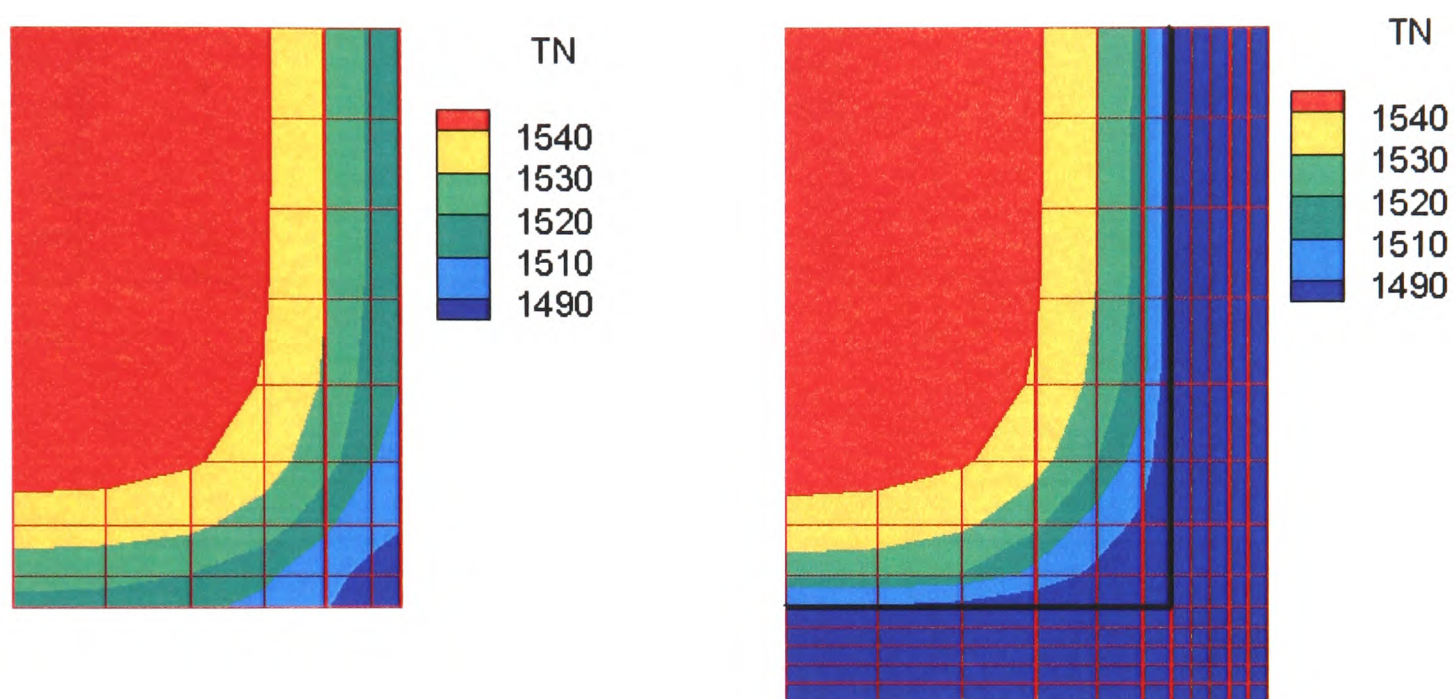
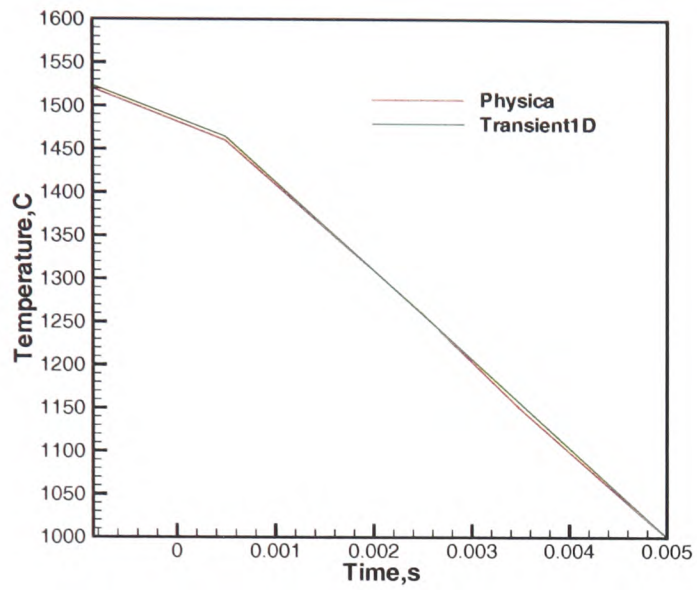


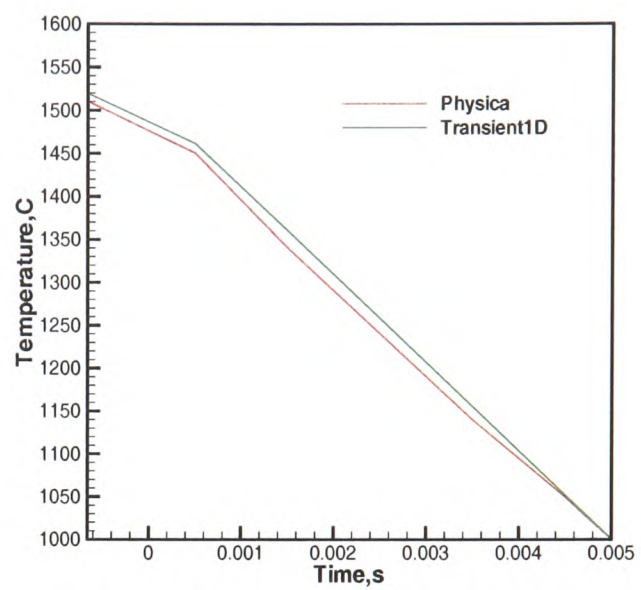
Figure 5.13: Comparisons of the contours of temperature with PHYSICA and 3D/1D model at 30.s

The comparisons of the temperature at four positions, cell 1, 5, 6 and 48, are seen in Figure 5.14. Figure 5.14 (a) presents the comparisons of the temperature from the centre of the cell 1 to the mould temperature. They are in very good agreement with each other. At cell 48 in Figure 5.14, there is some slight difference between the two methods. However at cell 5 and 6, Figure 5.14, there are obvious differences, which are caused by the 1D transient method. It can not calculate the dead corner in blue. It significantly affects the accuracy of this calculation in this area. The shortcoming of the 3D/1D model makes it restricted to some geometries.

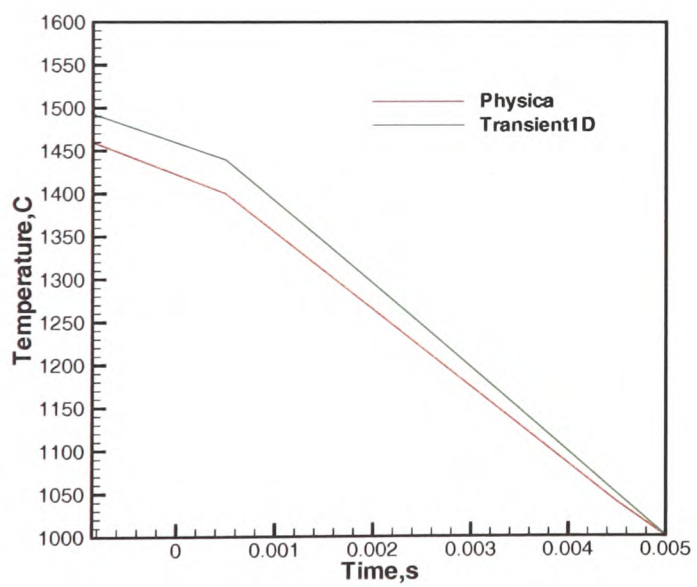
## Chapter 5. 3D/1D Coupled Transient Heat Transfer Model



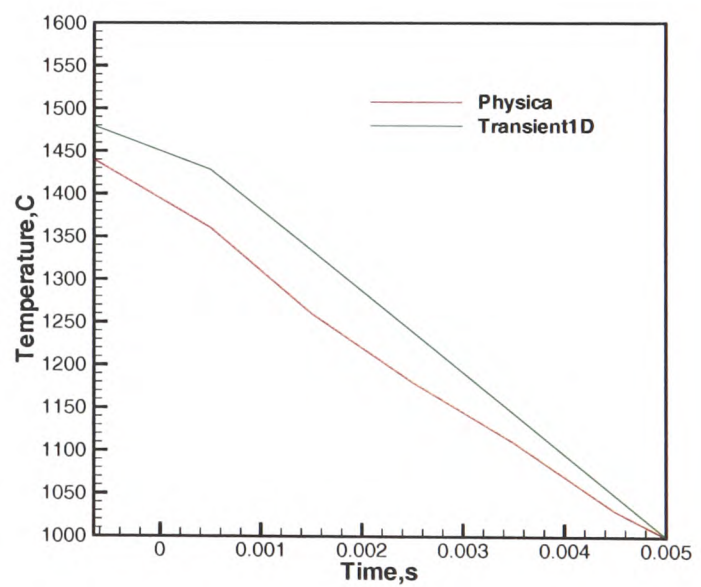
Cell 1



Cell 48



Cell 5



Cell 6

Figure 5.14: Comparisons of the mould temperature for methods, PHYSICA and 3D/1D model at cell 1, cell 48, cell 5 and cell 6 at 30.s



### 5.6.2.4 Run-time Comparisons

Table 5.5 shows the comparisons of the simulations with the two methods in computational time and the average number of iteration for the test case 2. The computational time with Method B is double that with Method A. There is no significant difference in the number of iterations for the two methods. It is seen that 3D/1D transient model not only saves time to mesh the mould but also this algorithm accelerates the simulations. It is expected that in a 3D complex geometry the savings will be proportionally greater.

Table 5.5: Comparisons of the simulations using 3D/1D transient model (A) and using PHYSICA (B) to model the heat transfer through the mould wall.

	Method A	Method B
Computational time (s)	16	35
Number of iterations per time step	2	2

## 5.7 Summary

The new 3D/1D approximation aims to get accurate thermal boundary and simplify the simulation of the heat transfer between the mould and the molten metal. The calculations for the mould material are applied through a computed Finite Difference mesh rather than a full 3D mesh. From the validations of the two test cases, it is noted that the results using the 3D/1D transient model to simulate the heat transfer in the thermal boundary layer are in agreement with those using PHYSICA. Furthermore, it greatly simplifies geometric model generation, particularly for complex geometries, and it reduces simulation time. Since the 1D grid is computationally inexpensive, it can be arbitrarily distributed to capture non-linear effects, such as the opening of an air gap due to shrinkage. However, for some geometries in which the ‘dead corner’ are present, there are discrepancies because the 3D/1D transient model can not be applied in these area. One has to be careful with boundary conditions in the ‘dead’ corner when the 3D/1D model is employed to computing thermal boundary.

## **5.8 Model Application: Validation of a Short Turbine Blade and Discussion of the Tilt Casting Parameters**

The practical development for this study has been carried out at the University of Birmingham. The process combines the melting of TiAl alloys in an ISM furnace and transferring the molten metal into a preheated ceramic mould with tilt casting. The casting results in the experiment were compared with computer simulations which were carried out in parallel at the University of Greenwich.

### **5.8.1 Experimental Description**

The Induction Skull Melting (ISM) crucible is positioned inside a vacuum chamber. It is attached to co-axial power feed-through to supply power to the induction coil and water to the ISM crucible and also allowing the ISM crucible to be rotated to pour metal into a mould. The mould was clamped to the top of the ISM crucible. Because of limited superheat, a mould heater is used to decrease the conduction loss between the molten liquid and the mould wall. After heating the mould, the mould heater has to be opened up and moved away, as shown in the Figure 5.15 [Harding *et al.* -07] prior to melting, since otherwise it would be affected by the high power induction field from the coil. Certain charge of metal has been loaded in the crucible, then the metal is melted. Once melting is complete, the ISM crucible and mould are rotated together to fill the mould. This is the tilt casting process.

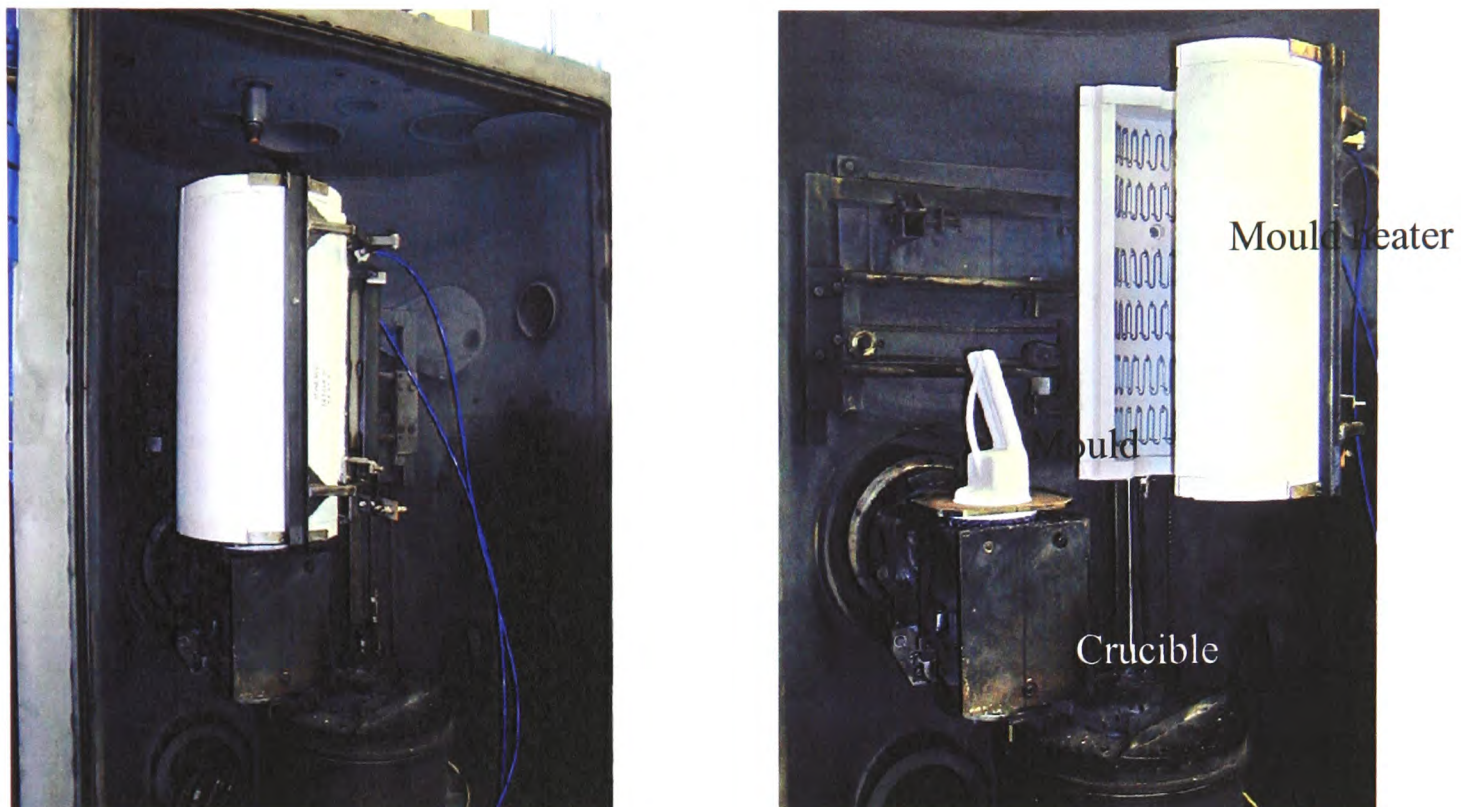


Figure 5.15: Tilt casting equipment (ISM) is heating the mould and mould heater is moved away in an open position.

### 5.8.2 Dimensions of Short Turbine Blades and Mould Design

In this trial, short turbine blades were cast. The design and dimensions of the short turbine blades used for the casting trials are shown in Figure 5.16 (a). The whole length is 130mm. The thinnest part, the trailing edge of the blade, is about 2mm. The trailing edge presents the biggest challenge for casting the blade in TiAl because of the low superheat. The design of the mould is shown in Figure 5.16 (b). The blades mounted as a pair are orientated with the thin trailing edge pointing down to ensure they would be the first part to fill during mould rotation. The blades were in addition angled at 15 degrees to ease gas evacuation. A vent was inserted to the end stub close to the leading edge of each blade and run back as a tube to the pouring basin/feeder, as shown in Figure 5.16 (b).



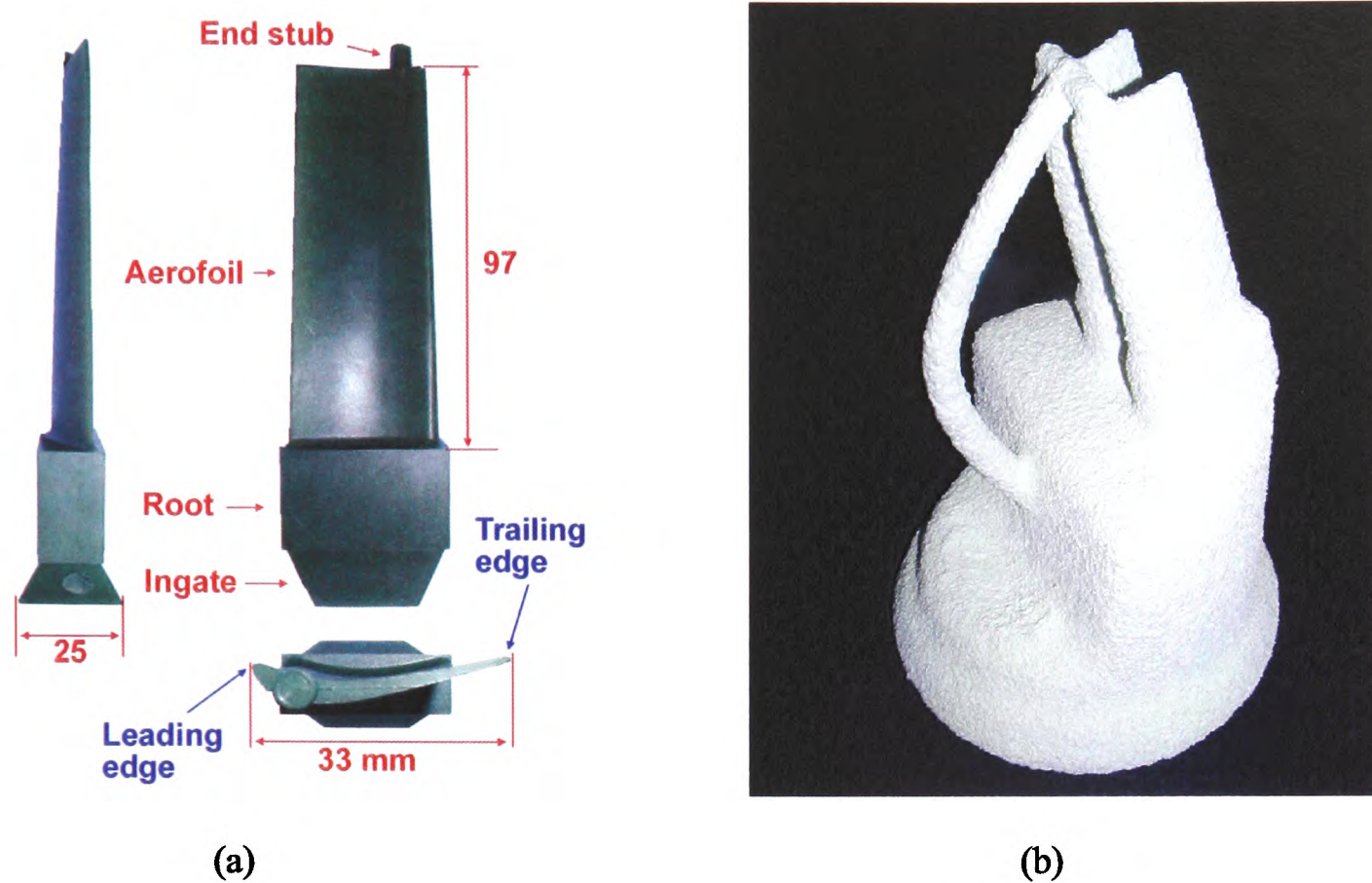


Figure 5.16: (a) The design and dimensions of the blades and (b) mould.

### 5.8.3 Computational Mesh

As the picture shown in Figure 5.16 (b), the blade is angled at 15 degrees. In the experiment there were two identical blade moulds attached to the pouring basin symmetrically with respect to the central vertical plane of the assembly. Taking account of symmetry, only half of the crucible, half of the basin and only one blade were meshed and simulated in order to reduce computational cost.

The full geometry is comprised of a cylindrical crucible with an attached feeding system and the blades. Some approximation (section thickness kept the same, but blade camber ignored in this test) was made in the aerofoil when the geometry was meshed. The mesh contained 28557 elements and 32057 nodes. The mesh was unstructured, as demonstrated in Figure 5.17.

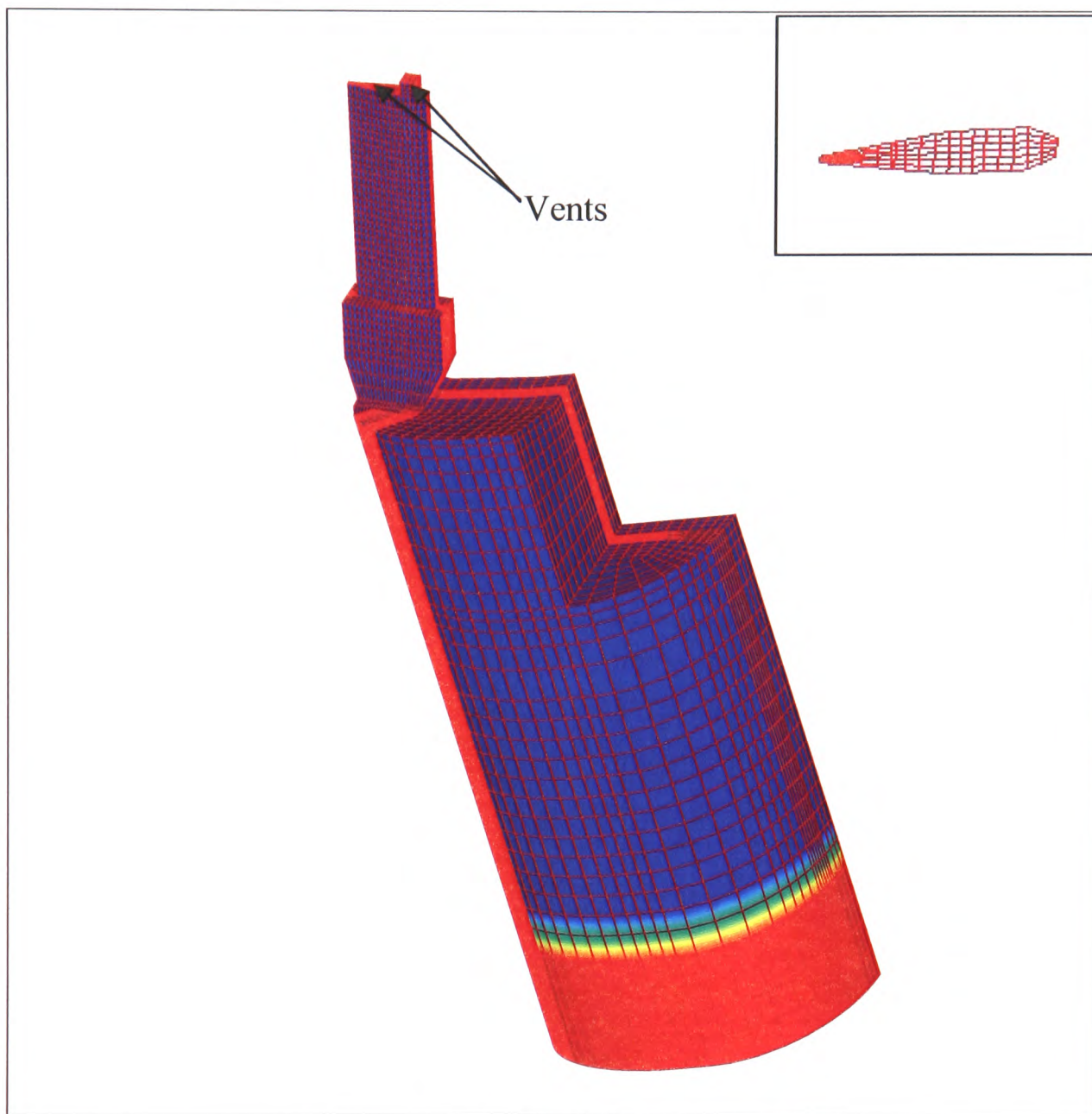


Figure 5.17: Computational mesh.

#### 5.8.4 Initial Conditions

In the trials, here were the initial conditions in Table 5.6:

Table 5.6: The initial conditions of the numerical model

Mould preheated temperature, °C	1200
Initial temperature of molten metal , °C	1600
vents	2
Superheat, °C	50



### 5.8.5 Venting

In the previous Chapter, it was seen that the air/liquid counter-flow in the blade has appeared without the presence of the additional venting. In some situations, the gas can not completely evacuate the mould cavity. The gas has to escape from the pouring basin. If the rotating speed is not slow enough, it is easy to cause gas entrapment. In order to avoid this sort of problem, some artificial vents have been introduced in the mould, which allow the gas to escape from them.

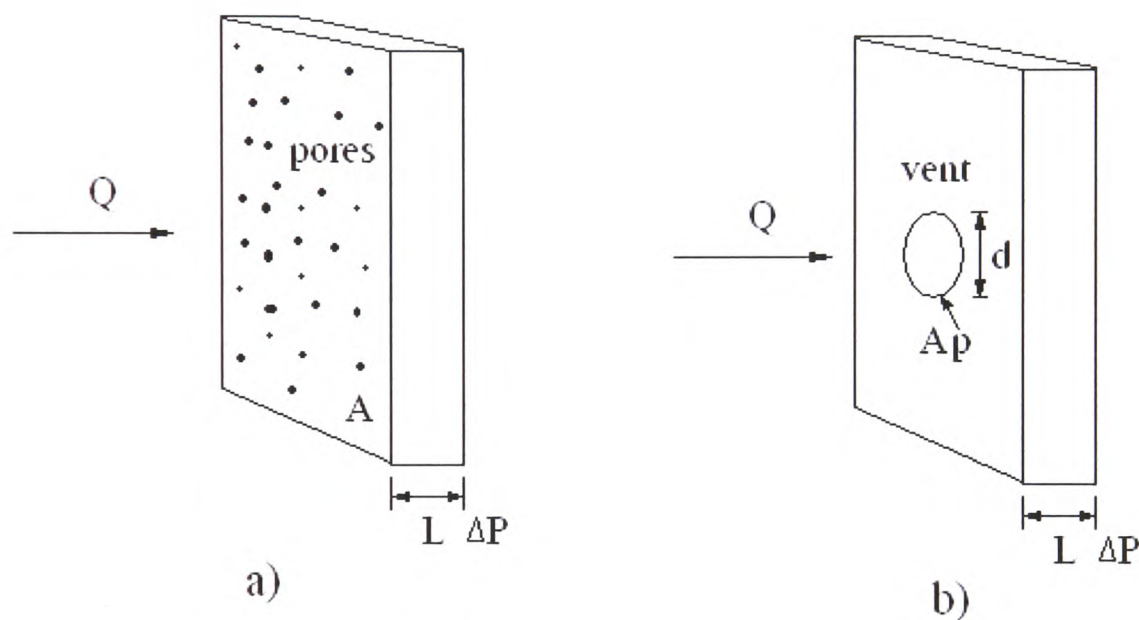


Figure 5.18: (a) Example of the porous medium and (b) Approximated vent in a mould.

In the experimental trial, a vent is actually a hole with very small diameter, such as 2mm. The flow through the vent (small hole) can be described as a pipe flow in terms of pressure drop. However in the numerical simulation, such a small diameter cylinder is hard to mesh, and completely impractical. Therefore in the numerical model, a bigger area is used instead of an exact section area of the vent. And it is assumed that the gas leak out this bigger area, as in porous medium, but the molten metal will be trapped somewhere in the porous medium due to the difference of the viscosity and ultimately solidification. The details about porous medium and pipe flow are presented in Appendix B. The schematic figure of the approximation between the porous medium and the pipe flow is illustrated in

Figure 5.18. The total discharge of the gas should be the same value for this approximation.

In the validations, two vents have been made: one is inserted to the end stub (2mm); the other is at the end of the trailing edge (<1mm).

### 5.8.6 Filling Mode

In the tilt casting process, the ISM crucible and mould would be rotated together to achieve mould filling, as shown in Figure 5.19 (a). As it is mentioned in Chapter 4, the tilt cycle is a very significant factor in the tilt casting for TiAl in order to achieve a tranquil metal transfer. It is wished to transfer the metal from the crucible as quickly as possible to avoid the high heat loss when the power to the induction coil is cut and the melt is collapsing into the crucible. However it is obvious that excessively increasing the rotation speed would lead to the surface turbulence. So there is a compromise between fast filling and reducing superheat loss.

The filling cycle shown in Figure 5.20 is designed at Greenwich. At the first stage of the filling, a fast rotating speed is used to transfer the metal quickly from the water cooled crucible into the ceramic pouring basin in order to minimise heat loss in the crucible. Then rotation is slowed down to allow the gas to evacuate from the blade, and to permit the metal to slowly move into the blades and so avoid generating surface turbulence. The essential rule for designing the tilt cycle for tilt casting is to make sure that the metal progressively fills in a tranquil manner and most of the metal is transferred horizontally, as seen in Figure 5.19 (b).

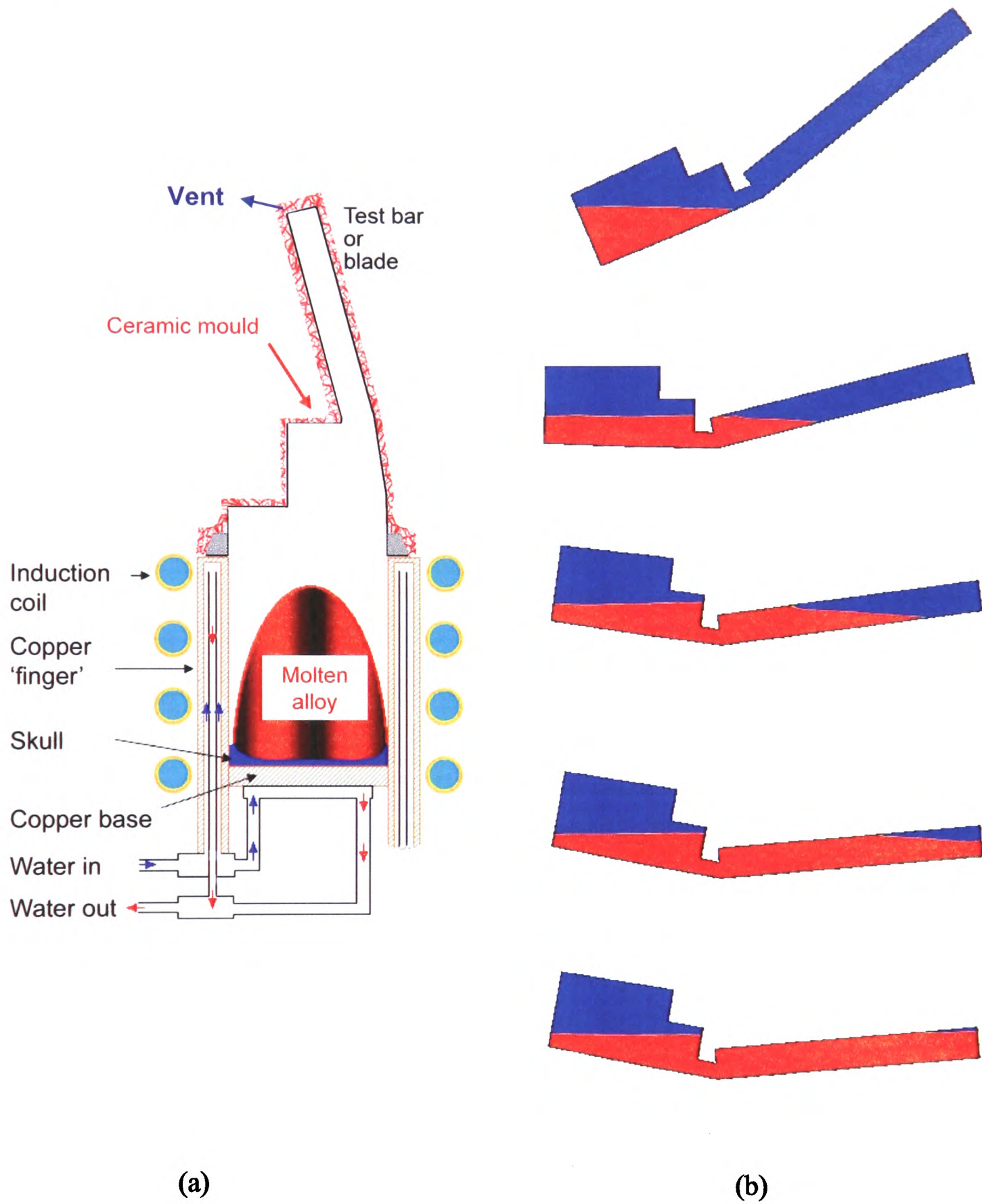


Figure 5.19: Tilt casting process: (a) Schematic; (b) Different stages of filling.



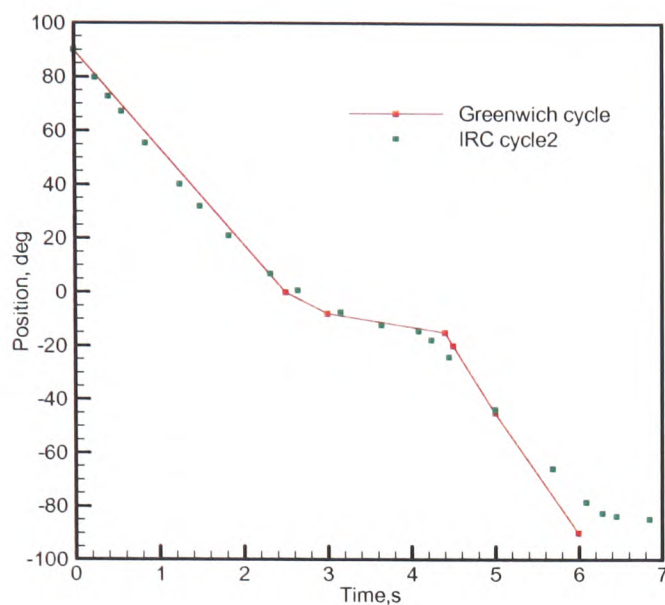


Table 5.7: Standard Programmed Cycle

Time, s	Rotating Angle
0.	0°
2.5	90°
3.	98°
4.4	105°
4.5	110°
5.	135°
6.	180°

Figure 5.20: Parabolic programmed cycle: the theoretical Greenwich code and Experimental cycle adopted in the actual trial by IRC Birmingham.

In the following simulations, fluid flow, heat transfer, solidification and free surface modules are switched on. As it is introduced in Section 2.2, Titanium aluminides have oxidation/corrosion resistance at elevated temperatures (over 800 degrees Celsius). Furthermore, the melting of TiAl alloys is carried out under a vacuum or a partial pressure of argon using ISM furnace, which avoid the oxidization of Titanium aluminides. As it is discussed in Chapter 4, the surface tension has slight effects on the mould filling if there is no oxide film on the metal surface. Hence, no surface tension effects are considered in the following result presentations.

### 5.8.7 Presentation of Results

Parallel computations were performed for the short (120mm) turbine blades with one vent and for two vents using the filling cycle shown in Figure 5.17 to investigate the impact of the number and the position of vents on mould filling. Then some comparisons of the simulation results with the experimental results have been presented.

### 5.8.7.1 Impact of the Number and the Position of Vent on the Mould Filling

The difference of one and two vents at 3.1s is caught and shown in the free surface contours in Figure 5.21. It is seen that some gas was trapped in the corner of the end of blade with one vent while there is no gas trapped in the blade with two vents.

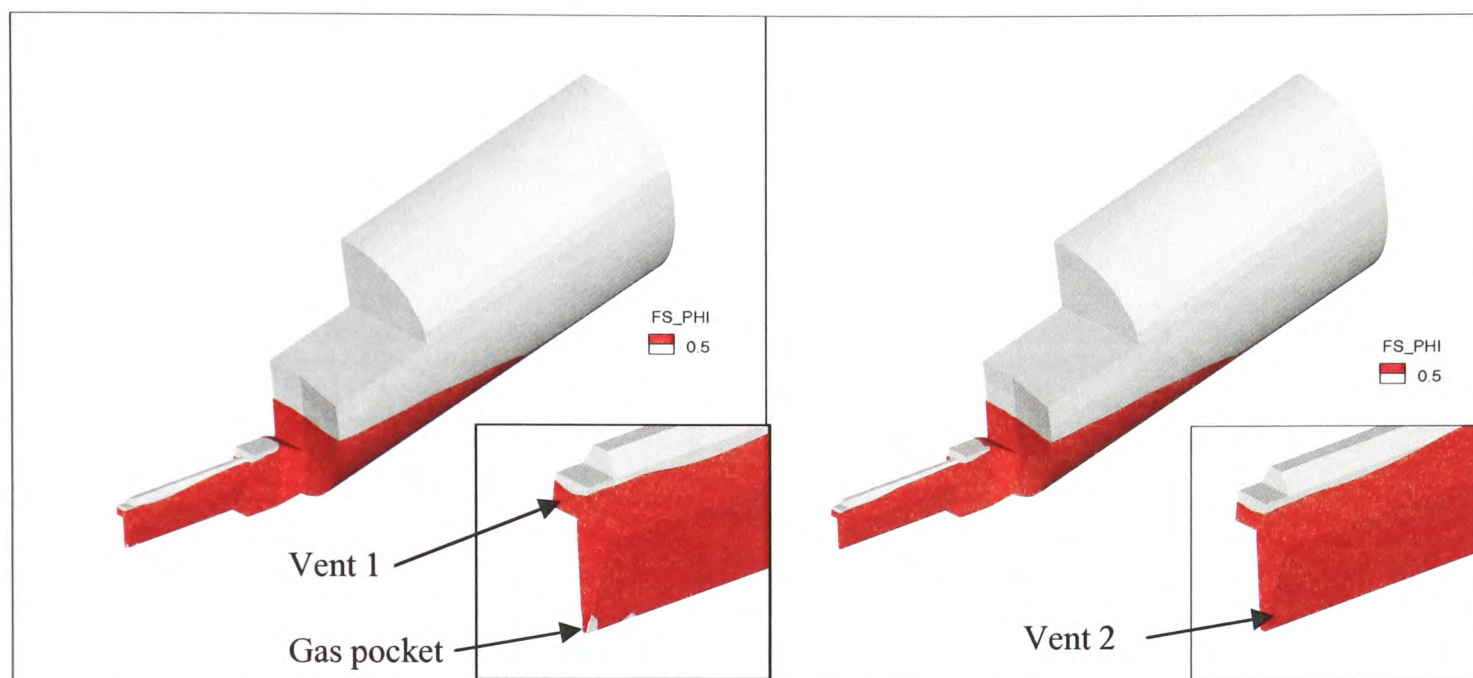


Figure 5.21: Difference of one vent and two vents in free surface contours at the 3.1s.

Stream line traces at 2.6s and 3.1s are shown in Figure 5.22 and Figure 5.23 for one vent and two vents, where the iso-surface in green is the interface between the gas and molten liquid at the scalar value  $\Phi=0.5$ , which represents the liquid volume fraction in a control volume cell. It is noticed that the number and the position of the vents has an impact on the fluid flow at different phases of the mould filling. At the 2.6 s, there is no big difference between one vent and two vents, all the gas seems to escape from the bigger vent, the one at the end stub.

However at 3.1 s, when the blade is almost full, apart from the gas is moving out from the main vent at the end stub, part of the gas is escaping from the vent at the end of the trailing edge, the small vent. It could be noted that some dots in green are in the corner of the end of the blade (Figure 5.23 (one vent)), which also predict some gas is trapped there.



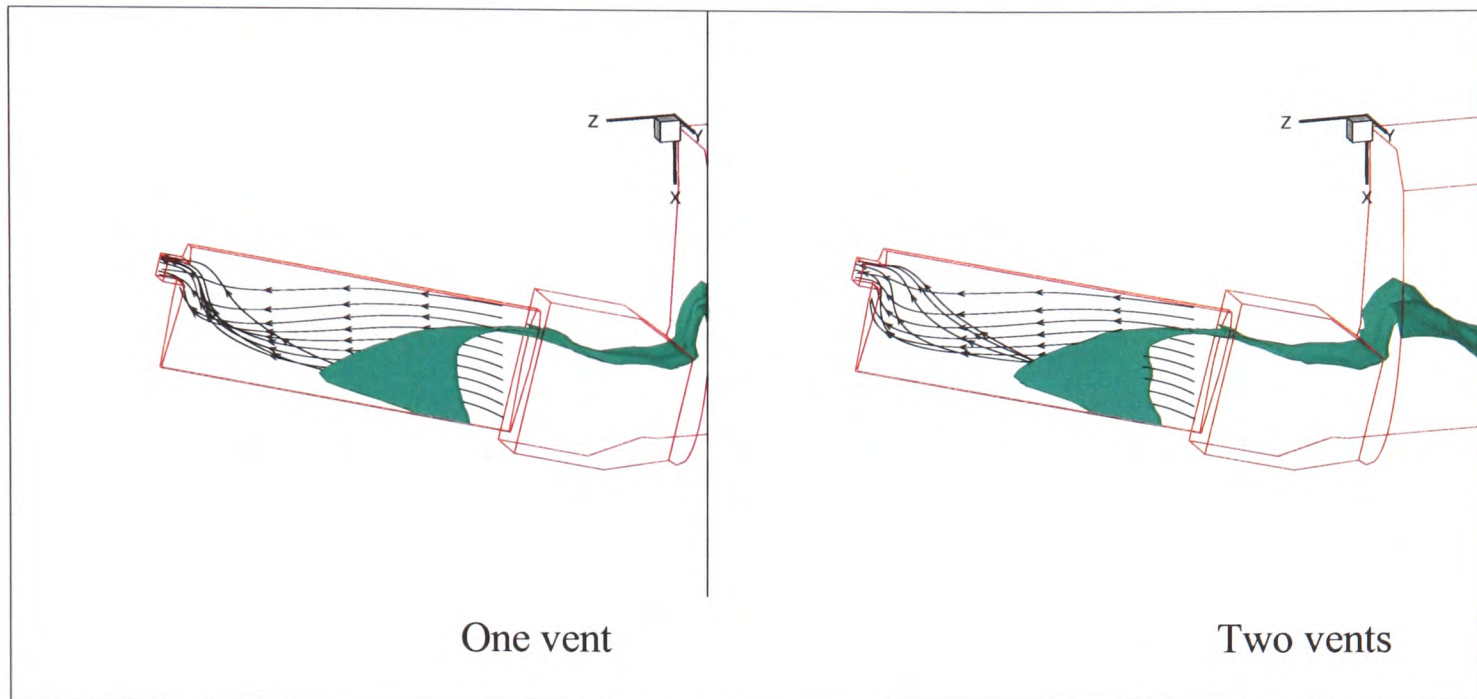


Figure 5.22: Difference of one vent and two vents in stream traces at the 2.6s.

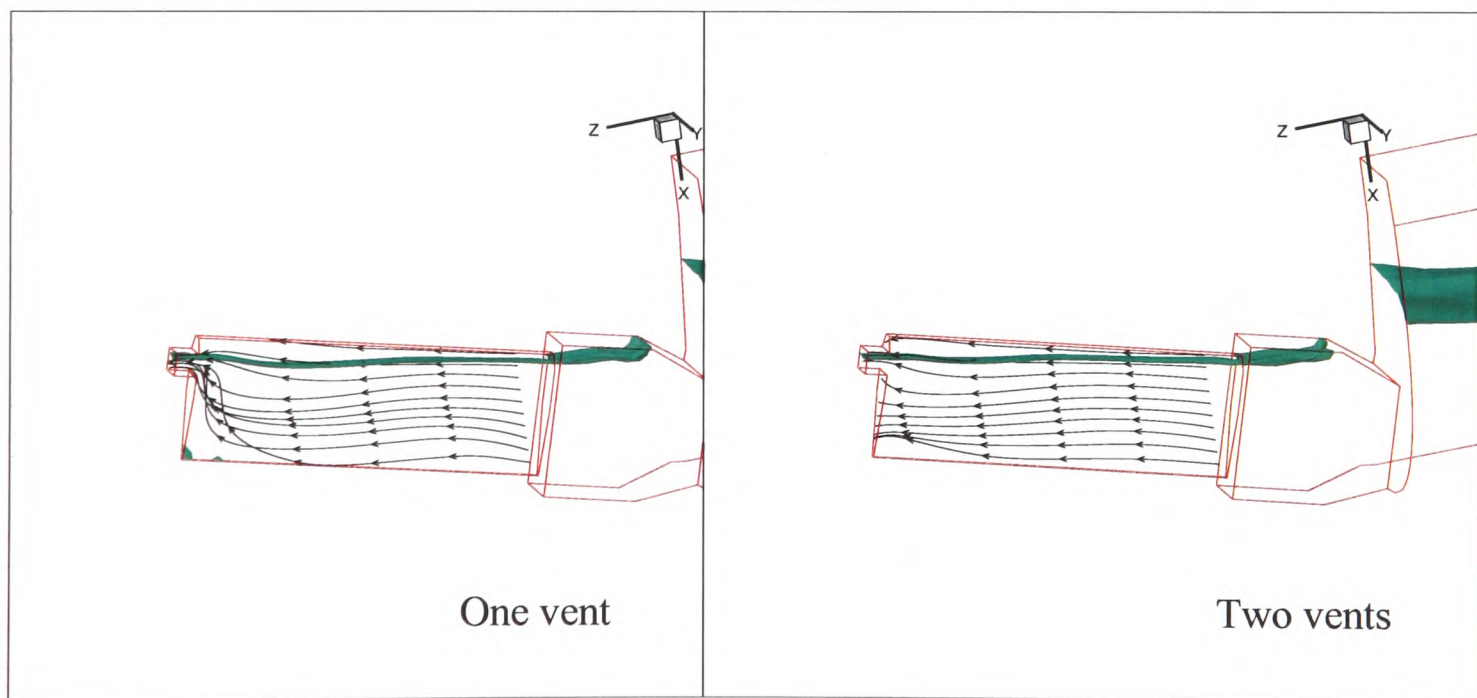


Figure 5.23: Difference of one vent and two vents in stream traces at the 3.1s.

From the above comparisons, it is noted that the number and the position of vents have an impact on the mould filling. The appropriate position of the vent can help avoid some gas trapped in the narrow edge or corners. Enough vents allow the gas to evacuate quickly from the blades.

### 5.8.7.2 Validation and Comparisons of the Experimental and Numerical Results

The comparison of the experimental and numerical results of the short turbine blades with one vent is presented in Figure 5.24. The numerical results demonstrate the temperature 'TN' of the blades. Comparing with the experimental results, which showed a mis-run in both the leading edge and at the trailing edge, the numerical model predicted where mis-run may take place is lower temperature, where liquid metal is freezing, solidifying. Numerical modelling can give a good indication of defect areas that result from the flow pattern created during filling and partial solidification.

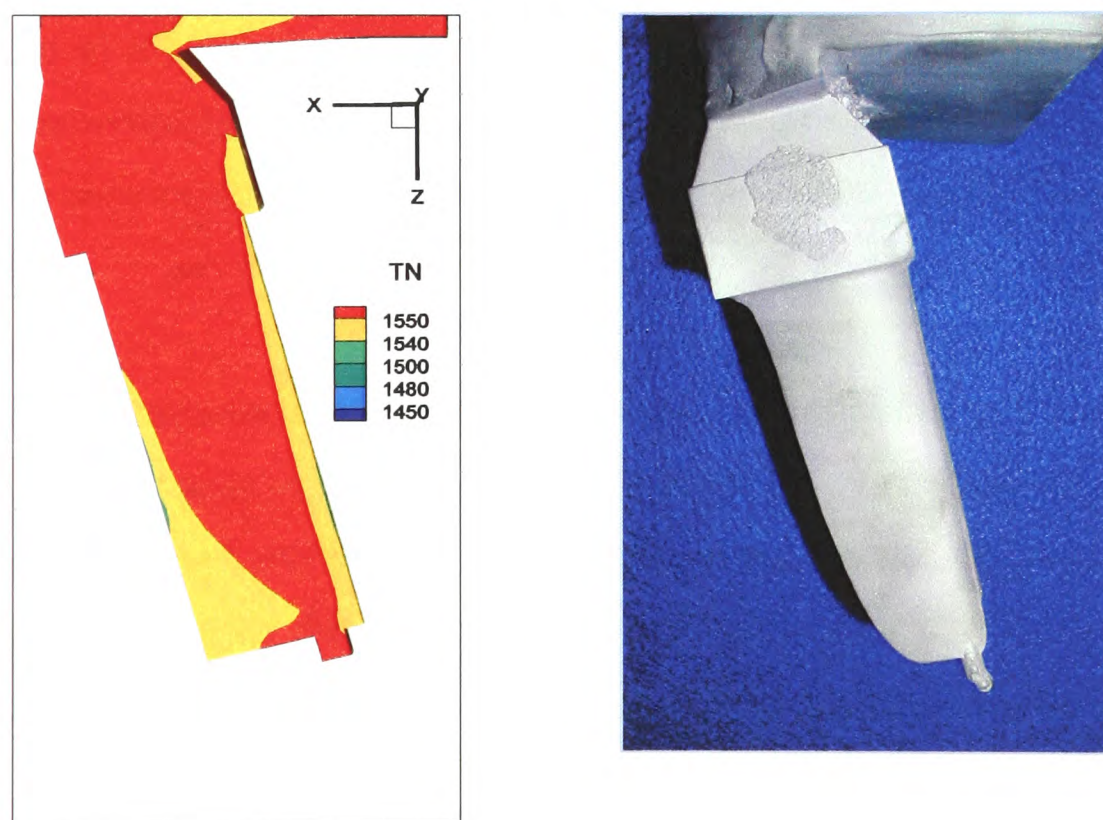


Figure 5.24: Comparisons of the experimental and numerical results with one vent.



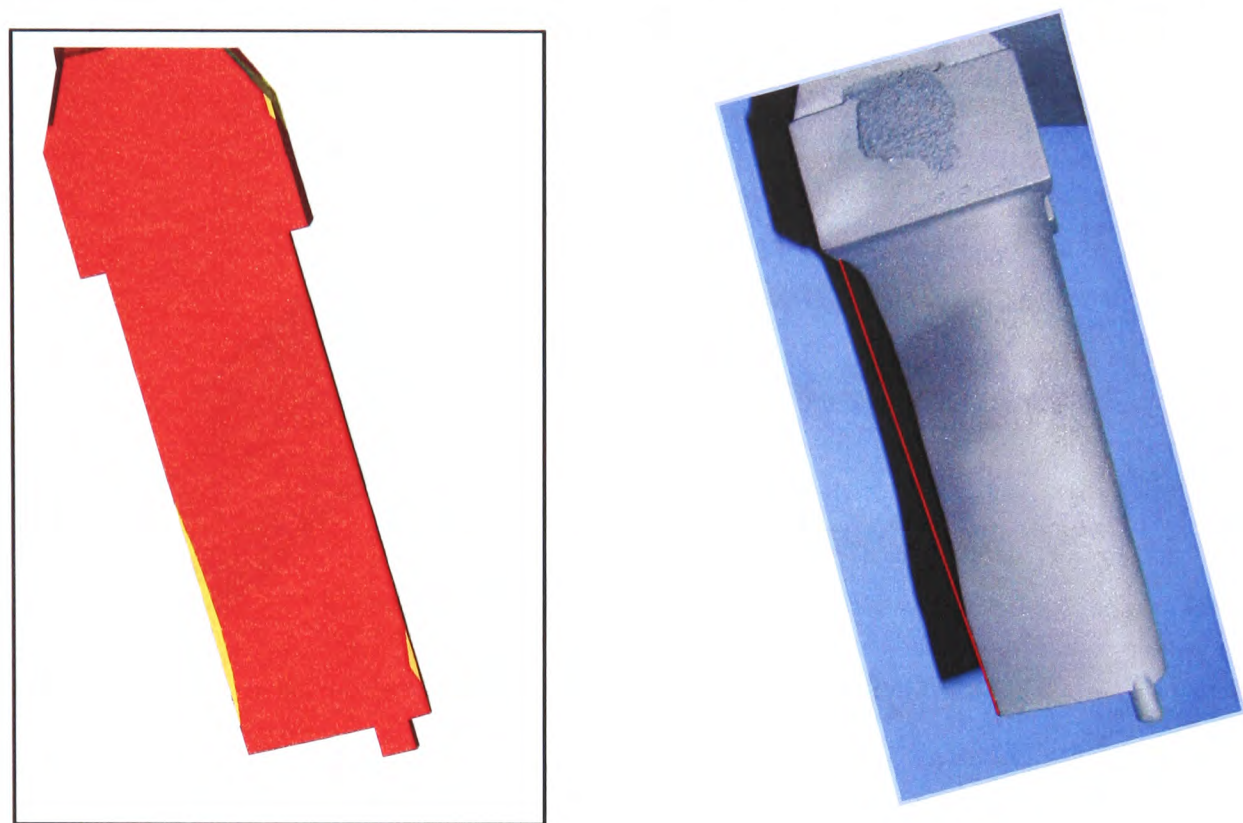
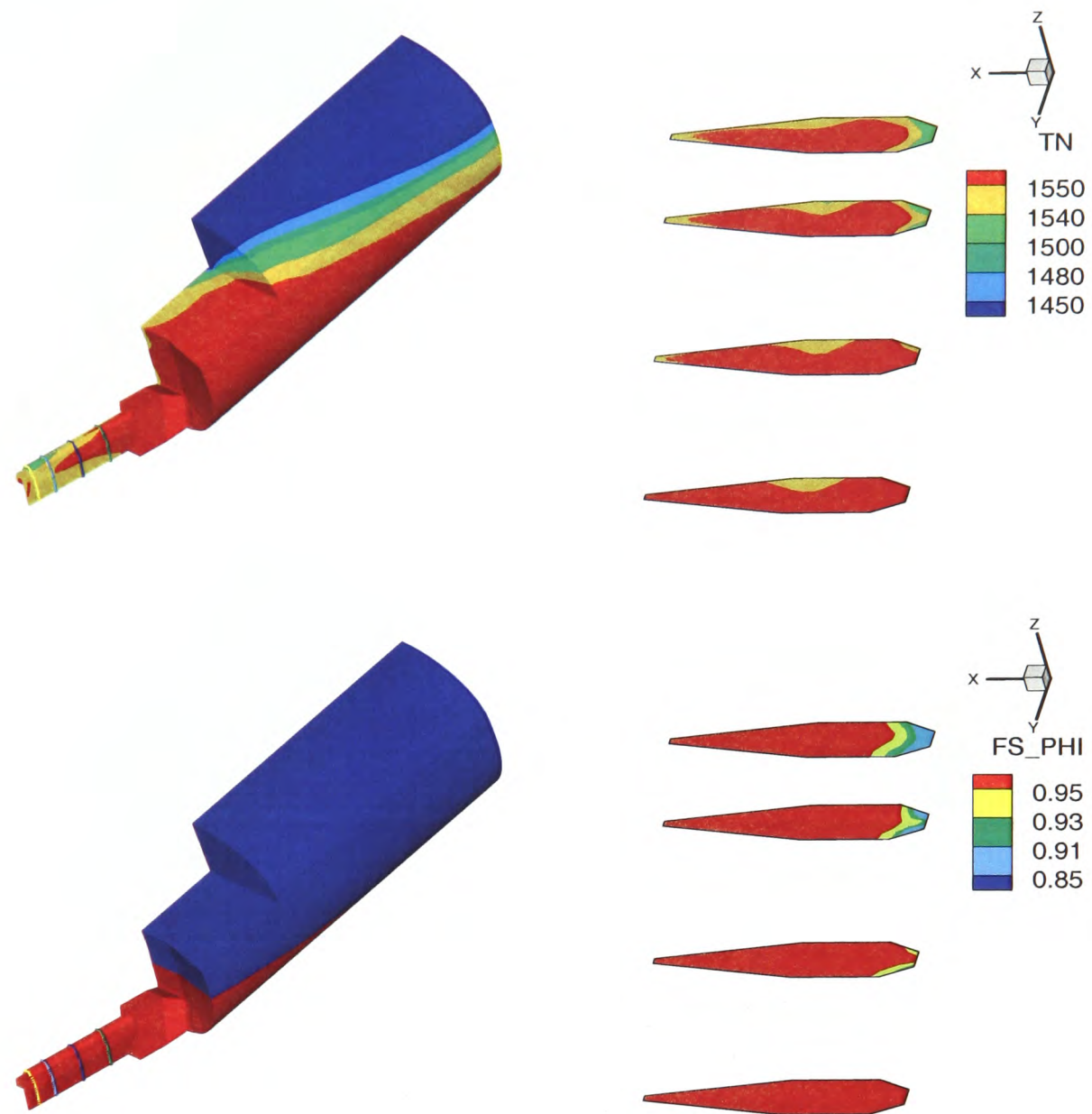


Figure 5.25: Comparisons of the experimental and numerical results with two vents.

The comparison of the experimental and numerical results with two vents is shown in Figure 5.25. The comparison is made in exactly the same way as the previous one. It can be seen that the numerical results in temperature 'TN' predicts the area where one could expect mis-run.

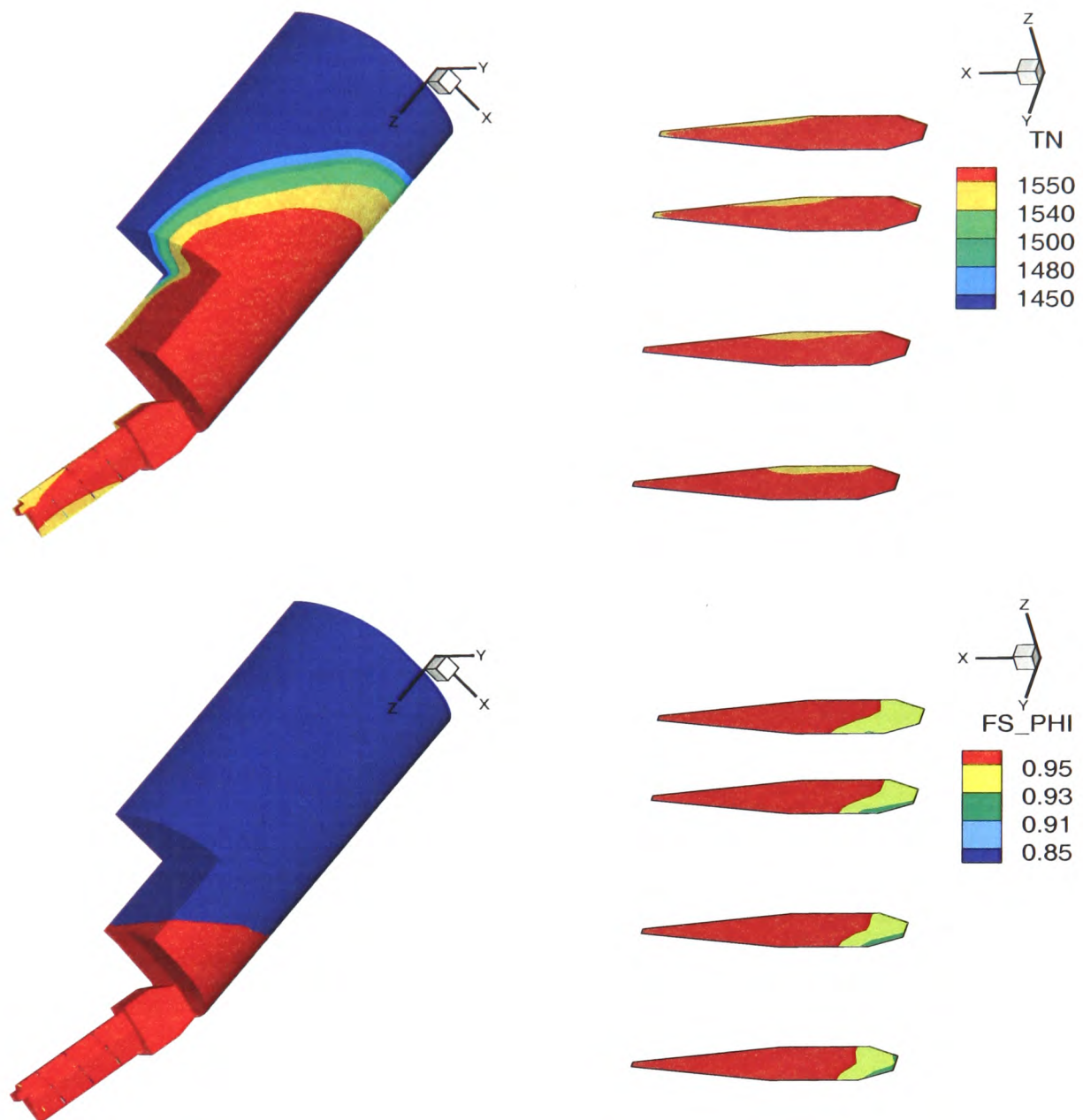
From the above comparisons, it is known that the mould of the casting of this short turbine with one vent is not as good as with two vents. The latter has more space to allow the gas to escape from the mould and avoid holding back molten metal filling into the mould because of the presence of the gas. In the following, Figure 5.26 and Figure 5.27 demonstrate the temperature and free surface contours at different heights of the blade cross-section, 0.415m, 0.4m, 0.375m and 0.35m. One is at the 4.5 s; the other is at 5.0 s into the cycle with the full cycle at 6.0s (vertical blade).



**TN:**  
 Liquidus temperature of TiAl is 1550°C; Solidus temperature of TiAl is 1500°C.

**FS\_PHI:**  
 FS PHI=1, in a liquid cell; FS PHI=0, in a gas cell.

Figure 5.25: Numerical results of the blade cross-section in heat transfer and in free surface contour with two vents at the 4.5s (6.0s).



**TN:**  
 Liquidus temperature of TiAl is 1550°C; Solidus temperature of TiAl is 1500°C.

**FS\_PHI:**  
 FS PHI=1, in a liquid cell; FS PHI=0, in a gas cell.

Figure 5.26: Numerical results of the blade cross-section in heat transfer and in free surface contour with two vents at the 5.0s (6.0s).



## Chapter 5. 3D/1D Coupled Transient Heat Transfer Model

---

It is noted that the metal temperature is the highest in the centre since that is where heat must diffuse the greatest distance. Also the metal has a lower temperature at the leading and trailing edges of the blade. The value of the gas fraction at the leading edge is higher than that in the remainder since during rotation this surface is at the top. The facts lead to casting defects in this area which may explain that in practice the top surface (the leading edge) is not as smooth as the rest as shown in Figure 5.27.

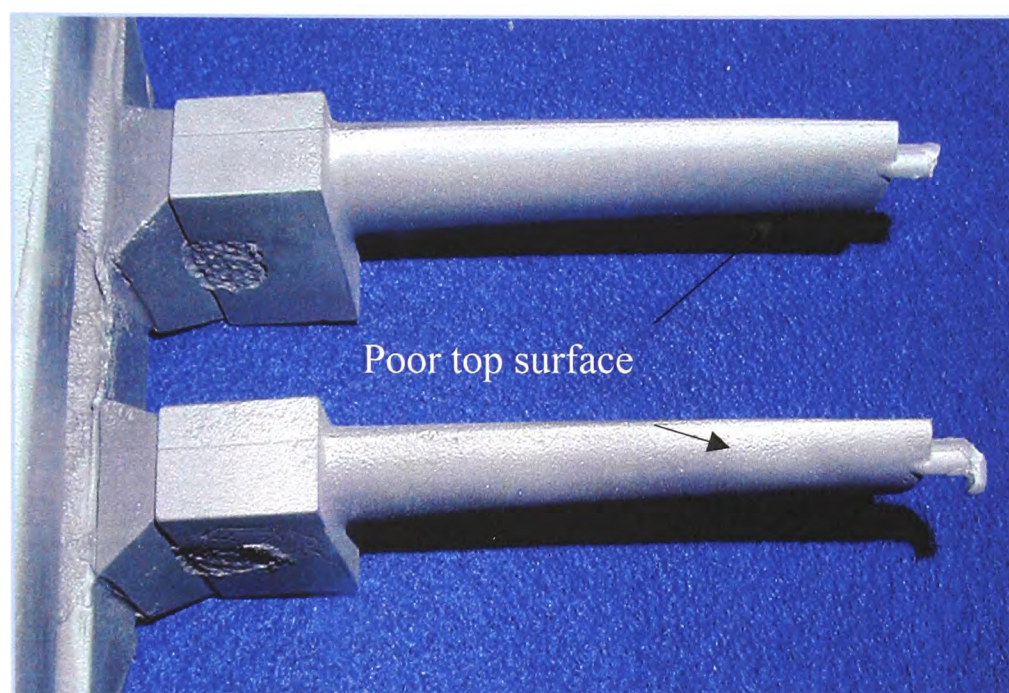


Figure 5.28: Poor top surfaces of experimental short turbine blades [Harding –Sep 06].

### 5.8.7.3 Comparisons of the Simulations with 1D Transient Heat Transfer Boundary and using the Fixed Heat Transfer Coefficient as a Thermal Boundary Condition

Some simulations were run using the same geometric model (that is not meshing the mould wall), the same initial conditions but different heat boundary conditions, estimated heat transfer coefficient was fixed at  $1000 \text{ W}/(\text{m}^2\text{K})$ , for the turbine blade and pouring basin.

Figure 5.29 shows the numerical results with the two methods, called Method A and Method B, used to set the thermal boundary conditions for the geometry having one vent. The pictures present the similar shapes in the temperature (TN) and in the liquid fraction (LFN) at 6.0 seconds. The 1D transient model functions very well. However, it is noted

## Chapter 5. 3D/1D Coupled Transient Heat Transfer Model

that the temperature using Method A is higher than that using Method B. This difference is arbitrary since when Method B is used, the value of the fixed heat transfer coefficient, 'COEFF\_VALUE', was simply chosen at 1000 W/ (m<sup>2</sup>K) to ensure a similar overall heat loss. In the simulations, this coefficient plays a very important role on the temperature scale. If COEFF\_VALUE equals 800 W/ (m<sup>2</sup>K), for example, the results with the two methods could match better.

Similar results were got for the geometry with two vents, as seen in Figure 5.30. From the above presentation, it is concluded that Method A is more accurate and more reliable than Method B.

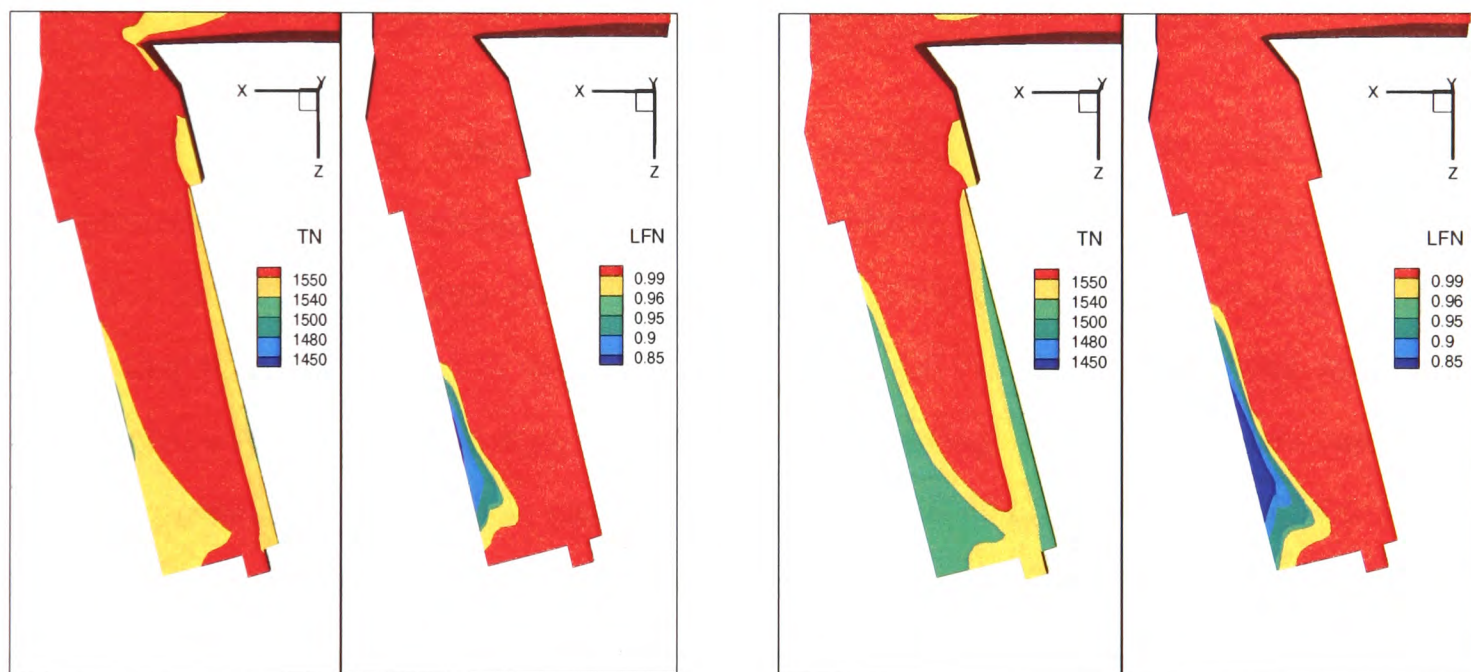


Figure 5.29: Comparison of the numerical results for one vent with 1D transient heat transfer boundary (method A: on the left) and the fixed heat transfer coefficient as the thermal boundary conditions (method B: on the right).



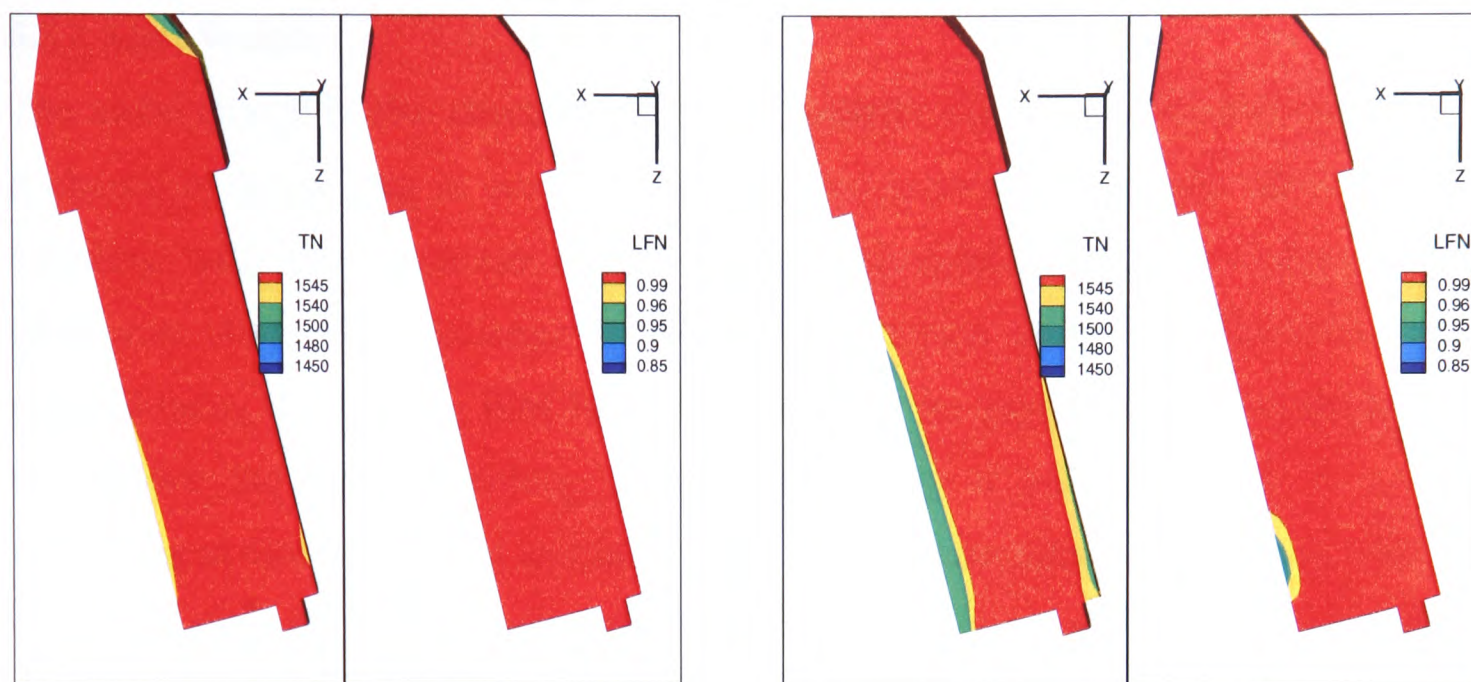


Figure 5.30: Comparison of the numerical results for two vents with 1D transient heat transfer boundary (method A: on the left) and the fixed heat transfer coefficient as the thermal boundary conditions (method B: on the right).

Table 5.8 shows the comparisons of the simulations with the two methods in computational time and the number of average iteration. The computing time with Method A is 2.5 hours greater than that with Method B. However it should be noted that the computing time of Method B is the simulating time for the geometric model, not meshing the mould, which must save some computing time. Instead, Method A has to compute the mould temperature every time step as well as the geometric model's. The 1D transient model does not actually slow down the simulation. And the average iteration times are slightly higher than those with Method B. The 1D transient model does not suffer from any difficulty of convergence in coupling into 3D model.

Table 5.8: Comparisons of the simulation with 1D transient heat transfer boundary (A) and that using fixed heat transfer coefficient as the heat boundary conditions (B).

	Method A	Method B
Computing time(h)	48	45.5
Number of iteration per time step	17.5 (approx.)	17 (approx.)

Note: Number of iteration is calculated for the two methods by summing the number of iteration at different runtimes and then averaging them.

### 5.8.8 Melt Weight

The metal charge is also characterised by its weight. The ISM furnace is optimised for a charge of about 5kg in weight. This has the optimal volume for electromagnetic coupling with the induction coil. Reduction in volume leads to lower superheat [Bjarevics -04]. The challenge is that only a limited amount of superheat can be reached using the existing ISM furnace. Increasing the superheat is no doubt an option to achieve the tranquil filling. In previous work, it was predicted in computer modelling at Greenwich and in trials in the IRC for Materials Processing at University of Birmingham that larger melts give a higher superheat, seen in Figure 5.31. However in the following section, the effect of the metal charge will alone be presented in terms of the mould filling assuming superheat remaining constant. Differences would then be observed due to larger hydraulic head in the pouring operation.

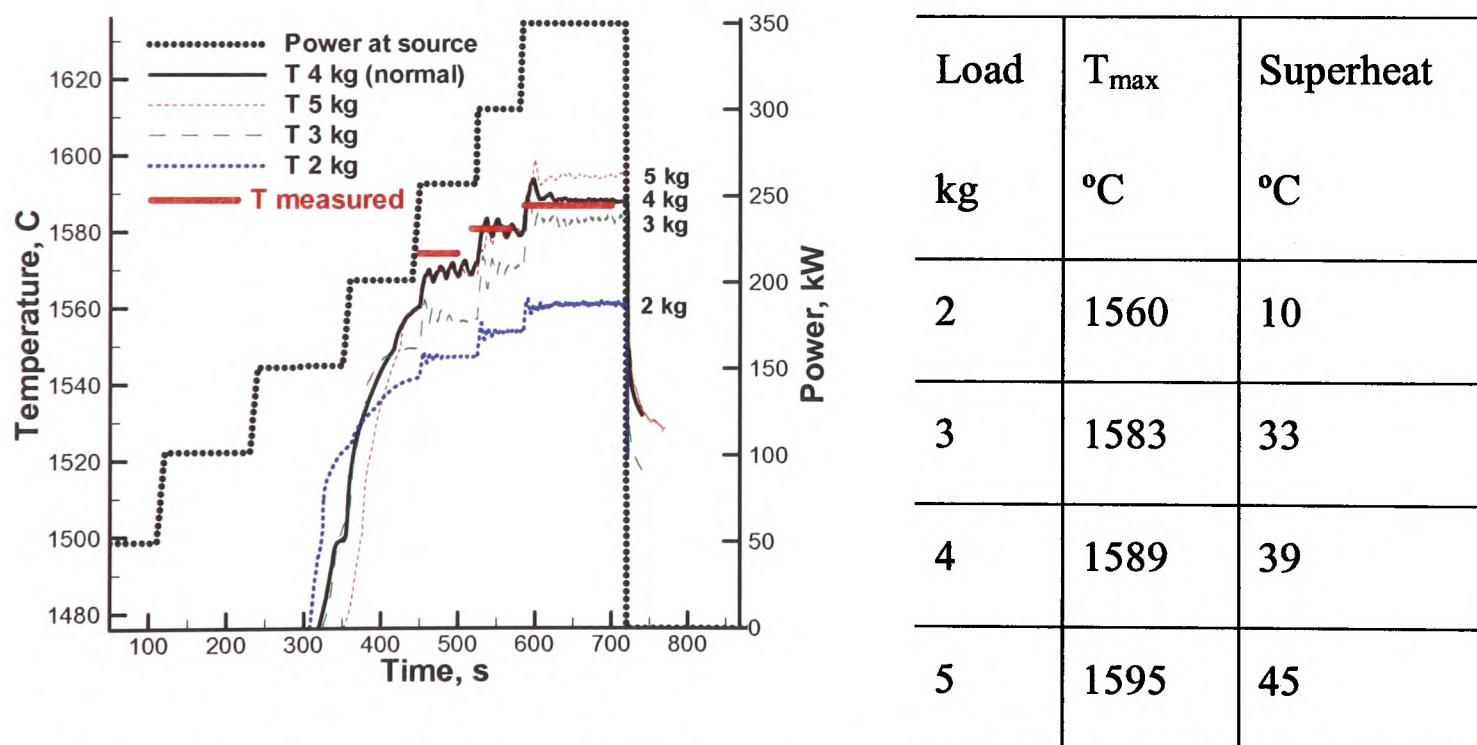


Figure 5.31: Comparison of simulated temperatures in various melt weights of TiAl during a typical stepwise melting schedule using a 7kHz AC field [Bjarevics -04].



### 5.8.8.1 Geometry and Computational Mesh

The same mesh presented in Section 5.8.3 is employed as the computational mesh in the following simulations. If a larger metal charge is used in the computing model, a corresponding big pouring basin (45 mm higher than small one) is needed, called the large bush.

### 5.8.8.2 Initial and Boundary Conditions

Tables 5.9 and 5.10 list the initial conditions of the numerical model for small bush and large bush. It is noted that the melt weight is different, however with the same superheat. There is no slip on all the walls. A full simulation of physics is attempted with free surface fluid flow, heat transfer and solidification present.

Table 5.9: The initial conditions of the numerical model for small bush

Mould preheated temperature, °C	1200
Initial temperature of molten metal , °C	1600
Melt weight (TiAl alloy), g	3169
Blade angled, deg	15
Continuous tilt cycle, deg/s	90
Number of vents	2
Superheat, °C	50

Table 5.10: The initial conditions of the numerical model for large bush

Mould preheated temperature, °C	1200
Initial temperature of molten metal , °C	1600
Melt weight (TiAl alloy), g	4767
Blade angled, deg	15
Continuous tilt cycle, deg/s	90
Number of vents	2
Superheat, °C	50



### 5.8.8.3 Presentation of Results

Figure 5.32 shows the liquid temperature contours which are very similar for these two cases. That means eventually the difference of the liquid temperatures is tiny even though large metal charge pushes the fluid to move in the mould more quickly (shown in Figure 5.33) if the superheat is the same. The still pictures were chosen to show the effect of the melt weight in mould filling with the same superheat 50 °C at 1.2 s/ 2.0s in Figure 5.33. The only visible effect is the progress of the metal filling. At 1.2s, there is more metal left in the pouring basin with the larger bush as compared to the smaller bush. The mould filling with the larger melt weight is faster than with low melt weight. This may be due to the impact on the liquid metal under the inertial force.

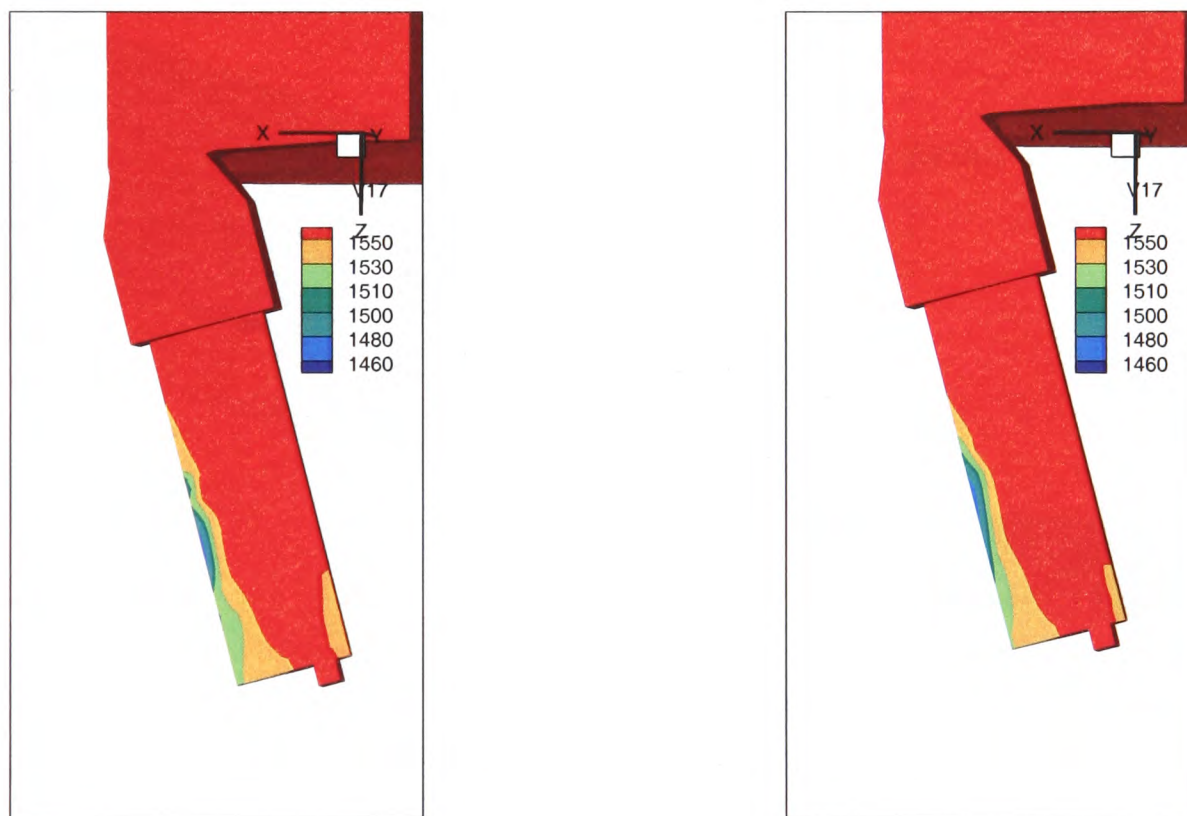


Figure 5.32: Comparisons of the simulations with large (left) and small bush (right) at the end of filling in liquid temperature.

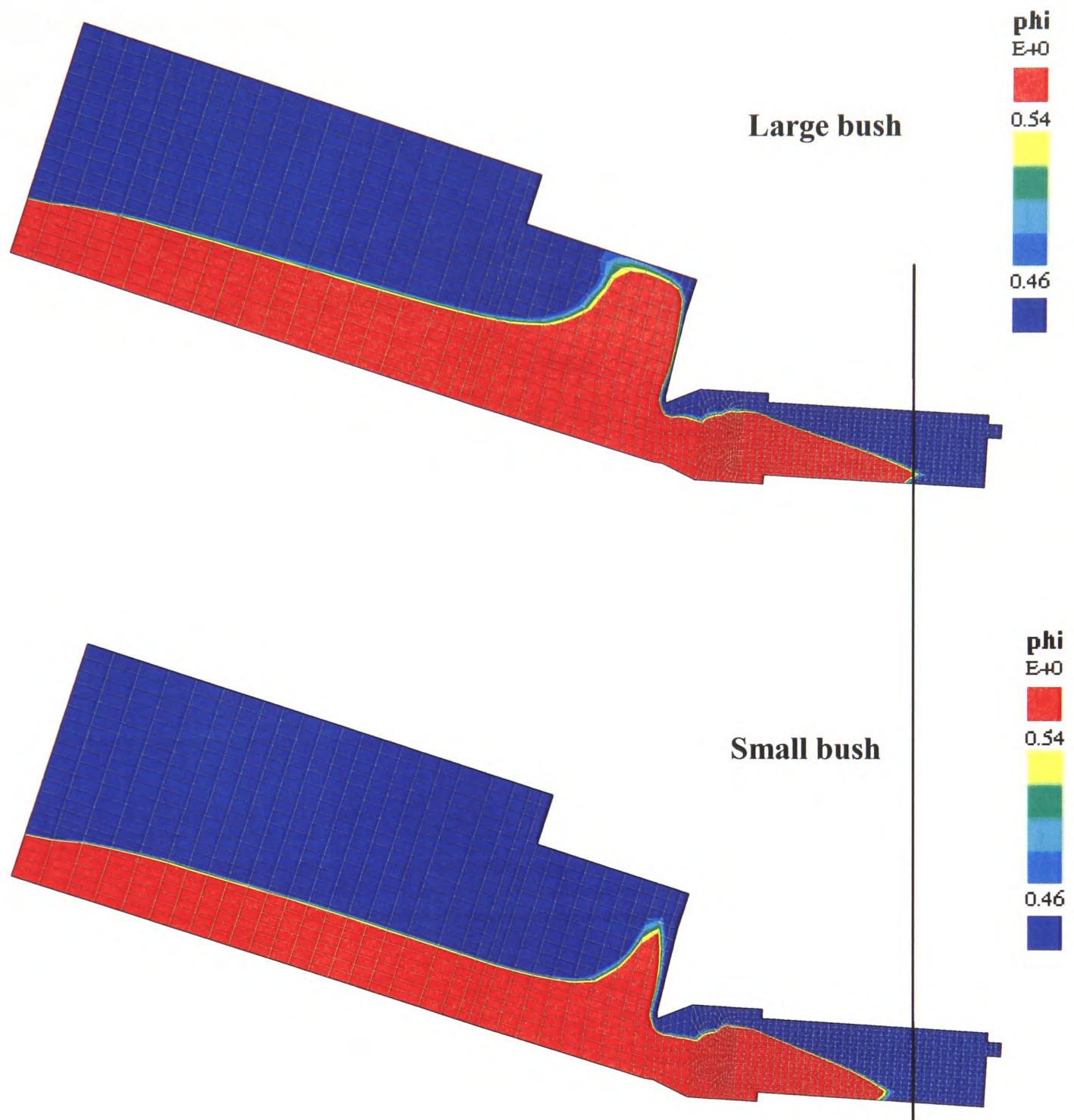


Figure 5.33: Comparisons of the simulations with large and small bush at 1.2s.

## 5.9 Summary

From the comparisons of the experimental and numerical results using 1D transient heat transfer boundary condition, it is seen that numerical modelling can give a good indication of defect areas that result from the low superheat during mould filling. Comparing with the numerical results obtained by using the fixed heat transfer coefficient as the thermal boundary condition, 1D transient model has improved the thermal boundary conditions

## Chapter 5. 3D/1D Coupled Transient Heat Transfer Model

---

and gives more accurate thermal prediction of the working field. Furthermore, no mould meshing is necessary. From the comparisons in the computing time and iteration times, 1D transient model not only simplifies the meshing but speeds up the simulations. For a massive and complex geometric model, that would lead to huge benefits in efficiency.

Even though the 3D/1D approach is able to reduce the computational time, the simulation is still very time-consuming using the existing free surface methods, which are discretised using an explicit scheme; these require very small time-step to satisfy CFL condition. Moreover, it also suffers from numerical diffusion. In the following Chapter, the geometry will be more complex and more elements and nodes contained in it. Further efforts need to be made to improve the free surface algorithm in terms of the free surface quality and computing speed.

## Chapter 6

# The Counter Diffusion Method

This chapter presents a novel ‘Counter Diffusion Method’ (or CDM) which is proposed as a corrective mechanism to counter the effects of numerical diffusion of the interface. This method discretises the free surface equation fully implicitly in a fast, efficient way without numerical diffusion. That allows this method to use much greater time steps in the simulation and so reduce the computational time.

The new method was first validated against the classical collapsing column experiment of [Martin and Moyce -52] and showed a very good agreement. The comparisons of the efficiency of CDM with other numerical methods: Van Leer, Donor Acceptor and Level Set Method have been made, and showed the advantages in reducing the computational time.

Finally the Counter Diffusion Method (CDM) is used to model long 40cm turbine blades, suitable for industrial gas turbines.

## 6.1 Introduction

When numerical simulations are attempted to start, time and space are divided into a discrete grid and the continuous differential equations of motion are discretised into finite difference equations. The discrete equations are in general more diffusive than the original differential equations which only have physical diffusion. The numerical diffusion leads to the simulated system behaving differently from the real physical system. The amount and character of the difference depends on the system being simulated and the type of discretisation used. The problem of numerical diffusion becomes very important at the moving liquid/gas interface (called free surface) which characterizes the filling process.

When the advection equation is discretised for tracking the interface between the two media, some approximation of the face values of the liquid/gas marker  $\Phi$  (i.e. upwind approximation in the Van Leer Method) results in the smearing of a sharp interface. A novel Counter Diffusion Method (CDM) is proposed as a corrective mechanism to counter this 'numerical diffusion'. This method discretises the free surface equation in a stable, fully implicit scheme. That is computationally very fast with the Finite Volume method. The idea for the correction method is from an analogy with the physical breaking of the interface in that any intermediate values of  $\Phi$  between 0 and 1 mean either droplets in gas or bubbles in liquid and one would like to cause the fragmented phase to re-join the main body of the fluid under gravity to reduce the smearing. This can be done in a way similar to the Algebraic Slip Method [Pericleous and Drake -86] for simulating real bubbles, droplets or particles. Rather than calculating the *slip velocity* of imaginary droplets or bubbles based on physical grounds, an interface-normal counter diffusion flux can be defined for each internal face of the computational mesh. The counter diffusion flux is applied to the elements straddling the marker variable as source terms with opposite signs. This can be prescribed in the interface zone in a way that is suitable for controlling the sharpness of the front, without leading to instability.



## 6.2 Mathematical Description

This method is based on Equation (6.1) which is the conservation equation for a scalar variable  $\chi$  [PHYSICA]:

$$\frac{\partial(T_\chi\chi)}{\partial t} + \text{div}(C_\chi\underline{u}\chi) = \text{div}(D_\chi\text{grad}(\chi)) + S_\chi \quad (6.1)$$

where  $T_\chi, C_\chi$  and  $D_\chi$  are the coefficients of the transient, convection and diffusion terms respectively and  $S_\chi$  is the source term in the equation. The scalar module allows any number scalar variables to be solved or stored.

A new scalar called 'marker' which takes any intermediate value from 0.0 to 1.0 is used and its value is obtained with the scalar module where the diffusion term is switched off, the diffusion coefficient  $D_\chi=0$  and the transient and convection coefficients are set to 1,  $T_\chi=1, C_\chi=1$ . Then Equation (6.1) is rewritten to:

$$\frac{\partial\Phi}{\partial t} + \text{div}(\underline{u} \cdot \Phi) = S \quad (6.2)$$

Where, the source  $S$  contains the CDM corrections to the convection determined by  $\underline{u}$ . Then the value of the 'marker' is copied to 'phi' instead of solving 'phi' with the free surface module. This process is realized by coupling an artificial counter diffusion flux into Equation (6.1) as the source term  $S$ . The artificial counter diffusion flux is calculated by Equation (6.3) [Harding *et al.* -07, 08]:

$$Q = C \cdot q \cdot (1 - \Phi_{down}) \cdot \Phi_{up} \quad (6.3)$$

where  $Q$  is artificial counter diffusion flux for each internal face;  $C$  is constant, used to adjust the local face normal velocity (convection flux), the strength of the counter

## Chapter 6. The Counter Diffusion Method

---

diffusion action;  $\Phi_{down}$ ,  $\Phi_{up}$  are respectively downwind and upwind values of 'phi' with respect to the artificial slip motion;  $(1 - \Phi_{down})$  is a factor which ensures the cells of completely full of liquid are not pushed into and  $\Phi_{up}$  is the factor which ensures not to take from cells without liquid;  $q$  is current iteration convection flux which is used to transport all scalar variables,

$$q = |\underline{u} \cdot \underline{n}| \cdot A \quad (6.4)$$

where  $|\underline{u} \cdot \underline{n}|$  local face normal velocity and  $A$  is the face area. The formula makes the counter diffusion action self-limiting as it is reduced to zero where the value of  $\Phi_{up}$  approaches zero (pure gas) and the value of  $\Phi_{down}$  is reaching one (pure liquid). In this form, the adjustment is conservative.

### 6.3 Algorithm

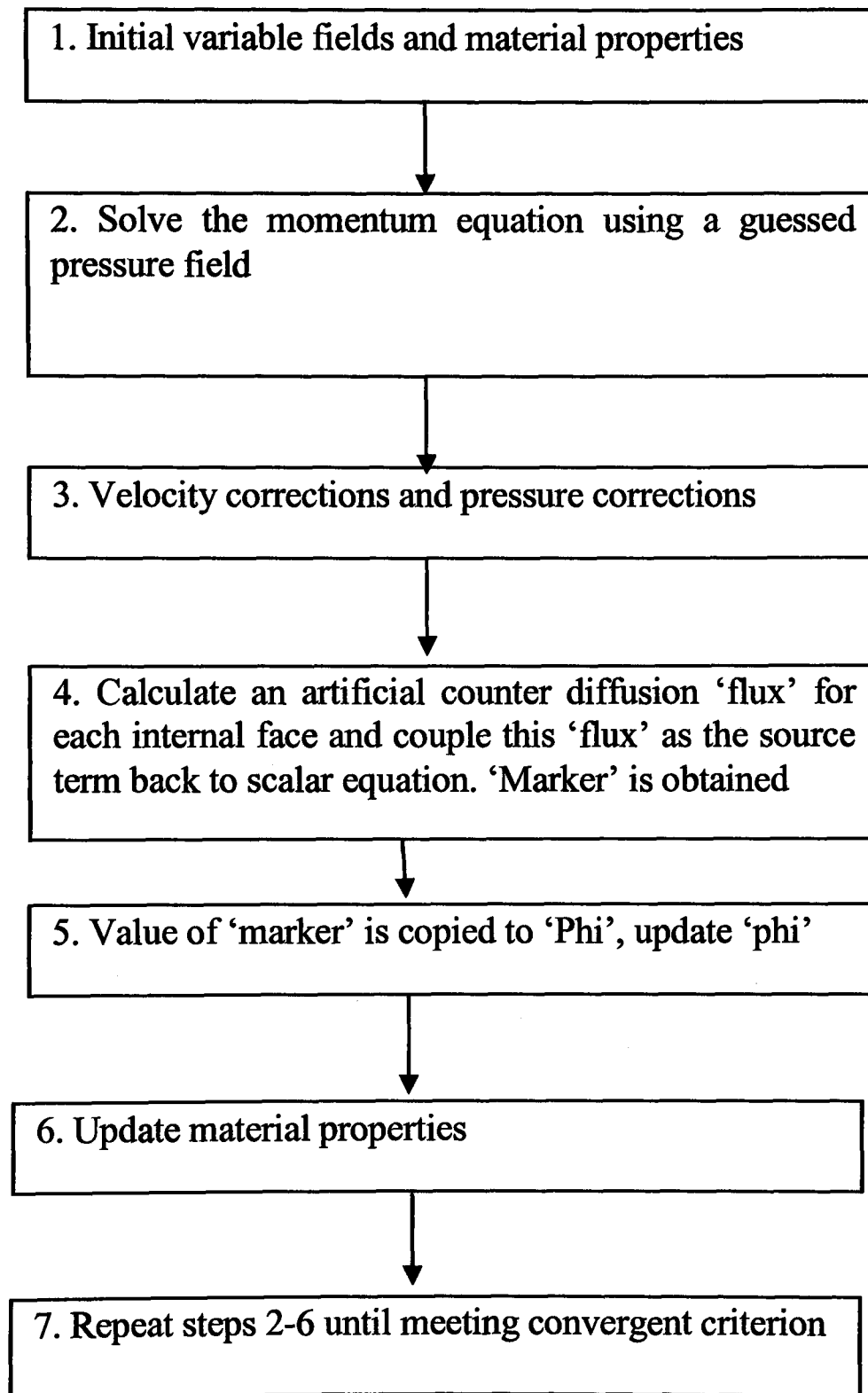


Figure 6.1: Solution Procedure for Counter Diffusion Methods.

## 6.4 Validation of the Counter Diffusion Method (CDM)

### 6.4.1 Test Case Specification

The Counter Diffusion Method is described as above. The validation is carried out by reproducing an experimental study of a collapsing water column by J. C. Martin and W. J. Moyce [Martin and Moyce -52]. Figure 6.2 demonstrates the configuration of the problem. A rectangular water column with a height of 2 m and a width of 1 m is initially confined between two vertical walls in hydrostatic equilibrium. Air is present as the outer medium. The water column is collapsing on to the plane  $y=0$  under the effect of gravity and spreads out along the  $x$  direction when the dam holding it is removed at  $t=0s$ .

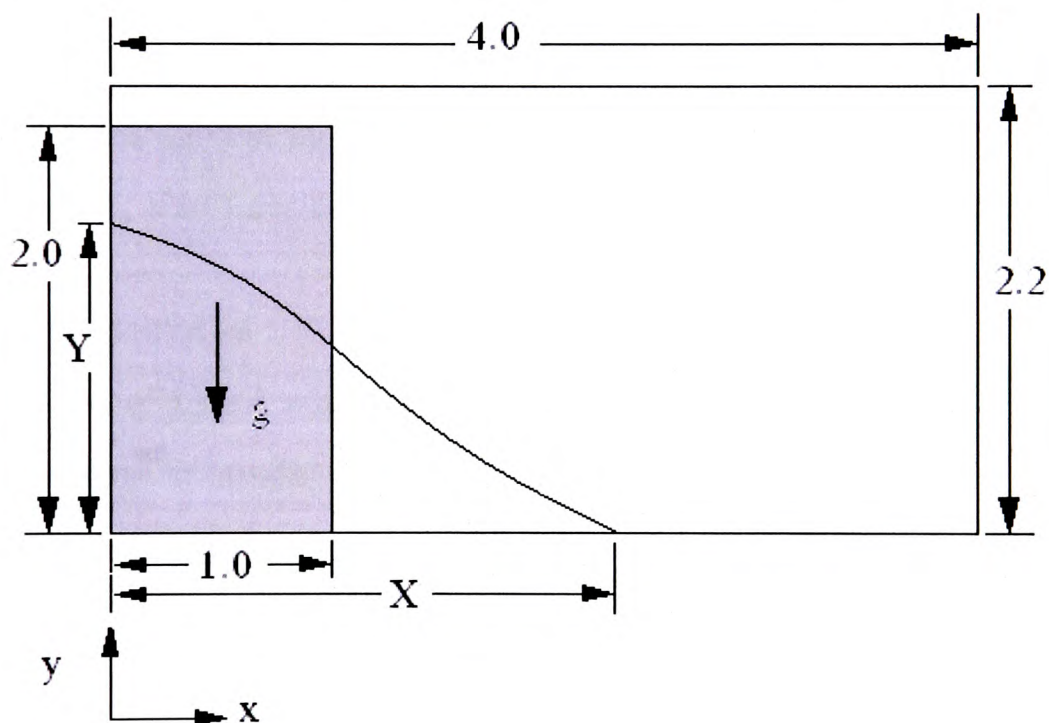


Figure 6.2: Configuration of water column collapsing

The dimensions of the problem are shown in Figure 6.2. The domain is meshed into 880 cells (40x22). A two-dimensional collapse is considered as in the experiment (1952).

### 6.4.2 Initial and Boundary Conditions

The simulation starts at time  $t=0.0s$ . At this time, the water column is held still and the value of  $\Phi$  is set to 1. A constant zero pressure is set on the right far face and the top of

## Chapter 6. The Counter Diffusion Method

---

the domain. There are two media involved: water and air. Their properties in the simulations are listed in Table 6.1.

It is assumed that non-slip is present on the walls,  $\partial \underline{u} / \partial x_i = 0$ . No thermal boundary conditions are employed in the simulations. The value of the gravity is  $1.0 \text{ m/s}^2$ .

Table 6.1: The fluid properties

	water	air
Density, ( $\text{kg/m}^3$ )	1000.0	1.
Kinematic viscosity, ( $\text{m}^2/\text{s}$ )	$1.012 \times 10^{-6}$	$1.5 \times 10^{-5}$

This calculation is carried out with the [PHYSICA] code using the novel method, Counter Diffusion Method (CDM) to capture the free surface (interface between the two media). The CDM is compared against the experiment and the other free surface methods already used: Donor Acceptor, Van Leer and Level Set.

### 6.4.3 Results and Discussion

#### 6.4.3.1 Comparisons of CDM with Experimental Results

Before any comparison is made, it should be noted that the experimental data reported were normalised by applying a scaling law [Martin and Moyce -52]. It is then convenient to compare the numerical results with the experimental results. The dimensionless variables are:

$$X^* = \frac{x}{a}, \text{ normalising the distance of the surge front along the base plane;}$$

$$T^* = nt \left( \frac{g}{a} \right)^{\frac{1}{2}}, \text{ normalising the time;}$$

$$Y^* = \frac{y}{n^2} a, \text{ normalising the height of the residual column;}$$

$$t^* = t \left( \frac{g}{a} \right)^{\frac{1}{2}}, \text{ normalising the time.}$$



## Chapter 6. The Counter Diffusion Method

---

where  $a$  is the base initial width of the column,  $g$  is gravity and  $n^2$  is the ratio of the column height to width, this study  $n^2=2$ .

The position of the water front and the residual height of the water column are plotted as the functions of the elapsing time compared with experimental data [Martin and Moyce - 52] which are referred to as Benchmark data shown in Figure 6.3 and Figure 6.4.

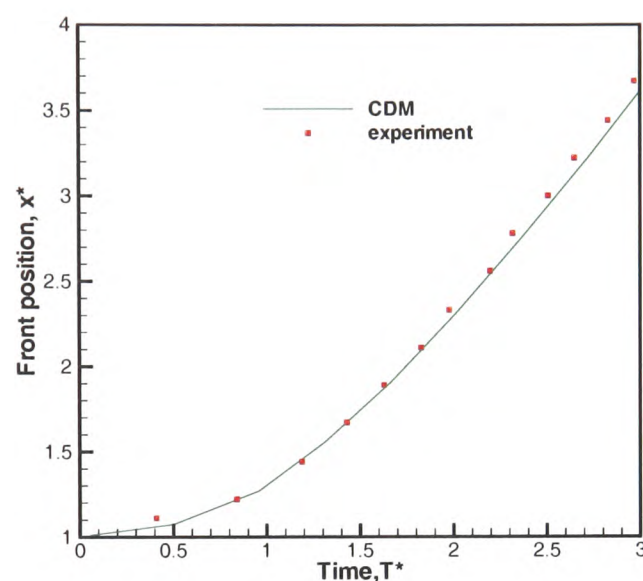


Figure 6.3: Comparisons of the numerical results with experimental results for the front position of the collapsing water column (Martin & Moyce in 1952)

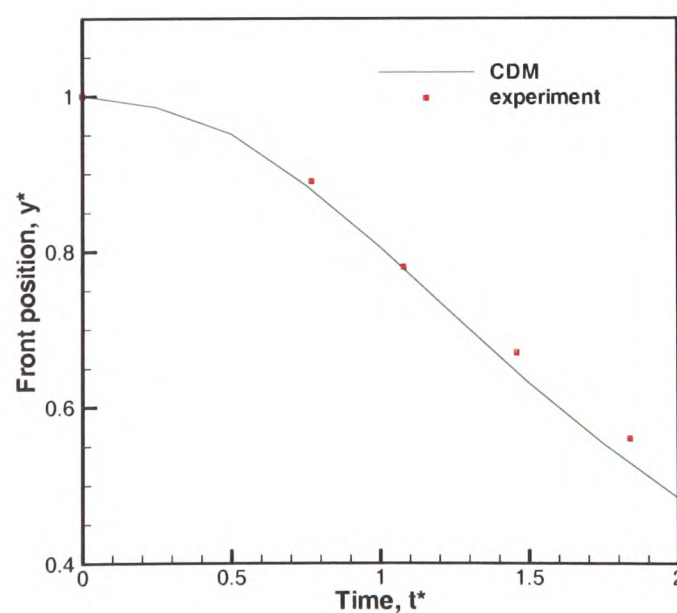


Figure 6.4: Comparisons of the numerical results with experimental results for the residual height of the collapsing water column (Martin & Moyce in 1952)

## Chapter 6. The Counter Diffusion Method

---

It can be seen from Figures 6.3-6.4 that there is generally in good agreement between the numerical results and the experimental data. However, some discrepancies are shown when  $t^*$  is greater than 1.2 at the residual height of the water and  $T^*$  is more than 2.2 at the front of water.

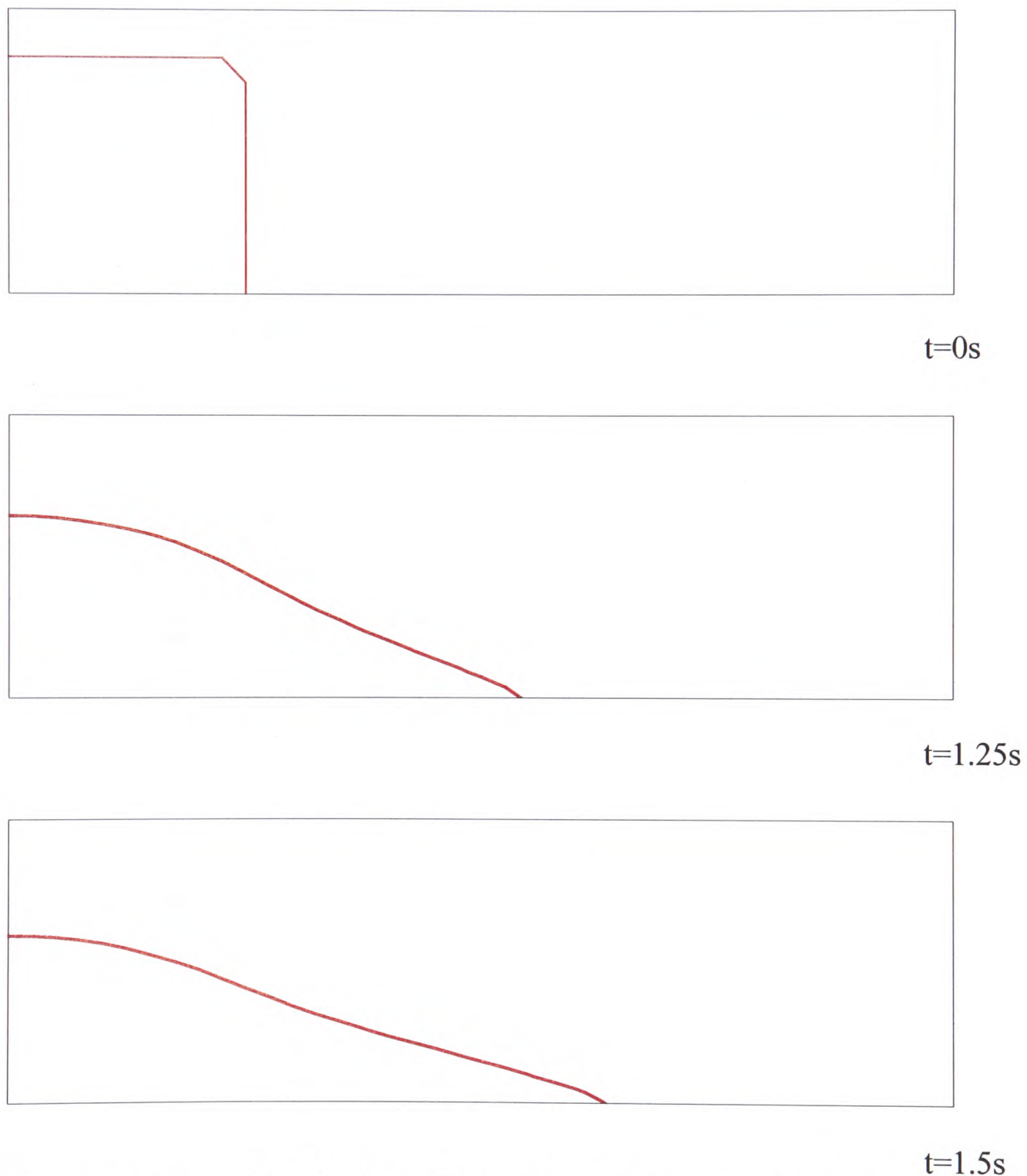


Figure 6.5: Free surface profiles for the collapse of water column with the CDM method

The interface profiles ( $\Phi = 0.5$ ) are plotted at different time in CDM method shown in Figure 6.5 and the progress of the surge front in the experiment [Martin and Moyce -52]



were recorded in Figure 6.6 where  $n^2=1$  portrays the now square section. The shape of the interface in the numerical results is smoother than that in the experiment which is fluctuating slightly. These may be due to numerical smear at the interface of the two fluids, or a 3D effect in the experiment.

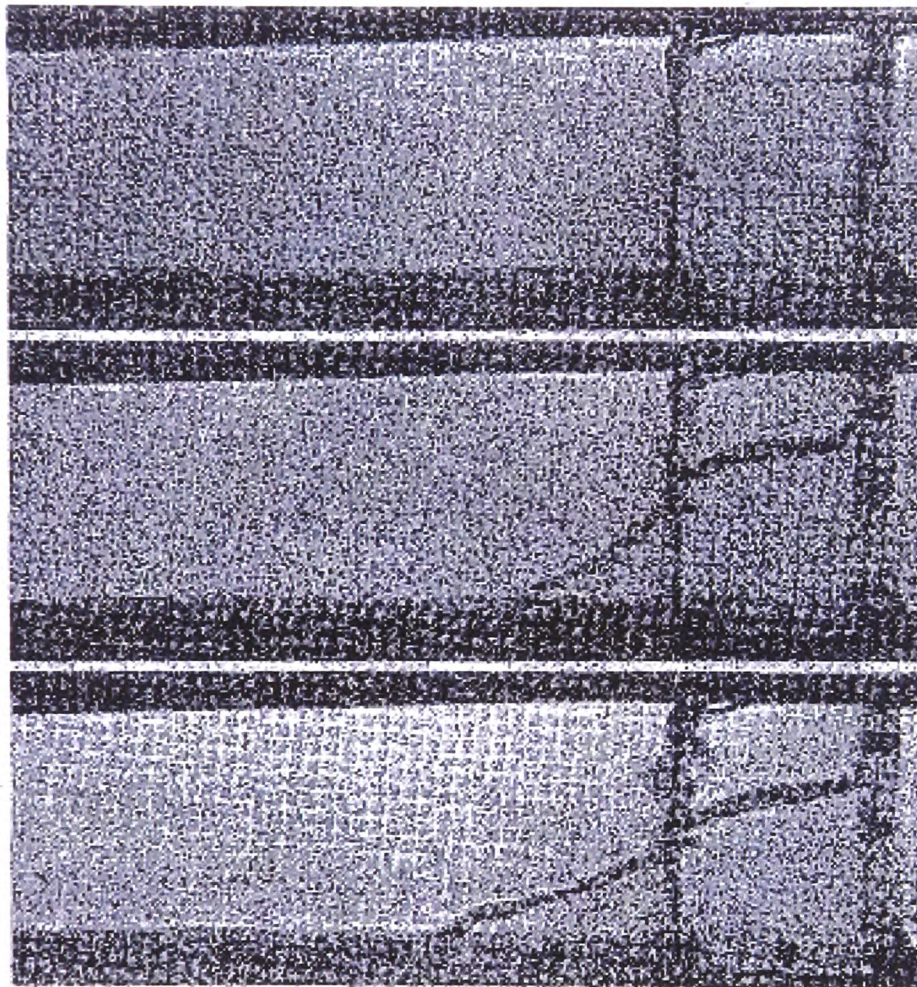


Figure 6.6: Free surface profiles of the collapsing water column in experiment (Martin & Moyce in 1952)

### 6.4.3.2 Comparisons of CDM with others Usual Numerical Methods

The simulations in Van Leer, Donor Acceptor and LSM were run under the same initial and boundary conditions for the collapsing water column. The comparisons of the numerical results are seen in Figure 6.7-6.8. CDM gives a very close prediction with Van Leer and Donor Acceptor with which very robust numerical results were obtained in the casting and have been widely used to track the free surface (interface between two media) for years. Discrepancies occurred between LSM and other three numerical methods, Van

## Chapter 6. The Counter Diffusion Method

---

Leer, Donor Acceptor and CDM. This may be caused by a weakness of LSM, mass non-conservative. It seems that the new method CDM works quite well.

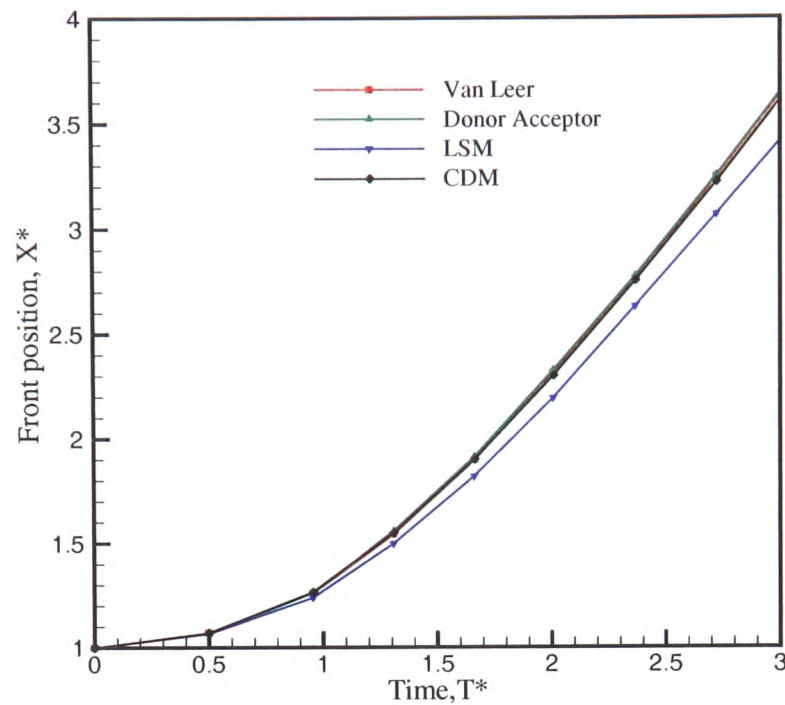


Figure 6.7: Comparisons of the numerical results in Van Leer, Donor Acceptor, LSM and CDM for the residual height of the collapsing water column.

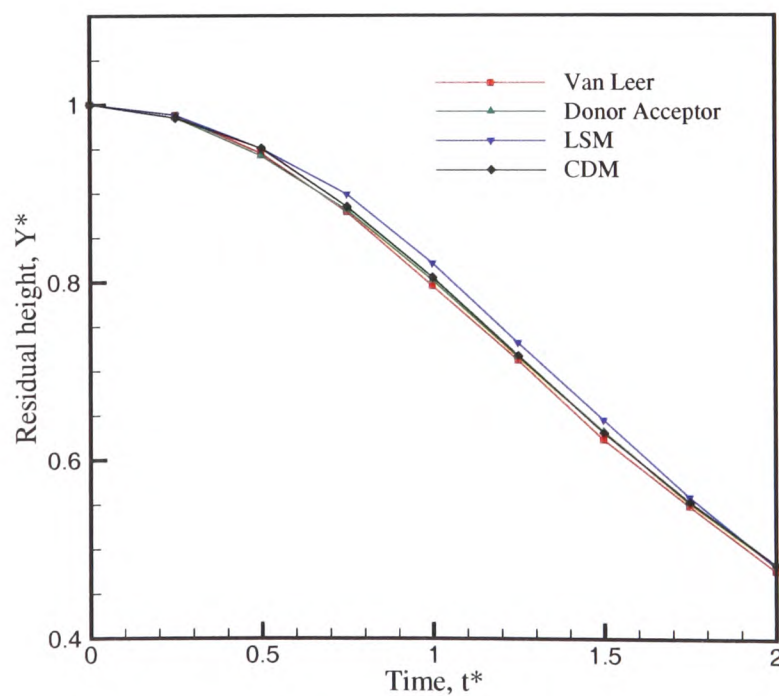


Figure 6.8: Comparisons of the numerical results in Van Leer, Donor Acceptor, LSM and CDM for the residual height of the collapsing water column.



## Chapter 6. The Counter Diffusion Method

---

Figure 6.5 and Figure 6.6 show the free surface profiles in numerical and experimental results. Here they are compared for the different numerical methods in Figure 6.9. It can be said that the shapes are very similar. From the point of view of numerical analysis, the interface tracked by the Counter Diffusion method is as sharp as the Donor Acceptor method (Figure 6.9), and less smeared than with Van Leer method.

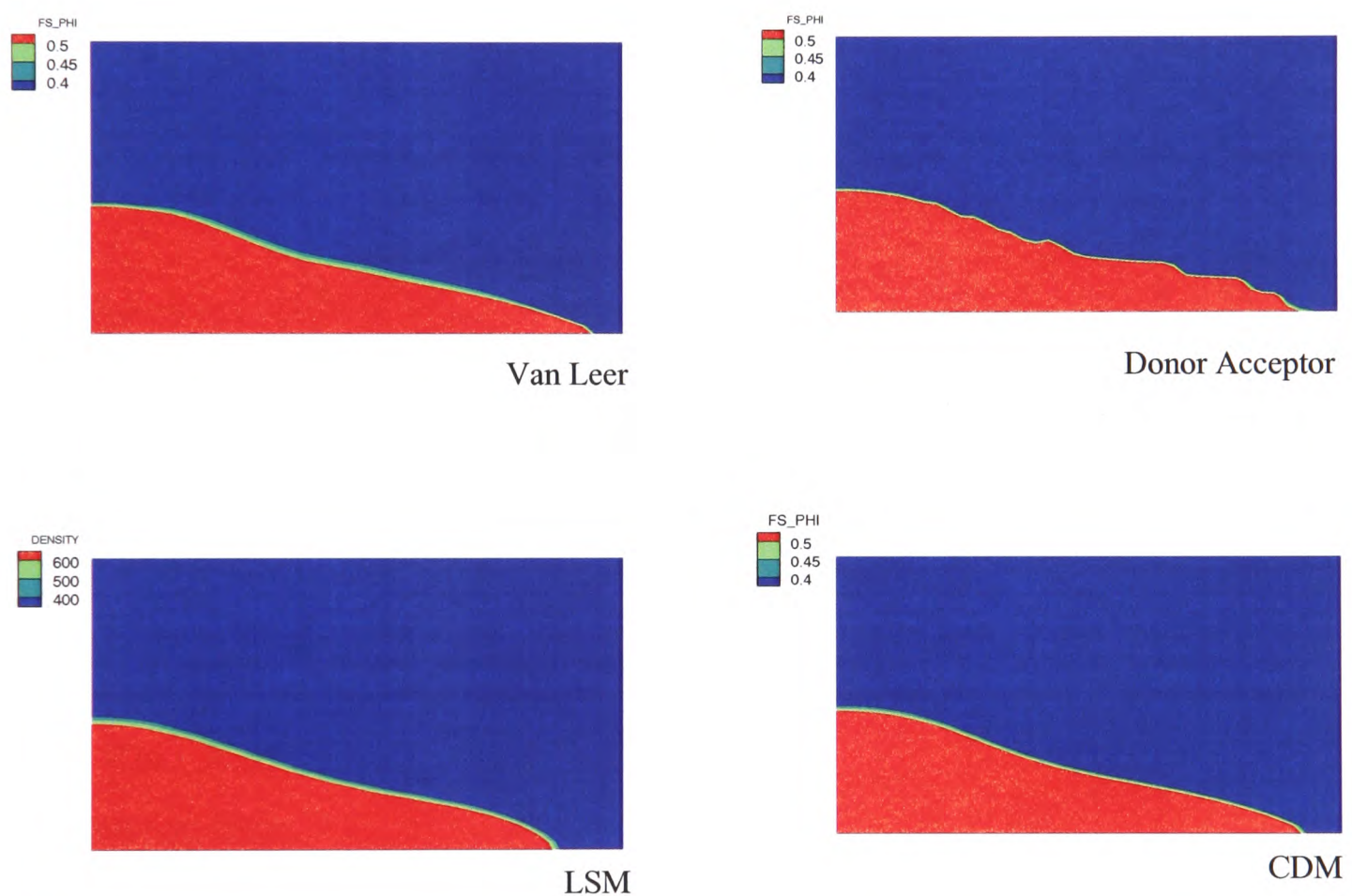


Figure 6.9: Comparisons of the numerical results in Van Leer, Donor Acceptor, LSM and CDM in  $\Phi$  at 2s.

From the above presentation, it is known that the numerical results with CDM are in excellent agreement with the experimental data. Is there any other advantage of CDM? Some comparisons of CDM with other three existing methods have been made from point of efficiency, presented in Table 6.2. It is seen that CDM can be applied with bigger time step than others. That is because CDM is developed fully implicit. Therefore this method does not need to obey the CFL conditions. With a bigger time step, simulation can be



## Chapter 6. The Counter Diffusion Method

carried out and the number of iterations is low. The first two columns show the time step for CDM could be ten times bigger than others'. The running time with time step 0.1s is half of running time with time step 0.01s for using the CDM. Even with the same small time step as others, the number of iterations with CDM is largely lower than others', seeing the last two columns. The running time with Van Leer is at least double that with CDM. The running time of the most popular Donor Acceptor method in the casting domain (present study) is almost four times than that with CDM when the same time step is used, or up to eight times faster when different time steps are used.

Table 6.2: Comparisons of the efficiency of CDM with others numerical methods

Method	$\Delta t_1=0.1s$		$\Delta t_1=0.05s$		$\Delta t_1=0.01s$	
	$N$	$t(s)$	$N$	$t(s)$	$N$	$t(s)$
Van Leer	error		Breaking CFL		Approx.10	47
Donor Acceptor	error		Breaking CFL		Approx.40	132
Level set	error		Breaking CFL		Approx.20	121
Counter Diffusion	Approx. 20	16	Approx.15	17	Approx.5	34

Note:  $\Delta t$ , Time\_step;

$t$ , Running time;

$N$ , the number of iteration per time step

For one small geometric model, this advantage is not so obvious. However for 3D casting simulations, the benefits of CDM are huge in saving computational cost since the geometric model could reach tens and even hundreds of thousands of cells. With such a geometric model, the simulation normally lasts days, but with CDM, it can be performed in hours.

To summarize, the comparisons of the numerical results for the collapsing water column with the experimental data obtained by Martin & Moyce have been presented. It was

found that simulation results using the recently developed CDM are in good agreement with experimental data. Besides validating CDM, the comparisons of the Counter Diffusion Method (CDM) with the other three numerical methods, Van Leer, Donor Acceptor, LSM, have been done. CDM effectively counters the numerical diffusions of the free surface. One more advantage of CDM is that this method greatly economizes the computational time, computational cost. This advantage is significant for computational fluid flow field, particular when the geometry is complex and massive amount of meshes are generated.

### **6.5 Application of the Counter Diffusion Method (CDM)**

The ultimate target of this study is to develop the tilt casting method to correctly predict a TiAl turbine blade length of 400mm.

#### **6.5.1 Geometry and Computational Mesh**

Figure 6.10 shows the real shape of the turbine blade which is twisted along its spin and up to 400mm long from the bottom of the root to the tip of the shroud. This is a generic design for use in IMPRESS. The intricate shape of the blade brought difficulties of generating computational mesh using the existing mesh generation tools. Figure 6.11 illustrates the mesh generated by [Harpoon]. The problem is caused by the twist of the blade in the blade edges where the cells are irregularly distorted along the edge. The distorted cells are highly non-orthogonal leading to the numerical instability when running in PHYSICA.



Figure 6.10: Real shape of 400mm long turbine blade.



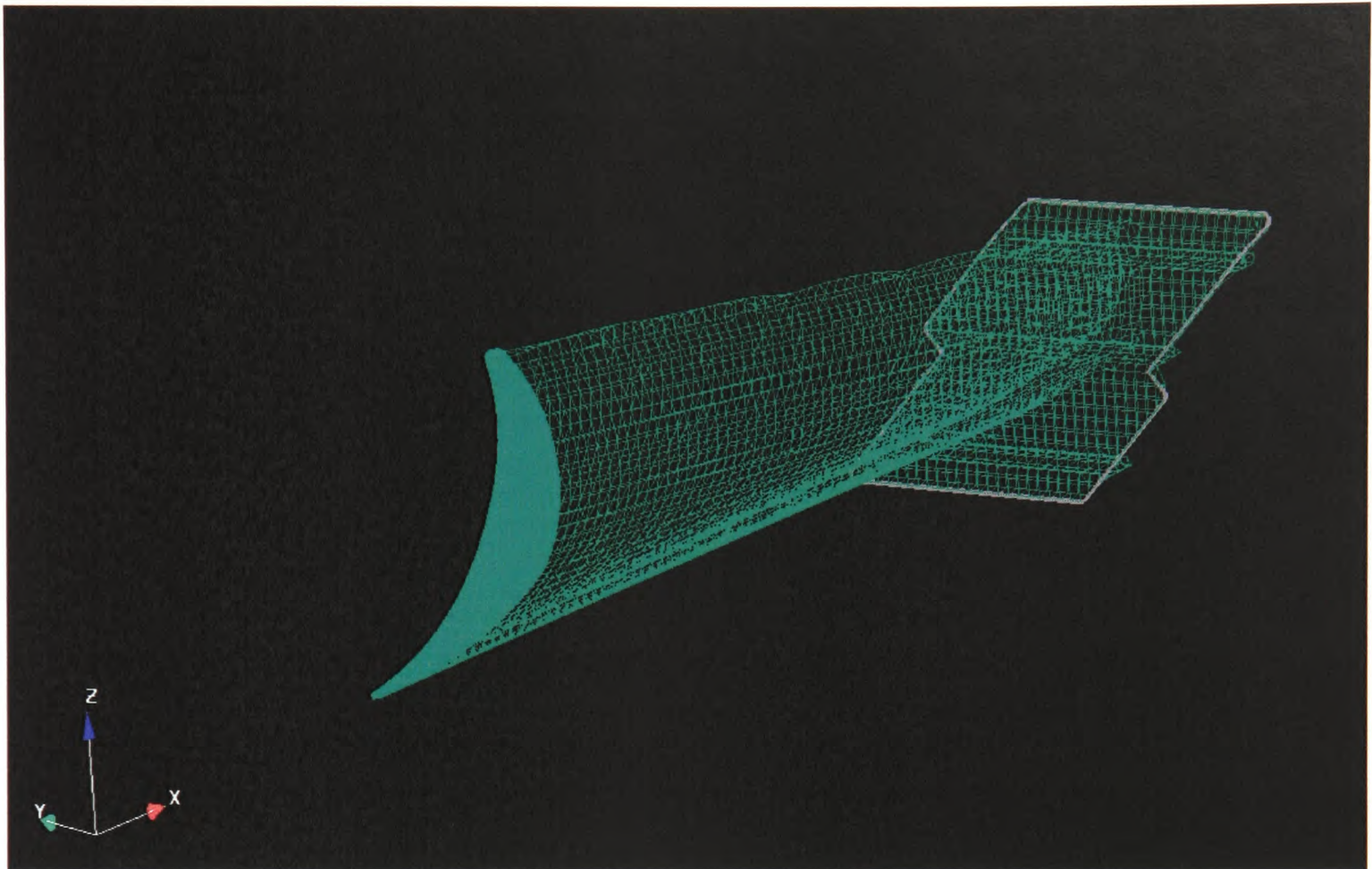


Figure 6.11: Computational mesh of real shape turbine blade in Harpoon.

Regarding to the above problems with the computational mesh, some approximations are made for the long twisted blade. The CAD package [Rhino] is used to build a 400mm long straight blade which is made based on one profile of the twisted blade extruded to 40cm; the root and the far end of the blade are approximated by simple rectangular plates, demonstrated in Figure 6.12. This blade is similar to that real blade but without a spanwise twist. Figure 6.13 shows the mesh for the straight blade, a clear, quite regular mesh.

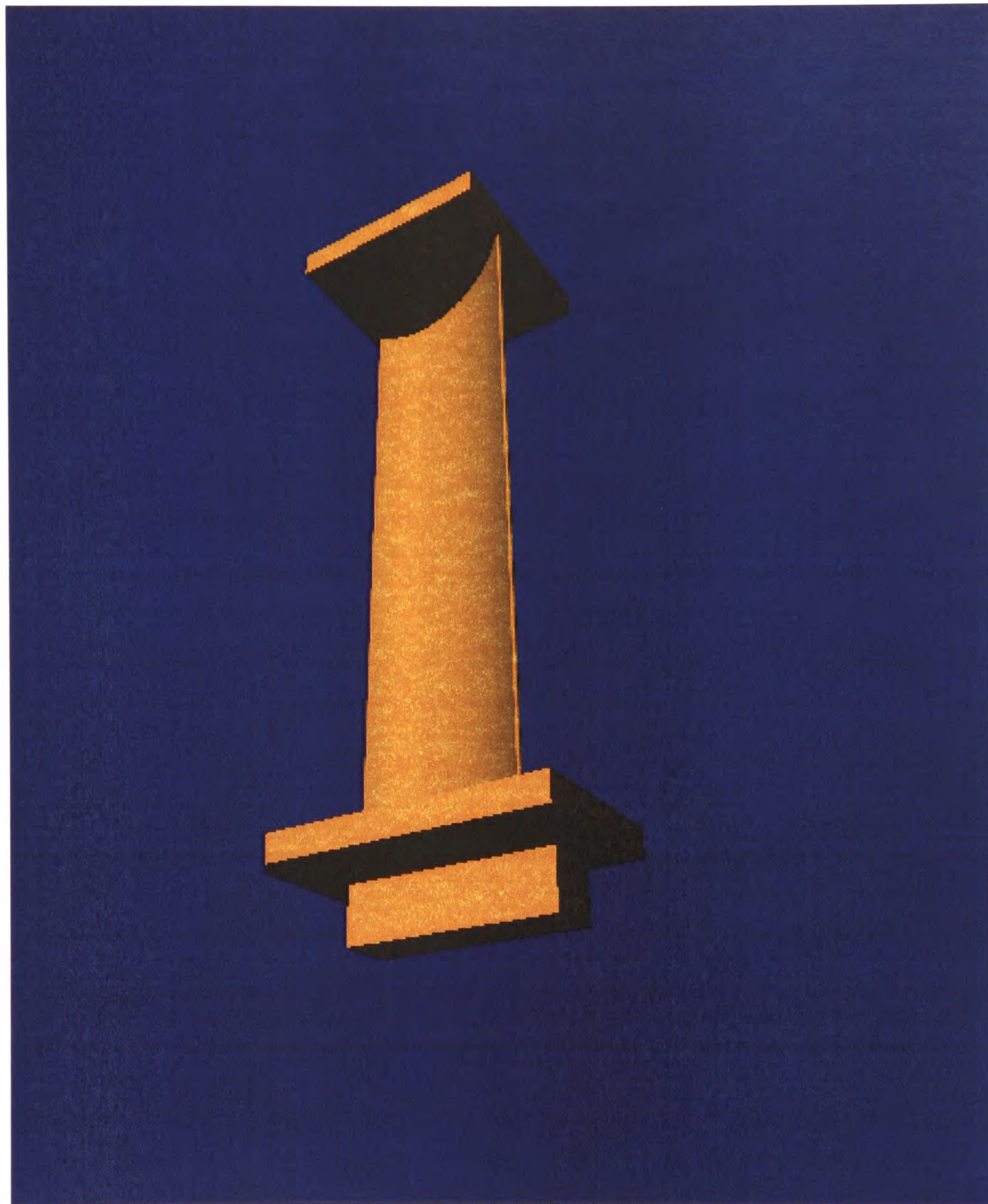


Figure 6.12: Approximated straight turbine blade.



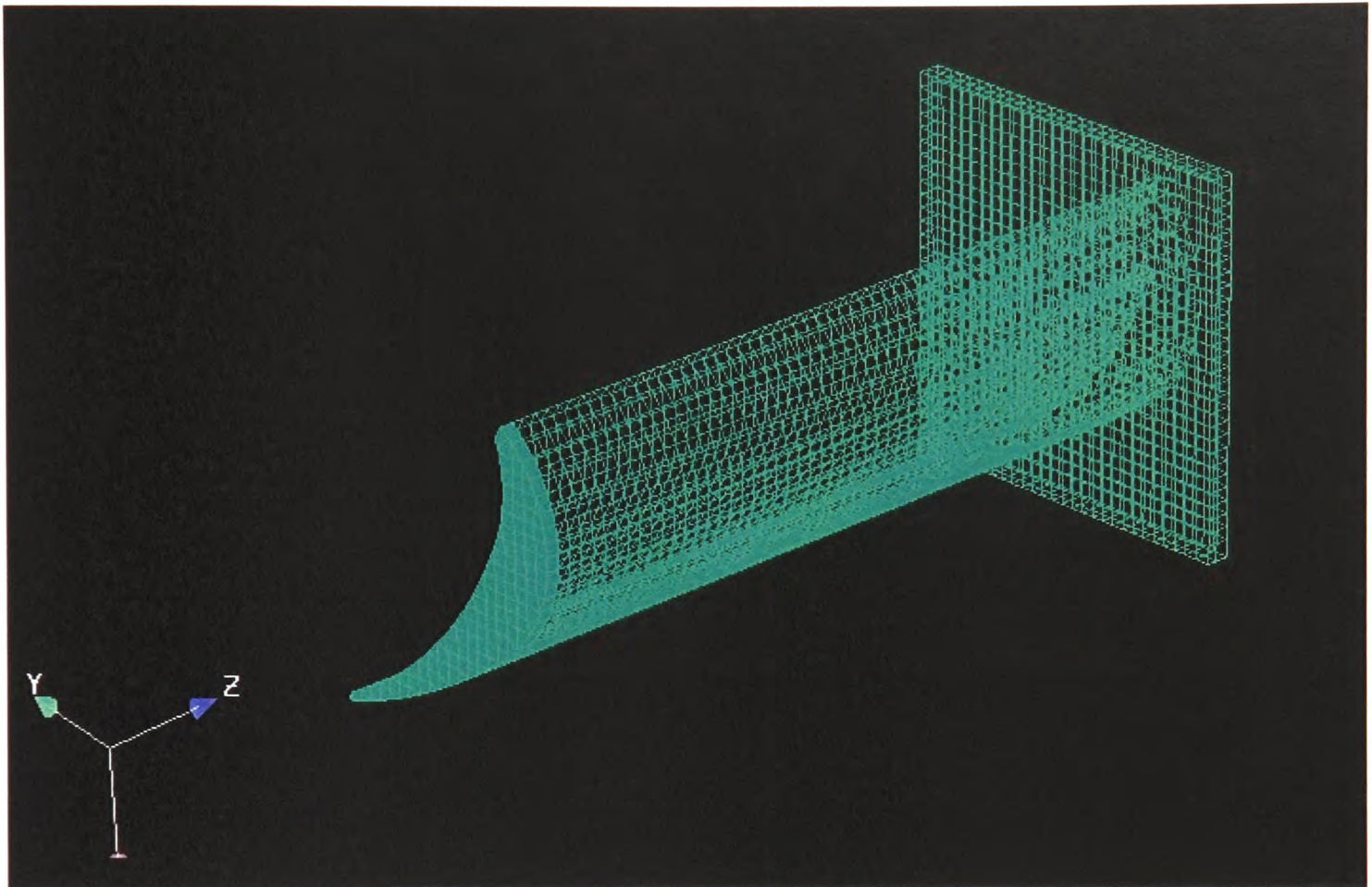


Figure 6.13: Sectioned view of the computational mesh of the approximated straight turbine blade length of 400mm in Harpoon.

The location of the blade root on the pouring basin affects the flow during filling. Two of the designs used are seen in Figure 6.14. In the first the blade root is placed perpendicular to the tilt plane and located to maintain full contact with basin; the other has the blade root perpendicular to the tilt plane and as far to right as possible, near the edge of the pouring basin. Furthermore, it is seen that the trailing edge (thinner edge) is lower than the leading edge when they are rotated to the horizontal position. That is to make the trailing edge fill first when the metal reaches in the blade to prevent premature freezing.

## Chapter 6. The Counter Diffusion Method

The complete model is composed of blade, pouring basin and crucible. In this model, a total of 78495 cells were generated. The two final meshes of the model are shown in Figure 6.15 and Figure 6.16.

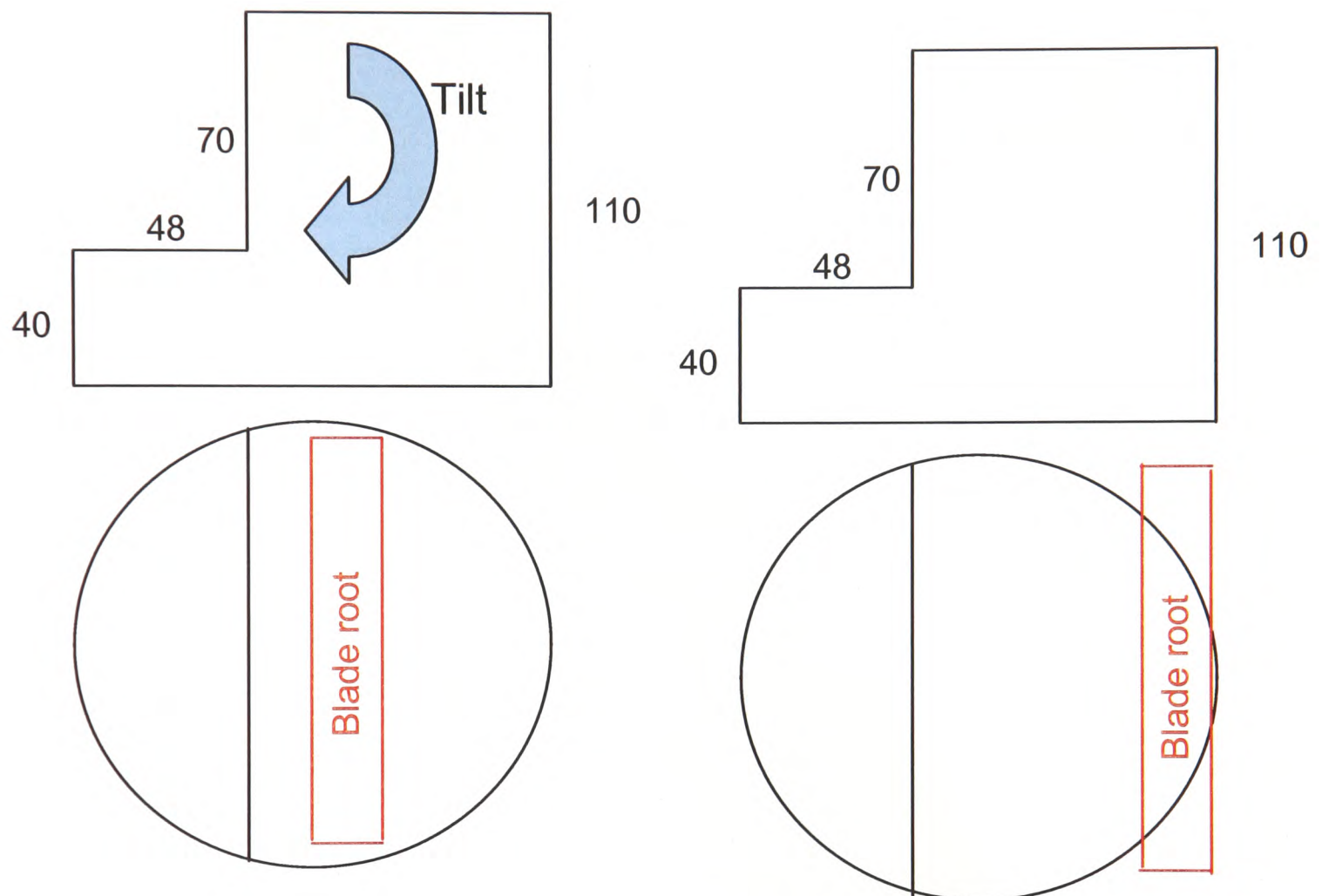


Figure 6.14: Locations: 1) Blade root perpendicular to tilt plane and located to maintain full contact with basin and; 2) Blade root perpendicular to tilt plane and as far to right as possible.

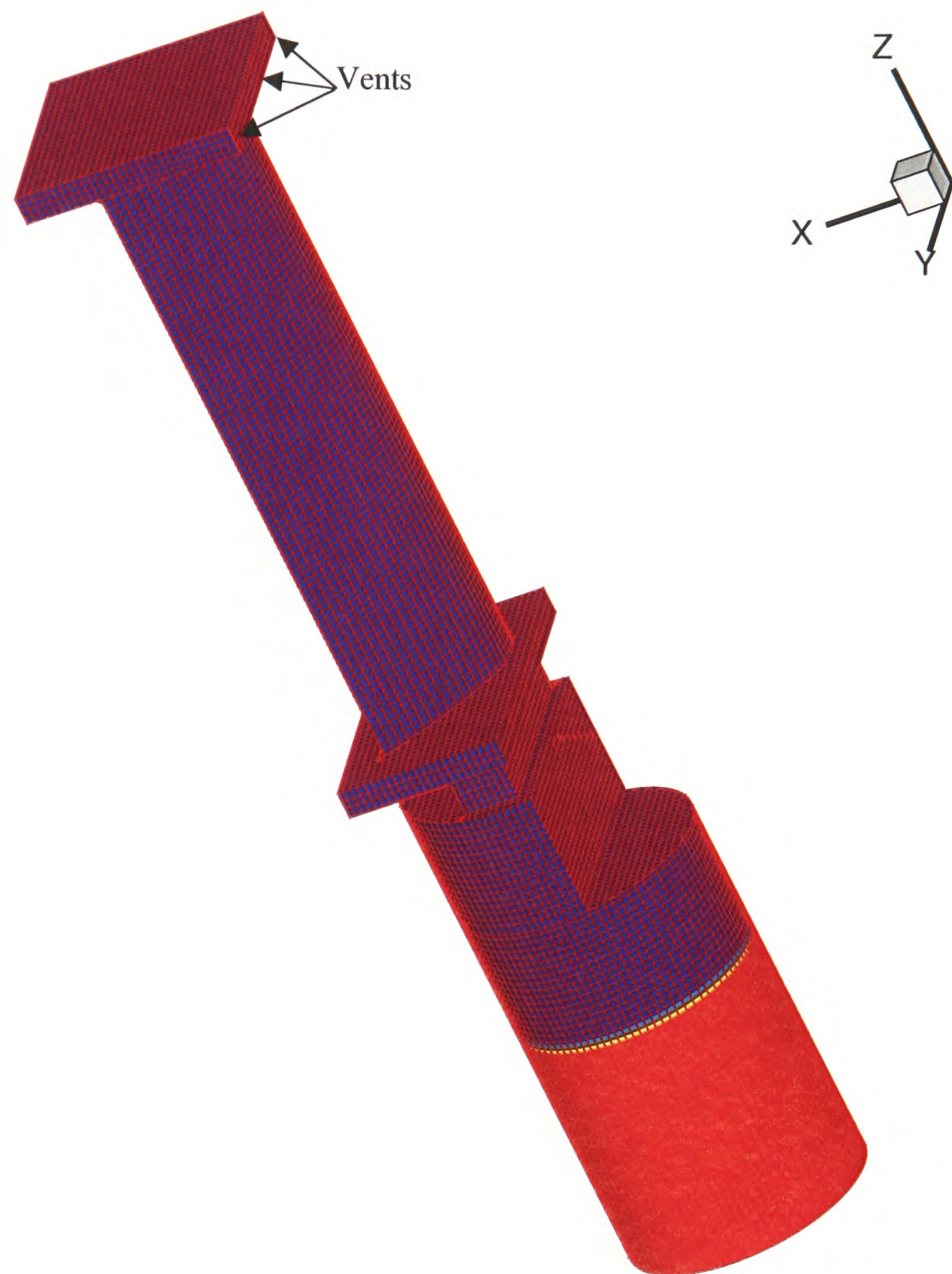


Figure 6.15: Computational mesh: blade located in the middle of pouring basin



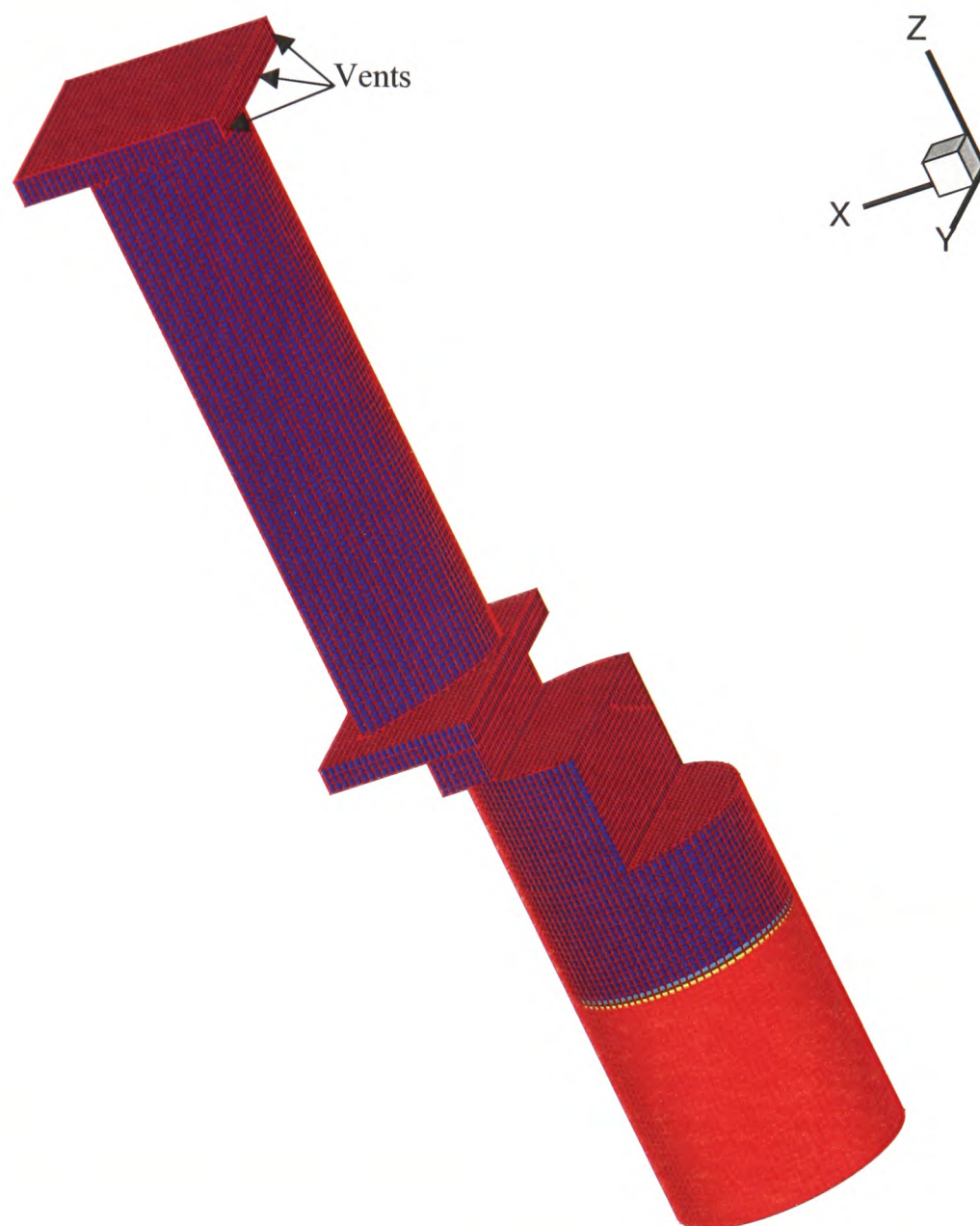


Figure 6.16: Computational mesh: blade located at the edge of the pouring basin



### 6.5.2 Boundary and Initial Conditions

Table 6.3 lists the initial conditions for the following simulations. There is assumed to be no slip on all the walls. The free surface module, Fluid flow module, Heat transfer module and Solidification module were switched on. The 3D/1D coupled transient heat transfer model is applied to compute the thermal boundary instead of using the empirical heat transfer coefficient used in the previous Chapter. The effect of the radiation is not included.

Table 6.3: The initial conditions of the numerical model

Mould preheated temperature, °C	1200
Initial temperature of molten metal , °C	1600
Melt weight, g	4500
Programmed cycle, s	Cycle 2 (see Table 5.7)
Superheat, °C	50

Three vents are made at the far end of the blade the feature that is the last to fill during tilting, as indicated by the arrows in Figures 6.15 and 6.16.

### 6.5.3 Presentations of Results

#### 6.5.3.1 Effect of the Locations of the Blade

Figures 6.17 and 6.18 show the mould filling with the two ingate locations at 2.7s and 3.2s. It is seen that the filling is faster for the blade located at the edge of the pouring basin than that placed in the middle. The trailing edge is first filled for both the two locations, the metal pouring to the side of the trailing edge. However, the metal tends to run in the centre of the blade rather than fill in the edge first as illustrated in Figures 6.19-6.22, which show the temperature (TN) and the volume fraction of metal (FS\_PHI) of the cross-section of the blade at the various heights from the root. They show the metal is flowing to the two edges once it enters the mould. However, the edges are hard to fully fill.

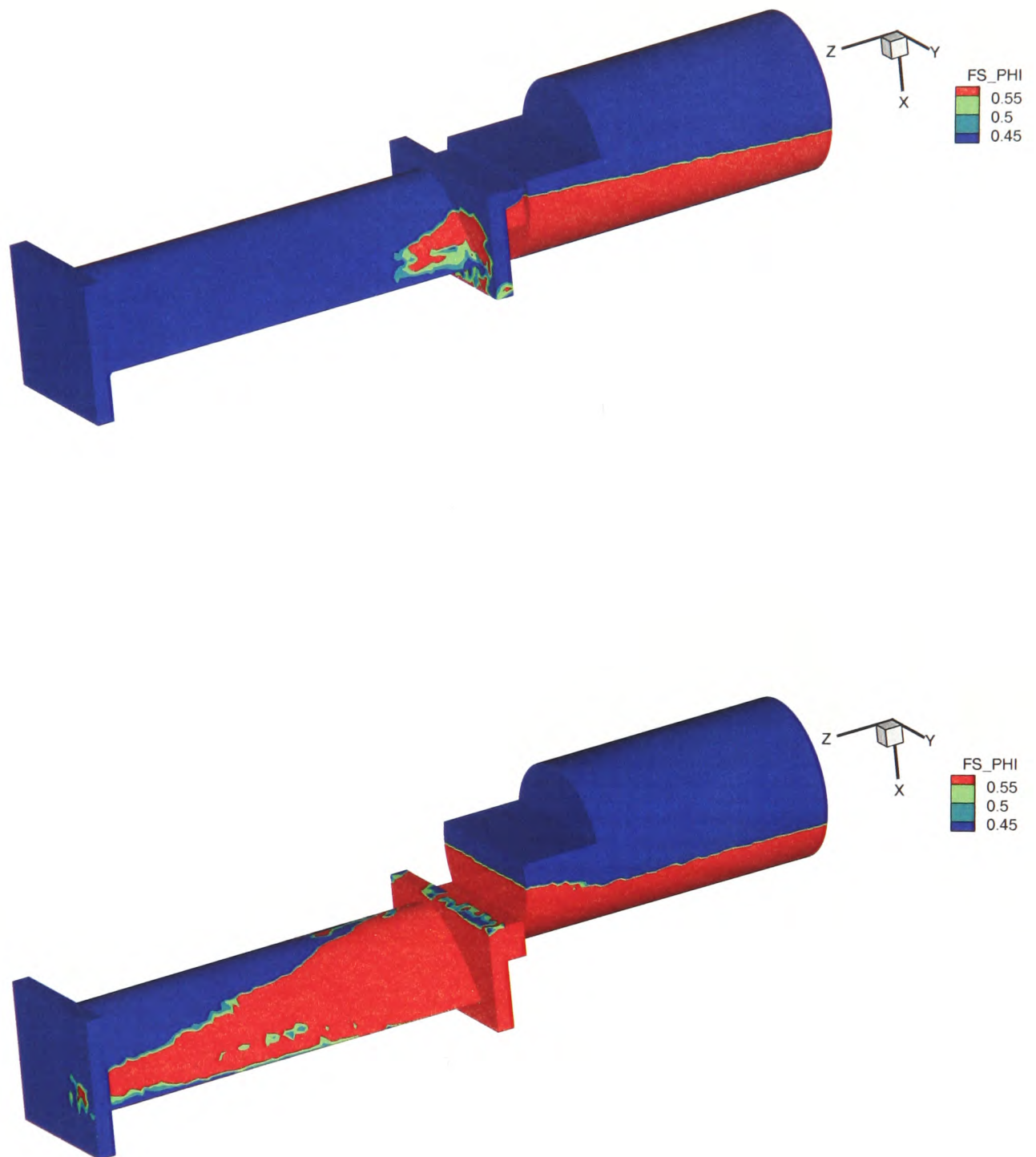


Figure 6.17: Comparisons of the volume fraction of metal ( $\Phi$ ) at 2.7 s for the two alternative blade ingate locations.

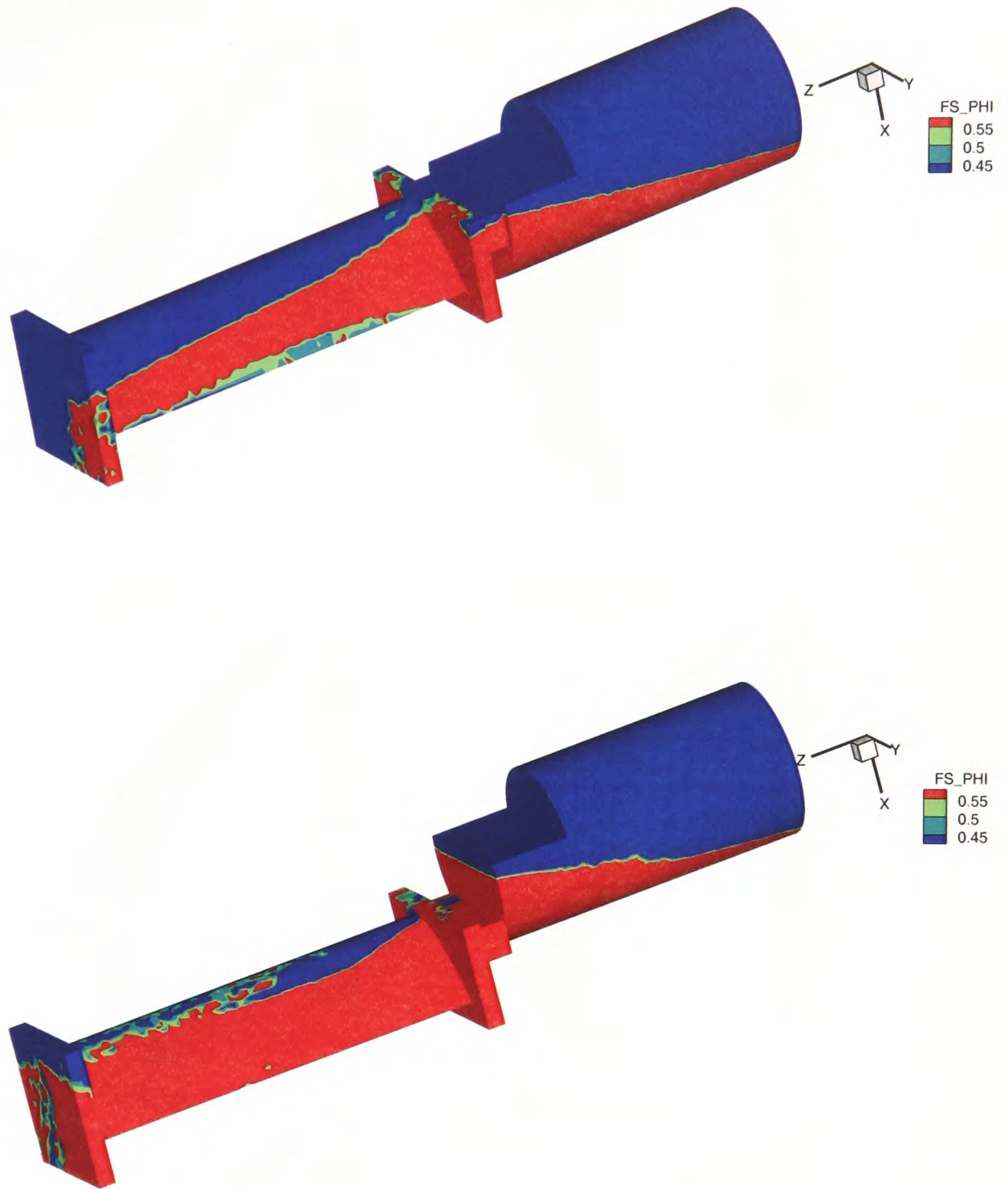


Figure 6.18: Comparisons of the volume fraction of metal ( $\Phi$ ) at 3.2s for the two alternative blade ingate locations.

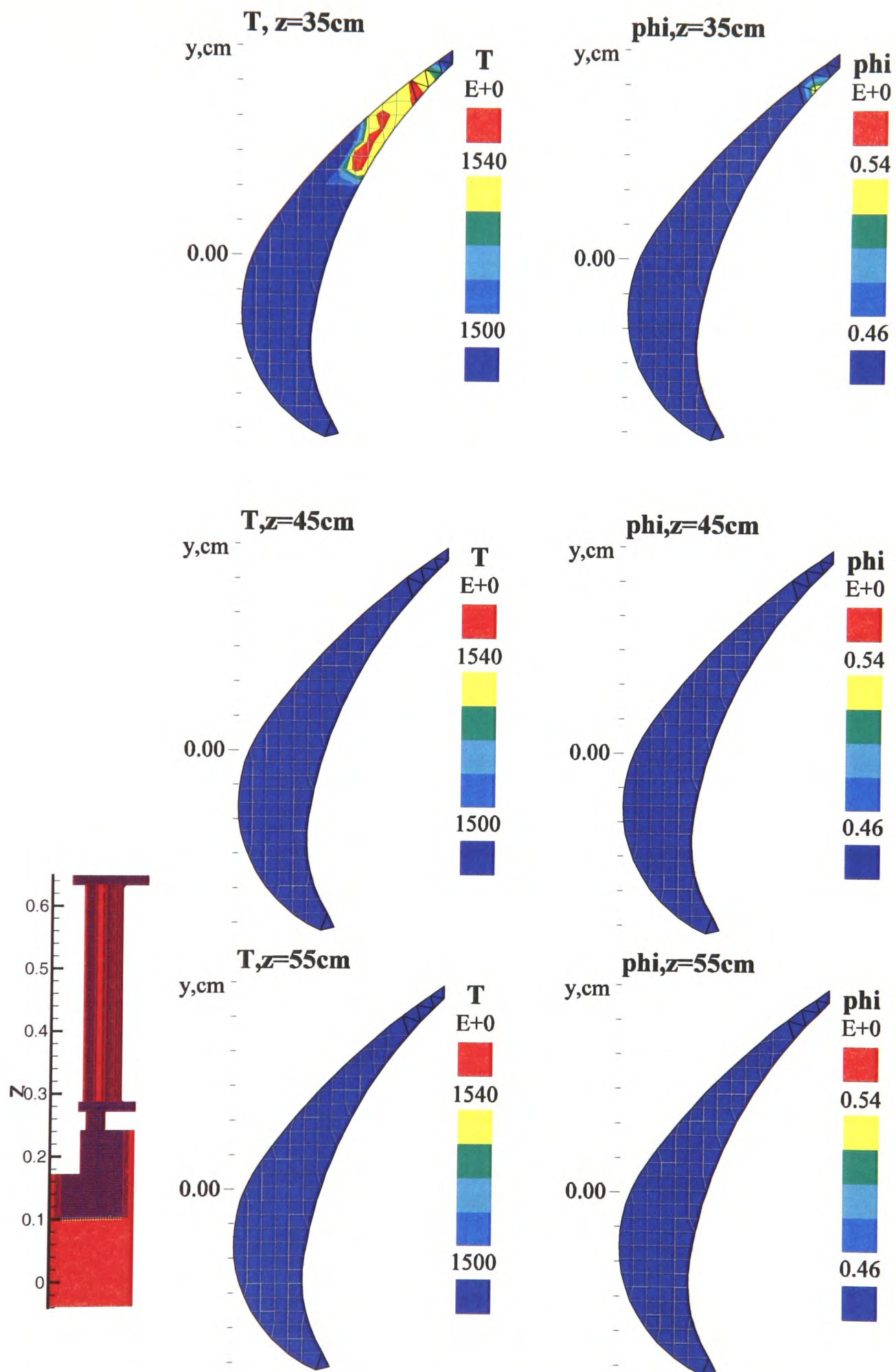


Figure 6.19: Comparisons of cross-section of the blade at the height 35, 45 and 55cm in volume fraction of metal (Phi) and in temperature at 2.7s for ingate location 1.



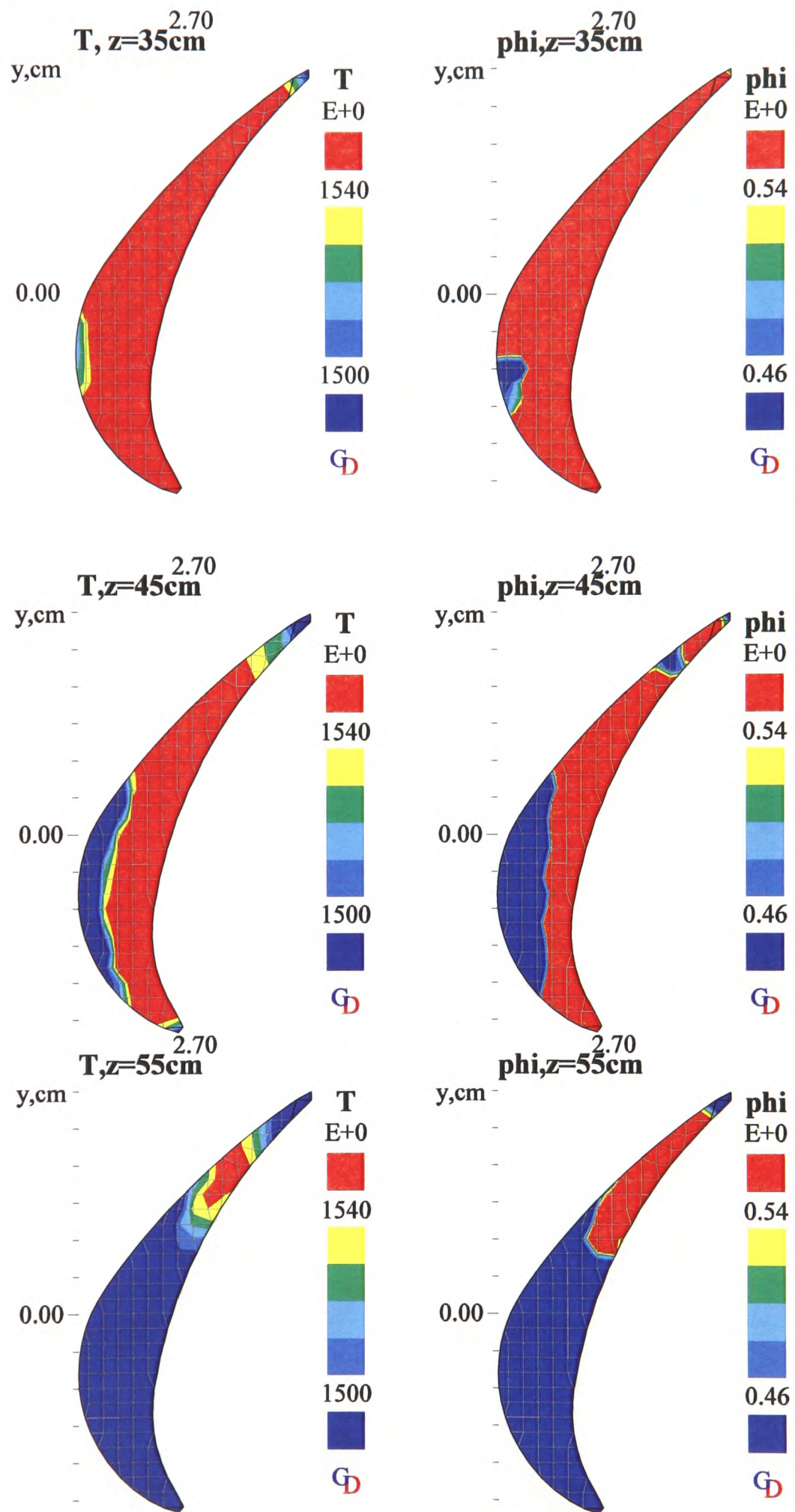


Figure 6.20: Comparisons of cross-section of the blade at the height 35, 45 and 55cm in volume fraction of metal ( $\Phi$ ) and in temperature at 2.7s for ingate location 2.

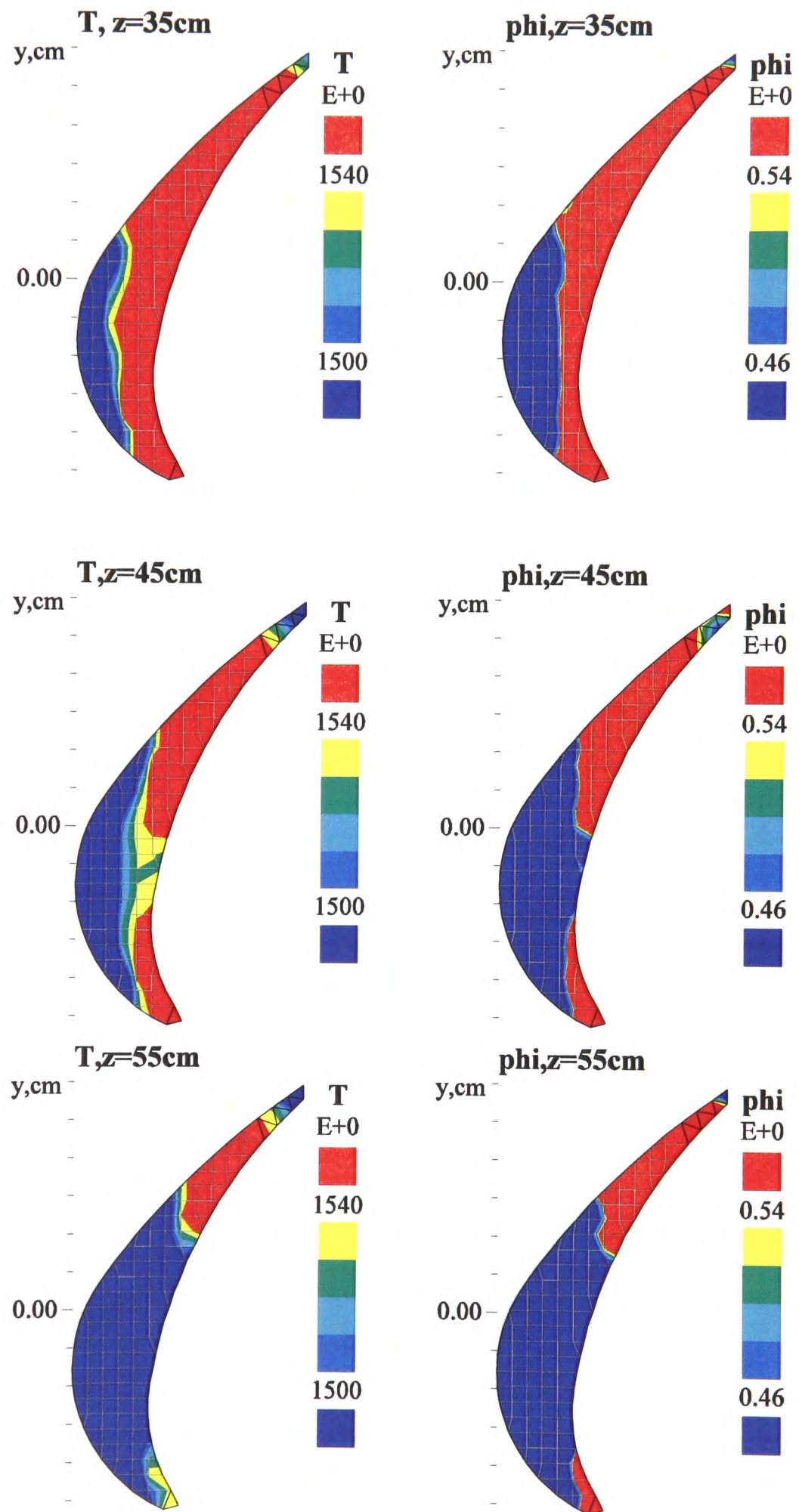


Figure 6.21: Comparisons of cross-section of the blade at the height 35, 45 and 55cm in volume fraction of metal (Phi) and in temperature at 3.2s for ingate location 1.



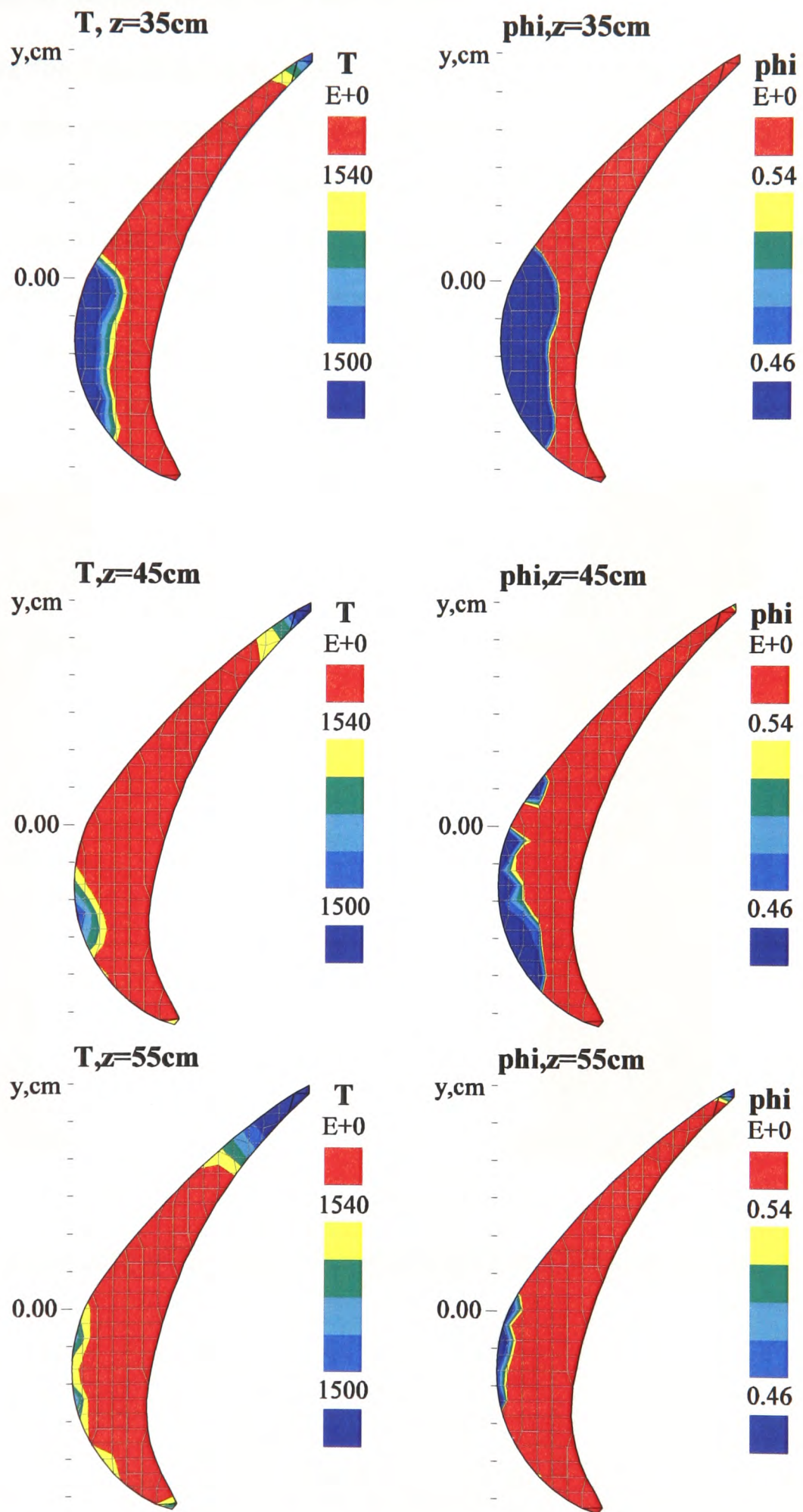


Figure 6.22: Comparisons of cross-section of the blade at the height 35, 45 and 55cm in volume fraction of metal (Phi) and in temperature at 3.2s for ingate location 2.

### 6.5.3.2 Predictions of Defects at the End of Filling

Figure 6.23 shows the liquid fraction (LFN) at 5.5 s and 6.0 s (the end of filling). The plots demonstrate that solidification already occurs along the trailing edge and the far end of the leading edge before finishing the mould filling. That could lead to the casting defects, or mis-runs. Figure 6.24 presents the volume fraction ( $\Phi$ ) at the end of filling. The lower value of  $\Phi$  in the highlights means there is a high risk of gas entrapment. One vent located at the far shroud is not sufficient and more vents are needed at both shrouds to minimize the possibility of trapped gas.

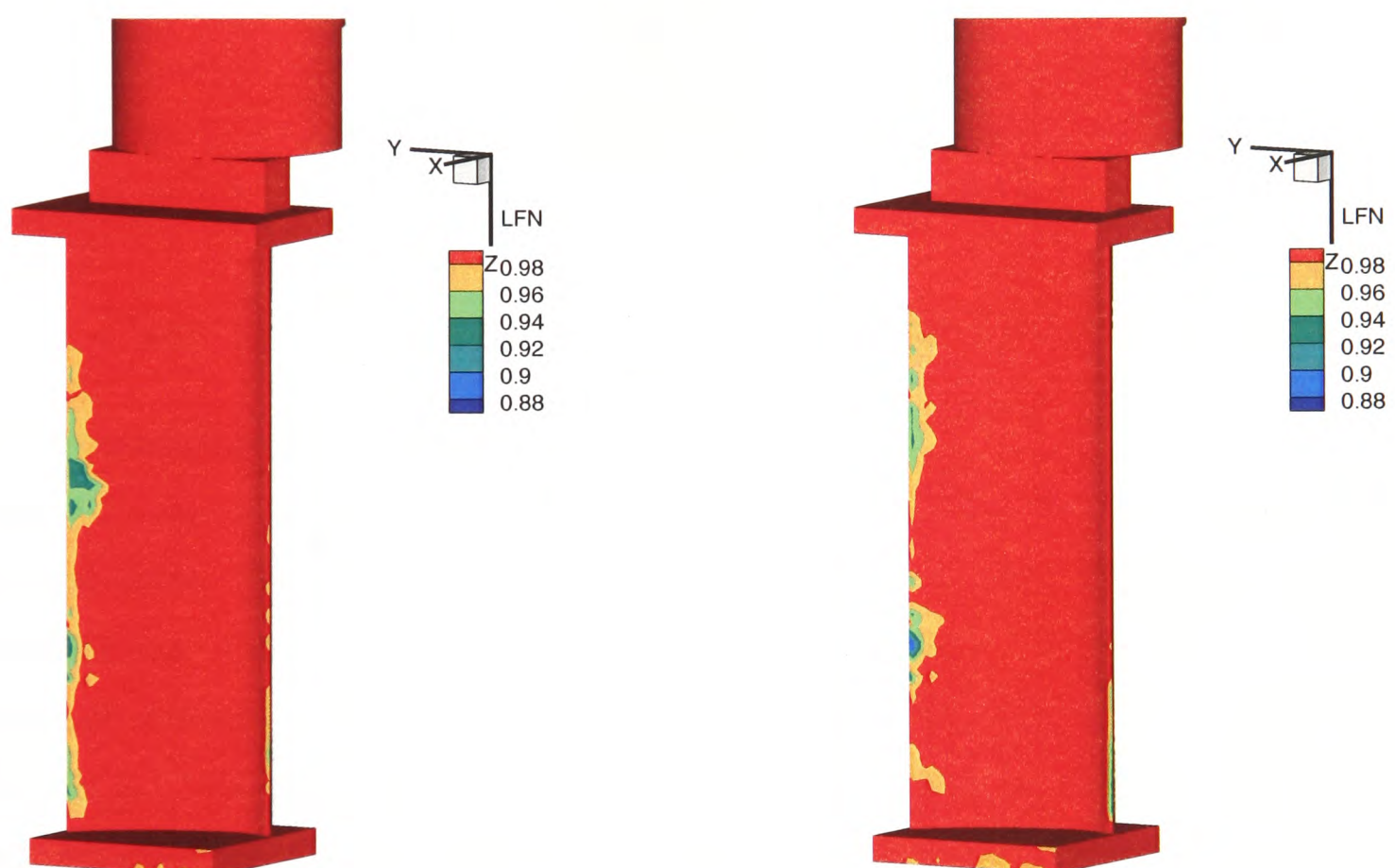


Figure 6.23: Comparisons of the liquid fraction (LFN) at 5.5 and 6s for ingate location 2.



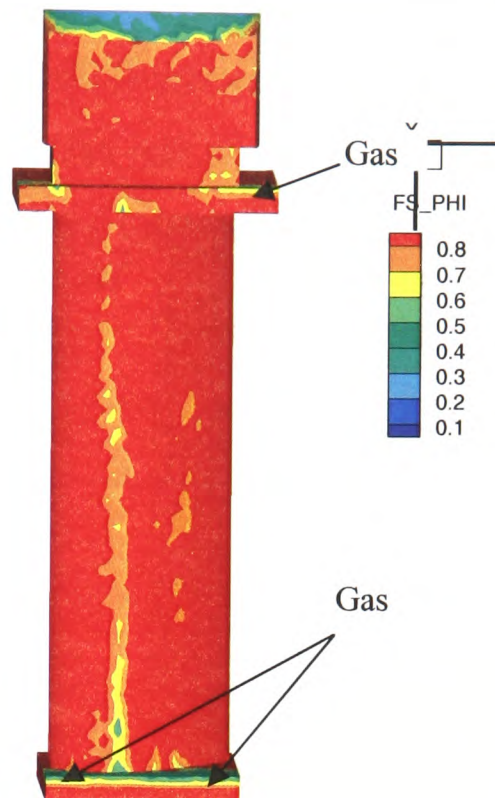


Figure 6.24: The volume fraction of metal ( $\Phi$ ) at 6s for ingate location 2.

### 6.5.3.3 Comparison of Two Methods: Van Leer and CDM

Figure 6.25 shows the comparison of the volume fraction of metal in two methods, Van Leer and CDM. The two methods present quite similar plots under the same scale. The only difference is that the interface in Van Leer is smoother than in CDM because of the numerical diffusion with the Van Leer method. Some fluctuation at the interface is emergent in CDM. That is because the characteristics of the different method: Van Leer is stable but smearing interface; CDM has no numerical diffusion but cell-by-cell corrections tend to amplify fluctuations. Further development is required to minimize these fluctuations.

In Table 6.4 the computational time using the two methods is compared. A larger `time_step` is employed in CDM than in Van Leer and Donor Acceptor. About 19 hours were used to complete the simulations. Comparing with CDM, Van Leer is numerically stable, but much more time was consumed to finish the calculations, up to 131 hours, around 7.5 times more than with CDM. The Donor Acceptor Method was finally not able

## Chapter 6. The Counter Diffusion Method

to be used in this simulation to carry on the simulation due to the numerical instability. That is the reason that CDM is developed. When a massive amount of cells are included in the geometry, the advantage of it is evident, less time-consuming.

Table 6.4: Comparison of computational time in Van Leer, Donor Acceptor and CDM

Method	Van Leer	Donor Acceptor	CDM
Computational time (h)	~131	diverge	~19
Time_step size (s)	0.001	0.001 or 0.0005	0.01

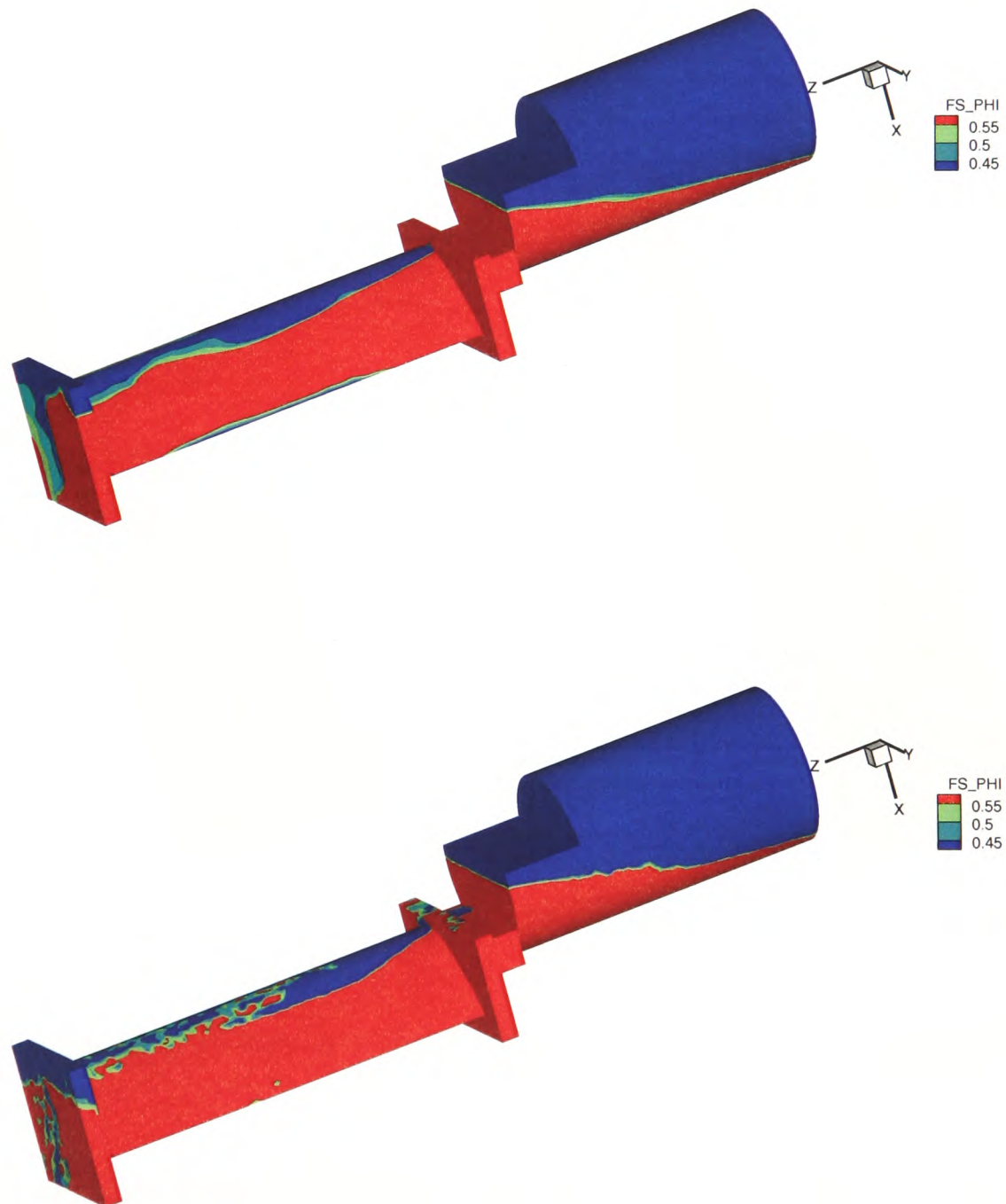


Figure 6.25: Comparisons of the volume fraction of metal ( $\Phi$ ) at 3.2s for the two methods: Van Leer and CDM.



#### 6.5.3.4 Comparison of the Mould Filling between Straight and Twisted Blades

Based on the computational mesh of the approximated straight blade, an approximate twisted blade is made by introducing a progressive twist from root to tip with the help of a FORTRAN code. The twisted blade is very close to the real shape of the turbine blade and is illustrated in Figure 6.26. The twist in the computational mesh has no effect on mesh skewness in this case.

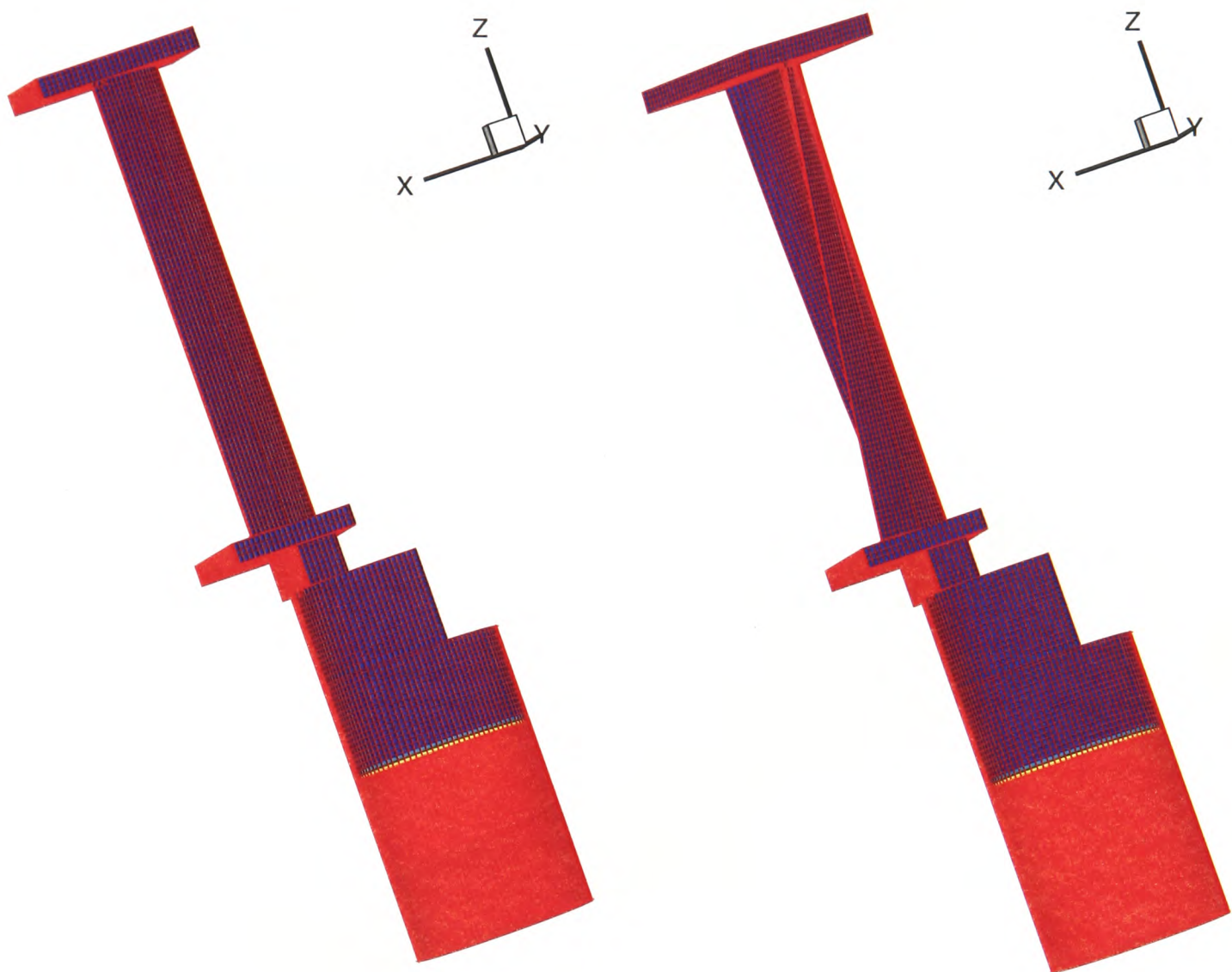


Figure 6.26: Comparisons of computational mesh between straight and twisted blades.

The same modelling modules were switched on as in the previous simulations for the straight blades. CDM was employed to track free surface in modelling the twisted blades. Figures 6.27 and 6.28 show a comparison of the mould filling between the straight and the twisted blade. No significant difference is present between the straight and the twisted

## Chapter 6. The Counter Diffusion Method

---

blades at 3.2s. At the end of the filling period, the gas is trapped in the same position. Appendix C shows a detailed filling sequence for the twisted blades.

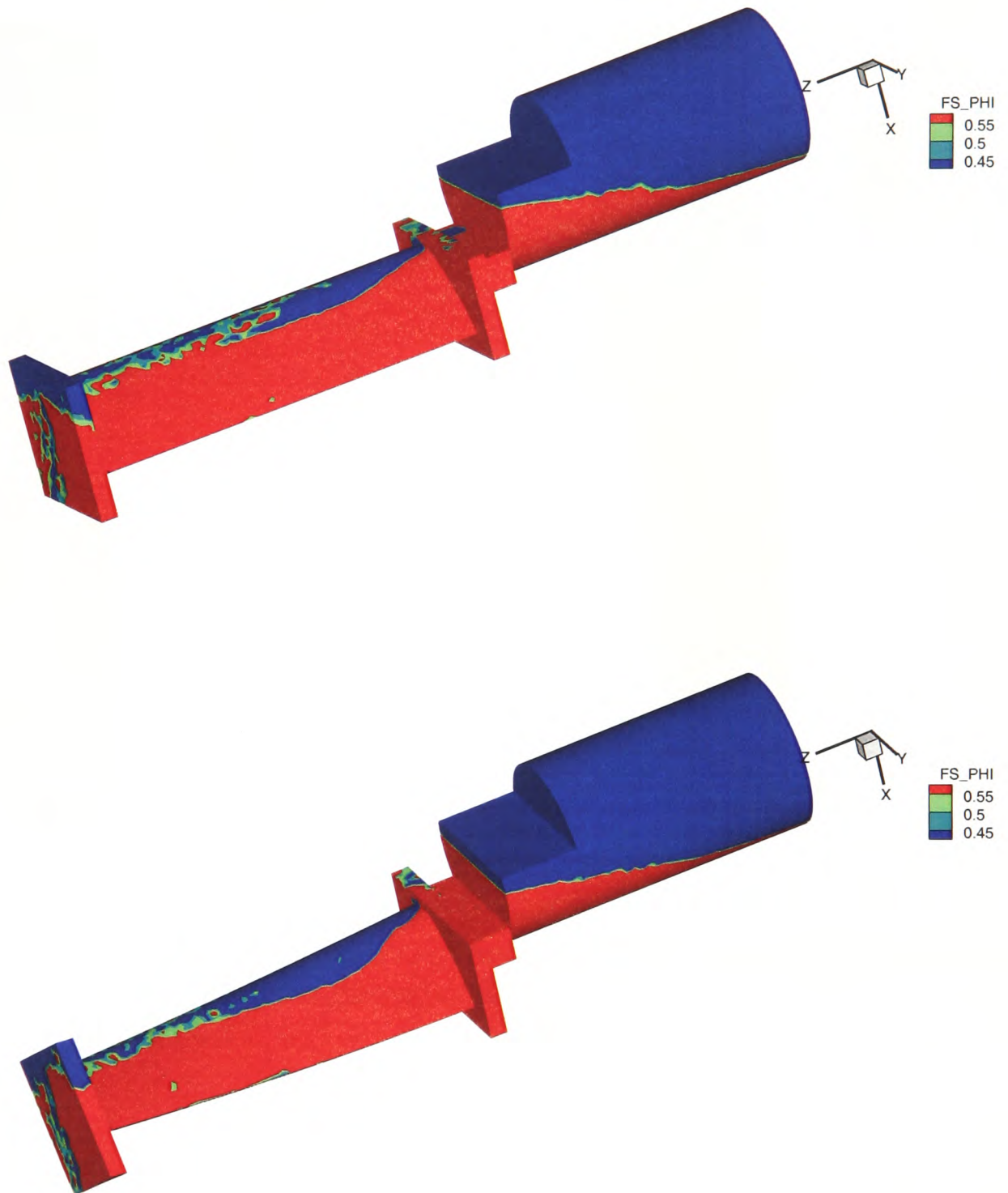


Figure 6.27: Comparisons of the volume fraction of metal ( $\Phi$ ) between straight and twisted blades at 3.2s.



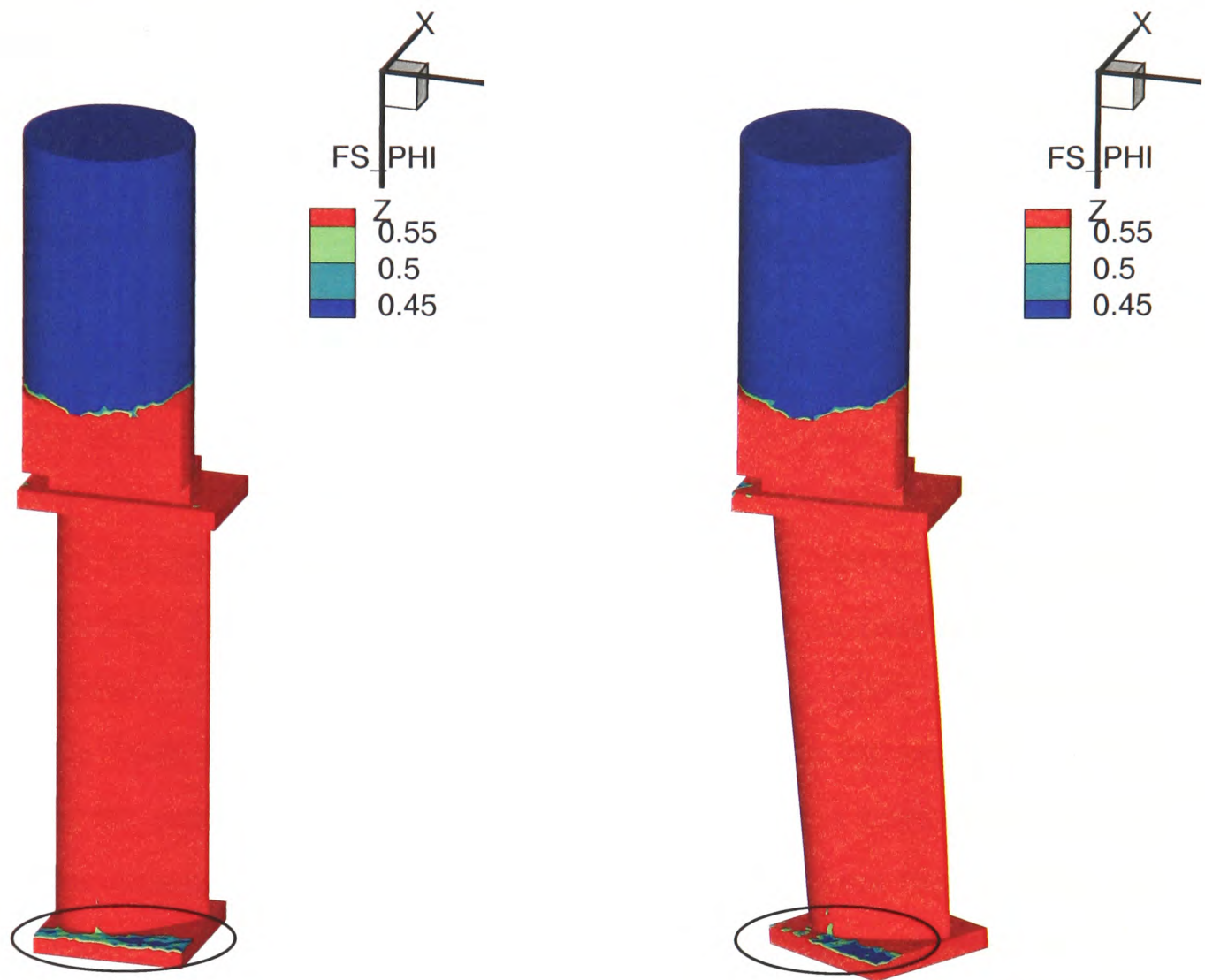


Figure 6.28: Comparisons of the volume fraction of metal ( $\Phi$ ) between straight and twisted blades at the end of filling.

## 6.6 Summary

A novel free surface tracking method, Counter Diffusion Method, has been developed to discretise the free surface equation in a fully implicit, fast, efficient way. CDM has been implemented in PHYSICA and is employed to combat the numerical diffusion.

The first part of this chapter has presented the validation of CDM against the classical collapsing column experimental data and against other numerical methods which are

## **Chapter 6. The Counter Diffusion Method**

---

generally used. A very good match is shown between numerical and experimental data. CDM has been compared with the other numerical methods, Van Leer, Donor Acceptor and Level Set Method. CDM effectively counters the numerical diffusions of the free surface. The interface tracked by using CDM is as sharp as Donor Acceptor method. CDM displays its advantage in saving computational time. All this provides the basis for the application modelled in the following part: a 40cm long turbine blade.

The second part has discussed the numerical results of the 40cm long straight turbine blade. Firstly, the effects of the position of the blade located in the pouring basin were discussed by comparing the modelling of two possible pouring basin designs. It was found that the position of the blade strongly affected the filling speed. The modelling results predict that the trailing edge and part of the leading edge may freeze prematurely in the long TiAl turbine blade. The discussion of the simulation results also gives a reference for the position of the vents located and it identifies that more vents are needed. In the following section, the comparisons of CDM with Van Leer show a huge difference in computational time although similar interface shapes result using these two methods. It was found that CDM has advantage in speeding up the simulation by a factor of 7.5. Finally, the modelling of a twisted blade (an approximation of the actual experimental blade) has been presented.

All these simulation results provide insight into the filling of a turbine blade which could be up to 40cm long. They have been used to support the experimental study.

## Chapter 7

# Solidification

This chapter presents the solidification process after a mould filling. Based on the 3D/1D Coupled Transient Heat Transfer model (see Chapter 5), a further development has been made to get accurate thermal boundary conditions and investigate solidification pattern during cooling. The gap formation is also studied, and the effects of heat conduction and radiation in the gap are included.

A twisted 40cm turbine blade is used to investigate solidification and gap formation. Two simulations are run: one with a gap and the other with no gap. Comparisons of temperature (TN) contours, liquid fraction (LFN) contours for the two cases have been made, and showed the effects of the gap on the solidification pattern. The changes of temperature in the last cell centre of the 3D domain and in the mould wall have been analysed for the two cases. The temperature of the interface between metal and mould, and of the external mould wall have been compared.

Finally, comparisons of liquid fraction contours, interface temperature and external mould wall temperature using variable gap sizes are given to show the effects of gap size.

## 7.1 Introduction

An accurate thermal boundary condition is essential to simulate the castings for TiAl for which a low superheat is available when using an ISM furnace to melt. In Chapter 5, the 3D/1D Coupled Transient Heat Transfer model was described for mould filling. However, in this model, a constant external mould wall temperature was assumed to simplify the model. This assumption has no significant effect on the accuracy of thermal boundary calculation because the mould filling has been completed within a few seconds for TiAl castings. But it is not applicable for the solidification after a filling. That is because the solidification process takes place in minutes rather than seconds. A more accurate thermal boundary condition is required to the external mould wall. Moreover, solidification is a very complex process which involves a gas gap formation, as it is discussed by John Campbell [Campbell -91] in his publications. Figure 7.1 shows variable gas gap in a shaped casting.

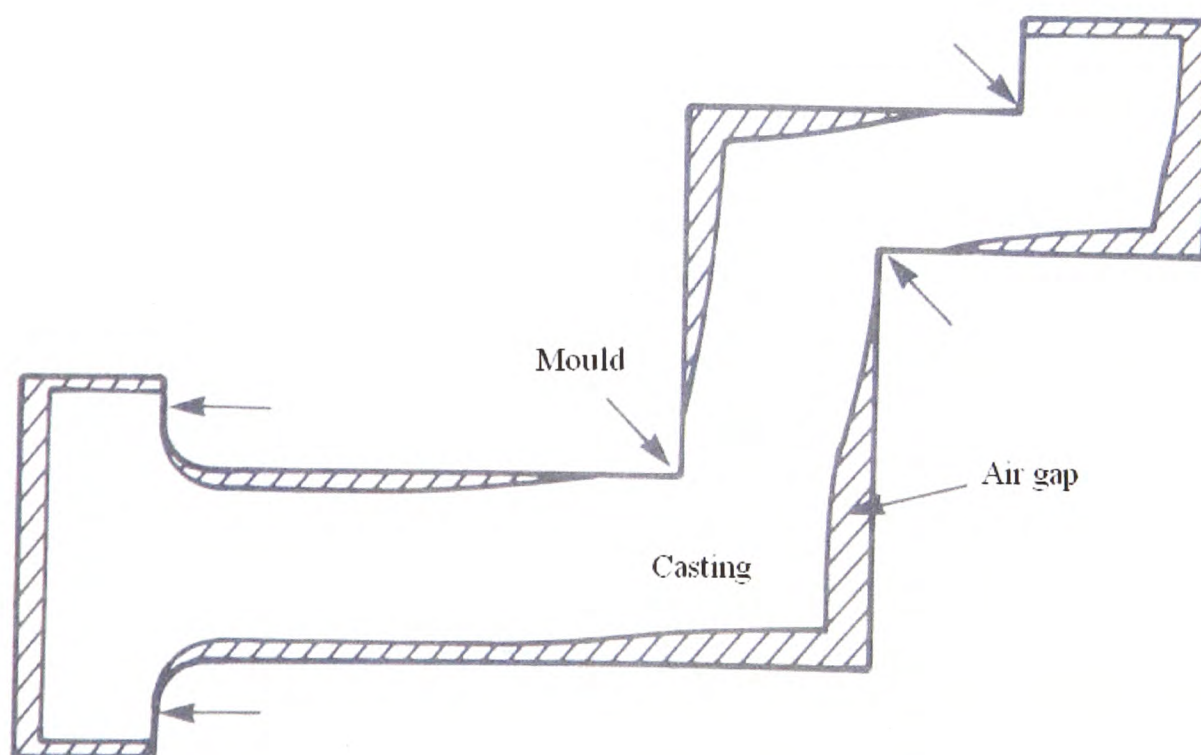


Figure 7.1: variable air gap in a casting (courtesy of John Campbell [Campbell -91]).

Obviously, anything in the way of a contraction will prevent the metal from moving in a particular direction and force the metal against the mould which leads to no gap formation. This happens in the corners at the ends of the straight sections.



It is extremely difficult to know when a gap starts to form and how the gap progresses, and to demonstrate the temperature change in the metal and the mould. The numerical model is used to simulate gap formation and the progress of the gap. So a further development of the 3D/1D scheme should be made to investigate the process.

## 7.2 Mathematical Description

Based on the 3D/1D model presented in Chapter 5, a radiation boundary condition is applied on the external wall of the mould and the heat transfer and radiation will be considered in the gas gap, the effect of convection in the gap is neglected since the casting is in partial vacuum.

### 7.2.1 Assumptions and Boundary Conditions

Since it is difficult to define the variable gap size, uniform gap size is assumed in this study. The formation of the gas gap is assumed to be once the metal temperature is lower than the freezing temperature which is taken by the average of liquidus and solidus. It is then assumed:

- The mould is free from the heat expansion;
- Gap is present when  $T_{3D} < T_{freezing}$ ;
- Gap size is uniform and estimated by referring to the castings by John Campbell [Campbell -91]:

$$d / D \approx \alpha_{metal} (T_{freezing} - T) + \alpha_m (T_m - T_o) \quad (7.1)$$

Where,  $d$  is the estimated size of the gap;  $\alpha_{metal}$ ,  $\alpha_m$  are the thermal expansion coefficients of the metal and the mould respectively;  $D$  is the diameter of the casting;  $T_{freezing}$  is the freezing point of the metal;  $T_m$  is the mould interface temperature;  $T_o$  is the original temperature of the mould;

In this study, on all the solid walls, no slip condition is valid and the radiation of the external wall of the mould is considered:

- On the solid walls,  $\underline{u} = 0$ ;

- A radiation boundary condition is applied on the external wall of the mould:

$$\lambda_{\text{mod}} \frac{T_n - T_{\text{out}}}{\Delta x_n} = \varepsilon_m \sigma (T_{\text{out}}^4 - T_{\infty}^4) \quad (7.2)$$

Where  $T_{\text{out}}$  is the outside temperature of the mould;  $T_{\infty}$  is the atmosphere temperature in the chamber, as shown in Figure 7.2;  $\varepsilon_m$  is the emissivity of the mould material;  $\lambda_{\text{mod}}$  is the thermal conductivity of the mould;  $\sigma$  is the *Stefan-Boltzmann constant* ( $\sigma = 5.67 \times 10^{-8} \text{ W / m}^2 \text{ K}^4$ ).

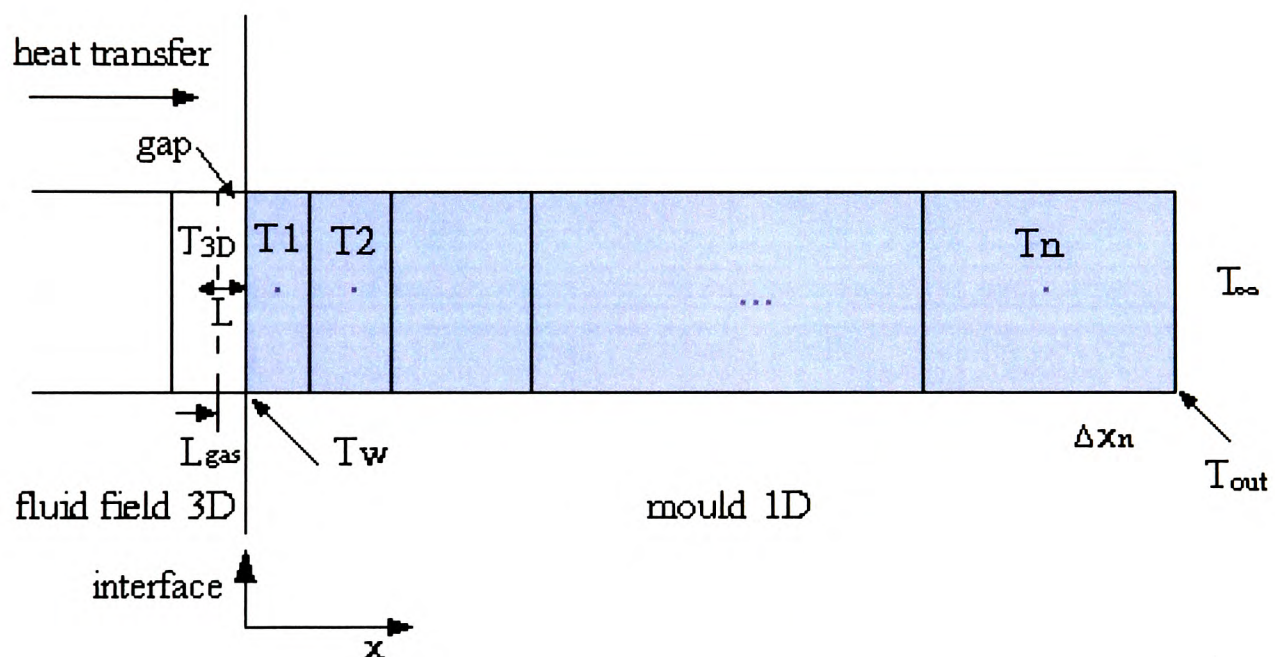


Figure 7.2: An air gap in a casting.

### 7.2.2 Coupling

Here, exactly the same method is employed as in Section 5.4 to couple the 1D model to the 3D model. The interface temperature  $T_w$  is calculated and then coupled back into 3D model. Because of the consideration of a gap formation between metal and mould, Equation (5.5) is rewritten into:

$$T_w = \frac{\frac{\lambda_{mix}}{\Delta x_{liq}} T_{3D} + \frac{\lambda_{mod}}{\Delta x_{mod}} T_1}{\frac{\lambda_{mix}}{\Delta x_{liq}} + \frac{\lambda_{mod}}{\Delta x_{mod}}} \quad (7.3)$$

Where  $T_{3D}$  is the temperature of the last cell centre of 3D domain to the mould;  $\Delta x_{liq} = L$  is the distance from the interface between metal and mould to the first cell centre of the mould;  $\Delta x_{mod}$  is the distance from the last cell centre to interface between metal and mould;  $\lambda_{mix}$  is the combination of the thermal conductivities of gas and liquid because of the present of the gas gap, they are given by:

$$\begin{aligned} \lambda_{mix} &= \lambda_{gas} && \text{if } L_{gas} \geq L \\ \lambda_{mix} &= \frac{1}{\frac{L_{gas}}{\lambda_{gas}} + \frac{L - L_{gas}}{\lambda_{liq}}} && \text{if } L_{gas} < L \\ \lambda_{mix} &= \lambda_{liq} && \text{if } L_{gas} = 0 \end{aligned} \quad (7.4)$$

Where  $L_{gas}$  is the gap size. The boundary temperature of the 1D model is coupled into the 3D model in the form of Equation (5.7):

$$\begin{aligned} q &= \lambda_{mix} \frac{T_{3D} - T_w}{\Delta x_{liq}} + \frac{\sigma(T_{3D}^4 - T_w^4)}{\left(\frac{1}{\varepsilon_l} + \frac{1}{\varepsilon_m} - 1\right)} \\ \Rightarrow q &= \left( \frac{\lambda_{mix}}{\Delta x_{liq}} + \frac{\sigma(T_{3D}^3 + T_{3D}^2 T_w + T_{3D} T_w^2 + T_w^3)}{\left(\frac{1}{\varepsilon_l} + \frac{1}{\varepsilon_m} - 1\right)} \right) (T_{3D} - T_w) \end{aligned} \quad (7.5)$$

Where  $q$  is heat flux per unit area;  $\varepsilon_l$  is the emissivity of the metal and  $\varepsilon_m$  is the mould material's.

$C$  and  $T_{ext}$  in Equation (5.7) are given by:

$$C = \left( \frac{\lambda_{mix}}{\Delta x_{liq}} + \frac{\sigma(T_{3D}^3 + T_{3D}^3 T_w + T_{3D} T_w^2 + T_w^3)}{\left(\frac{1}{\epsilon_l} + \frac{1}{\epsilon_m} - 1\right)} \right) \quad (7.6)$$

$T_{ext} = T_w$

## 7.4 Numerical Examples

### 7.4.1 Geometry and Computational mesh

The twisted turbine blade as described in Section 6.5.1 is employed as the test geometry, shown in Figure 7.3 (a). At the end of the mould filling, the blade is held vertically. As heat transfer takes place, a gap is formed between metal and mould once the metal temperature is lower than the freezing temperature, simply illustrated in Figure 7.3(b).

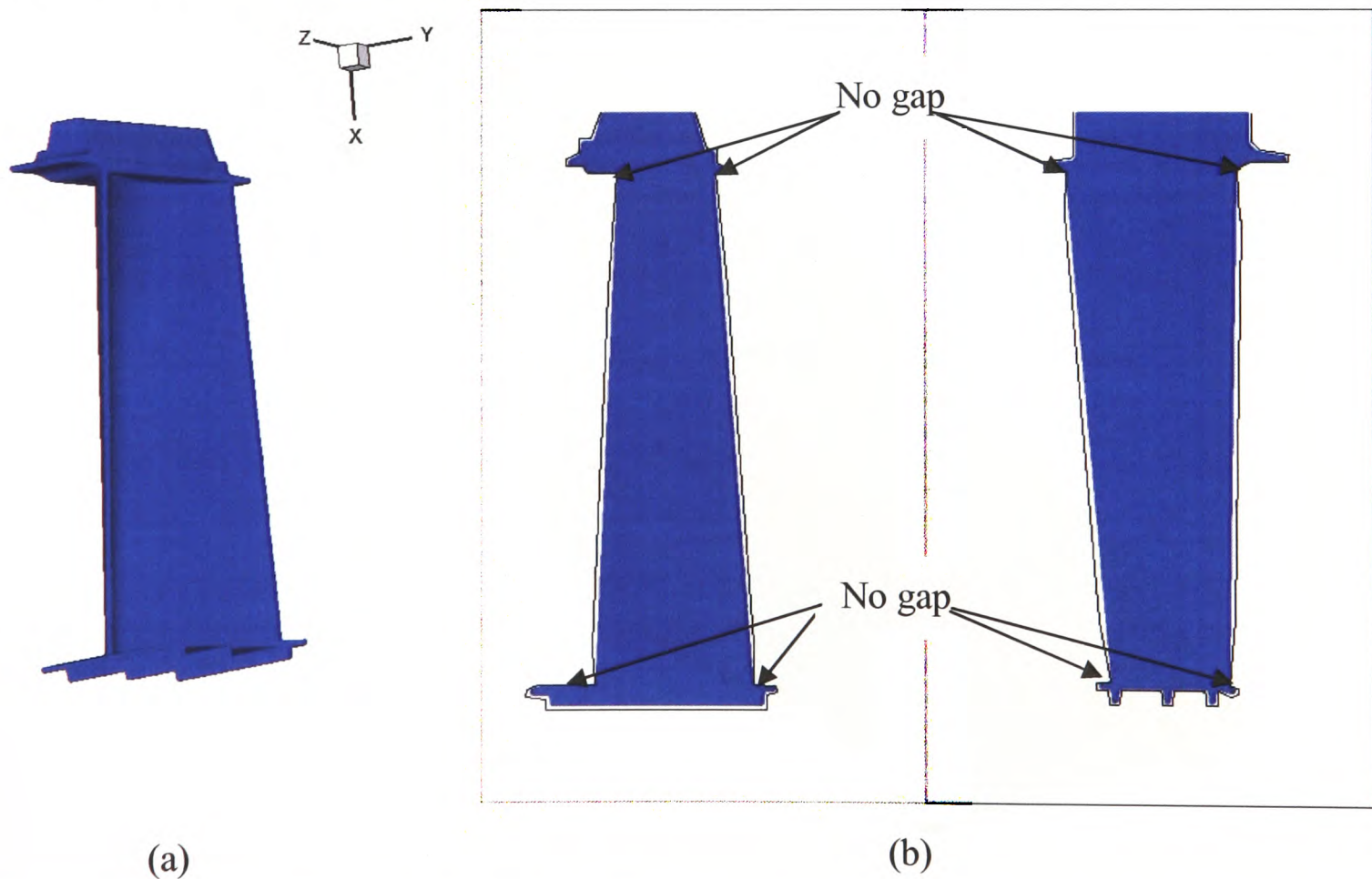


Figure 7.3: Geometry used in the simulations and possibly formed air gap in a casting.



## Chapter 7. Solidification

---

Arrows denote the probable locations of zero gaps. In the root of the blade, no gap occurs around the corners because of the effect of the gravity. In the shroud of the blade (the lower part), the contraction during cooling results in no gap when solidifying progresses. All the other surfaces of the blade are supposed to form a unique size gap which is estimated as Equation (7.1) by referring to the publications [Campbell -91].

Figure 7.4 illustrates the mesh generated by Harpoon for the twisted turbine blade. Since an extremely fine mesh is made, the effect of the twist of the blade in the blade edges is minimised. The geometry consists of only the blade, a total of 927973 elements included.

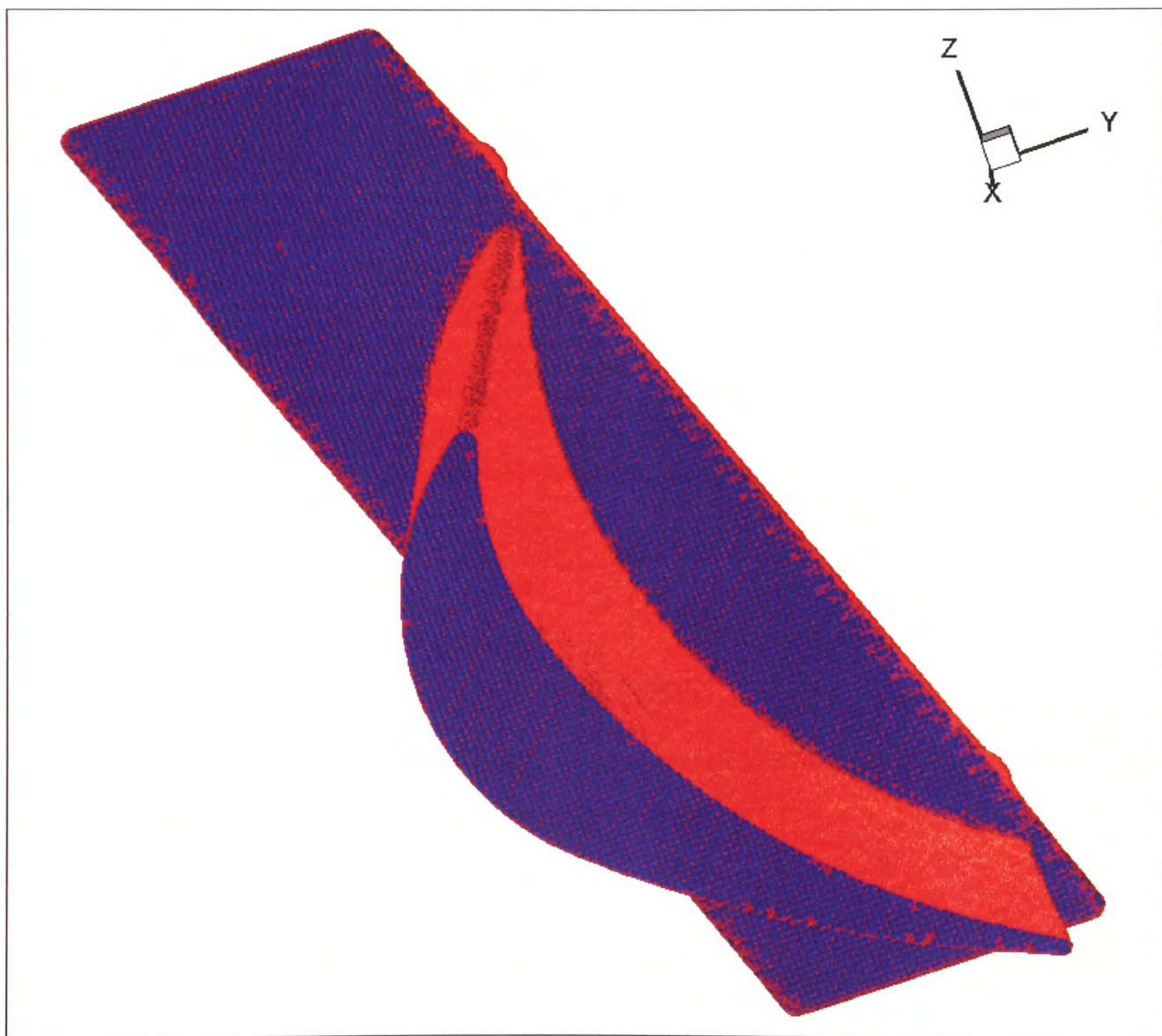


Figure 7.4: Computational mesh.

**7.4.2 Initial and Boundary Conditions**

The boundary and initial conditions for the simulations are respectively shown in Table 7.1 and Table 7.2. As it is shown, constant initial temperatures of metal and mould are assumed. A variable temperature obtained at the end of the filling is neglected due to the difficulties with mesh. Two PHYSICA modules are switched on in the simulations: Heat Transfer and Solidification modules.

Table 7.1: The boundary conditions of the numerical model

On external wall of the mould	Radiation boundary condition
At the end of blade root	a value (1200 W/m <sup>2</sup> K) of heat transfer coefficient

Table 7.2: The initial conditions of the numerical model

Mould preheated temperature, °C	1200.
Metal initial temperature, °C	1600.
Solidus temperature, °C	1500.
Atmosphere temperature, °C	0.
Superheat, °C	30.
Uniform gap size, mm	0.5 (estimated by Equation (7.1))

Two simulations are run: one with a gap (0.5mm) and the other with no gap. The difference (in INFORM text file) between the two simulations shown in the boundary conditions in the Heat Transfer Module is:

```
PATCH 1 USER_ROUTINE mould_heat1 11 .005 5 1. 1.0 1.6 2200. 1000. 1200.
0.0005 34001 1534.5
PATCH 1 USER_ROUTINE mould_heat1 11 .005 5 1. 1.0 1.6 2200. 1000. 1200.
0.000 34001 1534.5
```

The descriptions of the parameters in the 1D model are given in Table 7.3. The complete INFORM file for the simulation is seen in Appendix D.

Table 7.3: Description of the parameters in the 1D model

11	The number of parameters
0.005 m	The thickness of the mould
5	The number of cells on the mould wall
0.5 and 3.0	The factors are used to define the mesh, i.e. the mesh is uniform if 1. and 1.
1.6 W/(m·K)	Thermal conductivity of the mould material
2200 kg/m <sup>3</sup>	The density of the mould material
1000 J/(kg·K)	The specific heat of the mould material
1200 °C	The initial temperature of the mould
0.0005 mm	The gap size
34001	The label of reference element
1534.5 °C	The freezing temperature (when metal temperature is lower than this, a gap will form)

## 7.5 Results and Discussion

### 7.5.1 Effects of Gap

Figure 7.5 shows the comparisons of the temperature contours ‘TN’ of the blade between having a gap and no gap at 90s. Clearly, the blade temperature with no gas is falling very quickly. A gas gap is formed once metal temperature is lower than the freezing temperature. The gap acts as a thermal insulation layer and slows down the heat transferred from the metal domain.

Figures 7.6, 7.7 and 7.8 present the comparisons of the liquid fraction contours ‘LFN’ of the x-y, y-z cross sections of the blade between having a gap and no gap at 130s or 150s. Evidently, the liquid fraction with no gap is lower than that with a gap. The figures also

## Chapter 7. Solidification

---

show the part of the blade in the middle is cooling slower than the others across x-y, y-z sections and where it is the most possible to form 'hot spot' which could lead to a internal porosity of the castings.

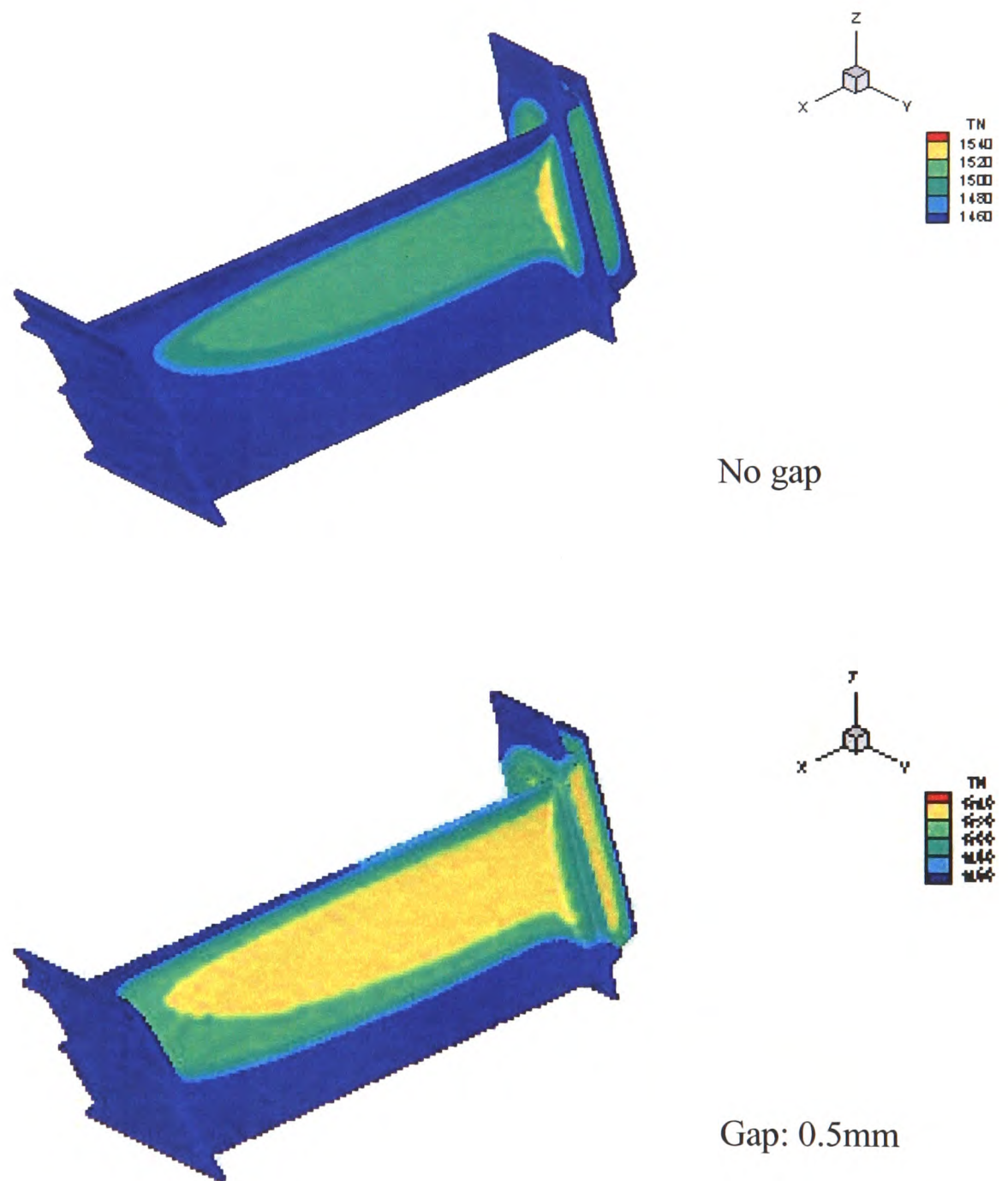


Figure 7.5: Comparisons of the temperature contours 'TN' of the blade between having a gap and no gap at 90s.



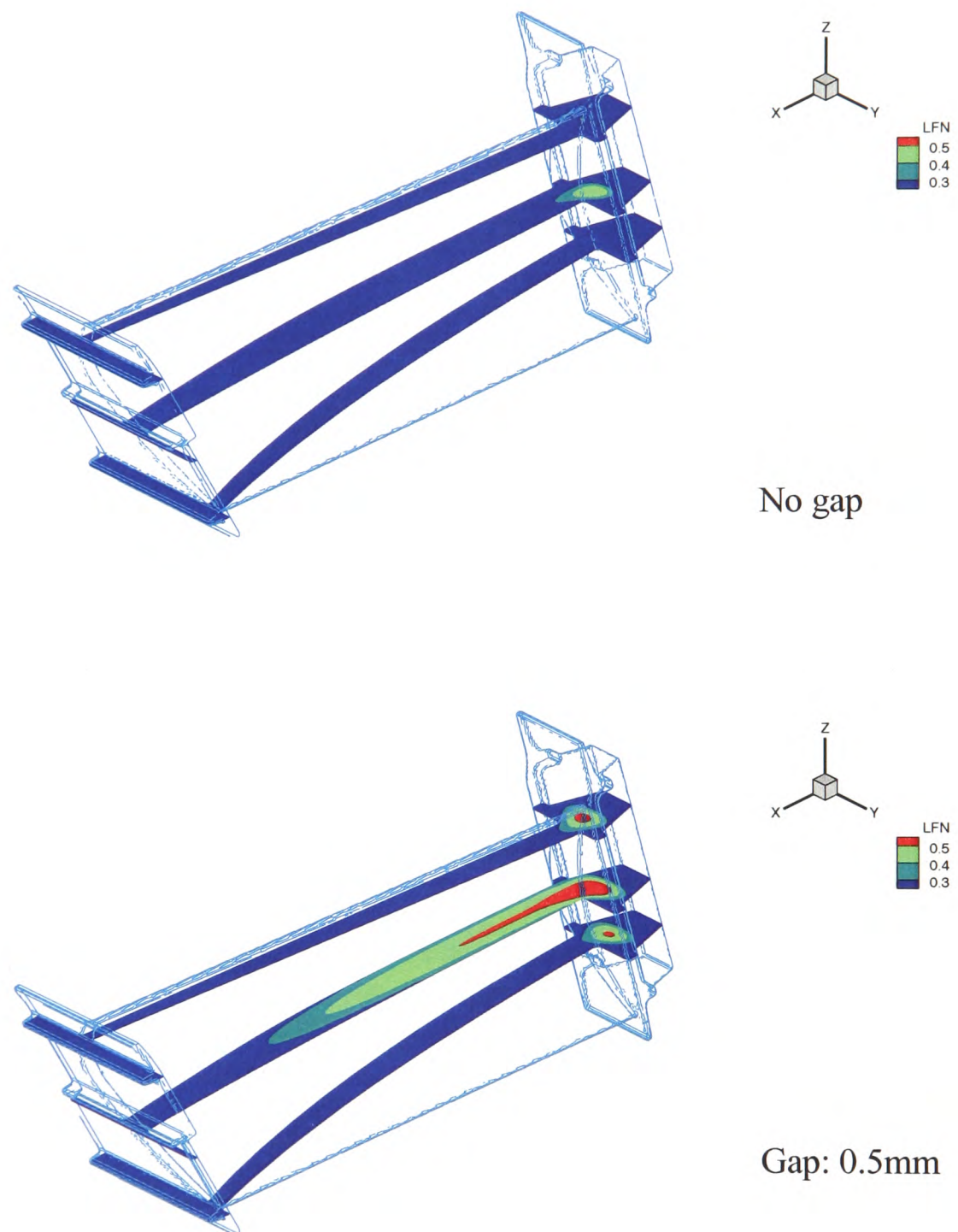


Figure 7.6: Comparisons of the liquid fraction contours 'LFN' of the x-y cross sections of the blade between having a gap and no gap at 130s.

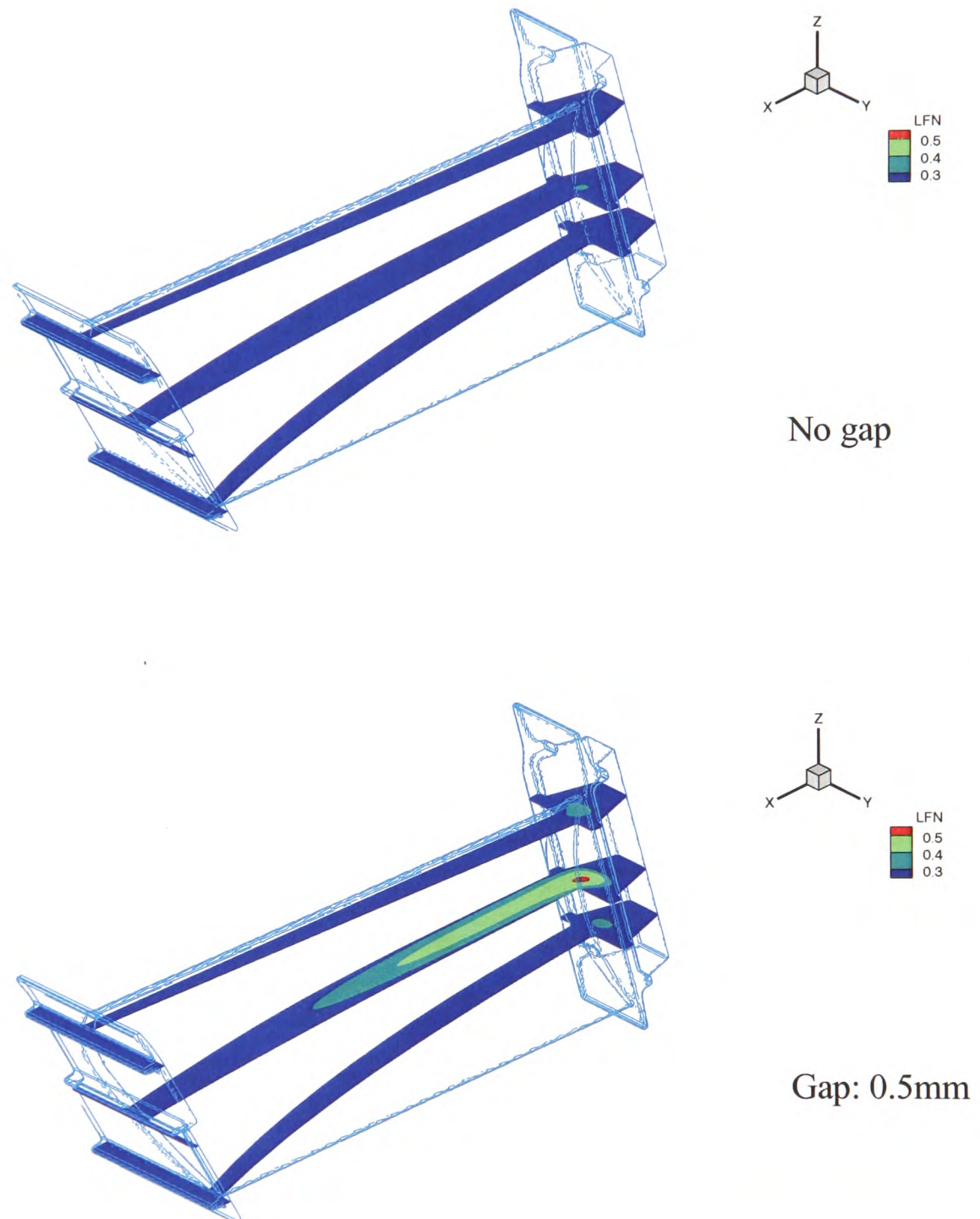


Figure 7.7: Comparisons of the liquid fraction contours 'LFN' of the x-y cross sections of the blade between having a gap and no gap at 150s.

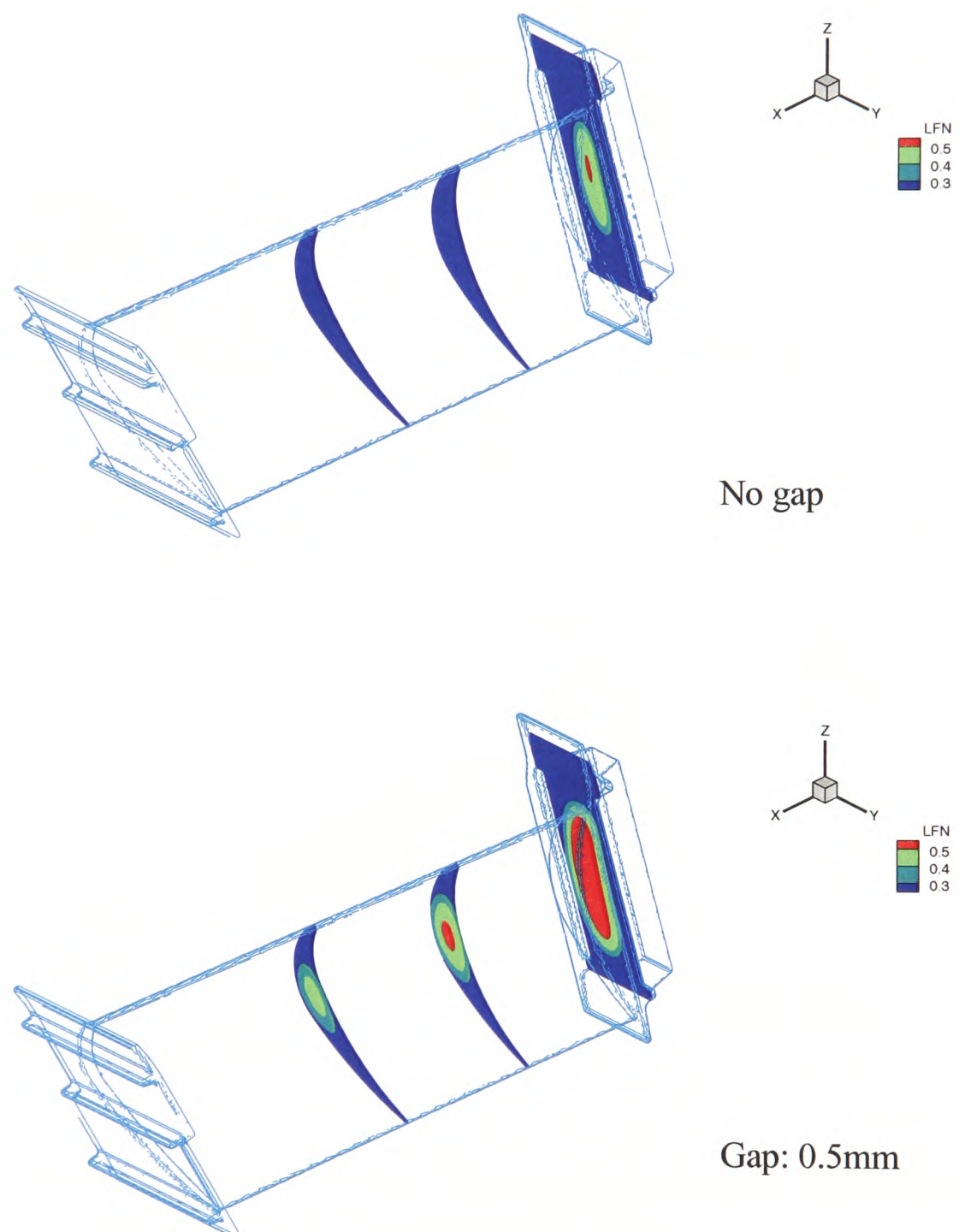


Figure 7.8: Comparisons of the liquid fraction contours 'LFN' of the y-z cross sections of the blade between having a gap and no gap at 130s.



**Figure 7.9: Comparisons of the liquid fraction iso-surface ‘LFN=0.35’ of the blade between having a gap and no gap at 130s.**

Figures 7.9 shows the comparisons of the liquid fraction iso-surface ‘LFN=0.35’ of the blade between having a gap and no gap at 130s. The last part to be solidified is in the root of the blade. Once a hot spot is formed, there would be the most dangerous to make internal porosity, one of casting defects. Such defects have been observed in the practical casting [Harding -08].



### 7.5.2 Temperature

Figure 7.10 shows simply the solidification pattern and the location of the temperature calculated in the following simulations. Figure 7.11 presents the temperatures in the last cell centre of 3D domain (metal) and in the mould wall temperature with no gap at variable time. It is noted that the temperature is gradually getting lower and lower in time both in the metal and in the mould. The reduction is monotonic.

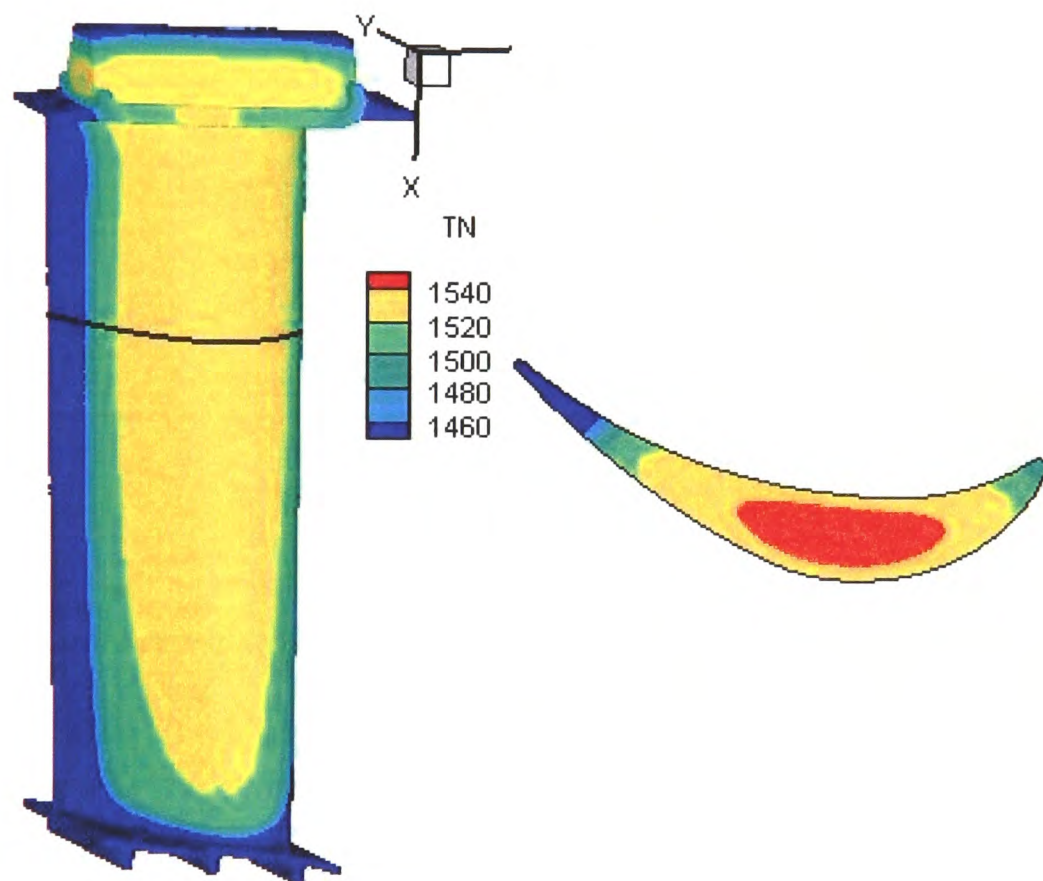


Figure 7.10: Reference location of simulations in the blade.

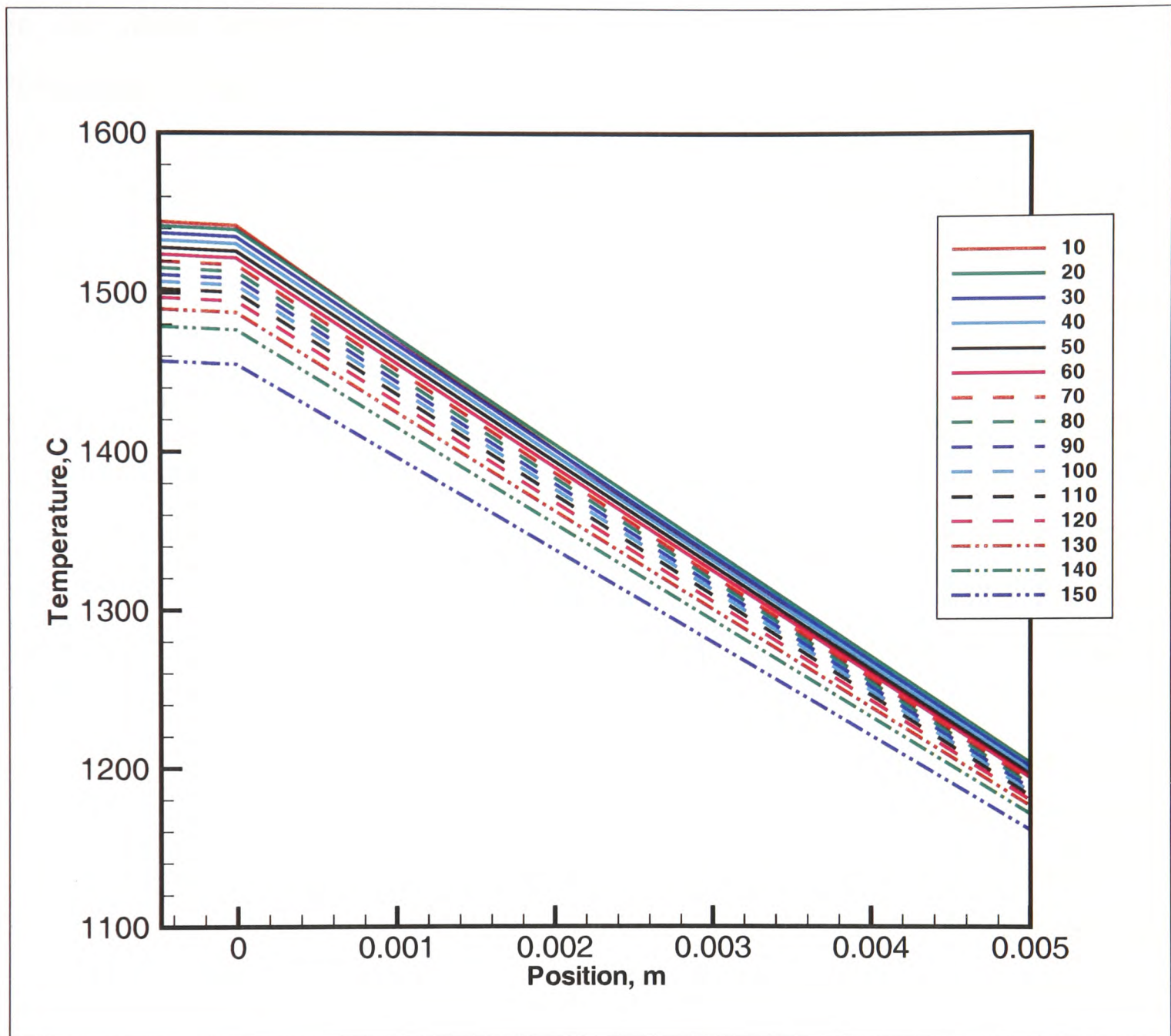


Figure 7.11: Temperatures in the last cell centre of metal and in the mould wall with no gap at variable time.

Figure 7.12 shows the temperatures in the last cell centre of 3D domain (metal) and in the mould wall temperature with a gap at variable time. Within the first 40s, the temperature is falling down gradually. From 40s to 50s, the temperature in the interface at 0.0mm (between metal and mould) suddenly decreases and the mould temperature slightly drops. During this time, a gap is formed as metal solidifies. The conduction through metal to mould (solid to solid) is low and negligible. Gas gap acts

as an insulation layer which slows down heat transferred from the hot metal. The fall in the metal surface temperature decreases and eventually stops. The mould temperature drops because of the radiation boundary conditions applied on the external mould wall. The temperatures of the last cell centre of the metal domain are shown in Table 7.4 during solidification. It is seen that the metal temperature just passes the critical temperature (1534.5 °C) between 40s and 50s. However, at 60s the temperature of the interface rises again as seen in Table 7.4. Once the gas gap is open, the reheating of the metal surface starts to take place. That leads to the temperature change of the metal. At 60s, the metal temperature is 1534.9 °C, just over the freezing temperature, seen in Table 7.4. In terms of numerical simulation, once the temperature is over the freezing temperature, the gap disappears. Once the temperature is lower than the critical temperature, then the gap is formed again. As it is seen, this takes place between 60s and 80s. Around 90s, the interface temperature bounces back. Then the temperature continues to fall down. Gas gap has been formed and has remained there as insulation. The mould cools rapidly. It is hard to predict exactly when the gap formation happens, but it can be said that the first time gap takes place between 40s and 50s; the second one could be between 60s and 80s. This can be seen in Figure 7.13 which shows temperatures of the interface between the metal and the mould with a gap and with no gap during 150s. With a gap, the interface temperature fluctuates twice, which is caused by gap formation and metal re-melted.

Figure 7.14 compares the temperatures of the external wall of the mould with a gap and with no gap during 150s. With no gap, the mould wall can absorb continuously heat from hot metal, which prevents the mould wall from quickly cooling down. With a gap, the gap greatly slows down heat transfer between metal and mould. The temperature on the external mould wall is dropping quickly because of radiation.



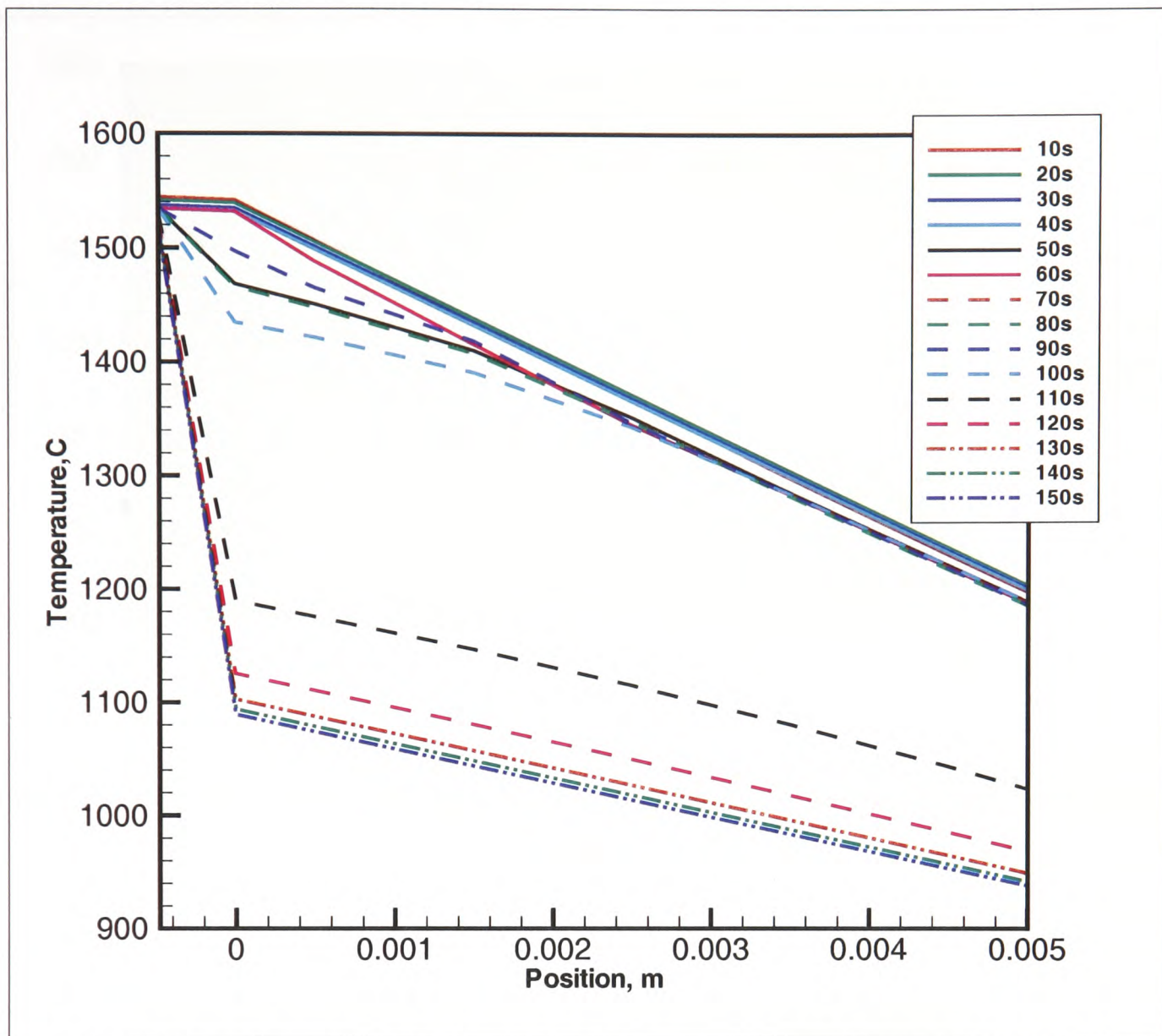


Figure 7.12: Temperatures in the last cell centre of metal and in the mould wall with a gap (0.0005 mm) at variable time.

Table 7.4: The metal temperature in the last cell centre to the mould wall during solidification (the freezing temperature 1534.5 °C)

Time(s)	0	10	20	30	40	50
Temperature(°C)	1600	1553.7177	1547.1844	1541.3252	1536.1316	1534.1207

Table 7.4 continue:

Time(s)	60	70	80	90	100
Temperature(°C)	1534.9193	1534.0396	1534.8121	1535.0164	1533.2797

Table 7.4 continue:

Time(s)	110	120	130	140	150
Temperature(°C)	1530.0673	1526.5714	1523.5889	1520.8770	1518.3031



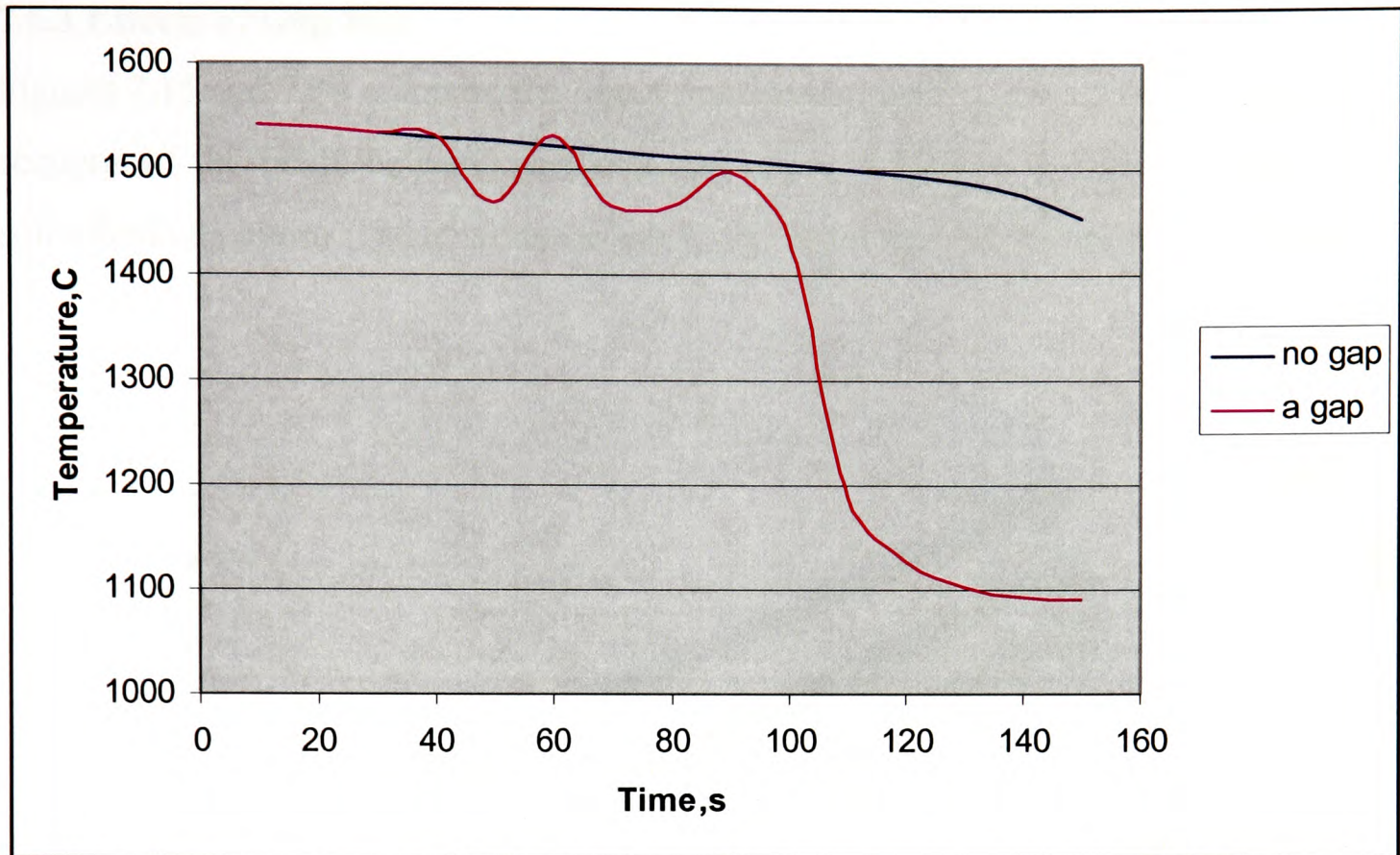


Figure 7.13: Temperatures of the interface between metal and mould with a gap and with no gap during 150s.

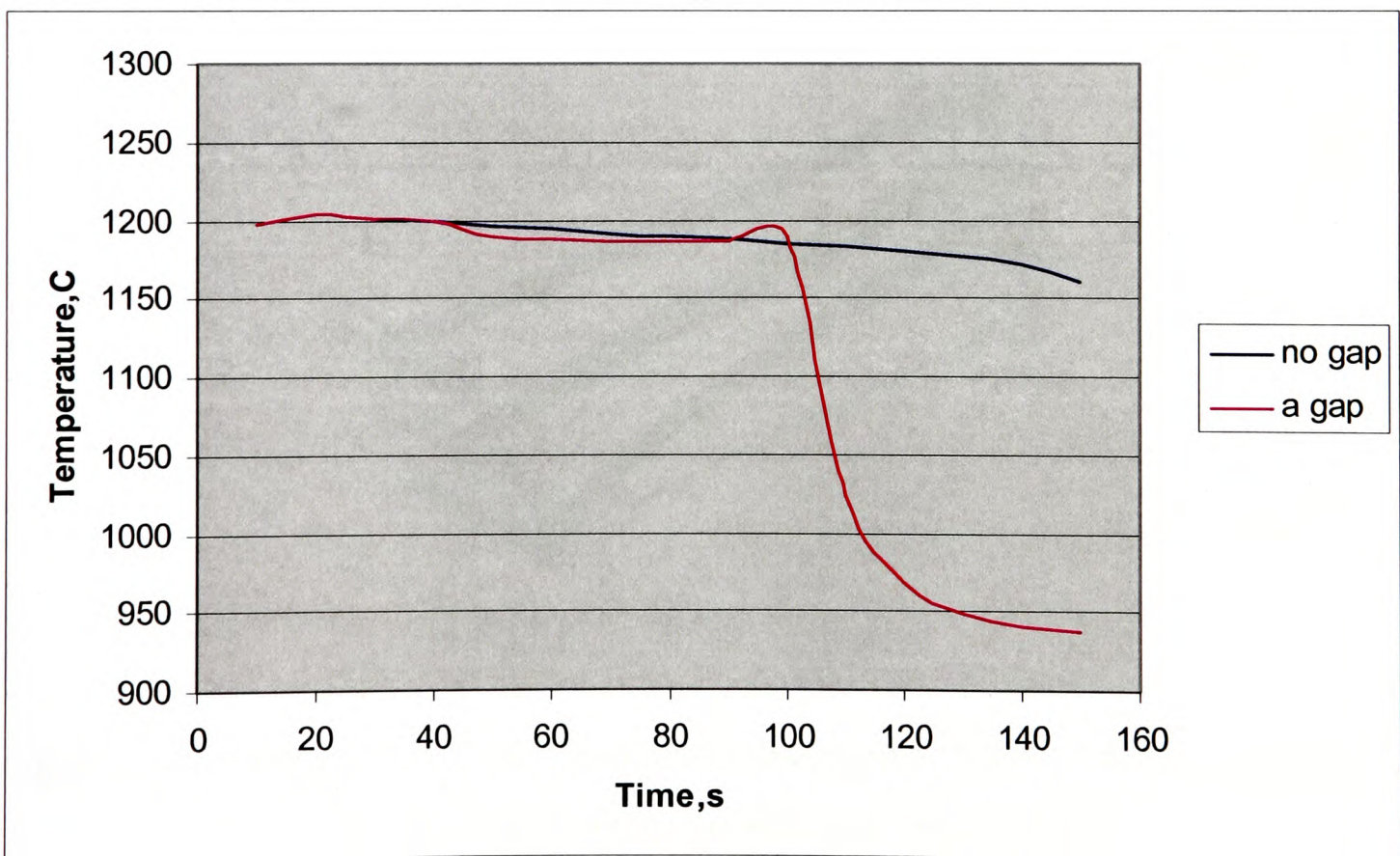


Figure 7.14: Temperatures of the external mould wall with a gap and no gap during 150s.

### 7.5.3 Effects of Gap Size

Figures 7.15 and 7.16 compare the liquid fraction contours 'LFN' of the x-y and y-z cross sections of the blade between different gap sizes at 150s. Gap size has effects on the solidification pattern. The smaller the gap is, the faster the solidification progresses.

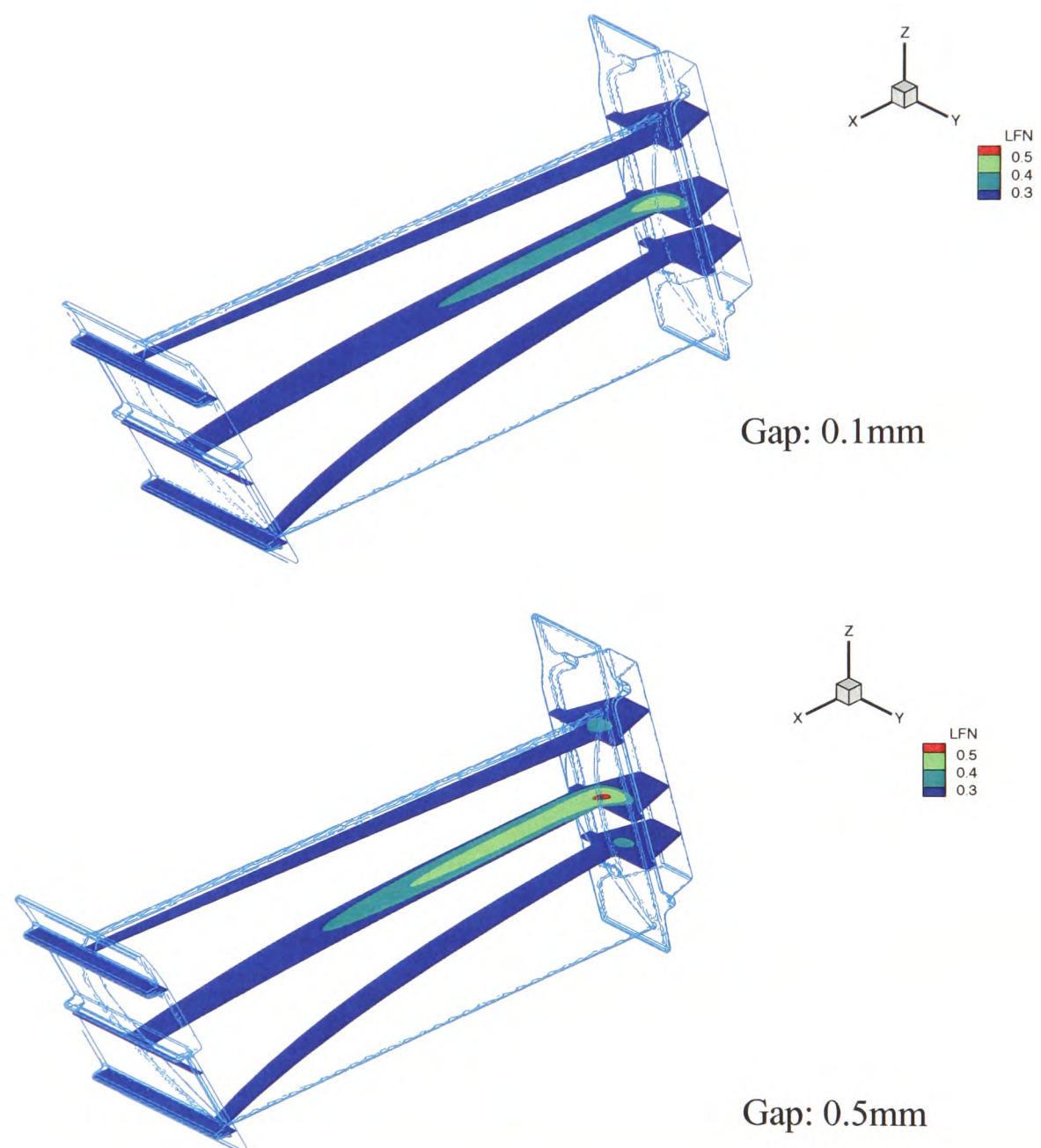


Figure 7.15: Comparisons of the liquid fraction contours 'LFN' of the x-y cross sections of the blade between variable gap sizes at 150s.



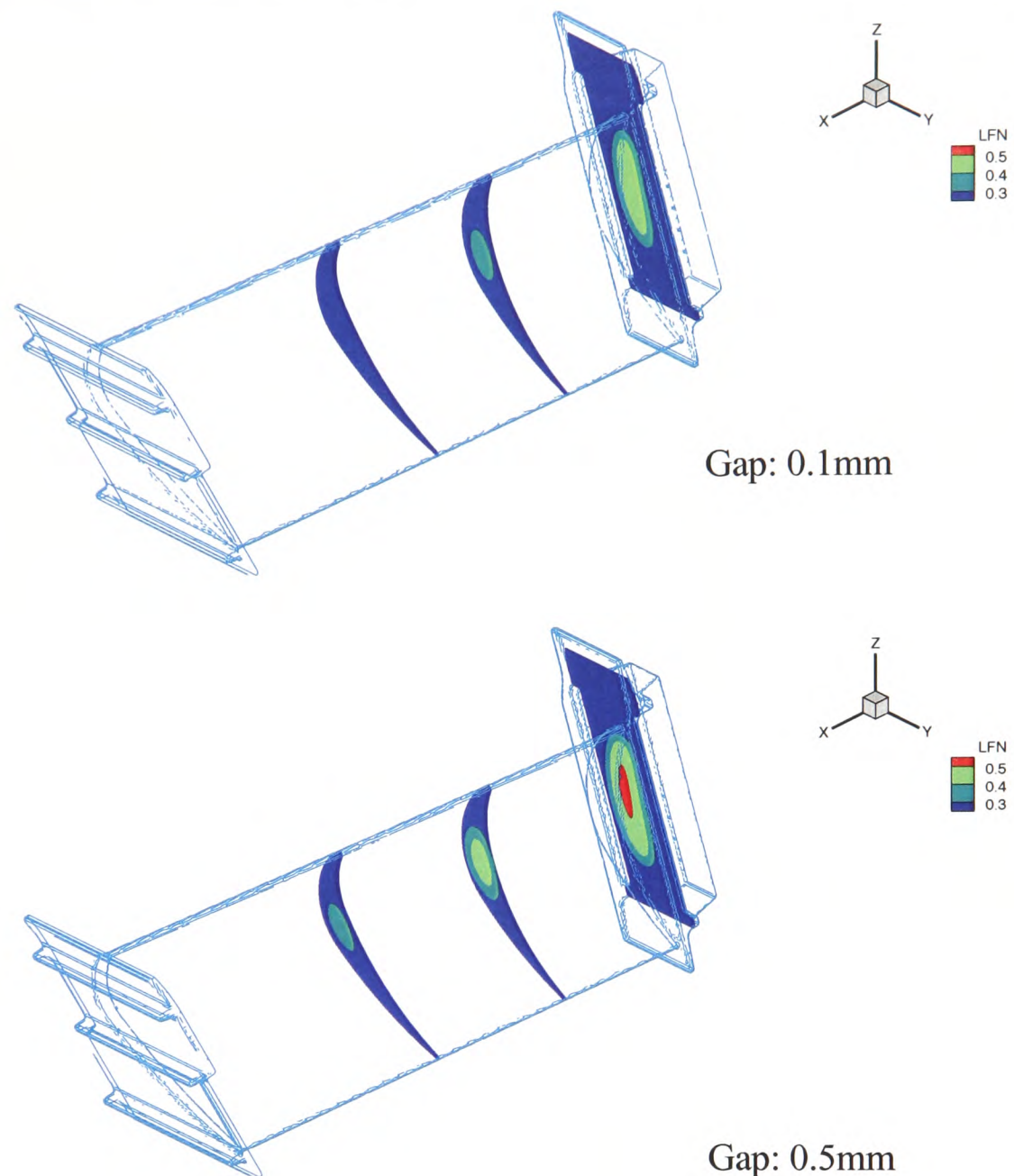


Figure 7.16: Comparisons of the liquid fraction contours 'LFN' of the y-z cross sections of the blade between variable gap sizes at 150s.

Figures 7.17 and 7.18 compare the temperatures of the interface between the metal and the mould, and of the external mould wall with variable gap sizes during 150s. During the first 40s, the same interface temperatures are shown since no gap is formed within this time. With a smaller gap size (0.1mm), only once the gap has been formed because only one fluctuation is present in the curve. Between 110s and 150s, the interface temperature with smaller gap is higher than that with greater gap. This also happens to the external mould wall.

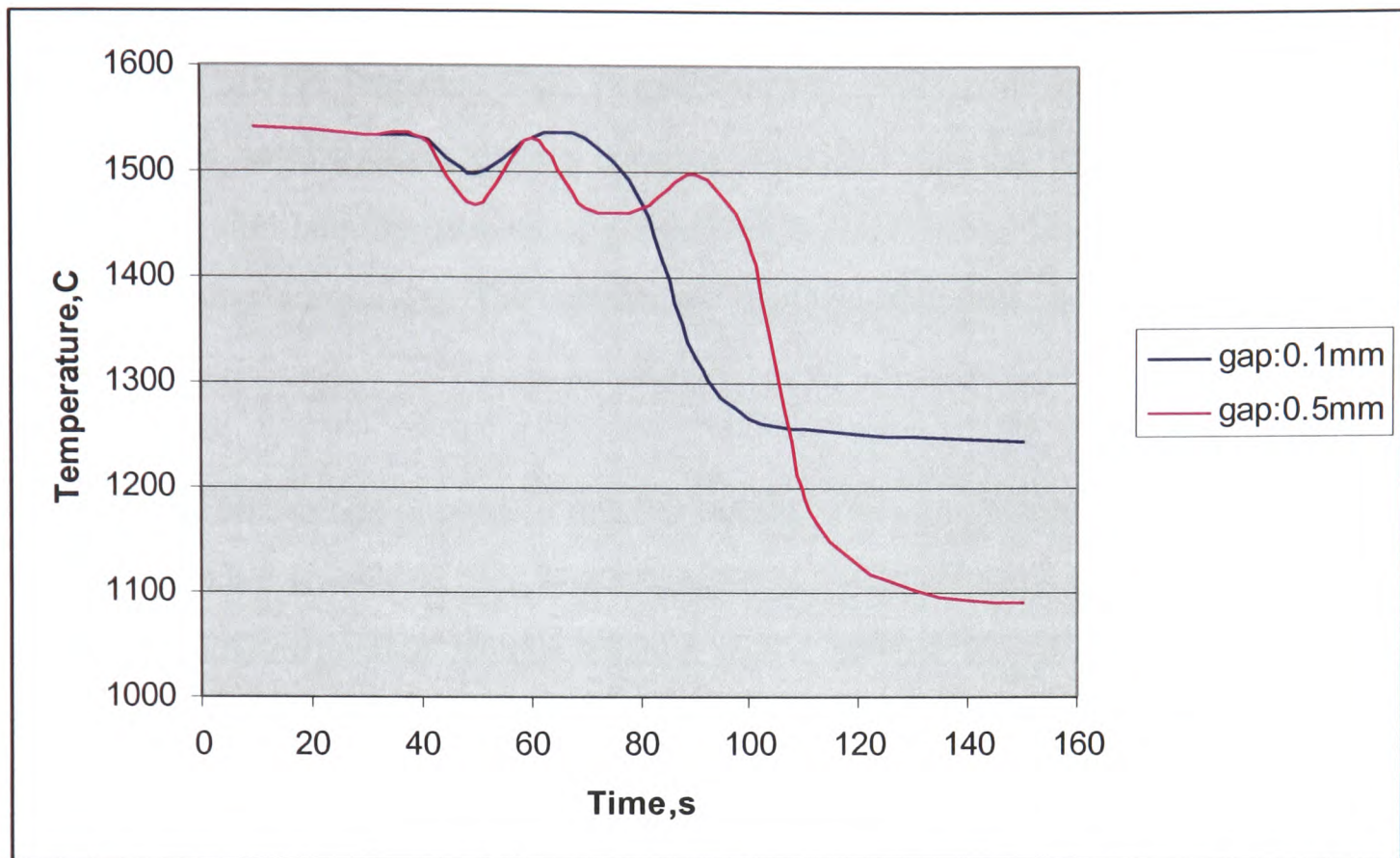


Figure 7.17: Temperatures of the interface between metal and mould with variable gap sizes during 150s.

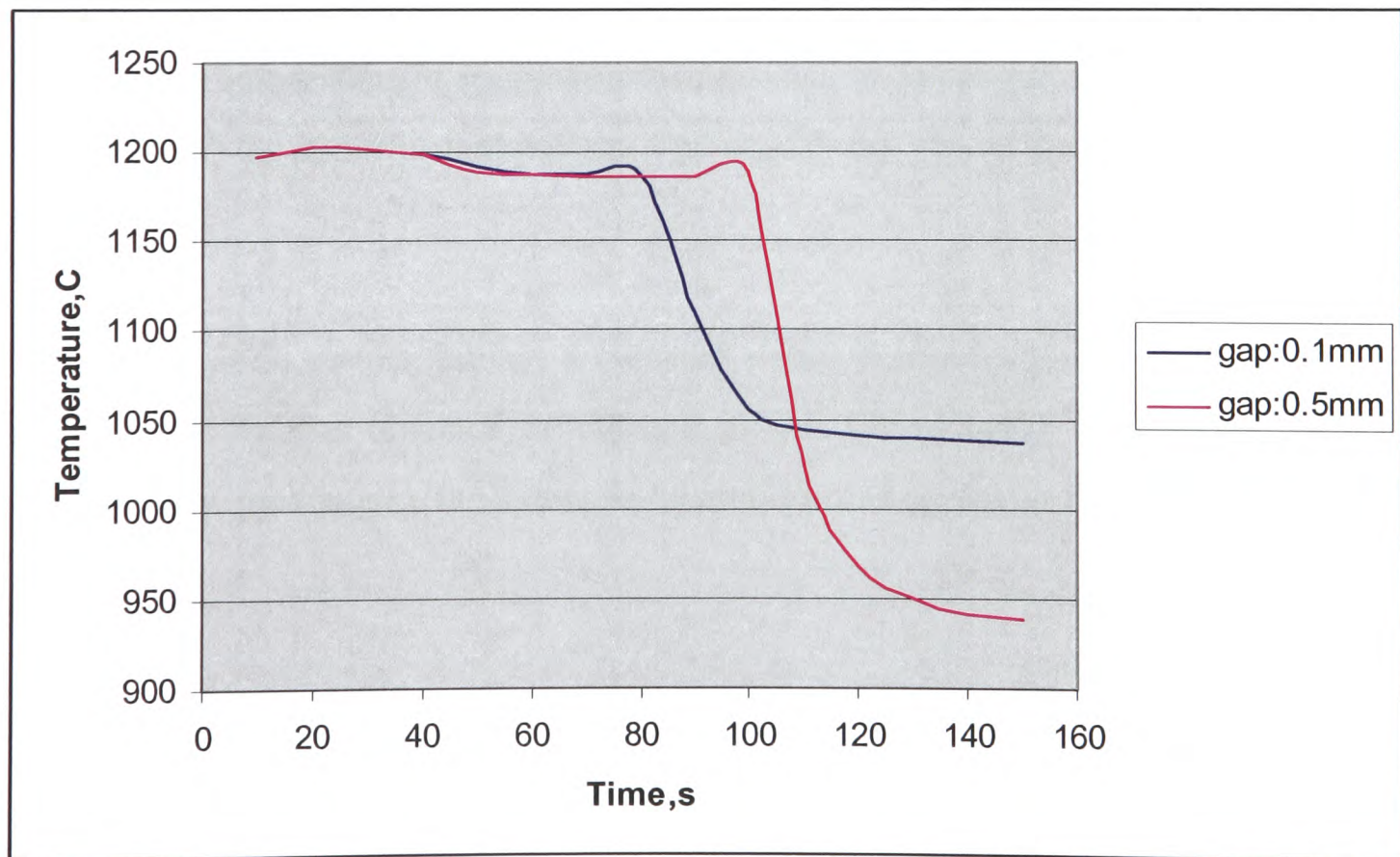


Figure 7.18: Temperatures of the external mould wall with variable gap sizes during 150s.



### 7.6 Summary

Based on the 3D/1D Transient Heat Transfer model, a further development has been made to investigate solidification during cooling. Accurate thermal boundary conditions are employed to simulate the process of solidification after filling. The model can be used to predict the gap formation. The effects of heat transfer and radiation in the gap are included.

A twisted turbine blade is used to test the model. Two simulations are run: one is with a gap and the other is with no gap. The numerical results have been discussed. Gap has great effect on the solidification pattern. Once a gap is formed, it acts as a thermal insulation layer which significantly slows down the heat transfer from metal. Hence, it increases the solidifying time. The discussions on the temperatures of the interface between metal and mould, of the external mould wall and in the mould wall with no gap during 150s give more details about how the temperature changes and during what time the gap could be formed.

Finally, the comparisons of simulation results using different gap size are given. Gap size has effects on the solidification pattern. The smaller the gap is, the faster the solidification progresses.

The solidification results assume a constant initial temperature of metal and mould, so neglecting variations obtained at the end of the filling cycle. Difficulties with mesh orthogonality, prevented a fluid flow simulation for this particular blade geometry.

## Chapter 8

# Conclusions and Future Work

### 8.1 Conclusions

The goal of this research has been concerned with modelling the tilt casting process and the development of numerical techniques for the phenomena involved in metal casting in multi-physics simulations. It is now possible to predict the tilt cast filling and solidification of a 40cm long TiAl turbine blade. Numerical results have been used to support casting experiments.

A model has been developed to simulate the tilt casting process. Initial validation of the model has been made against the X-ray movie of the tilt filling of an 'I'-shaped test piece in aluminium. The tilt casting model clearly described the path by which the gas was evacuating as it was seen in the X-ray movie made during the trials. The comparisons show a good match when surface tension, 3.0N/m, was artificially enlarged to account for the possible presence of an aluminium oxide film on the metal surface. Furthermore, numerical results also predicted the counter-flow in the test piece produced due to the absence of artificial vents.

However, the simulated materials are titanium aluminides for which ISM only provides a limited low superheat in this research. Very thin or narrow cavities are included in the

## Chapter 8. Conclusions and Future Work

---

geometrical model. This makes this study focus on getting more accurate thermal boundary conditions as one of the objectives. That is essential to properly predict the early freezing of thin sections. This has led to the development of a 3D/1D coupled transient heat transfer model as presented in Chapter 5 and a further development of the 3D/1D model to investigate the solidification pattern discussed in Chapter 7. As it is known, free surface flow is one of the major features in the mould filling. The existing free surface methods: Van Leer, Donor Acceptor and Level Set Method, are subject to different problems, such as Van Leer suffering from interface smearing; Donor Acceptor having instability problem. A very small time step had to be used so that the computing is very slow. The improvement on free surface algorithm is vital. Under these circumstances, a novel free surface tracking method, Counter Diffusion Method (CDM) has been developed and implemented within the CFD code PHYSICA as discussed in Chapter 6.

Both moving and static flows were used to validate the 3D/1D model. They have showed that the results using 3D/1D transient model to simulate the heat transfer through the mould wall are in agreement with those using a full 3D model in PHYSICA. However, for some geometries, there are 'dead' corners present where 3D/1D transient model can not cover. This affected slightly the accuracy of the thermal boundary.

Comparisons against the experimental results, undertaken at the University of Birmingham, demonstrated that 1D transient heat transfer model has provided a very good prediction for mis-runs in both the leading and at the trailing edge. Numerical modelling can give a good indication of defect areas that result from the low superheat during mould filling. Furthermore, the 3D/1D model has advantages in reducing computing and problem set up time since the mould mesh can be excluded from the simulation.

Chapter 7 has discussed post-filling solidification using a 40cm twisted blade. Based on the development of the 3D/1D model, a further development has been made to investigate the effect of mould-metal gaps on solidification pattern. In this study, a constant initial temperature of metal and mould is assumed. The numerical results show that the gap had

## Chapter 8. Conclusions and Future Work

---

great effects on the solidification pattern. Once a gap is formed, it acts as an insulator which significantly slowed down the heat transfer from the metal. This increases the solidification time. The model also predicts the temperature changes of the interface between metal and mould, and of the external mould wall during solidification. It is found that there are temperature fluctuations because of the presence of the gap and the reheating of the metal surface. In addition, the gap size had the effect on the solidification that the smaller the gap was, the faster the solidification progressed. The model was able to numerically describe the complete solidification process.

The CDM method was developed to suppress numerical diffusion and track free surface faster. The validation against the classical collapsing column experiment by Martin & Moyce showed good agreement. Comparisons of CDM with others existing numerical methods, Van Leer, Donor Acceptor and Level Set Method has also presented a good match. In addition, CDM shows the strong advantage in terms of reducing the computational time. In the modelling of a 40cm long twisted blade, CDM provides very fast simulations with a computational time reduced by up to 7.5 times compared to the Van Leer method.

Throughout the validations and the applications of 3D/1D model and the novel free surface tracking method, the factors affecting the casting quality have been discussed: venting, tilt cycle, metal weight and surface tension. It has been very useful to succeed in modelling the complete tilt casting process and providing to experiments. It was shown, (i) venting is necessary to help gas evacuate to reduce the risk of gas entrapment. The position and the number of the vents were shown to be very important when designing the mould; (ii) the tilt cycle is a very crucial parameter for a TiAl tilt casting. Fast rotation reduces the contact between the molten metal and the cold crucible to minimise mis-run. However it could lead to surface turbulence which results in casting defects, i.e. bubbles. Slow rotation can minimise surface turbulence. However it inevitably causes high heat loss and induces incomplete filling; (iii) a higher melt weight can provide a higher superheat, which has been proved by the computer modelling and the experimental



measurements. That can reduce mis-run. In terms of the mould filling, higher melt weight pushes the molten metal into the mould faster than lower one. But melt weight has no obvious effect on the final castings after comparing the numerical results in the liquid temperature; (iv) surface tension slightly slows down the mould filling as discussed in Chapter 4 for the validation of an 'I'-shaped test piece in aluminium. A high value of surface tension are used to show the effect that the greater the value of surface tension is, the more influence the surface tension has on the filling.

## 8.2 Future Work

Further study is required to improve the new development and investigate more remained areas relating to the castings.

### 8.2.1 Further Investigation on Surface Tension

Surface tension is expected to play an important role on the mould filling. This research discussed the effect of the surface tension which is coupled within the free surface methods: Van Leer, Donor Acceptor and CDM. The surface tension can be seen to only slow down the flow in the thinnest sections of the casting.

However, the algorithm does not include the effect of the contact angle. In this study, the default value of the contact angle is  $90^\circ$ . From the numerical results, the shape of the metal front can not be identified. Further work should include the effect of contact angle when investigating the surface tension in the future.

### 8.2.2 Heat Transfer and Solidification

The 3D/1D coupled transient heat transfer model has been working very well on getting an accurate thermal boundary conditions during filling for some type of geometry. Good comparisons have been made against the experimental results. The 3D/1D model has been further extended to study solidification pattern and gas gap formation during cooling.

## Chapter 8. Conclusions and Future Work

---

However, the 3D/1D model is restricted to some type of geometry. For the geometry which has 'dead' corner present, the thermal boundary is not accurate around the 'dead' corner. In future work, this shortcoming of the 3D/1D model should be investigated and be overcome. In this study the gap size is assumed to be uniform. All the post-filling simulations were started by assuming a constant initial temperature of metal and mould due to difficulty in meshing the full problem. In the future, variable gap sizes should be involved in the model and achieve the investigation of solidification based on a continuous temperature database at the end of the filling cycle.

### **8.2.2 Casting Defects during Solidification**

The defects developed during the mould filling have been discussed such as mis-run, bubbles. The study on the development of casting defects during solidification remains an interesting area. The possible castings defects after filling such as internal porosities, surface porosities should be worked on and implemented into the model. This has not been done due to lack of time in this research.

## References

[Agonafer, Liao and Spalding -96]

D. Agonafer, G.-L. Liao, and D.B. Spalding. 'The LVEL turbulence model for conjugate heat transfer at low Reynolds numbers.' *Application of CAE/CAD Electronic Systems*, ASME, 18 (1996), 23–26.

[Appel *et al.* -2000]

Appel F, Brossmann U, Christoph U, Eggert S, Janschek P, Lorenz U, Mullauer J, Ohring M, Paul J D H, *Recent progress in the development of gamma titanium aluminide alloys*, *Adv. Eng. Mat.* 2 No.11699-720, 2000.

[Austin and Kelly -95]

Austin C M and Kelly T J, *Progress in Implementation of Cast Gamma Titanium Aluminide*, in *gamma titanium aluminide 1995*, ed. by Y-D Kim *et al.*, Warrendale: TMS, 1995, p. 21.

[Amsden and Harlow -70]

Amsden A A and Harlow FH, *The SMAC method: A numerical technique for calculating incompressible fluid flows*, Report LA-4370, Los Alamos Scientific Lab, USA, 1970.

[Batchelor -67]

Batchelor G K, *An Introduction to Fluid Dynamics*, Cambridge University Press, 1967.

## References

---

[Bailey -96]

Bailey C, Chow P, Cross M and Pericleous K. 'Multi-physics modelling of the metals casting process.' Proc. R. Soc. London A., 452:459-486, 1996.

[Barkhudarov and Hirt -95]

Barkhudarov M and Hirt C W, *In Modelling of Casting, Welding and Advanced Solidification Process*, M. Cross and J. Campbell, eds., TMS, Warrendale, PA, 1995, pp.936-946.

[Berger and Oliger -84]

Berger M and Oliger J, *Adaptive mesh refinement for hyperbolic partial differential equations*, Journal of Computational Physics, 53:484–512, 1984.

[Berger and Colella -89]

Berger M and Colella P, *Local adaptive mesh refinement for shock hydrodynamics*, Journal of Computational Physics, 82:64–84, 1989.

[Bhamidipati -91]

Bhamidipati J.R., Kaddah N.El, *Calculation of Electro-magnetic Field and Melt Shape in the Magnetic Suspension Melting Process*, MHD in Process Metallurgy, ed. J.Szekely et al., Minerals, Metals & Material, pp. 69-74, 1991.

[Bhamidipati -95]

Bhamidipati J.R., *Mathematical Modelling of Electromagnetic Field, Free Surface, Heat Transfer and Fluid Flow Phenomena in Electromagnetic Confinement Systems*, PhD Thesis, University of Alabama, 1995.

[Blum *at el.* -01]

Blum M, Fellmann H G, Franz H, Jarczyk G, Ruppel T, Segtrop K, Laudenberg H J, *Commissioning of a prototype plant for the economical mass production of TiAl-*



## References

---

*valves*, Structural Intermetallics 2001, ed. by K. J. Hemker, Warrendale: TMS, 2001, p. 131-135.

[Bounds *et al.* -00]

Bounds S, Moran G, Pericleious K, Cross M and Croft N T, *A Computational Model for Defect Prediction in Shape Castings Based on the Interaction of Free Surface Flow Heat Transfer and Solidification Phenomena*, Metall. Mater. Trans. B, 2000, Vol. 31B, 515-527.

[Bojarevics -03]

Bojarevics V, Pericleous K, Harding R A and Wickins M, *Induction skull melting dynamics for different materials: numerical modelling comparisons with experiments*, In: TMS, Modelling of Casting, Welding and Advanced Solidification Processes X, Ed. D M Stefanescu *et al.*, 2003, 591-598.

[Bojarevics -04]

Bojarevics V, Pericleous K, Harding R A and Wickins M, *The development and Experimental Validation of a Numerical Model of an Induction Skull melting Furnace*, Met and Mat. Tran. B, 2004, 35B, 785-803.

[Chouhury *et al.* -97]

Choudhury A, Blum M, Jarczyk G, Busse P, Lupton D, Gorywoda M and Heraeus W A, *Low cast production of TiAl automotive valves using cold wall induction melting and permanent mold centrifugal casting*, 30<sup>th</sup> International Symposium on Automotive Technology and Automation (ISATA), Florence, June, pp. 473-480, 1997.

[Campbell -04]

Campbell J: *Castings practice: The 10 Rules of Castings*, 2004, Butterworth-Heinemann.

## References

---

[Campbell -91]

Campbell J: Castings, 1<sup>st</sup> Edition, 1991, Butterworth-Heinemann.

[CFX]

CFX, [www.ansys.com](http://www.ansys.com)

[Chan and Street -70]

Chan R K and Street R L, *Computer studies of finite amplitude water waves*, J. Comp. Phys., Vol 6, pp.68,1970.

[Chan -91]

Chan K S, Pericleous K A and Cross M, *Numerical simulation of flows encountered during mould-filling*, Appl. Math. Modelling, 1991, Vol. 15, pp. 624-631.

[Chang et al. -96]

Chang Y C, Hou T Y, Merriman B, Osher S, *A level set formulation of eulerian interface capturing methods for incompressible fluid flows*. Journal of Computational Physics, 124:449-464, 1996.

[Chapra and Canale -88]

Chapra S C, Canale R P, 'Numerical Methods for Engineers', McGraw-Hill, New York, 1988.

[Chen -95]

Chen S, Johnson D and Raad P, *Velocity boundary conditions for the simulation of free surface fluid flow*, Journal of computational physics, 116:262-276, 1995.

[Chen -97]

Chen S, Johnson D, Raad P and Fadda D, *A simple level set method for solving Stefan problems*, International Journal of Numerical Method, 25:749-778, 1997.

## References

---

[Clemens -2000]

Clemens H, Kestler H, *Processing and applications of intermetallic gamma-TiAl-based alloys*, Adv. Eng. Mat. **2** No.9, pp. 551-570, 2000.

[Cox -00]

Cox M, Wickins M, Kuang J P, Harding R A and Campbell J, *Effect of top and bottom filling on reliability of investment castings in Al, Fe and Ni based alloys*, Mat. Sci. Tech., 16:1445-1452, 2000.

[Cox and Townsend -00]

Cox M and Townsend D W, *Design and manufacture of nickel aluminium bronze sand castings*, Ship Department Publication 18 MoD, 1975, Updated as Ministry of Defence Standard 02-747 (NES 747) pt5, 2000.

[Cox -03]

Cox M, Harding R A and Campbell J, *Optimised running system design for bottom filled aluminium alloy 2L99 investment castings*, Mat. Sci. Tech., 19:613-625, 2003.

[Cox and Harding -07]

M. Cox and R.A. Harding, Mat. Sci. Tech., 23, 214–224 (2007).

[Crank -84]

Crank J, *Free and Moving Boundary Problems*, Oxford University Press, NY, USA, 1984.

[Chung -02]

Chung T J, *Computational Fluid Dynamics*, Cambridge University Press, 2002.

[Daido -08]

Daido Steel, [www.daido.co.jp](http://www.daido.co.jp)

## References

---

[Dhinsa -06]

Dhinsa K, *Development and Application of Low Reynolds Number Turbulence Models for Air-cooled Electronics*, PhD, the University of Greenwich, 2006.

[Durville -13]

Durville P H G, Brit. Patent GB191323719 (1913).

[Enright -02]

Enright D, Fedkiw R, Ferziger J and Mitchell I, *A hybrid particle level set method for improved interface capturing*, *Journal of Computational Physics*, 183:83–116, 2002.

[FEMGV]

Femsys Ltd, <http://www.fmsys.co.uk>

[Ferziger and Peric -02]

Ferziger J H and Peric M. *Computational Methods for Fluid Dynamics*, 3<sup>rd</sup> edition, 2002.

[FLOW3D]

FLOW3D, [www.flow3d.com](http://www.flow3d.com)

[FLUENT]

FLUENT, [www.fluent.com](http://www.fluent.com)

[Foran -95]

Foran R K, Hansen T and Mueller B, *In Modelling of Casting, Welding and Advanced Solidification Process*, M.Cross and J.Campbell, eds., TMS, Warrendale, PA, 1995, pp.771-777.

[Green and Campbell -93]



## References

---

Green N R and Campbell J, *Statistical distributions of fracture strength of cast Al-7Si-Mg ally*, Mat. Sci. Eng., 1993, A173:261-266.

[Harding -01]

Harding R A, Wickins M and Li Y G, *Progress towards the production of high quality-TiAl castings*, Structural Intermetallics 2001, Ed K. J. Hemker et al, TMS, 181-189, 2001.

[Harding -03]

Harding R A, *Recent developments in the induction skull melting and investment casting of titanium aluminides*, In Proc. Int. Conf. on Advanced Metallic Materials. Smolenice Castle, Slovakia 2003, ed. by J.Jerz *et al.* 106-113.

[Harding and Wickins -03]

Harding R A and Wickins M, *Temperature measurements during induction skull melting of titanium aluminide*, Materials Science and Technology, September 2003, 19 (9), 1235-1246.

[Harding *et al.* -05]

Harding R A, Wickins M, Keough G, Pericleous K, and Bojarevics V (2005), *The Use of Combined DC and AC Fields to Increase Superheat in an Induction Skull Melting Furnace*, Int. Symp. Liquid Metal Processing and Casting, Santa Fe, New Mexico, 2005.

[Harding -05]

Harding R A, *Annual progress report of IMPRESS project –D3a-1*, Dec 2005.

[Harding –06]

Harding R A, *The use of tilt filling to improve the quality and reliability of castings*, World Foundry Congress 2006, Harrogate, 5-8 June 2006.

## References

---

[Harding –Sep 06]

Harding R A, *Progress report of IMPRESS Tilt Casting Trials*, September- October, 2006

[Harding *et al.* -07]

Harding R A, Wickins M, Wang H, Djambzaov G and Pericleous K, *The tilt casting of titanium aluminides*, Liquid Metal Processing and Casting, LMPC 2007.

[Harding *et al.* -08]

Harding R A, Wickins M, Wang H, Djambzaov G and Pericleous K, *The Development of a Tranquil Tilt Pouring Process for Casting Titanium Aluminides*, TMS Symposium on Structural Aluminides for Elevated Temperature Applications, New Orleans, 2008.

[Harding -08]

Harding R A, *Presentation in project meeting of IMPRESS*, Genoa, Italy, May 2008.

[Harlow and Welch -65]

Harlow F and Welch J, *Numerical calculation of time-dependent viscous incompressible flow of fluid with free surface*, Physics of Fluids, 8:2182-2189, 1965.

[Harlow and Welch -68]

Harlow F H and Welch J E, *Numerical calculation of time-dependent viscous incompressible flow of fluid with free surface*, Phys. Fluids, Vol. 8, pp.2182, 1965.

[Harpoon]

[www.sharc.co.uk](http://www.sharc.co.uk)

[Harten *et al.* -87]

Harten A, Enquist B, Osher S and Chakravarthy S, *Uniformly high-order accurate essentially non-oscillatory schemes III*, Journal of Computational Physics, 71:231–303, 1987.

## References

---

[Hartfield-Wunsch -95]

Hartfield-Wunsch S E, Sperling A A, Morrison R S, Dowling W E, and Allison J E, *Titanium Aluminide Automotive Engine Valves*, in *gamma titanium aluminide 1995*, ed. by Y-D Kim *et al.*, Warrendale: TMS, 1995, p. 31.

[Hildebrand -56]

Hildebrand F B, *Introduction to Numerical Analysis*, McGraw-Hill, New York, 1956.

[Hirt and Nichols -81]

Hirt C W and Nichols B D, *Volume of fluid (VOF) method for the dynamics of free boundaries*, J. Comp. Phys., Vol 39, pp.201-225,1981.

[Hirt and Shannon -68]

Hirt C W and Shannon J P, *Free surface stress conditions for incompressible flow calculations*, J. Comp. Phys., Vol 2, pp.403-411,1968.

[Hitchiner -08]

Hitchiner: [www.hitchiner.com/HIMCO/Moderncasting.html](http://www.hitchiner.com/HIMCO/Moderncasting.html)

[Hulin -86]

Hulin J P, 'Transport in porous medium.' Kluwer Academic Publishers, 1986,

[Kuang -00]

Kuang J P, Harding R A and Campbell J, *Examination of defects in gamma titanium aluminide investment castings*, Int. J. Cast Metals Research, 13:125-134, 2000.

[Lauder and Spalding -74]

Lauder B E and Spalding D B, *The Numerical and Computation of Turbulent Flows*, Computer Methods in Applied Mechanics and Engineering , Vol. 3, pp.269-289.

## References

---

[Liu –March 86]

Liu J, *The scalar equation method for the prediction of free surface flows*, PDR/CFDU IC/25, CFDU, Mech. Eng. Dept., Imperial College, London UK, March,1986

[Liu –October 86]

Liu J, *Computer modelling of flows with a free surface*, PhD Thesis, CFDU, Mech. Eng. Dept., Imperial College, London UK,October,1986

[Lin and Hwang -88]

Lin H J and Hwang S W, *Combined fluid flow and heat transfer analysis for the filling of castings*, American Foundrymen's Society Transactions, Vol. 144, pp. 447-458, 1988.

[Lin and Hwang -89]

Lin H J and Hwang W S, *Three-Dimensional fluid flow simulation for mould filling*, American Foundrymen's Society Transactions, Vol. 171, pp. 855-862, 1989

[Liu and Spalding -88]

Liu J and Spalding D B, *Numerical Simulation of Flows with Moving interfaces*, PCH PhysicoChemical Hydrodynamics, 1988, Vol.10, No.5/6, pp.625-637

[Losasso -04]

Losasso F, Gibou F and Fedkiw R. 'Simulating water and smoke with an octree data structure.' ACM Trans Graph (SIGGRAPH Proc) 23:457–462, 2004.

[Losasso -06]

Losasso F, Fedkiw R and Osher S. 'Spatially adaptive techniques for level set methods and incompressible flow.' Computer & Fluids, 35:995-1010, 2006.



## References

---

[MAGMASOFT]

MAGMASOFT, [www.magmasoft.com](http://www.magmasoft.com)

[Martin and Moyce -52]

Martin J C and Moyce W J, *An experimental study of the collapse of liquid columns on a rigid horizontal plane*, Phil.Trans.R.SOC, Vol. 244, No.882, 1952, pp.312-324.

[McDonal-71]

McDonal P W, *The computation of transonic flow through two-dimensional gas turbine cascades*, ASME paper 71-GT-89, 1971.

[Mi -02]

Mi J, Harding R A, Wickins M and Campbell J, *The tilt casting process*, Int. J. Cast Metals Research, 14:325-334, 2002.

[Mi -03]

Mi J, Harding R A, Wickins M and Campbell J, *Entrained oxide films in TiAl castings*, Intermetallics, 11:3377-385, 2003.

[Mi -04]

Mi J, Harding R A, Wickins M and Campbell J, *Effects of the entrained surface film on the reliability of castings*, Met. Mat.Trans. 35a:2893-2902, 2004

[Molina- 07]

Molina J M, Voytovych R, Louis E, Eustathopoulos N, *The surface tension of liquid aluminium in high vacuum: the role of surface condition*, International Journal of Adhesion and Adhesives, Vol. 27, pp. 394—401, 2007.

[Moran *et al.* -99]

## References

---

Moran G.J., Bounds S.M., Pericleous K. A. and Cross M., *Prediction of cold shuts using an unstructured mesh finite volume code*, TMS, pp. 101-108, 1998.

[Neumann and Spelt -96]

Neumann A W and Spelt J K, *Applied Surface Thermodynamics*, Marcel Decker, Inc., 1996.

[Nichols and Hirt -71]

Nichols B D and Hirt C W, *Improved free surface boundary conditions for numerical incompressible flow calculations*, J. Comp. Phys., Vol 8, pp.433-448,1971.

[Noda -98]

Noda T, *Application of cast gamma TiAl for automobiles*, Intermetallics, 6:709-713, 1998.

[Osher and Sethian -88]

Osher S and Sethian J, *Fronts propagating with curvature-dependent speed: algorithms based on Hamilton–Jacobi formulations*, Journal of Computational Physics, 79:12–49, 1988.

[Patankar and Spalding -72]

Patankar S V and Spalding DB, *A calculation procedure for heat, mass and momentum transfer in three-dimensional parabolic flows*, International Journal of Heat and Mass Transfer, Vol. 15, 1972.

[Patankar -80]

Patankar S V, *Numerical Heat Transfer and Fluid Flow*, Hemisphere, Washington DC, 1980.

## References

---

[Patom -87]

Patom I S, Application of the VOF method to the sloshing of a fluid in a partially filled cylindrical container, *Int. J. for numerical Meth. In Fluids*, vol. 7, pp.535-550, 1987

[Pericleous and Drake -86]

Pericleous K A and Drake N, *An algebraic Slip Model of PHOENICS for multi-phase applications*, *Lecture Notes in Engineering*, 18, Springer-Verlag, 375-385 (1986).

[Pericleous -93]

Pericleous K A, Chan A and Cross M, *Three-dimensional simulation of the filling of moulds by liquid metals*, *Mathematical modelling for material processing*, 1993, pp.273-281.

[Pericleous *et al.* -95]

Pericleous K, Chan K S and Cross M, *Free surface flow and heat transfer in cavities*, *Numerical Heat Transfer*, 27(B):487-507, 1995.

[Pericleous -97]

Pericleous K.A., Bojarevics V., Cross M. and Tinios G., *The Development of Dynamic CFD Model of the Magnetic Semi-Levitation of Liquid Metals*, *Iner Conf on CFD in Mineral & Metal Processing and Power Generation*, CSIRO, 1997.

[Pericleous -98]

Pericleous K.A., Moran G. J. Bounds S.M. and Cross M., *Three-dimensional free surface modelling in an unstructured mesh environment for metal processing applications*, *Applied Mathematical Modelling*, pp. 895-906, 1998.

[Pericleous -02]

Pericleous K, *Computing the dynamic interaction of magnetic fields and turbulent conducting fluids in metals processing*, *Computational Modelling of Materials*,

## References

---

Minerals and Metals Processing, TMS Annual Meeting, Seattle WA., Feb. 2002, pp.2-22, ISBN 0-87339-513-1.

[PHYSICA]

PHYSICA, [www.physica.co.uk](http://www.physica.co.uk)

[PROCAST]

PROCAST, [www.esi-group.com](http://www.esi-group.com)

[Raad -95]

Raad P, Chen S and Johnson D, *The introduction of micro celled to treat pressure in free surface fluid flow problems*, Journal of Fluids Engineering, 117:683-690, 1995.

[Ramshaw and Trapp -76]

Ramshaw J D and Trapp J A, *A Numerical Technique for Low Speed Homogeneous Two Phase Flow with a Sharp Interface*, Journal of Computational Physics, 21:438-453, 1976.

[Rhino]

[www.rhino.com](http://www.rhino.com)

[Richtmyer and Morton -67]

Richtmyer R D and Morton K W, *Difference Methods for Initial Value Problems*, 2<sup>nd</sup> ed. Wiley, New York, 1967

[Rishel -99]

Rishel L L, Pollock T M and Cramb A W, *Induction skull melting of titanium aluminides*, Proc. 1999 Int. Symp. on Liquid Metal Processing and Casting, Santa Fe, NM, Feb. 21–24, 1999.



## References

---

[Shu and Osher -88]

Shu C W and Osher S, *Efficient implementation of essentially non-oscillatory shock capturing schemes*, Journal of Computational Physics, 77:439–471, 1988.

[Shu and Osher -89]

Shu C W and Osher S, *Efficient implementation of essentially non-oscillatory shock capturing schemes II (two)*, Journal of Computational Physics, 83:32–78, 1989.

[Stahl -86]

Stahl G W, *Twenty-five years tilt pouring aluminium*, AFS Trans., 1986, 94, 793-796.

[Strain -99 b]

Strain J, *Fast tree-based redistancing for level set computations*, Journal of Computational Physics, 152:664–686, 1999.

[Strain -99 a]

Strain J, *Tree methods for moving interfaces*, Journal of Computational Physics, 151:616–648, 1999.

[Sussman *et al.* -94]

M. Sussman, P. Smereka and S. Osher. ‘A level set approach for computing solutions to incompressible two-phase flow.’ Journal of Computational Physics, 114:146-159, 1994.

[Sussman and Puckett -00]

Sussman M and Puckett E G, *A coupled level set and volume-of-fluid method for computing 3d and axisymmetric incompressible two-phase flows*, Journal of Computational Physics, 162:301–337, 2000.

## References

---

[TECPLOT]

Tecplot, [www.tecplot.com](http://www.tecplot.com)

[Thomas -99]

Thomas J W, *Numerical Partial Differential Equations: Finite Difference Method*, Springer, 1999

[Van Leer -77]

Van Leer B, *Towards the ultimate conservative difference scheme iv: A new approach to numerical convection*, Journal of Computational Physics, 23:276, 1977.

[Versteeg and Malalasekera -95]

Versteeg H K and Malalasekera W, *An Introduction to Computational Fluid Dynamics: The Finite Volume Method*, Addison Wesley Longman, Ltd. Harlow, England 1995.

[Voller and Cross -93]

Voller V R and Cross M, *Solidification process, algorithms and codes*, Mathematical Modelling of Materials Processing, OUP, Oxford, p. 93-111, 1993.

[Voller -90]

Voller V R, Swaininahan C R and Thomas B G, *Fixed grid techniques for phase change problems- a review*, Int. J. Num. Methods Eng., Vol. 30, p 875-898, 1990.

[Watanbe -00]

Watanbe Y, Fukui Y, *Microstructure and mechanical properties of functionally graded material fabricated by centrifugal casting method*, Metallurg Mater Sci 2000, 4:51-93.

## References

---

[Wheeler -00]

Wheeler D, *Computational Modelling of Surface Tension Phenomena in Metals Processing*, PhD thesis, University of Greenwich, London, 2000.

[Winslow -66]

Winslow A W, *Numerical simulation of the quasi-linear poisson equation in a non-uniform triangular mesh*, *Journal of Computational Physics*, 1:149-171,1966.

[Wu -04]

Wu X H, Hu D and Loretto M H, *Alloy and process development of TiAl*, *J. Mats. Sci.*, 39 (12): 3935-3940, 2004.

[Wu -06]

Wu X H, *Review of Alloy and process development of TiAl*, *Intermetallics* 14, pp.1114-1122, 2006.

[Zhu and Harding -96]

Zhu X.R. and Harding R.A., *The computer Modelling of the Semi-levitation Melting of Metals*, *Electro-magnetics and Induction Heating*, IEE Colloquium, 1996.

## Appendix A

# INFORM File for the Validation of the 3D/1D Model

*INFORM file of the validation of 3D/1D for test case 1: using PHYSICA*

```
GEOMETRY_MODULE
  MESH split.mbl
END
```

```
GENERIC_MODULE
  TRANSIENT_RUN
  DELTA_T
  FOR_ALL_TIME_STEPS 0.002
  END
  TOTAL_TIME_STEPS 250
  END
  MAX_SWEEPS 250
END
```

```
USER_MODULE
  OUTPUT_FREQUENCY 0.1
  BASE_U 0.20
  HALF_WIDTH 0.003
END
```

```
MATERIAL_PROPERTY_MODULE
  DENSITY
  MATERIAL 1 USER_ROUTINE FS_PROP 2 3850. 3.85
  MATERIAL 2 CONSTANT 2200.
  END
```

```
VISCOSITY
  MATERIAL 1 USER_ROUTINE FS_PROP 2 0.5e-6 5.e-5
```



## Appendix A

---

MATERIAL 2 CONSTANT 0.1  
END

THERMAL\_CONDUCTIVITY  
MATERIAL 1 USER\_ROUTINE FS\_PROP 2 21.6 0.1  
MATERIAL 2 CONSTANT 1.6  
END

SPECIFIC\_HEAT  
MATERIAL 1 USER\_ROUTINE FS\_PROP 2 1147. 1.  
MATERIAL 2 CONSTANT 1000.  
END

LIQUIDUS\_TEMPERATURE  
MATERIAL 1 USER\_ROUTINE FS\_PROP 2 1550. 0.  
MATERIAL 2 CONSTANT 3100.  
END

SOLIDUS\_TEMPERATURE  
MATERIAL 1 USER\_ROUTINE FS\_PROP 2 1500. 0.  
MATERIAL 2 CONSTANT 3000.  
END

LATENT\_HEAT  
MATERIAL 1 USER\_ROUTINE FS\_PROP 2 411500. 100.  
MATERIAL 2 CONSTANT 100000.  
END  
END

FREE\_SURFACE\_MODULE  
STORE\_FREESURF  
INITIAL\_VALUES ALL 0.  
END  
END

FLUID\_FLOW\_MODULE  
BOUND\_FACE\_PRESSURE ON

SOLVE\_U-MOMENTUM  
GROUPS  
ALL OFF  
MATERIAL 1 ON  
END  
INITIAL\_VALUES ALL 0.0  
BOUNDARY\_CONDITIONS  
PATCH 1 FIXED\_VALUE VALUE 0.20  
PATCH 10 WALL\_COEFF 1. VALUE 0.  
END

## Appendix A

---

END

SOLVE\_V-MOMENTUM

GROUPS

ALL OFF

MATERIAL 1 ON

END

INITIAL\_VALUES ALL 0.0

BOUNDARY\_CONDITIONS

PATCH 1 FIXED\_VALUE VALUE 0.0

PATCH 10 WALL COEFF 1. VALUE 0.

END

END

SOLVE\_PRESSURE

GROUPS

ALL OFF

MATERIAL 1 ON

END

INITIAL\_VALUES ALL 0.0

BOUNDARY\_CONDITIONS

PATCH 2 FIXED\_VALUE VALUE 0.0

END

RESIDUAL\_REFERENCE 10.

END

END

SCALAR\_MODULE

SOLVE\_walls

TRANSIENT\_TERM OFF

CONVECTION\_TERM OFF

DIFFUSION\_COEFFICIENT

ALL CONSTANT 1.

END

INITIAL\_VALUES ALL 0.0

BOUNDARY\_CONDITIONS

PATCH 10 FIXED\_VALUE VALUE 0.0

END

USER\_SOURCE\_TERMS

LEVEL 0

END

END

END

HEAT\_TRANSFER\_MODULE

SOLVE\_TEMPERATURE

INITIAL\_VALUES ALL 1000.

BOUNDARY\_CONDITIONS

PATCH 1 FIXED\_VALUE VALUE 1600.

## Appendix A

---

```
PATCH 6 FIXED_VALUE VALUE 1000.
PATCH 10 PERIODIC
END
RESIDUAL_REFERENCE 500.
END
END

SOLIDIFICATION_MODULE
INITIAL_FRACTION_LIQUID PER_MATERIAL
MATERIAL 1 1.
MATERIAL 2 0.
END
FRACTION_LIQUID_FUNCTION
MATERIAL 1 LINEAR_FUNCTION
MATERIAL 2 LINEAR_FUNCTION
END
PERMEABILITY_COEFFICIENT 1.E-6
UPDATE_TEMP ON
END

MONITOR_MODULE
OUTPUT_INTERVAL 50
MONITOR_LOCATION 0.101 0.0 0.0
END

POST-PROCESSING_MODULE
TECPLOT_FORMAT
WRITE_INITIAL_VALUES ON
TECPLOT_FILE_NAME H
TIME_FREQUENCY .1
END
END

STOP
```

## Appendix A

---

*INFORM file of the validation of 3D/1D for test case 1:3D/1D transient model*

```
GEOMETRY_MODULE
  MESH    bla150.md
END
```

```
GENERIC_MODULE
  TRANSIENT_RUN
    DELTA_T
      FOR_ALL_TIME_STEPS 0.002
    END
    TOTAL_TIME_STEPS 250
  END
  MAX_SWEEPS 150
  MIN_SWEEPS 5
END
```

```
USER_MODULE
  OUTPUT_FREQUENCY 0.1
  BASE_U 0.20
  HALF_WIDTH 0.003
END
```

```
MATERIAL_PROPERTY_MODULE
  DENSITY
    MATERIAL 1 USER_ROUTINE FS_PROP 2 3850. 3.85
  END
```

```
VISCOSITY
  MATERIAL 1 USER_ROUTINE FS_PROP 2 0.5e-6 5.e-5
END
```

```
THERMAL_CONDUCTIVITY
  MATERIAL 1 USER_ROUTINE FS_PROP 2 21.6 0.1
END
```

```
SPECIFIC_HEAT
  MATERIAL 1 USER_ROUTINE FS_PROP 2 1147. 1.
END
```

```
LIQUIDUS_TEMPERATURE
  MATERIAL 1 USER_ROUTINE FS_PROP 2 1550. 0.
END
```

```
SOLIDUS_TEMPERATURE
  MATERIAL 1 USER_ROUTINE FS_PROP 2 1500. 0.
END
```

```
LATENT_HEAT
```

## Appendix A

---

```
MATERIAL 1 USER_ROUTINE FS_PROP 2 411500. 100.  
END  
END
```

```
FREE_SURFACE_MODULE  
STORE_FREESURF  
INITIAL_VALUES ALL 0.  
END  
END
```

```
FLUID_FLOW_MODULE  
BOUND_FACE_PRESSURE ON
```

```
SOLVE_U-MOMENTUM  
INITIAL_VALUES ALL 0.0  
BOUNDARY_CONDITIONS  
PATCH 1 FIXED_VALUE VALUE 0.2  
# PATCH 3 WALL COEFF 1. VALUE 0.0  
END  
END
```

```
SOLVE_V-MOMENTUM  
INITIAL_VALUES ALL 0.0  
BOUNDARY_CONDITIONS  
PATCH 1 FIXED_VALUE VALUE 0.0  
# PATCH 3 WALL COEFF 1. VALUE 0.0  
END  
END
```

```
SOLVE_PRESSURE  
INITIAL_VALUES ALL 0.0  
BOUNDARY_CONDITIONS  
PATCH 2 FIXED_VALUE VALUE 0.0  
END  
RESIDUAL_REFERENCE 10.  
END  
END
```

```
SCALAR_MODULE  
SOLVE_walls  
TRANSIENT_TERM OFF  
CONVECTION_TERM OFF  
DIFFUSION_COEFFICIENT  
ALL CONSTANT 1.  
END  
INITIAL_VALUES ALL 0.0  
BOUNDARY_CONDITIONS  
PATCH 3 FIXED_VALUE VALUE 0.0  
END
```



## Appendix A

---

```
USER_SOURCE_TERMS
  LEVEL 0
END
END
END

HEAT_TRANSFER_MODULE
  SOLVE_TEMPERATURE
  INITIAL_VALUES ALL 1000.
  BOUNDARY_CONDITIONS
    PATCH 1 FIXED_VALUE VALUE 1600.
#   PATCH 6 FIXED_VALUE VALUE 1000.
    PATCH 3 USER_ROUTINE mould_heat 9 .005 5 0.5 3.0 1.6 2200. 1000. 1000. 1000.
  END
  RESIDUAL_REFERENCE 500.
END
END

SOLIDIFICATION_MODULE
  INITIAL_FRACTION_LIQUID PER_MATERIAL
  MATERIAL 1 1.
END
  FRACTION_LIQUID_FUNCTION
  MATERIAL 1 LINEAR_FUNCTION
END
  PERMEABILITY_COEFFICIENT 1.E-6
  UPDATE_TEMP ON
END

MONITOR_MODULE
  OUTPUT_INTERVAL 150
  MONITOR_LOCATION 0.101 0.0 0.0
END

POST-PROCESSING_MODULE
  FEMGV_FORMAT
END
  TECPLOT_FORMAT
  TECPLOT_FILE_NAME H
  TIME_FREQUENCY .1
END
END
STOP
```

## Appendix B

# Mathematic Descriptions for Porous Medium and Pipe Flow

### Porous Medium

A porous medium or a porous material [95] is a solid permeated by an interconnected network of pores (voids) filled with a fluid such as liquid or gas. Usually both the solid matrix and the pore are assumed to be continuous so as to form interpenetrating continua. Many natural substances such as rocks, soils and man-made materials such as ceramics and foams can be considered as porous media. A porous medium is characterised by its porosity, permeability as well as the properties of its constituents.

Through a porous medium, the flow of a fluid is described by Darcy's law. It is a simple proportional relationship between the instantaneous discharge rate through a porous medium and the local hydraulic gradient (change in hydraulic head over a distance). This relationship of proportionality is individually conservative for all the pores:

$$Q = -A \cdot \frac{k}{\eta} \cdot \frac{\Delta P}{L} \quad (\text{B.1})$$

where  $Q$ , the total discharge ( $\text{cm}^3/\text{s}$ ),  $k$  is the permeability of the porous medium;  $L$  is the length of the porous medium field;  $\Delta P$  is the pressure difference and  $\eta$  viscosity;  $A$  is the

## Appendix B

---

area of the cross section. The permeability  $\phi$  is got by using the Kozeny-Carmen equation [95]:

$$k = \frac{\phi^3}{C(1-\phi)^2 \cdot A_s'^2} \quad (\text{B.2})$$

$C$ , a constant, empirically  $C=5$ ;  $A_s'$ , the specific area, defined to:

$$A_s' = \frac{\text{area of grain walls}}{\text{volume of them}} = \frac{4\pi \left(\frac{d_{\text{grain}}}{2}\right)^2}{\frac{4\pi}{3} \left(\frac{d_{\text{grain}}}{2}\right)^3} = \frac{6}{d_{\text{grain}}} \quad (\text{B.3})$$

$d_{\text{grain}}$ , the diameter of the grain of porous medium. The equation is expressed:

$$k = \frac{d_{\text{grain}}^2 \cdot \phi^3}{180 \cdot (1-\phi)^2} \quad (\text{B.4})$$

Where  $\phi$  is the porosity which is defined as:

$$\phi = \frac{\text{volume of pores}}{\text{total volume of domain}} \quad (\text{B.5})$$

In the numerical model, the parameters, such as porosity  $\phi$ , the diameter of the grain  $d_{\text{grain}}$  and the thickness of the porous medium  $L$  are applied to simulate the flow in the porous medium.

## Pipe Flow

For pipe flow, the Darcy-Weisbach equation [96] is an important and widely used in hydraulics. It is often applied to calculate the head loss due to the friction within a given length of pipe.

$$h_f = f \cdot \frac{L}{d} \cdot \frac{v^2}{2g} \quad (\text{B.6})$$

This equation can be rewritten in terms of pressure loss:

$$\Delta P = \lambda \cdot \frac{L}{d} \cdot \frac{\rho v^2}{2} \quad (\text{B.7})$$

## Appendix B

The pipe diameter  $d$  is assumed to be constant.  $L$  and  $d$  are the length and the diameter of the pipe;  $v$  the average velocity of the fluid through the pipe;  $\lambda$  is the coefficient of laminar or turbulent flow. This coefficient varies according to the parameters of the pipe and the velocity of the flow. For laminar flows ( $Re < 2000$  in pipes),  $\lambda$  is simply equal to:

$$\lambda = \frac{64}{Re} \quad (B.8)$$

$Re$  is Reynolds Number. For turbulent flows ( $Re > 3000$  in pipes),  $\lambda$  is determined from experimental curve fits. One such fit is provided by Colebrook:

$$\frac{1}{\sqrt{f}} = -2 \cdot \log \left( \frac{e/D}{3.7} + \frac{2.51}{Re \sqrt{f}} \right) \quad (B.9)$$

The solutions to this equation plotted versus  $Re$  make up the popular Moody Chart [97] for pipe flow:

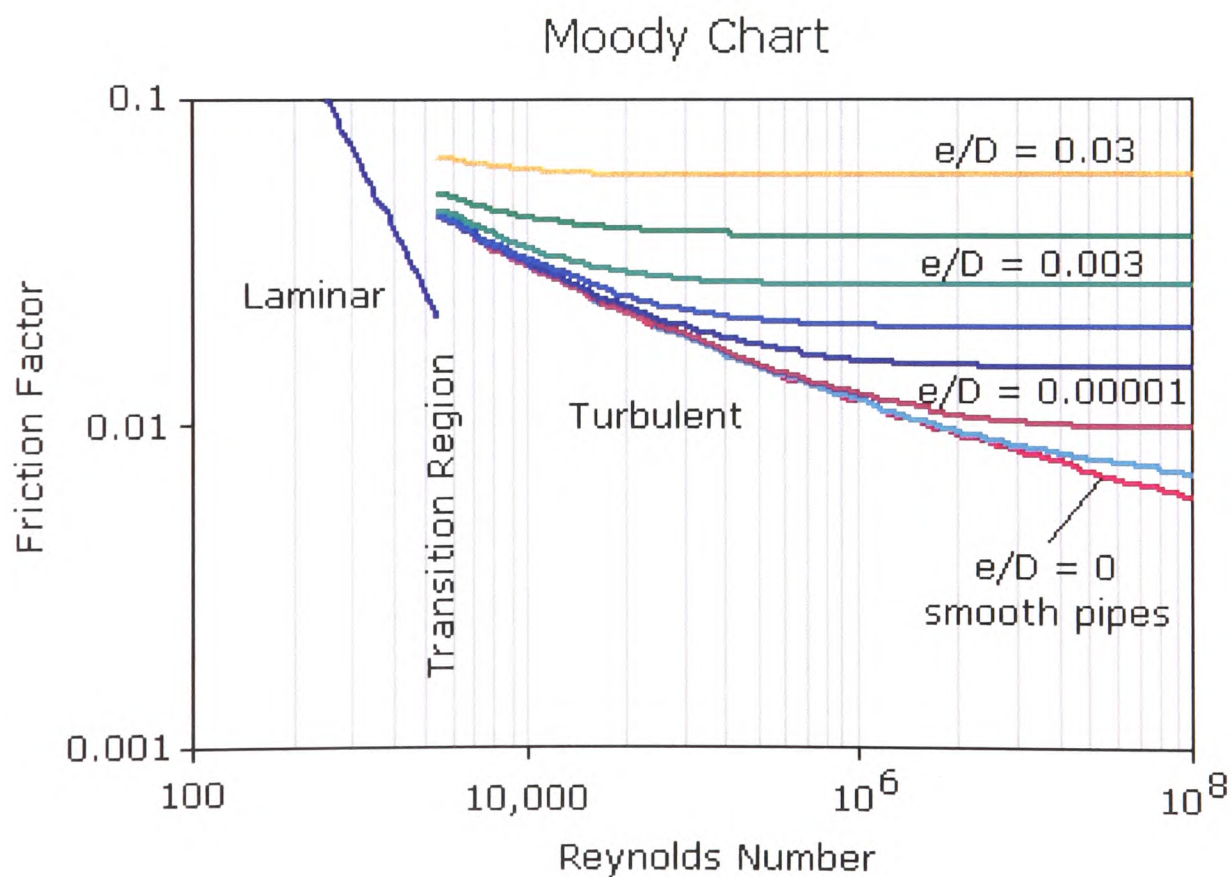


Figure B.1: Moody chart for pipe flow.

In this study, the flow in the mould is considered as laminar flow. So the Equation (B.7) is rewritten to:

## Appendix B

---

$$\Delta P = 64 \cdot \frac{\eta}{\rho v d} \cdot \frac{L}{d} \cdot \frac{\rho v^2}{2} = 32 \cdot \frac{\eta}{d} \cdot \frac{L}{d} \cdot \bar{v} \quad (\text{B.10})$$

The average velocity is:

$$\bar{v} = \frac{1}{32} \cdot \frac{d^2}{\eta} \cdot \frac{\Delta P}{L} \quad (\text{B.11})$$

The total charge by the pipe  $Q$  is:

$$Q = \bar{v} \cdot A_p = \bar{v} \cdot \frac{1}{4} \pi d^2 = \frac{1}{128} \cdot \frac{\pi d^4}{\eta} \cdot \frac{\Delta P}{L} \quad (\text{B.12})$$

## Approximation

Comparing the Equation (B.1) with the Equation (B.12), the following equation is got:

$$Q = \frac{1}{128} \cdot \frac{\pi d^4}{\eta} \cdot \frac{\Delta P}{L} = A \cdot \frac{k}{\eta} \cdot \frac{\Delta P}{L} \quad (\text{B.13})$$

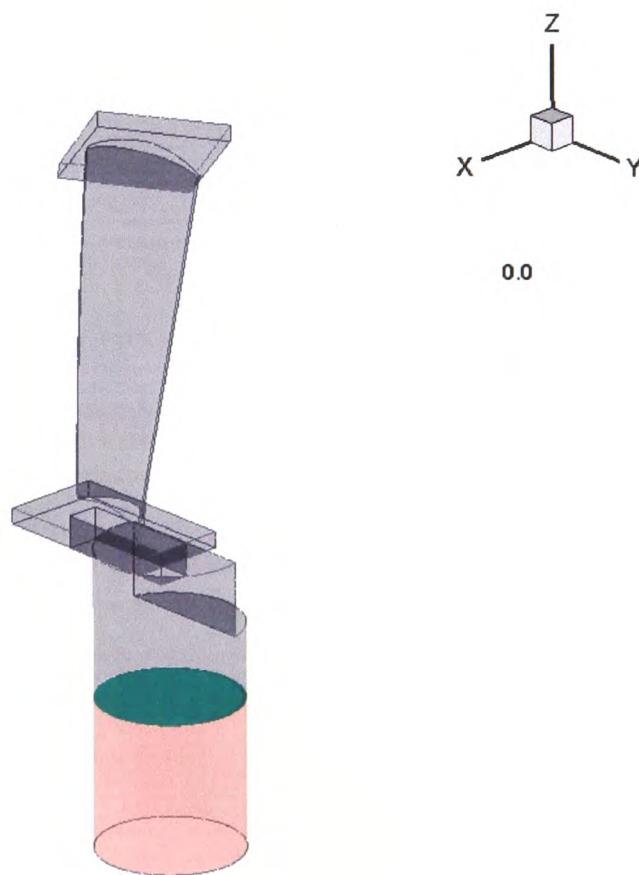
The relation between the permeability and the artificial diameter of the vent is:

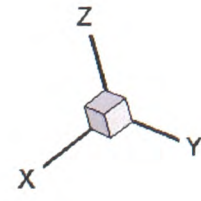
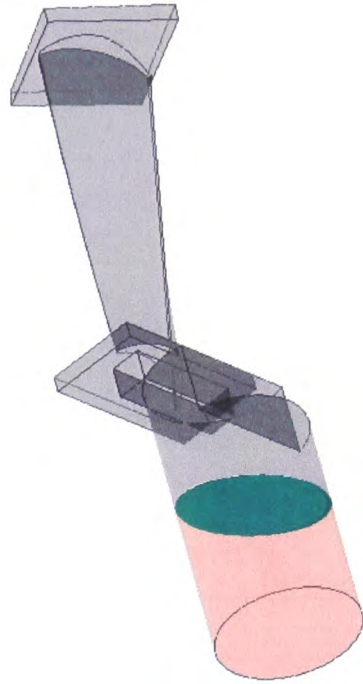
$$d = \sqrt[4]{128 \cdot A \cdot k} \quad (\text{B.14})$$



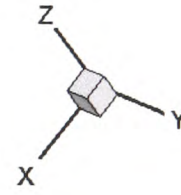
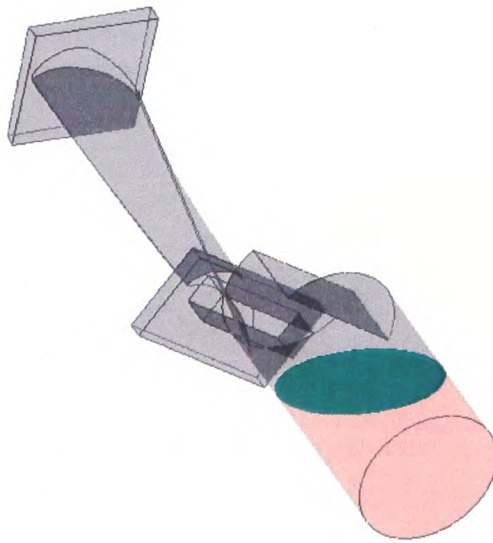
## Appendix C

### Mould Filling for a Twisted Blade

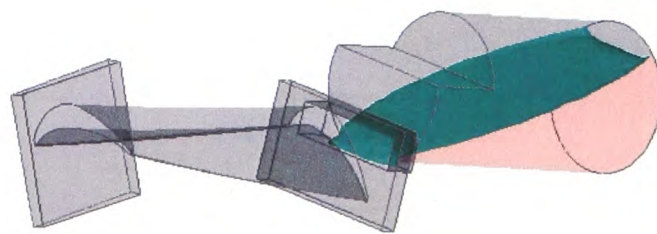
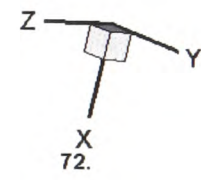
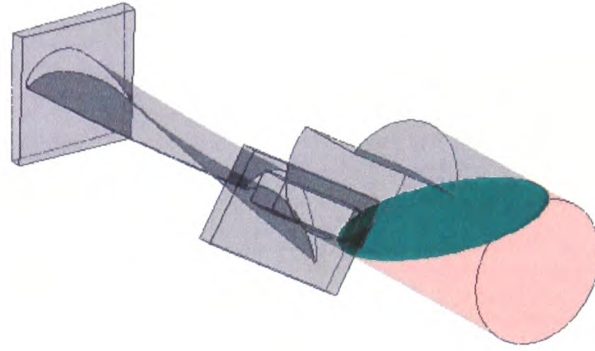
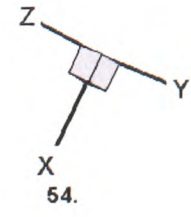




18.

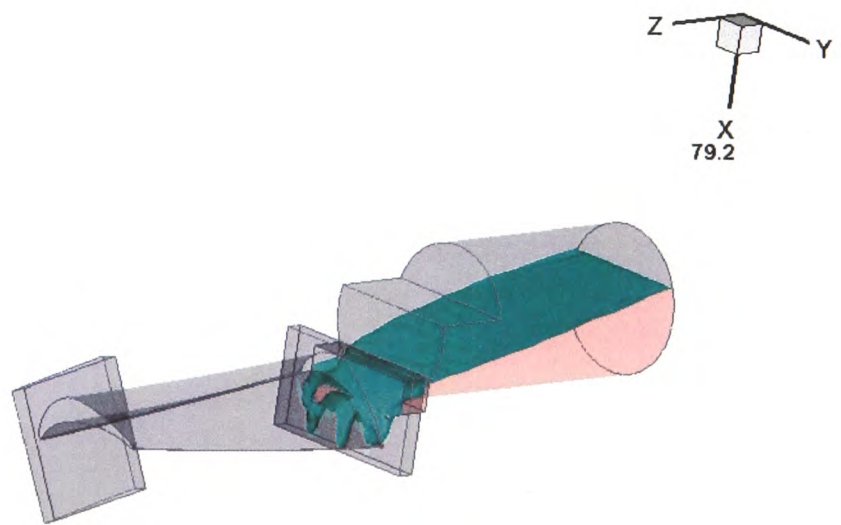
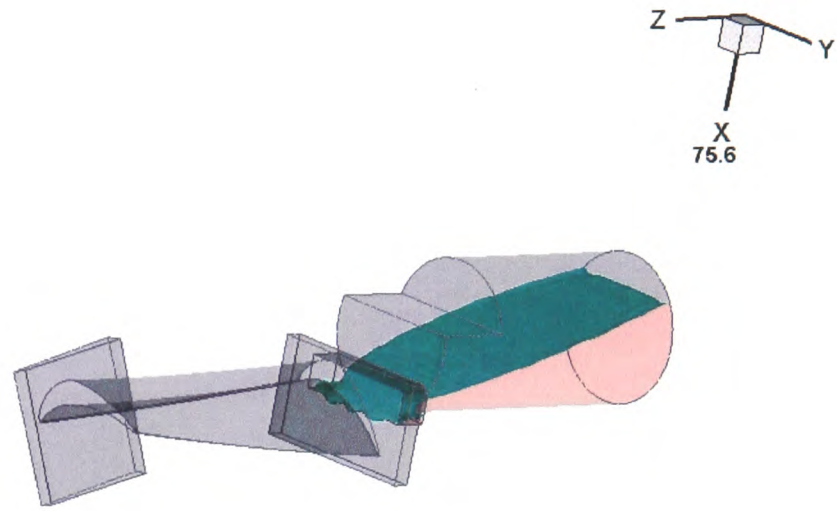


36.



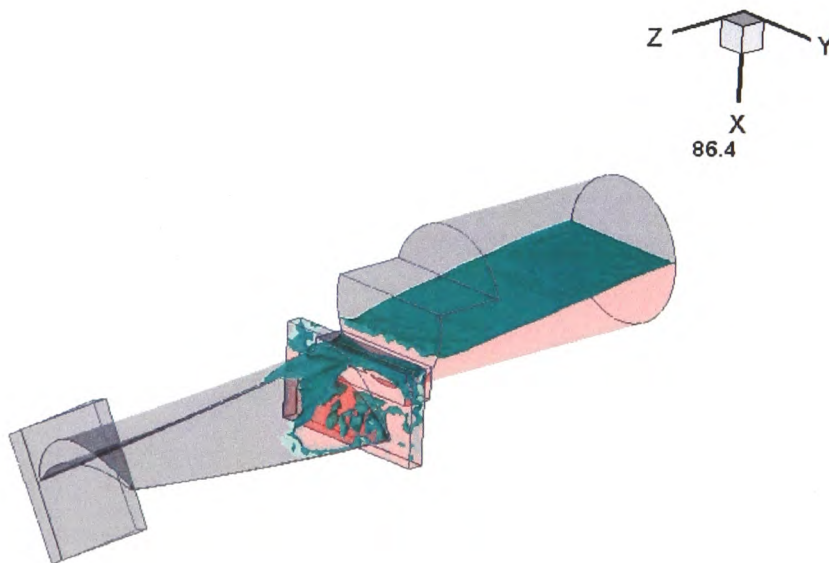
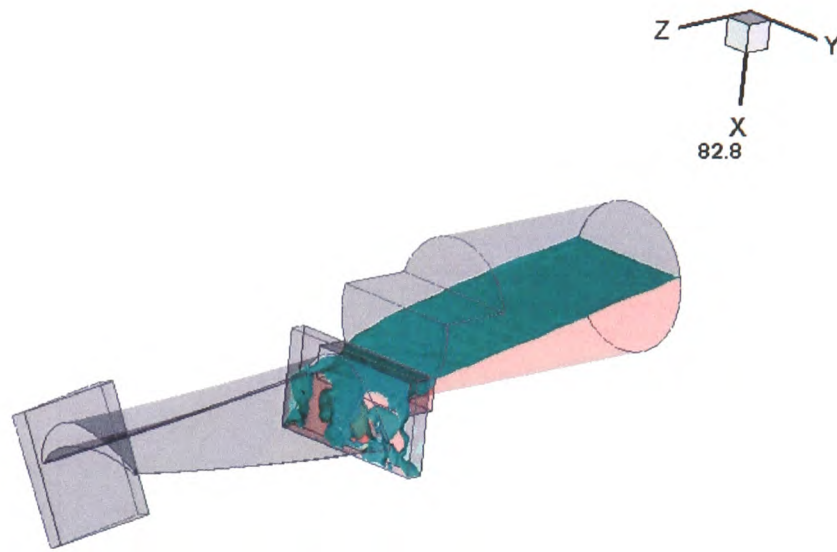
# Appendix C

---



## Appendix C

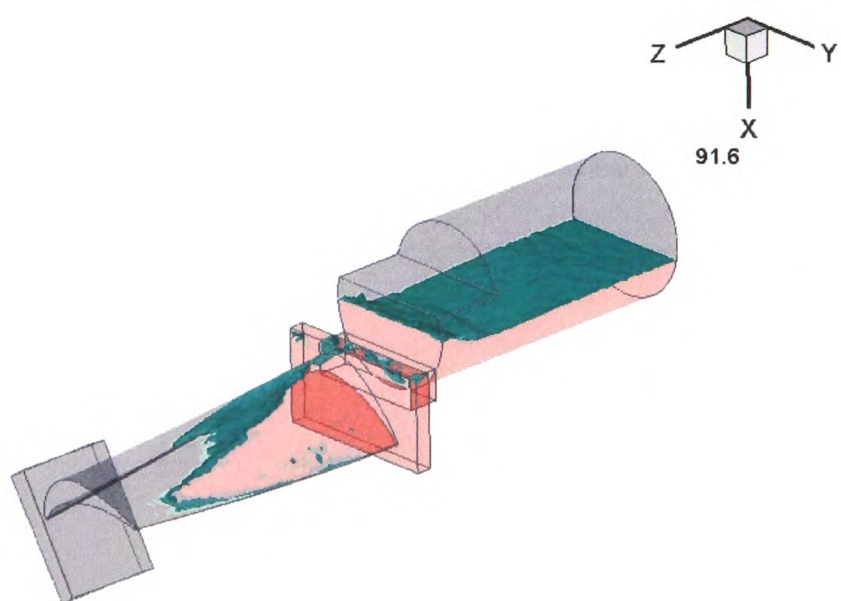
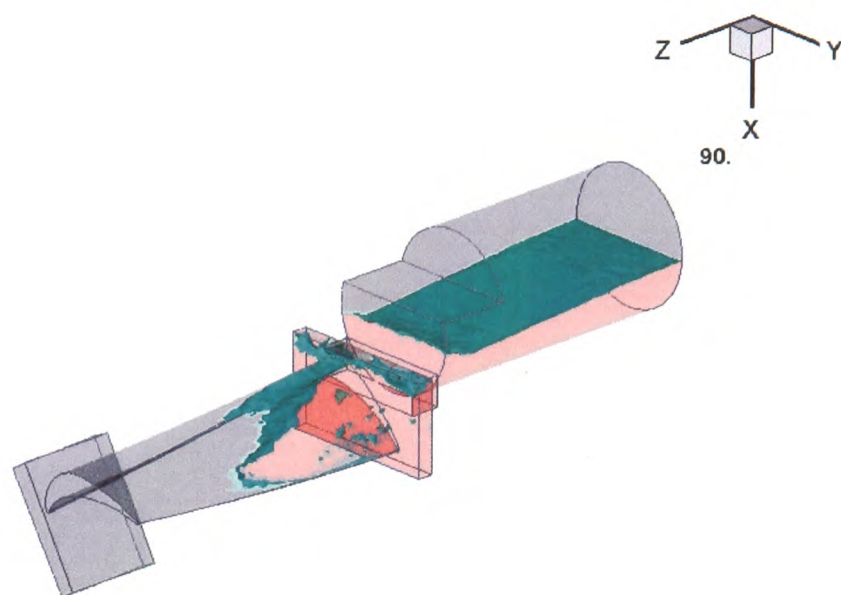
---





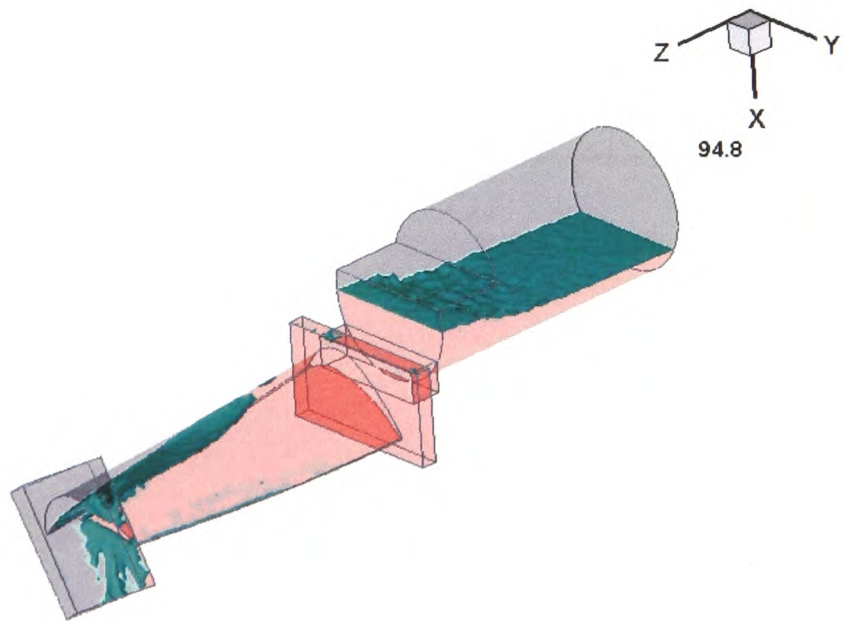
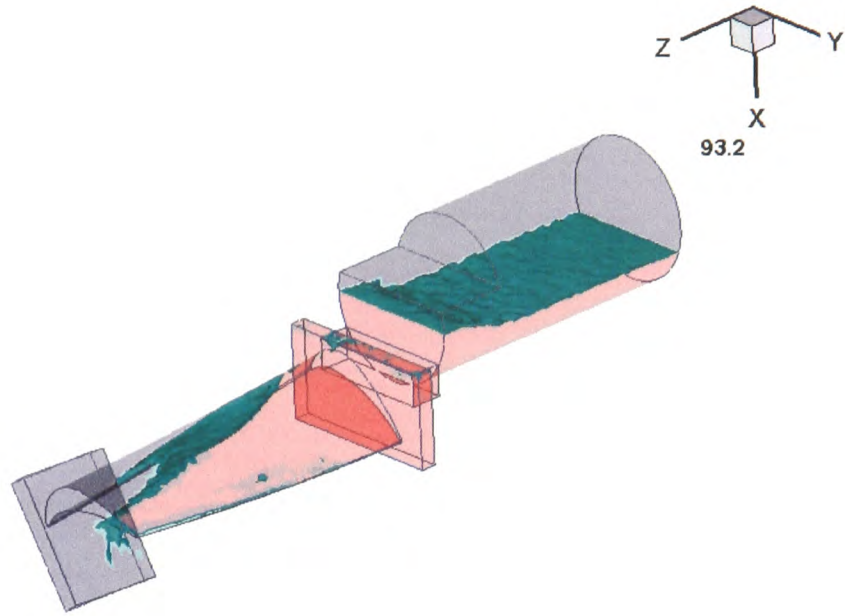
# Appendix C

---



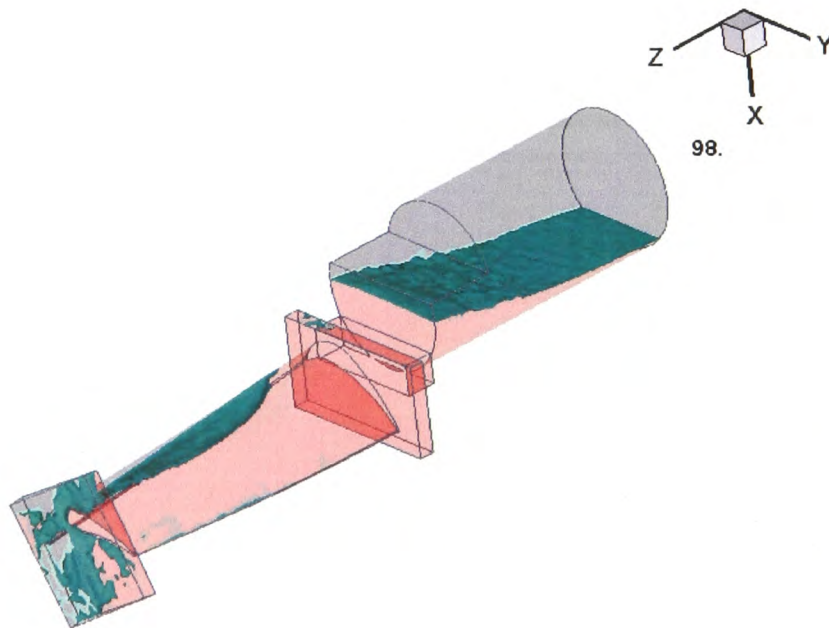
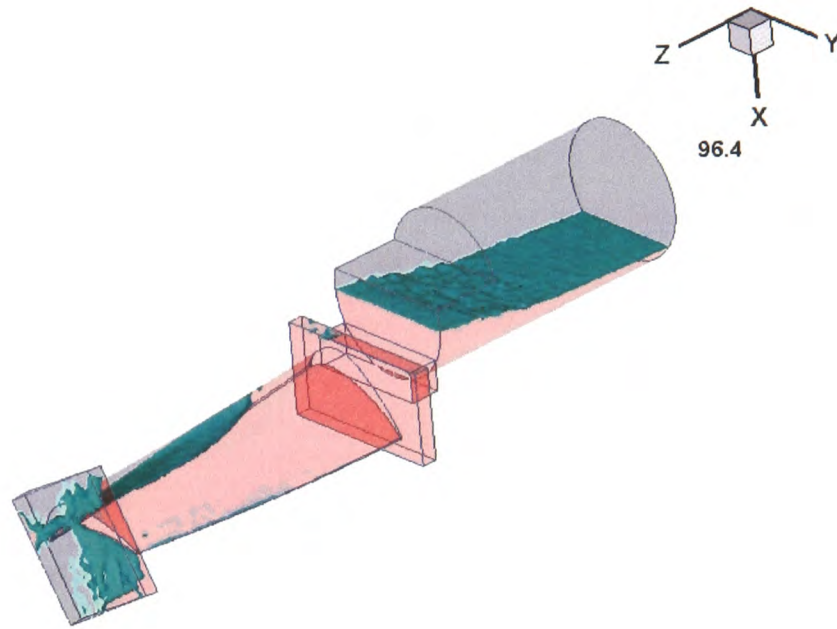
# Appendix C

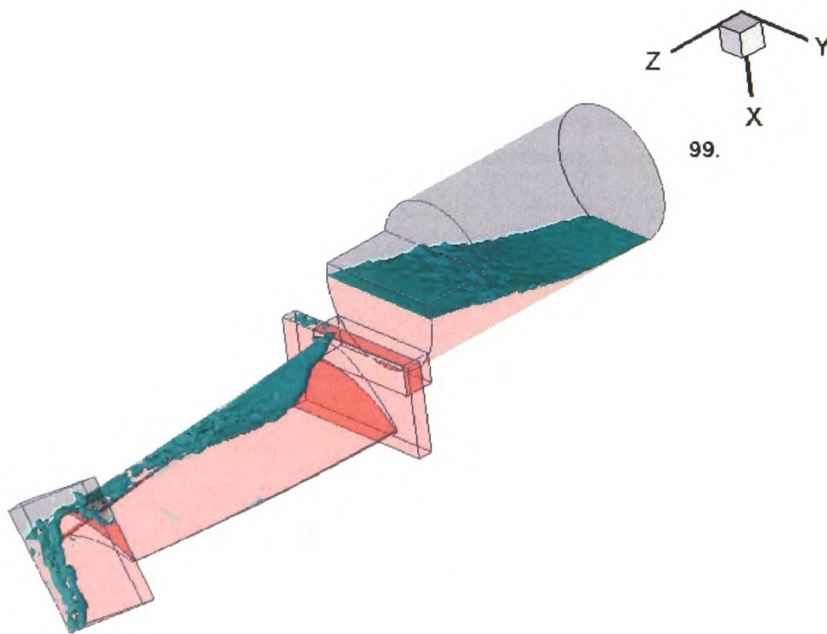
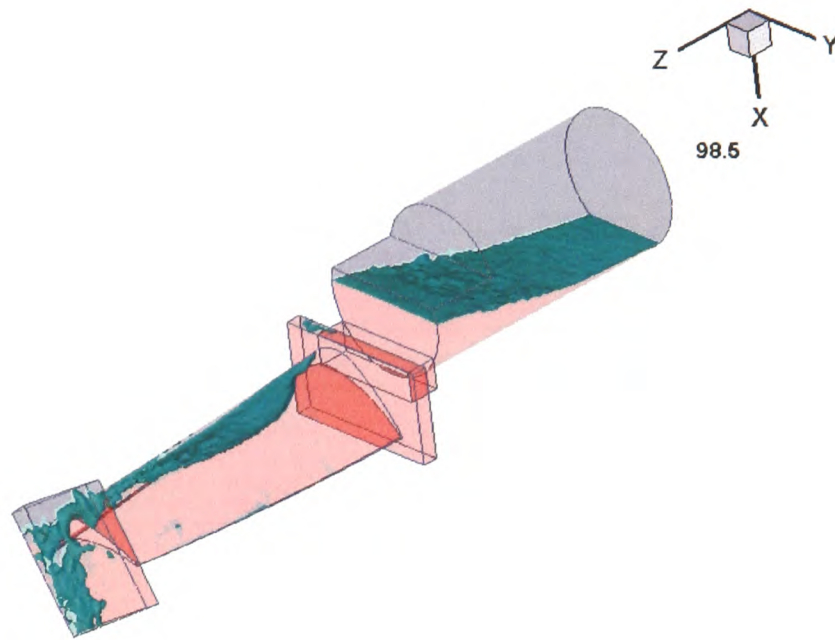
---



# Appendix C

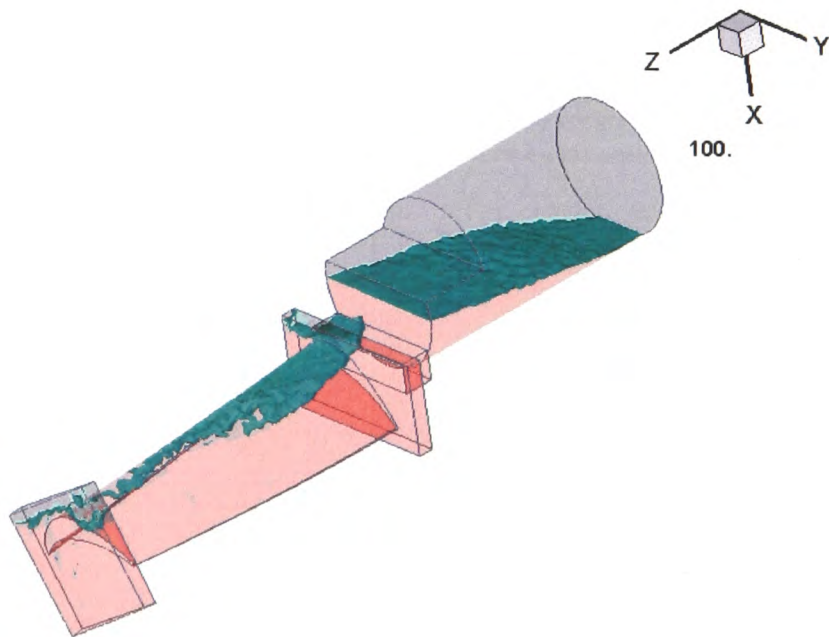
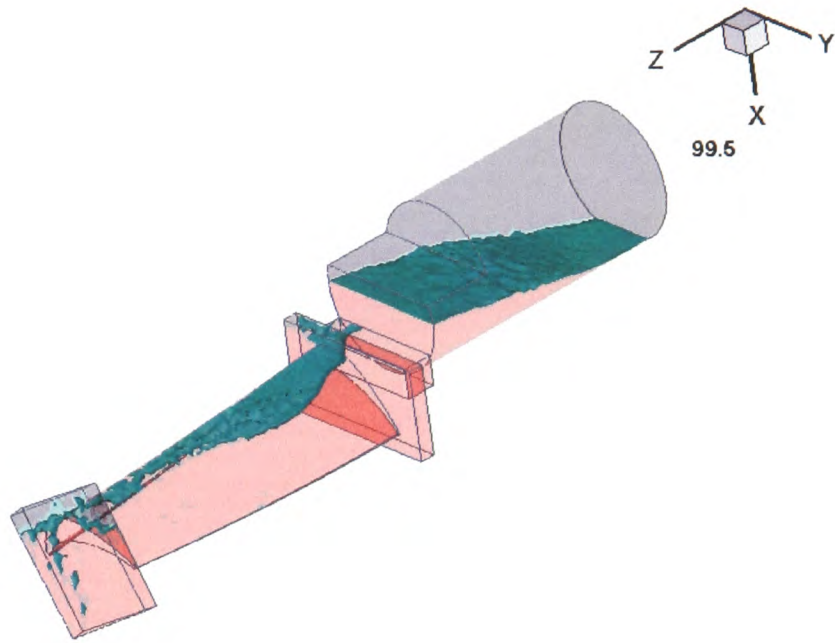
---





Appendix C

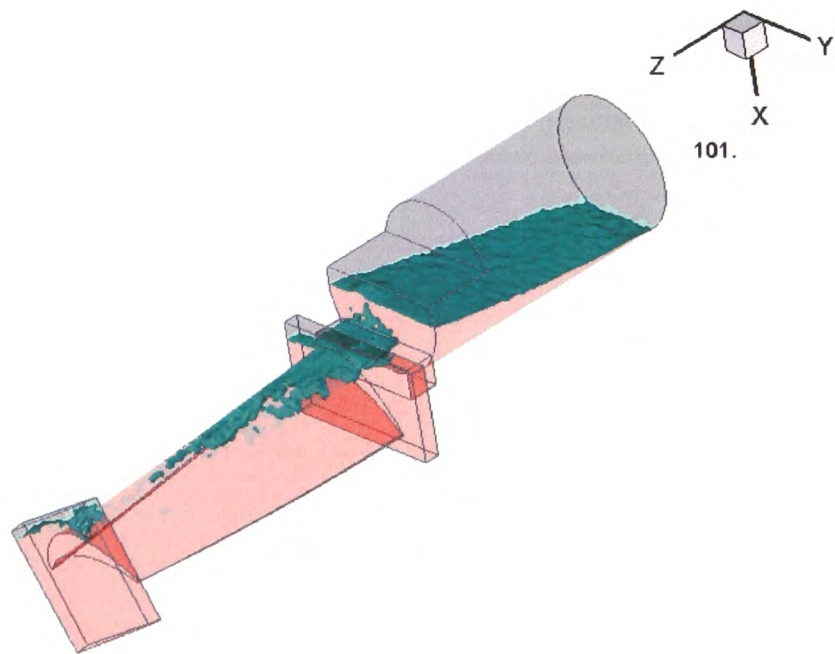
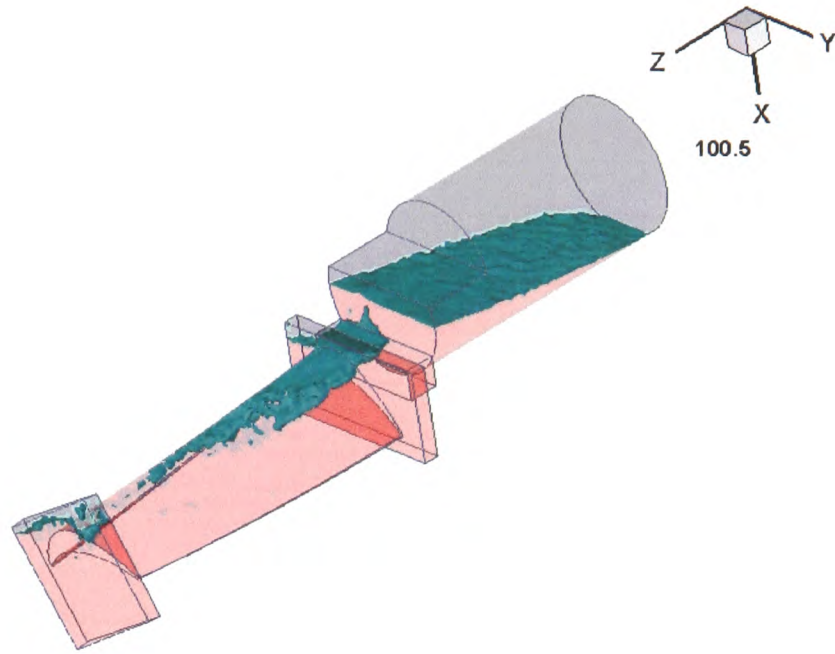
---





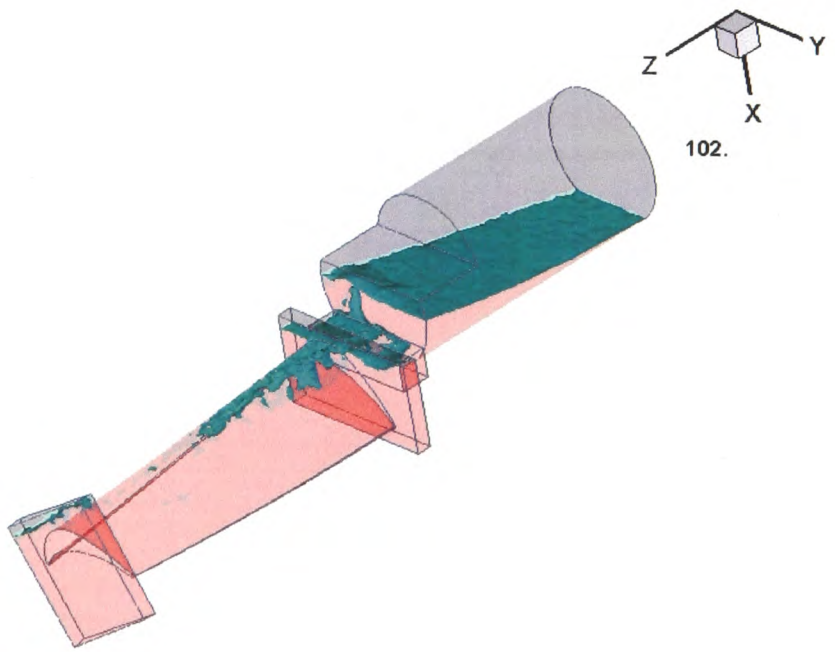
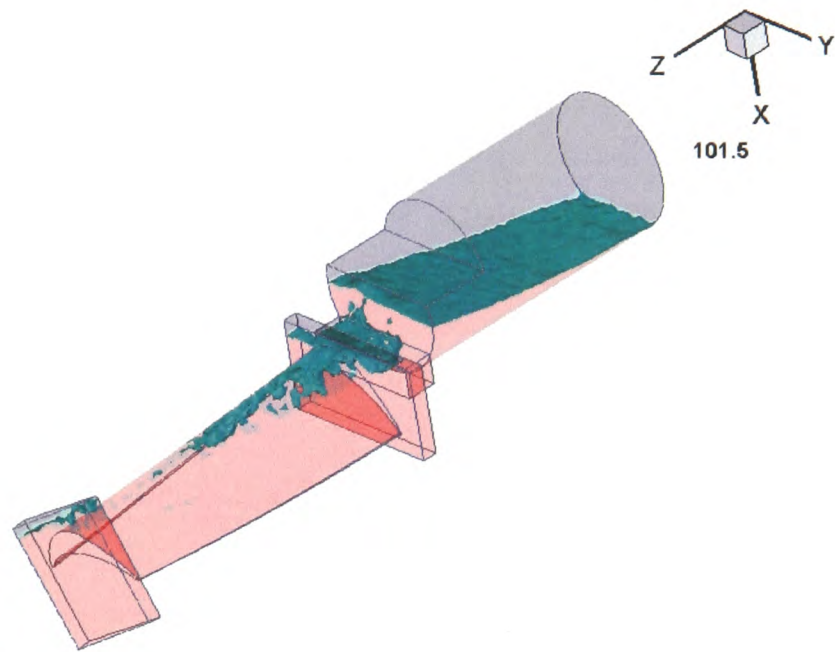
# Appendix C

---



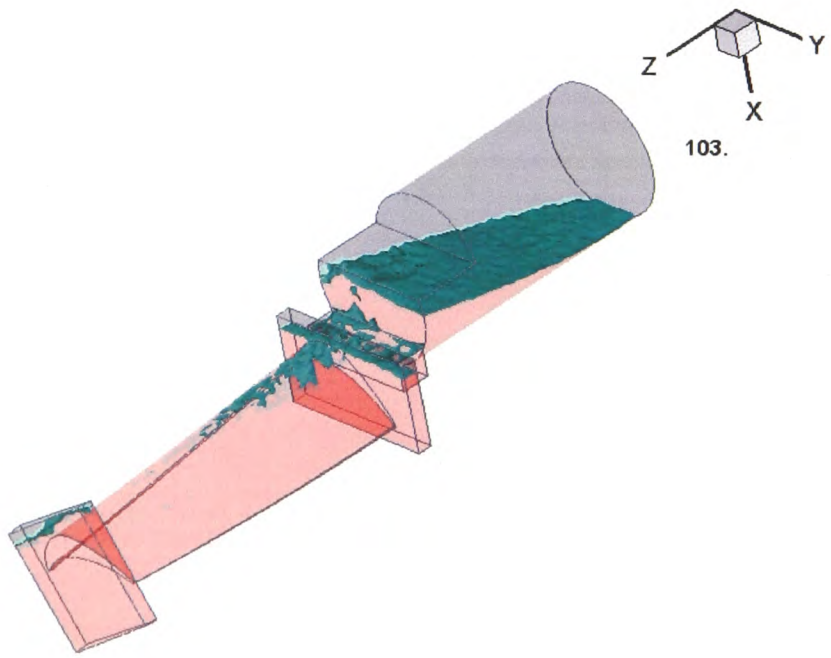
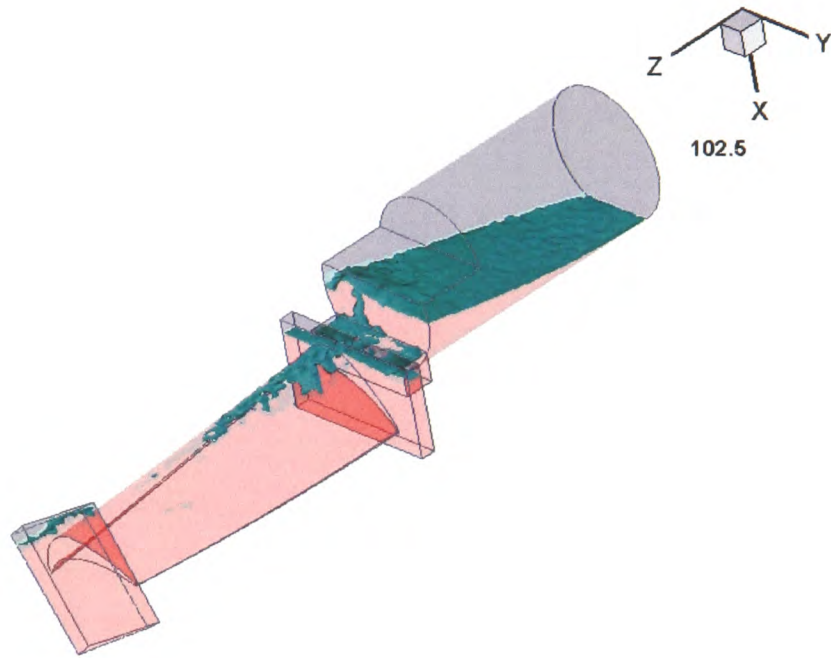
# Appendix C

---



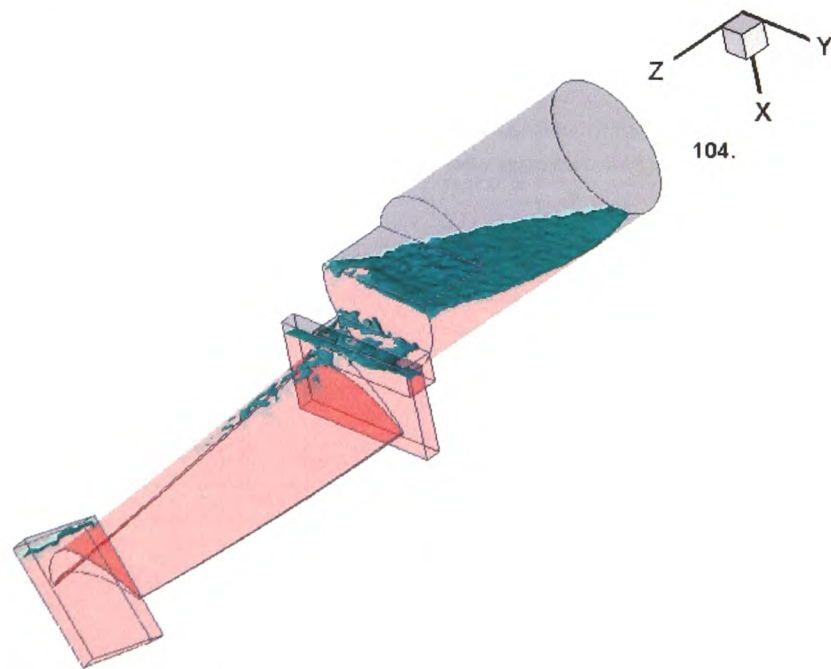
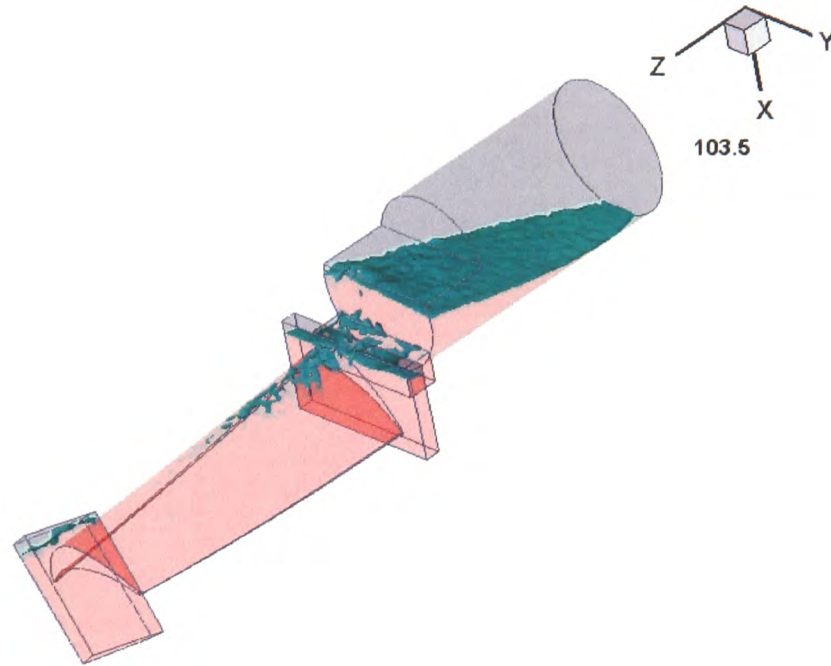
Appendix C

---



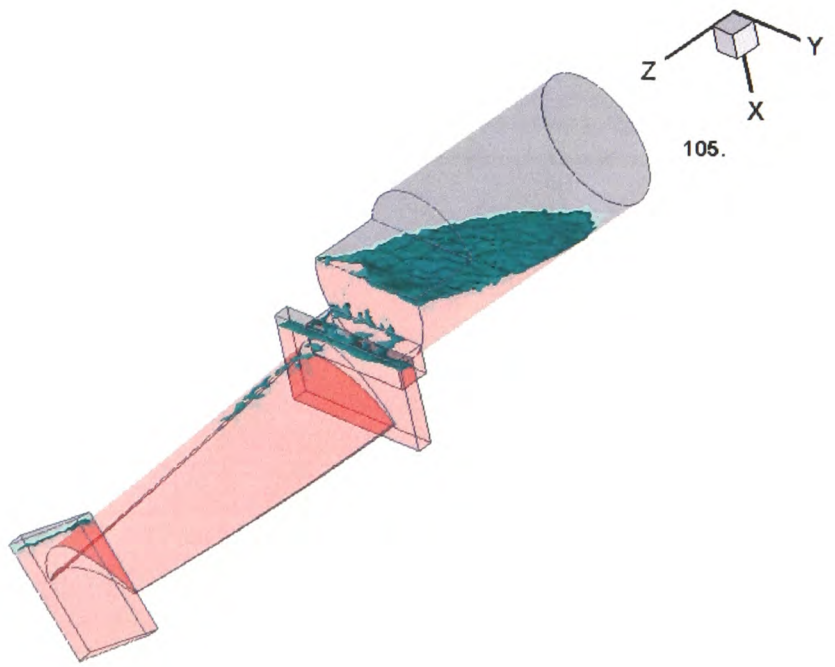
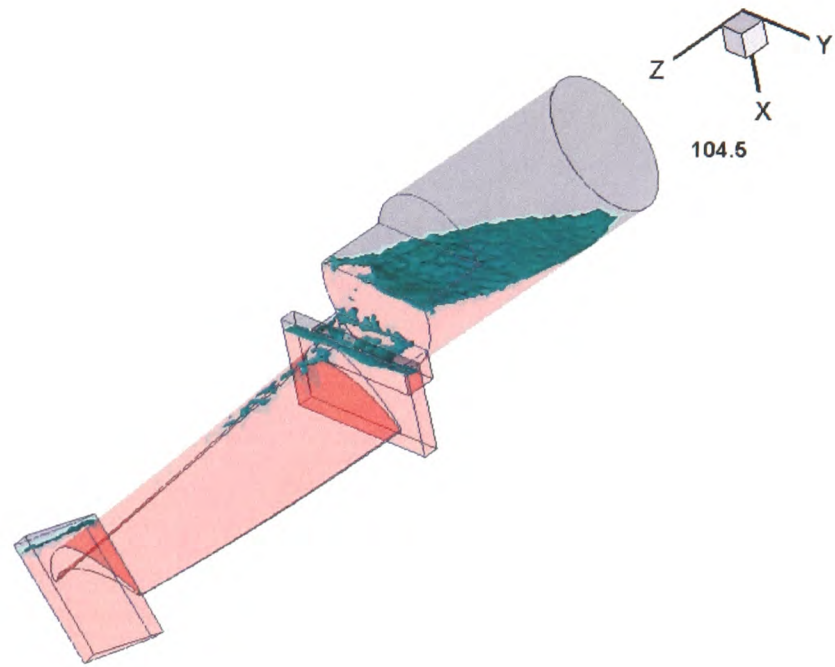
# Appendix C

---

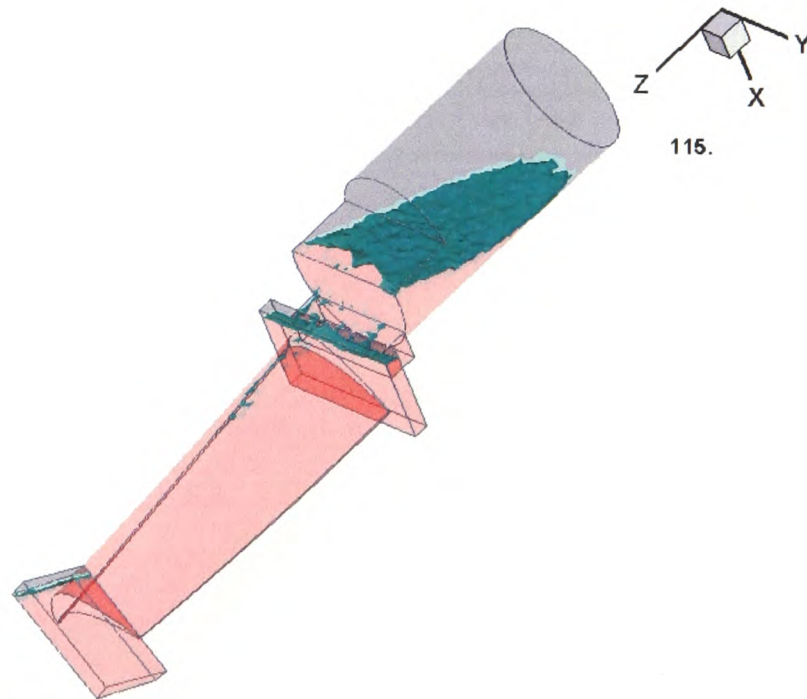
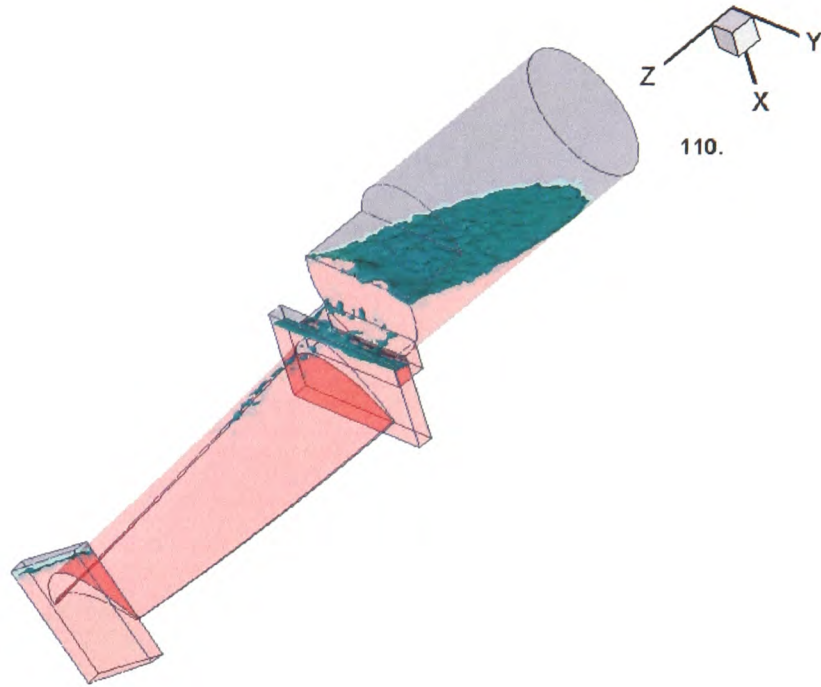


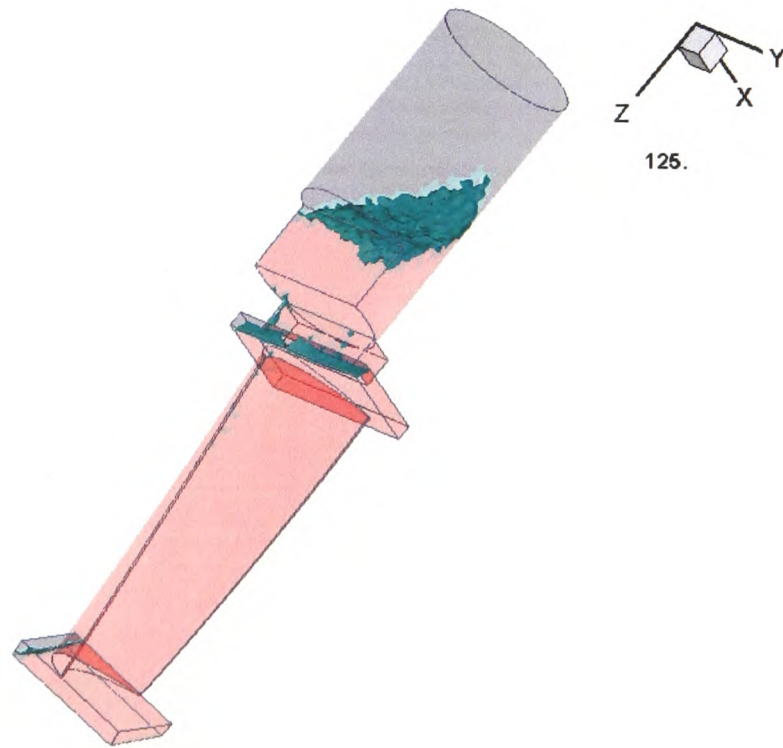
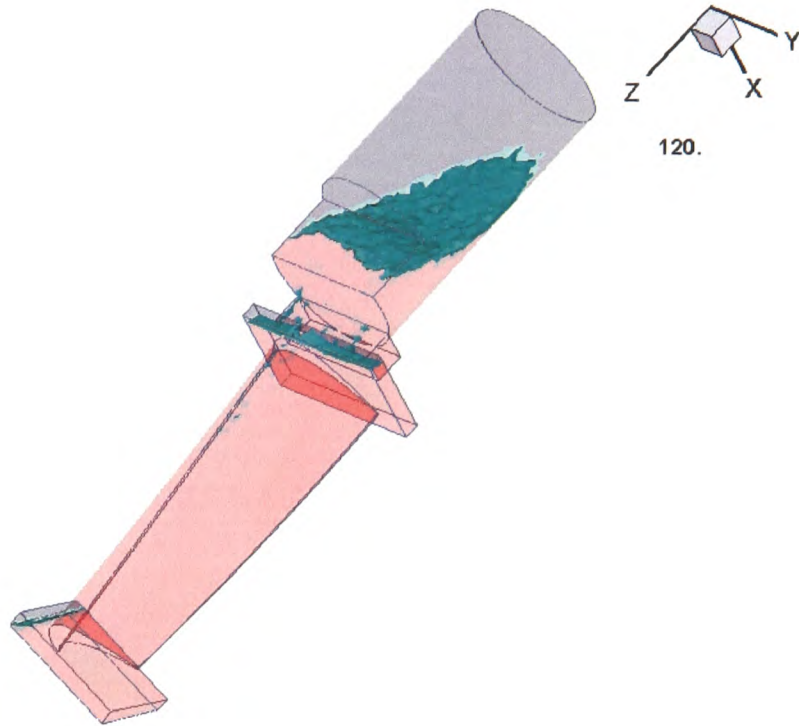
# Appendix C

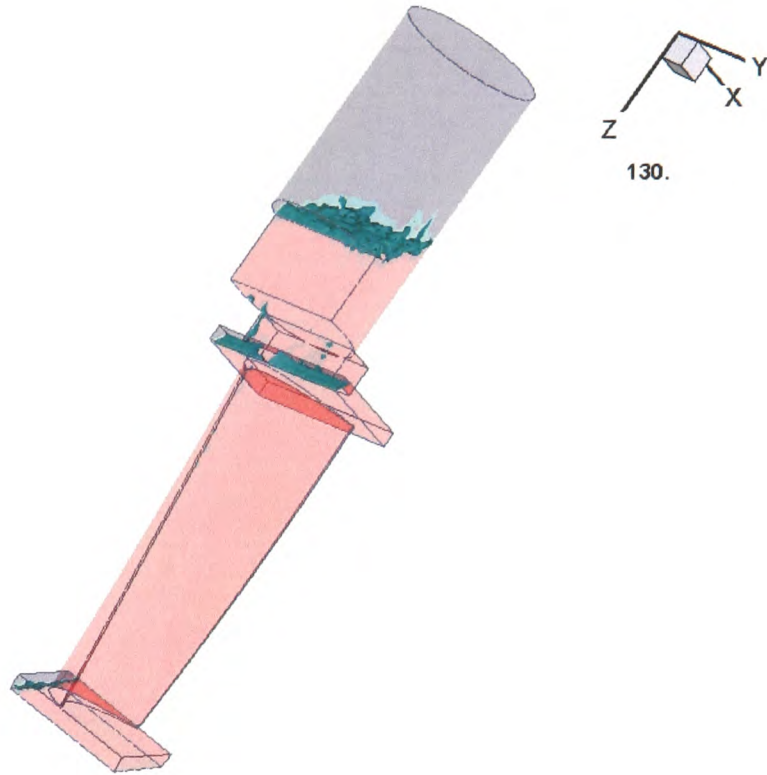
---



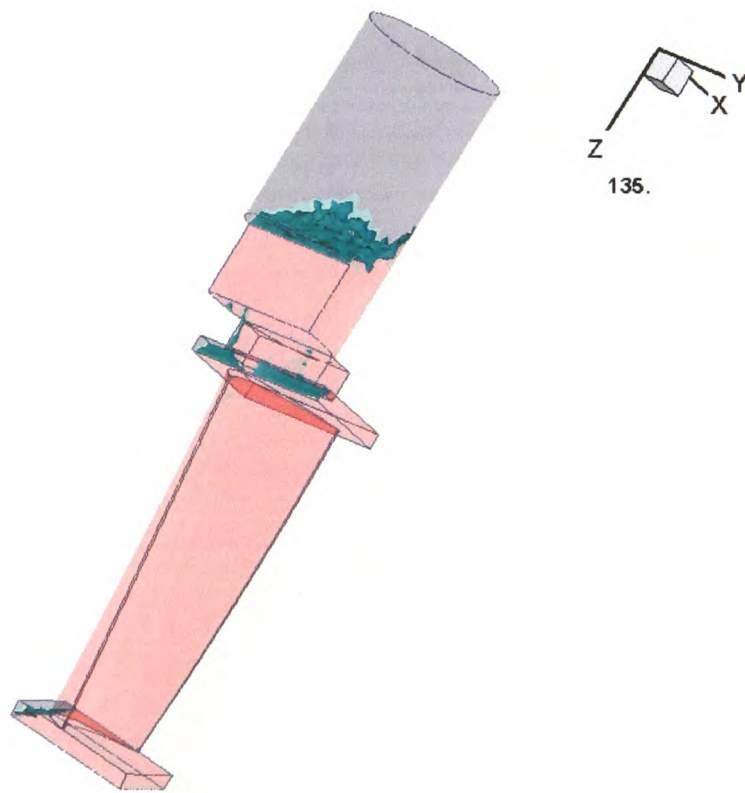




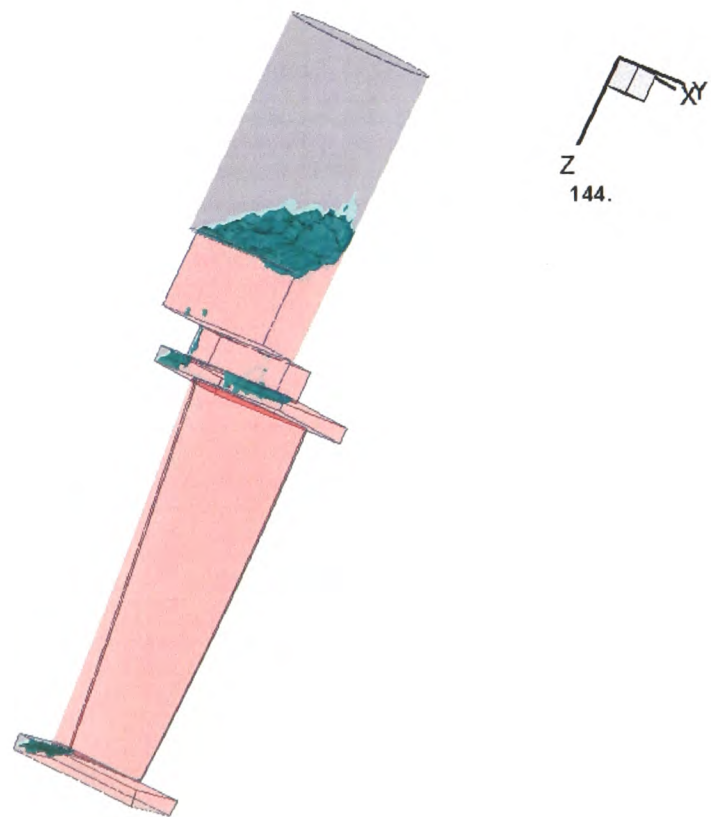
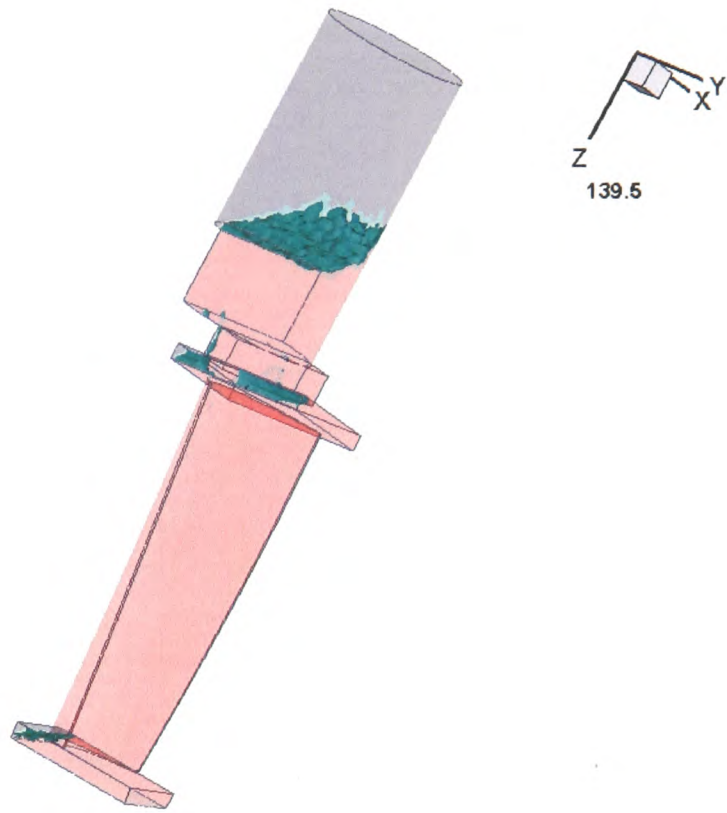


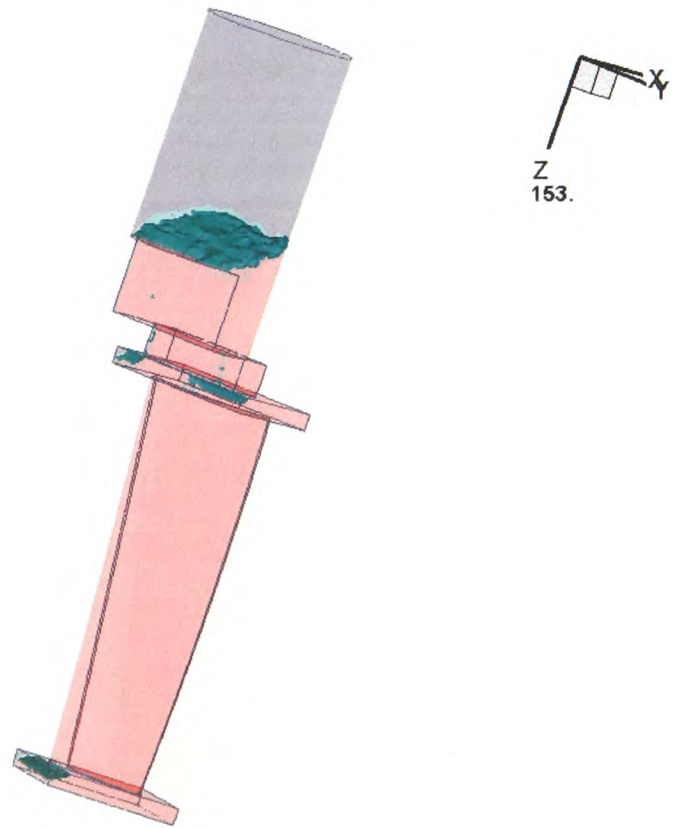
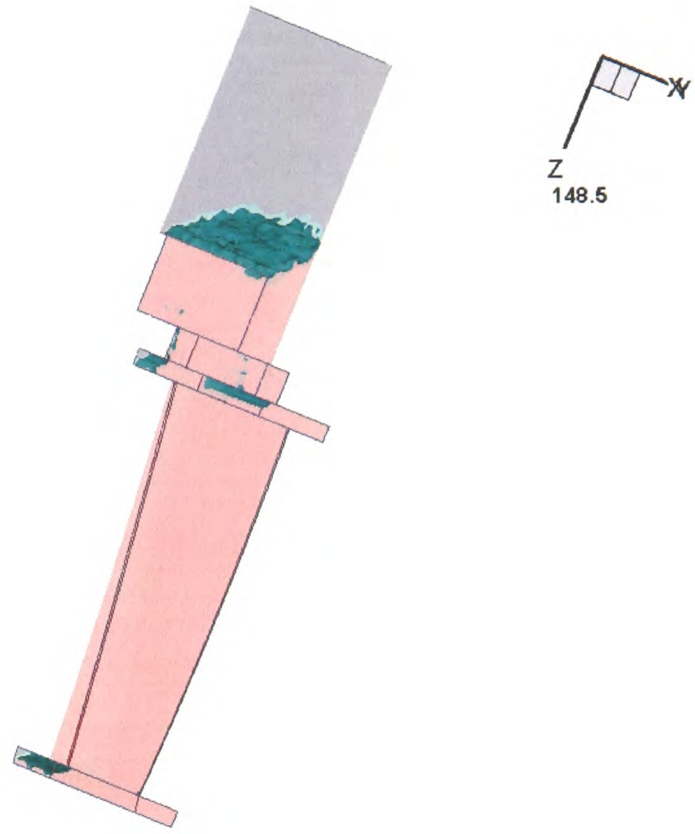


130.

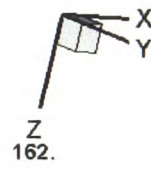
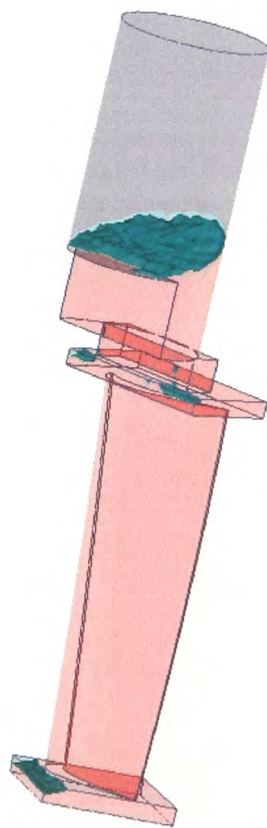
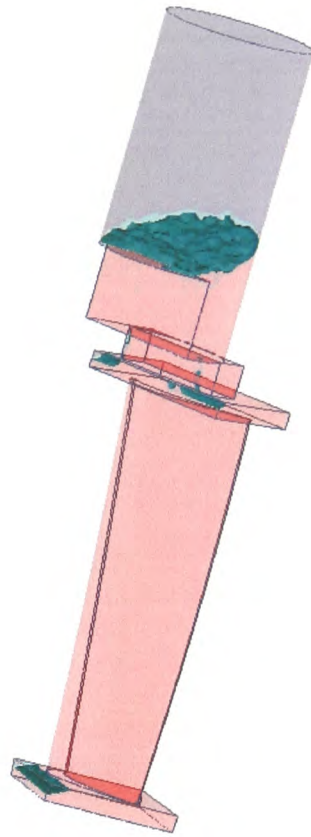


135.



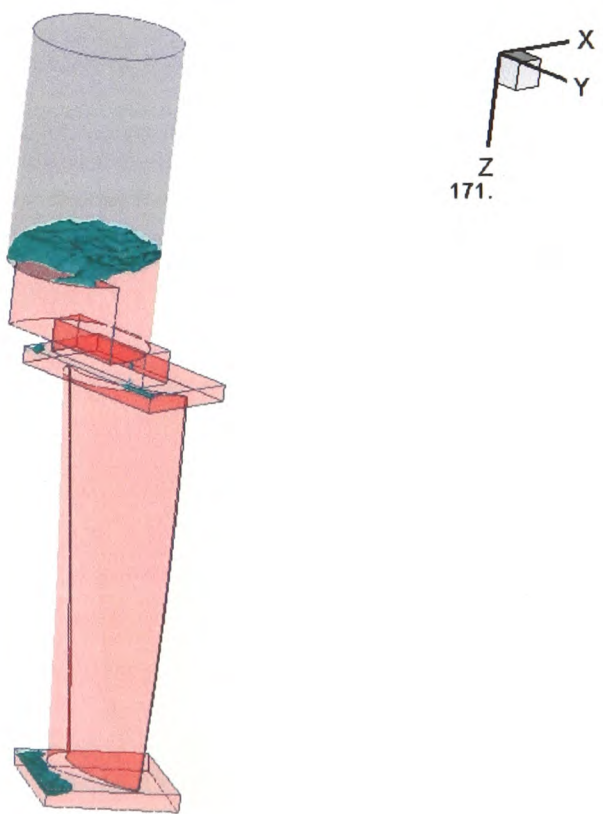
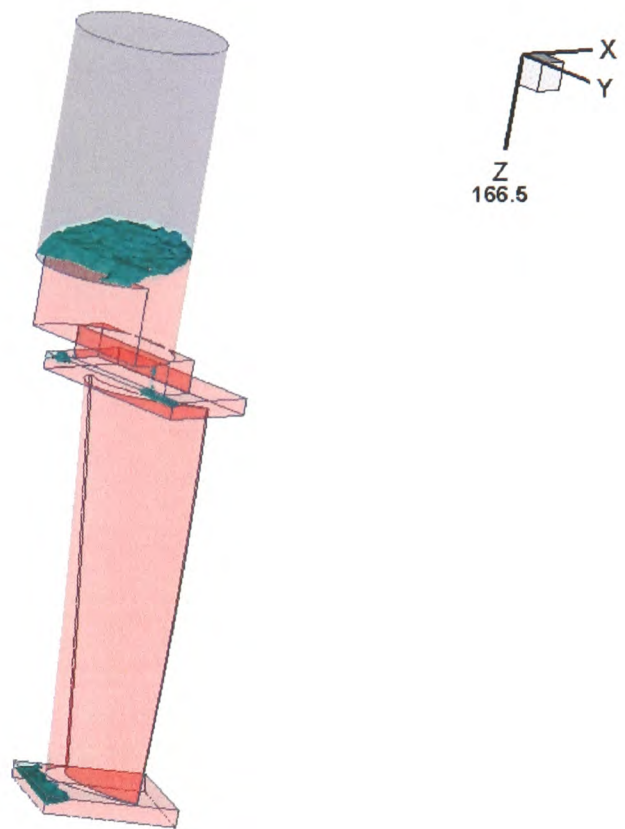


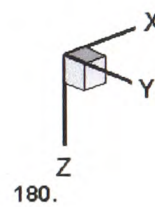
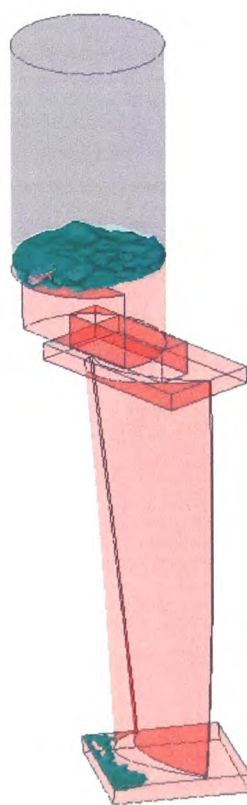
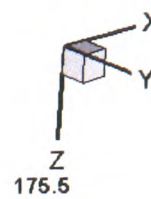
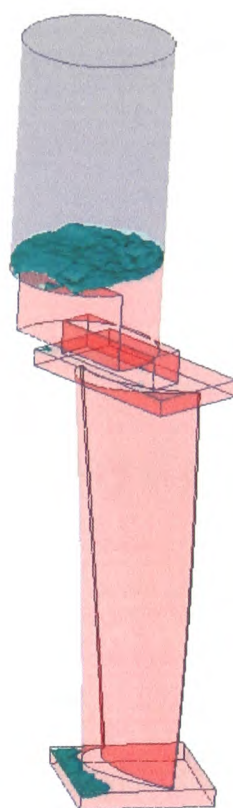




# Appendix C

---





## Appendix D

# INFORM File for Modelling the Solidification

```
GEOMETRY_MODULE  
  FILENAME blade  
  GRAVITY_X 9.81  
END
```

```
GENERIC_MODULE  
  TRANSIENT_RUN  
  DELTA_T  
  USER_DELTA_T  
  FOR_ALL_TIME_STEPS 1.  
  END  
  END_TIME 150.00  
  SAVE_AT_EVERY_TIME_STEP -1  
  END  
  MAX_SWEEPS 50  
  MIN_SWEEPS 2  
END
```

```
DATABASE_MODULE  
  OUTPUT_DATABASE solid150  
# INPUT_DATABASE solid2  
END
```

```
MATERIAL_PROPERTY_MODULE  
  DENSITY  
  MATERIAL 1 CONSTANT 3850.  
  END
```

```
THERMAL_CONDUCTIVITY  
  MATERIAL 1 CONSTANT 21.6
```

## Appendix D

---

```
END

SPECIFIC_HEAT
  MATERIAL 1 CONSTANT 1000.
END

LIQUIDUS_TEMPERATURE
  MATERIAL 1 CONSTANT 1569.
END

SOLIDUS_TEMPERATURE
  MATERIAL 1 CONSTANT 1500.
END

LATENT_HEAT
  MATERIAL 1 CONSTANT 355000.
END

VISCOSITY
  MATERIAL 1 CONSTANT 1.6e-6
END
END

HEAT_TRANSFER_MODULE
  SOLVE_TEMPERATURE
    INITIAL_VALUES ALL 1600.
  BOUNDARY_CONDITIONS
    PATCH 1 USER_ROUTINE mould_heat1 10 .005 5 1. 1.0 1.6 2200. 1000. 1200.
0.0001 34001
    PATCH 3 USER_ROUTINE mould_heat1 10 .005 5 1. 1.0 1.6 2200. 1000. 1200. 0.00
34001
    PATCH 4 USER_ROUTINE mould_heat1 10 .005 5 1. 1.0 1.6 2200. 1000. 1200. 0.00
34001
    PATCH 5 USER_ROUTINE mould_heat1 10 .005 5 1. 1.0 1.6 2200. 1000. 1200. 0.00
34001
    PATCH 2 COEFF_VALUE COEFF 1000 VALUE 1200.
  END
  RESIDUAL_REFERENCE 100.
END
END

SOLIDIFICATION_MODULE
  INITIAL_FRACTION_LIQUID PER_MATERIAL
    MATERIAL 1 1.
  END
  FRACTION_LIQUID_FUNCTION
    MATERIAL 1 LINEAR_FUNCTION
  END
  PERMEABILITY_COEFFICIENT 1.E-6
```



## Appendix D

---

UPDATE\_TEMP ON  
END

MONITOR\_MODULE  
OUTPUT\_INTERVAL 10  
FRACTION\_DIGITS 5  
BLOCK\_FORMAT Off  
END

POST-PROCESSING\_MODULE  
TECPLOT\_FORMAT  
WRITE\_INITIAL\_VALUES ON  
TECPLOT\_FILE\_NAME S  
TIME\_FREQUENCY 10.  
END  
END

STOP